Ground Vibration Testing and Finite Element Model Updating of Very Flexible Aircraft

by

Bilal Sharqi

A dissertation submitted in partial fulfillment
of the requirements for the degree of
Doctor of Philosophy
(Aerospace Engineering)
in the University of Michigan
2024

Doctoral Committee:

Professor Carlos E. S. Cesnik, Chair
Professor Branko Kerkez
Professor Daniella E. Raveh
Professor Veera Sundararaghavan

Bilal Sharqi
bilalsh@umich.edu
ORCID iD: 0000-0001-6837-9967

DEDICATION

To Dexter.

To the people who helped me along the journey. To those that made this work possible, and to those who will build upon it.

ACKNOWLEDGMENTS

When I first started my grad school journey at Michigan, I had no intention of staying for a PhD. I remember walking into one of the labs during the Structural Dynamics class, and seeing a weird looking flying wing, the X-HALE. I asked the person overseeing the lab, Dr. Jessica Jones, about the aircraft and kept pestering her until I understood why it existed and if it flew. I am grateful to Jessica for taking the time to not only answer my questions, but to mentor me. She spent a substantial amount of time in her final semester helping me, and I would probably would not have been here had she not shown me the patience and kindness she did at the beginning. I then went and asked Prof. Carlos E.S. Cesnik if I could work on flight testing of the X-HALE since I thought that would be cool. I would like to thank my advisor and friend Carlos for giving me the opportunity to work with him at the Active Aeroelasticity and Structures Research Lab. I am grateful to Carlos not only for his mentorship, but also for always having my back and challenging me to do better. I do not think I am an easy person to work with, and at times, can be difficult to advise or manage. I hope I lived up to his expectations and will be forever grateful for his guidance and for accepting me into his research group. I can only hope that one day I am able to give a similar opportunity to someone. During my time at the A^2SRL, I participated in planning and orchestrating multiple flight tests, along with wind tunnel or ground tests on various experimental test articles. This motivated my desire to dive deeper into the topics my research focuses on.

A shout out to my committee members, thank you for accepting my invitation to serve on the committee and for the valuable inputs in my dissertation. A special thank you to Prof. Daniella E. Raveh, who collaborated with us on both work and social activities whenever she would visit Michigan.

Thank you to my parents who supported me in my journey, as I moved to different countries to pursue my goals. Thank you to my sisters, who have been a constant source of inspiration and learning. I have been absent for a lot of the growing up my sisters had to do, and that is something I hope to make up for in the coming years.

As for my colleagues, I had the distinct pleasure of working with some of the best people I have known in my life. I wish every single one of them the best and would be glad if our paths cross again in the future. The road to the PhD was filled with vibration and noise, but you guys dampened it out and turned some of the disturbances into potential and kinetic energy. I

would like to thank everyone I have interacted with at A^2SRL for their support, guidance and friendship. I have created a lot of pleasant memories in Ann Arbor that I cherish and will keep with me. In alphabetical order, thank you: Ana, for the purplesaurus flex; Anne, for being one of the kindest people I have known; Braden, for the infectious excitement about the small things; Bernardo, for the debugging; Chris Lupp, for helping me with MTK, and providing a different perspective than everyone else; Cristina, for being an emotional pasta cooker, and an amazing professor; Divya, for always being simultaneously critical, sarcastic and helpful; Guillaume, for the implication; Guilherme, for his fondness for alcohol and expertise in electromechanics; Jasmine, for her indexing and wire management abilities; Jessica, for the rock solid support when I started; Joao, for the deep conversations on religions; Leandro, for being unhinged and always getting in and out of trouble; Larissa (and Kayc), for Bill, Frank, and wish you were here; Manon, for being so quick at learning new things that I learnt a few things back from her; Nathan, for the stress baking and enthusiasm about helping people; Oscar, for the sound effects and the Oscar multiverse theory; Patricia and Renato, for being great friends and some of the nicest people I know; Patrizio, for the Taiwanese movies; Qingzhao, for God of War; Rafael, for being a rockstar in every situation; Thiago G, for his passion and friendship; Thiago V, for showing me there's always time for football and a beer.

I have had the opportunity of working with various students from different disciplines, and while there are too many to list here, I enjoyed mentoring and learning new things from each one of them. The undergrad and graduate students that I worked with have contributed to substantial parts of my research. Every time I had an interest in a topic parallel to my own research, and did not have the bandwidth to engage on that topic, I was lucky enough to find a student who I could explore that topic with, and learn from their research. I would highly recommend graduate students pursue more mentoring responsibilities, it truly gives back more than you put into it. Something that I value and take away from these experiences is the ability to dive into a problem before fully knowing how to solve it – take calculated risks. My students, without either me or them realizing it, helped me get better at tackling a relatively abstract problem and breaking it down into solvable chunks. I wish them the best in their future. Their successes are an endless source of joy for me.

I would like to thank our collaborators from external research groups, especially Profs. Moti Karpel and Daniella Raveh from Technion, and Matthew McCrink from Ohio State University. Tsoof, Noam, Dhuree and Ross, thank you for your help with setting up and conducting the various tests on the A3TB-WT.

A very special shout out to the technicians in the Aerospace department. Thank you Aaron, Chris, Dave, Doug, and Tom. You guys are awesome and really went above and beyond in supporting me as I worked on the various experiments that constitute this work (and some that are beyond the scope of this dissertation).

This work was initially supported by the Center for Unmanned Aircraft Systems (C-UAS), where the primary sponsor was AeroVironment and the point of contact was Derek Lisoski. I would like to thank Derek for his support and insightful interactions regarding HALE aircraft and bringing about a sense of how our academic work on the X-HALE scales to industry. I would also like to thank the D. Dan & Betty Kahn Foundation for the financial support that enabled completing this work.

TABLE OF CONTENTS

LIST OF FIGURES

FIGURE

LIST OF TABLES

TABLE

LIST OF ACRONYMS

OOP out-of-plane bending

IP in-plane bending

FEM finite element model

GVT ground vibration test

FRF frequency response function

DV design variable

VFA very flexible aircraft

UAV unmanned aerial vehicle

LE leading edge

TE trailing edge

SD static deflection

MAC modal assurance criterion

HALE high-altitude long-endurance

DOFs degrees of freedom

MDOF multiple degrees of freedom

A^{2}SRL Active Aeroelasticity and Structures Research Laboratory

ABSTRACT

As aircraft wings become more flexible as a consequence of searching for more fuel efficient and higher performance solutions, structural nonlinearities become more apparent. Geometric nonlinearities make the structure's modal parameters a function of the deformed shape and, therefore, of the loading condition. Modal characterization of very flexible structures is challenging due to these nonlinearities and the very low natural frequencies (the fundamental mode is typically below 1 Hz). Therefore, testing practices that are well established and mature for traditional, relatively rigid aircraft need to be re-examined.

Ground vibration testing consists of conducting a series of experimental tests on an aircraft to identify its modal parameters (natural frequencies, mode shapes, and damping ratios). These parameters are then used as a reference for updating the aircraft's finite element model such that it is dynamically representative of the actual vehicle. This work proposes examining the conventional ground vibration testing and finite element model updating processes for very flexible aircraft and identifying the impact of flexibility and geometric nonlinearities on the process. The modified ground vibration testing and finite element model updating methodology are then applied to and verified on numerical models of very flexible test cases. Results are provided to showcase the applicability of the model updating process on the test cases, along with a discussion of the limitations and additional considerations required to enhance the process.

As part of ensuring compatibility with current/conventional processes for finite element model updating, the finite element model updating technique developed in this work was demonstrated using experimental data from a 3D printed swept wing that does not exhibit large deformations (i.e., is not very flexible). Tests were conducted on the structure to characterize its as-built behavior and then its numerical model was updated using the model updating methodology developed in this work to better match the experimental results. The model updating process was modified to account for uncertainties coming from the 3D printing process as well as to consider the effects of nonlinear boundary conditions, which yield a different set of challenges than the effects of flexibility, and highlight some of the limitations of the process.

By properly characterizing the suspension or support system in the structure's numerical model, experimental results from various deformed conditions allow for recovering the structure's true modal parameters once the influence of the suspension is modeled, tuned, and removed from the

finite element model. This ground vibration testing and finite element model updating methodology was demonstrated experimentally on a very flexible beam and validated on a very flexible aircraft. Results from the finite element model updating process indicate that the new methodology proposed and verified as part of this work improves upon the established finite element model updating technologies when considering very flexible structures undergoing loads causing large displacements.

CHAPTER 1

Introduction

1.1 Motivation

Very flexible aircraft (VFA) are a consequence of the trend towards reducing fuel consumption and improving overall flight efficiency in both civil transport aircraft and high-altitude long-endurance (HALE) vehicles. To accomplish these goals, design choices are made such as moving to longer wing spans, reducing structural weight [5], and utilizing advanced composite materials. These choices increase airframe flexibility [6], which results in larger structural deflections under normal operating load conditions [7] and in lower natural frequencies compared to contemporary, stiffer configurations.

The consequences of design choices made to increase endurance and reduce emissions include:

- Large deflections in the flight envelope
- Nonlinear dynamic aeroelastic response
- Coupling of flight dynamics and aeroelastic modes
- Lack of sufficient numerical and experimental data in the nonlinear regime

A key conclusion from NASA's Helios mishap [1] was that the conventional design procedures based on linear tools were not adequate to provide an accurate risk assessment of the effects of flexibility and configuration changes needed to fly the very flexible aircraft. The authors of the report recommended developing ground-test procedures and techniques appropriate to this class of vehicle to validate new analysis methods and predictions. Operating in the linear regime constrained by conventional design and analysis techniques does not sufficiently capture the complex interactions between the structure and the various other factors influencing the airframe during flight. Figure 1.1 shows the difference between the jig (undeformed) shape of the Helios compared to the range of deformed shapes the HALE aircraft experienced during flight.

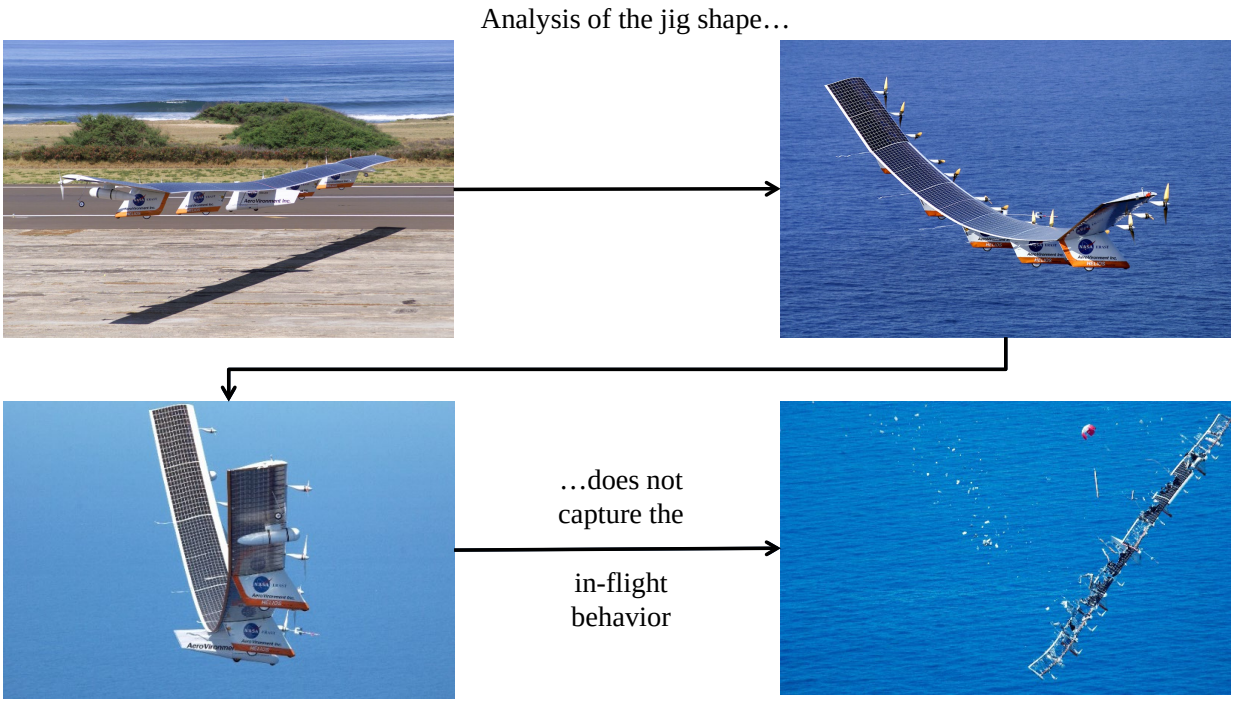

Figure 1.1: Undeformed shape along with the various levels of deformation achieved by the Helios during flight. Images taken from NASA report on Helios mishap [1].

In order to effectively design, simulate, and validate VFA, tools and practices developed for moderately flexible configurations need to be re-examined.

1.2 Literature Review

This section presents the ground vibration testing and finite element model updating strategies that have been explored in literature or implemented on conventional aircraft structures. Techniques for vibration testing span from testing the structure suspended under various suspension mechanisms to exciting the structure using a variety of excitation sources. Model updating is the step after the experimental tests and aims to better correlate the numerical models with the experimental findings. Special emphasis is given to structures that exhibit large flexibility or have features that can excite nonlinearities associated with large deflections during flight.

1.2.1 Ground Vibration Testing

Ground vibration testing (GVT) consists of conducting a series of experimental tests on an aircraft to identify its modal parameters (natural frequencies, mode shapes and damping ratios). These

parameters are then used as a reference for updating the aircraft finite element model such that it is dynamically representative of the actual vehicle. GVT are a major milestone in the aircraft certification process and are used to validate and improve the structural dynamics models [8, 9]. They are also used to support the prediction of the flutter behavior and plan for flight tests [10]. Since these tests are often performed late in the aircraft development cycle, there is an increasing interest in quicker turnarounds [11]. Short installation times, low errors, and high reliability are desirable characteristics of the instrumentation used for performing ground vibration tests [12, 13]. The process of conducting GVT [14] on the aircraft structure for identifying the modal parameters (natural frequencies, mode shapes, and damping ratios) is well established for moderately flexible configurations [15, 16, 17, 18].

However, GVT on VFA is challenging [19] due to the presence of geometric nonlinearities and low-frequency natural vibration modes [20]. VFA show significantly different deformed shapes when subject to different loads and boundary conditions. This requires testing the aircraft in multiple deformed configurations representative of in-flight trim shapes to completely characterize its structural dynamics [21]. Moreover, measuring the aircraft's dynamic response during ground vibration testing is further complicated by suspension system influence on the deformed shape and its dynamic coupling with the structure [22].

Elastic supports for suspending aircraft are generally attached close to the center of mass [23]. However, Schoor et al. [7] observed that this would cause the wing tip deflection of the suspended configuration to be in the opposite direction with respect to the in-flight shape for a VFA. Sharqi et al. [2] demonstrated this deflection based on suspension location, shown in Fig. 1.2. An additional consideration regarding attachment of elastic supports is structural fragility, as in the case of the GVT of the Pathfinder [24]. In 1994, when the GVT of the Pathfinder was being conducted, structural fragility restricted suspension locations along with shaker attachment points. Another consideration is the interaction between the structure and the suspension. During Predator B's GVT in 2002 [25], the dynamics of the suspension system consisting of bungee cords attached to a crane started to interact with the aircraft structure. Modeling the influence of the crane structure in the aircraft's finite element (FE) model allowed the test team to account for the presence of the suspension setup in the GVT results. Chang and Hodges [26] developed a theoretical formulation for modeling bungee cords used for suspending VFA during GVT and conducted a parametric study to identify the effects of bungee cord location and stiffness on the GVT results [27]. However, they did not present a validation of the methodology with experimental tests. In 2011, Boeswald et al. [3, 28] discussed practical concerns regarding very soft suspension setups and the need for decoupling rigid-body modes from the elastic modes of the Solar Impulse. A soft suspension system as a boundary condition is good practice during GVT, to decouple the rigid body modes from the elastic modes. However, this was not possible in the case of the Solar Impulse since

the suspension system required to do that would be extremely flexible, resulting in displacement amplitudes of several meters for the rigid body motions. This was not compatible with the GVT set up in their test facility. Figure 1.3 shows the full aircraft set up in its hangar.

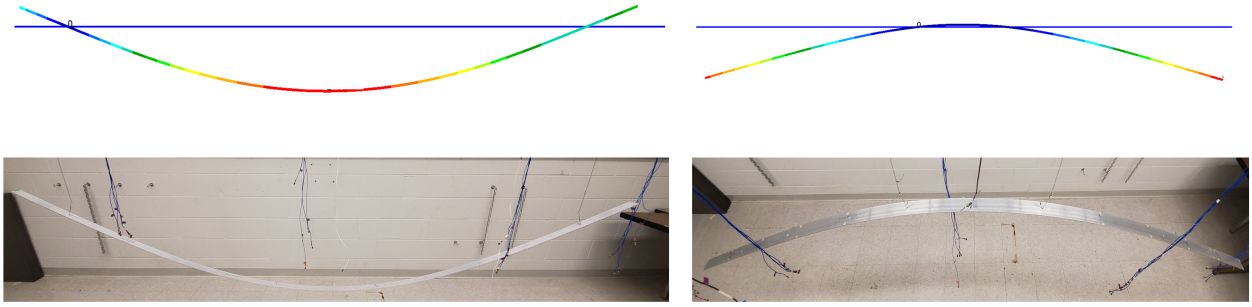

Figure 1.2: Static deformation for a very flexible beam under self weight based on suspension location [2]. Computational model on top, corresponding experimental set up on bottom.

Figure 1.3: Lightweight, but not very flexible Solar Impulse[1] [3] (Photo by Matth1). The large volume and light weight of the structure required additional considerations to accurately capture the apparent mass effect.

During GVT, the lightweight and extremely large structure of the Solar Impulse exhibited significant motion in directions perpendicular to aerodynamic surfaces. This required modeling the apparent mass of the air surrounding the structure and to couple the structural and aerodynamic models in order to improve correlation between experimental GVT results and numerical analyses. However, no effort was made to identify the modal parameters of the rigid body modes associated with the suspension or the effective experimental parameters associated with the slide bearings in the gimbal constructed to suspend the airframe. They also indicated that geometric stiffness effect was not significant so that a GVT in different statically deformed configuration was not necessary.

In 2005, Goge et al. [29] proposed a strategy for identifying nonlinearities in modal space based on the force-state mapping approach [30]. Using identified nonlinear modal parameters, nonlinear-

[1] Photo by Matth1, licensed under CC BY-SA 3.0.

ities in a single vibration mode of an aerospace structure were characterized. While the technique is promising, it requires considering one mode at a time and thus would be very time consuming for a large structure with several modes in the frequency range of interest. It also assumes weak nonlinearities, hence it is not fit for very flexible structures. More recently, Dossogne et al. [31] studied the nonlinear behavior of aerospace structures using sine-sweep testing. Boswald at al. [32] also explored new concepts in GVT based on output-only modal analysis using taxi vibration testing (TVT).

There have been efforts to address the impact of the suspension system on the supported structure during GVT for isolating the true structural frequencies and modal damping values. The work discussed in Refs. [33, 34] proposed a method of identifying the impact of the support system on a one-degree-of-freedom (1 DOF) system for identifying the true natural frequency and damping characteristics of the system. The methodology was also extended for multi-degree-of-freedom (MDOF) systems. These efforts were largely directed at relatively rigid structures where deformation due to suspension or self weight was not a consideration and the study was to identify the effect of support stiffness on the modal parameters of a test structure.

The main challenges associated with suspension for GVT of VFA are:

- The low stiffness and low fundamental frequency requires a very soft suspension system to get a reasonable separation between the structure and the support
- It is challenging to find a suspension that is very low stiffness and can support the weight of the test structure without deforming plastically

Since low stiffness suspension see large deformations, it often becomes necessary to use additional fixtures to calibrate the stiffness of the suspension system or turn directions. This introduces nonlinearities, both numerically and experimentally. Commercial airliners are often tested with suspension systems installed at the landing gear [35]. However, because of the test structure's mass, high-stiffness bungee cords can be used in parallel to achieve the desired stiffness. Whereas for a VFA, this is difficult because often even a single bungee cord is too stiff to maintain an order of magnitude separation between the suspension related mode and the structure's elastic mode(s). There are also practical concerns regarding the need for a large area to stretch the spring/bungee based suspension set up.

Despite the above contributions, there is still a lack of established experimental testing procedures for GVT of VFA, which includes characterizing and modeling the effective suspension parameters. This may include the effects of a pulley, or slide bearing/gimbal and other mechanisms used in the suspension setup. Another topic of consideration is the impact of large displacements on the response of the structure. This work formulates a methodology for GVT of VFA which consists of preliminary testing for characterizing the suspension system influence, developing a

suspension model based on the results from preliminary testing, and performing GVT on a VFA for various deformed shapes. The methodology is demonstrated and verified on a very flexible aluminum beam and is then applied to an existing VFA experimental testbed, the X-HALE [10] developed at the University of Michigan. The X-HALE was designed as a platform to study VFA behavior experimentally and to collect accurate GVT and flight test data for validating VFA analysis tools. The X-HALE shows geometric nonlinearities due to flexible, lightweight structural components that result in large deflections during flight and cause the deformed shape to be highly sensitive to the loads [36]. Moreover, the configuration shows very low natural vibration frequencies that result in couplings between the suspension system and the airframe during GVT.

1.2.2 Finite Element Model Updating

Finite element models (FEM) are widely used for simulating the behavior of complex structures, including very flexible aircraft. Accurately predicting the dynamic behavior of these structures using FEM requires precise knowledge of their geometry, material properties, and boundary conditions. GVT provide the modal parameters of a structure within a frequency range of interest [14]. Once this data is collected, numerical results are compared against the experimental and used for model calibration [37, 38]. The FEM of the structure needs to be tuned or calibrated such that it better matches the characteristics of the as-built structure [39, 8]. An updated FEM requires satisfactory correlation between numerical and experimental results for the modal parameters [40, 9]. FEM updating is a continually improving topic of research as new algorithms and techniques are developed. Ereiz et al. [41] provide a summary of some of the methods currently employed for model updating. Sharqi and Cesnik [38] developed a FEM updating process building upon state-of-the art model calibration techniques and added the ability to account for large displacements and geometric nonlinearities to update the FEM of very flexible structures. Recently, Li and Zhang [42] studied the FEM updating problem by using an unscented Kalman Inversion to solve the FEM updating problem in a gradient-free manner.

It is a critical requirement in flight-worthiness certification [43, 39] to have FEM updated with GVT results. These experimentally identified structural parameters are the natural frequencies, damping, and mode shapes [37, 44] within a frequency range of anticipated excitation. There are inherent differences in the structural dynamics response of a very flexible structure's experimental GVT results and initial FEM modal analysis due to the various uncertainties associated with the numerical modeling and experimental test setup [45, 46]. The FEM updating process typically involves the adjustment of material and/or geometry properties to achieve a better agreement with GVT results. This type of problem is often written in the form of a mathematical optimization, with the mass and stiffness matrix entries of the structural model as the design variables (DV) [47].

The procedure of FEM updating can be done in a multitude of ways, ranging from using in-house optimization tools [40] to trial and error, or manually adjusting model properties within reason [48]. However, manual adjustment, due to its subjective nature, does not yield consistent results across a variety of models. The process of updating the FEM is a widely researched topic [49, 50, 51, 52] and has been used in applications ranging from aerospace [28, 53] to automotive [54] and civil structures [55]. Space structures have their own suite of work regarding FE modeling and updating [56, 57]. NASA led an effort to evaluate and model the suspension devices for GVT of large space structures [58] and update the FEM of the flexible structure in the presence of the suspension [59]. In 2017, Zhao et al. [60] defined a sub-component based finite element model strategy for an aircraft where they updated the mass and stiffness parameters of substructures like the center body and the isolated wing separately using experimental data obtained from a GVT and then assembled the complete FEM. The mass properties of the assembled numerical model are once again compared to the experimental values and refined until a desired tolerance is achieved.

Holmberg [61] performed a FEM update using MacNeal-Schwendler Corporation (MSC) Nastran's built-in optimization toolbox, SOL200, to investigate multiple configurations of pylons and external loads (i.e., multiple configurations in the same optimization problem) for a new Gripen E fighter aircraft. They weighed all the test objects *a priori*, so the mass and center of gravity (c.g.) of each FEM configuration was updated before any GVT was conducted and the mass model was fine-tuned using non-structural masses distributed over the structure. Inman et al. [46] proposed that the model updating problem in structural dynamics is similar to the eigenstructure assignment problem found in control theory. In other words, they used control theory's pole placement strategy in a closed loop setup to solve the model updating problem and further subdivided the problem into four smaller blocks to be tackled sequentially in order to build towards the final goal: an updated FEM. Boeswald et al. addressed the challenge of performing GVT and validating the numerical model [28] on superlight aircraft structures where the influence of surrounding air on experimentally identified modal data is not negligible [3]. They developed an approach for the analytical determination of eigenfrequencies and mode shapes while accounting for the apparent mass effects of the surrounding air.

Govers et al. [62] studied FEM updating from uncertain experimental data where they described a process to identify and model the mean and covariance matrices of the modal parameters from uncertain experimental modal test data. They then used a two-step process of updating the mean of the parameters first and then the covariance matrix. At the National Aerospace Laboratory of Netherlands (NLR), Prananta et al. [63, 64] also used MSC Nastran SOL200 with parameter grouping to reduce the number of design parameters during the optimization process to calibrate the model of a small aircraft using GVT data.

However, while there has been substantial research into finite element modeling, ground vi-

bration testing and tuning the FEM to better correlate with the experimental results of relatively stiff, geometrically linear structures, there is a lack of reported studies regarding the process to be used for very flexible aircraft (VFA) or very flexible structures in general. This is partly due to the challenges associated with GVT of this class of structures [20, 19, 2] and partly because very flexible structures show significantly different deformed shapes when subject to different loads (see Fig. 1.4) and boundary conditions [65] (see Fig. 1.5). The modal testing, linear in nature, potentially requires testing the structure in multiple deformed configurations to capture its non-linear behavior. It is currently uncertain how many deformed configurations (or if more than one configuration) are needed when calibrating the FEM representation of a geometrically-nonlinear structure.

Figure 1.4: Boeing's 787[2]wing flexing during flight (Photo by Norwegian Air Shuttle).

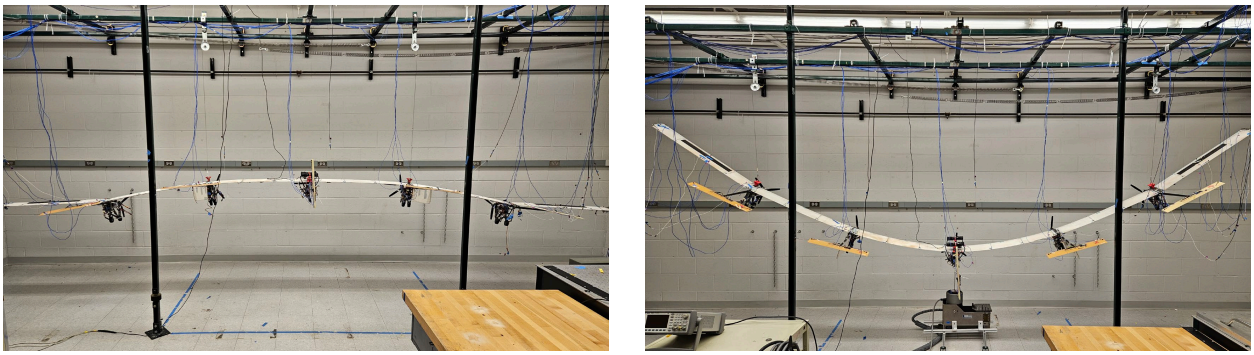

Figure 1.5: The University of Michigan's X-HALE. Wing deflections change based on different boundary conditions.

[2]Photo by Norwegian Air Shuttle, licensed under CC BY-SA 3.0.

This work explores and presents a methodology for FEM updating of very flexible structures where their shape can vary significantly in the vicinity of their operating conditions. In order to obtain a sample set of possible deformed shapes the structure can reach within its operating envelope, one can vary the structural support under gravity field imposed onto the structure during GVT [27, 2] or other ways to vary the loads (e.g., as experienced by the structure during maneuvers [10]). This new methodology is numerically demonstrated on a built-up FEM of very flexible wing structures and then applied to update the FEM of multiple experimental test cases. The main objective of this work is to provide insight into how structural flexibility affects the model updating procedure and the impact of deformed shape on both the modal parameters and the optimization approach.

Performing GVT and FEM updating for very flexible aircraft presents several additional challenges. First, the dynamic behavior of these structures is nonlinear and varies with deformed shapes and boundary conditions. As a result, uncertainties in the experimental setup or modeling assumptions can lead to significant errors in the results. Second, the high flexibility of these structures can make it difficult to measure their responses accurately, particularly in the low-frequency range. This is compounded by the fact that the sensors used to measure the response must be carefully positioned to avoid interference from the aircraft's engines or other external factors. Finally, the large amount of data generated during GVT and FEM updating requires sophisticated analysis techniques to extract meaningful insights and identify areas for improvement. Overcoming these challenges requires a multidisciplinary approach that integrates expertise from a range of fields, including structural engineering, aerospace engineering, and data analytics.

1.3 Challenges of GVT and FEM Updating for Very Flexible Aircraft

The main challenges of performing a GVT on very flexible aircraft and updating their FEM to match the experimental results are:

1. Suspension design and modeling for approximating 'free-free' boundary conditions: The way the aircraft is supported determines its boundary conditions, and in order to simulate the real aircraft in flight, the support needs to be as close as possible to the free-flying condition. In reality, a truly free boundary condition is an oxymoron. If there is a boundary condition, there will be something external to the aircraft connected to it that is going to impact the response of the structure under excitation. Ideally, the natural frequency associated with the support system should be separated from the lowest elastic frequency of the test structure by at least an order of magnitude. While this is already challenging for con-

ventional, rigid aircraft, the low stiffness and low fundamental frequency of a VFA requires a very soft suspension system to get a reasonable separation between the structure and the support mechanism. It can also become challenging to find a suspension/support that has the right stiffness characteristics and can support the test structure without deforming excessively.

2. Large deflections experienced based on loading and boundary conditions: VFA can exhibit significantly different deformed shapes when subject to different loads in flight. Being very flexible, they also deform substantially based on boundary conditions in laboratory conditions. This requires testing the aircraft in multiple deformed configurations representative of in-flight trim shapes to completely characterize its structural dynamics. A variety of numerical studies have been performed demonstrating the variation in shapes of very flexible structures based on suspension location (essentially adjusting the boundary condition) and their impact on the structure. However there is a lack of reported studies experimentally demonstrating the impact of the deformed shapes and the variation in the structure's response based on the shape.

3. Finite element model updating for VFA: There has been substantial research into finite element modeling, ground vibration testing and tuning the FEM to better correlate with the experimental results of relatively stiff, geometrically linear structures. However, there is a lack of reported studies regarding the process to be used for VFA or very flexible structures in general. The modal testing, linear in nature, requires testing the structure in multiple deformed configurations to potentially capture its nonlinear behavior. It is currently uncertain how many deformed configurations (or if more than one configuration) are needed when calibrating the FEM representation of a geometrically-nonlinear structure. For VFA, their shape can vary significantly in the domain of their operating conditions. It is unclear how structural flexibility affects the model updating procedure.

4. Finite element model updating considering material property variability and novel manufacturing techniques: 3D printing has grown in use over the last few years and can now be used to construct fiber reinforced 3D printed parts [66, 67], manufacture large structures within the construction industry [68], and lends itself well to the medical industry [69, 70]. Creating and validating the FEM of such parts is an ongoing challenge currently being tackled by researchers [68, 71, 72], and part of the challenge includes updating their FEM based on the results of experimental tests. Abbot et al. [71] showed that the infill percentage of the 3D printed parts had a substantial impact on their failure loads under compression tests. They also concluded that the 3D printed test specimens yielded significantly different results than their simulated models, as modeling the internal makeup of the 3D printed lattice required

simulation tools that are not currently commercially available [73]. Tahmasebinia et al. [68] concluded that quality control in 3D printing is a key area that requires further investigation. 3D printed construction brings some unique modeling and construction challenges. While 3D printing allows for enhanced modularity and quicker turnaround time when building or repairing the components, there is an increased variability between the material properties of 3D printed parts [74, 75]. As such, finite element modeling and calibration of such components are challenging [76, 69]. Govers and Link [62] studied FEM updating from uncertain experimental data, while Böswald et al. [28] investigated GVT and model validation under the uncertainties associated with the influence of the surrounding air on a lightweight aircraft. However, there is a lack of reported studies regarding validating or updating the FEM of such 3D printed structures.

1.4 Thesis Overview

The work performed and presented in this dissertation attempts to address the challenges described in Section 1.3. The bulk of the novelty of this thesis is in the exploration of how flexibility can affect the response of a structure, how to account for it in experimental tests and numerical models, and how to update the numerical models of very flexible structures. Testing practices that are well established and mature for traditional, relatively rigid aircraft are re-examined to account for structural flexibility and strategies for improving the testing and updating the structural models are investigated. Finally, in order to ensure compatibility with current and more importantly, well established methodologies for conventional structures, the ground vibration testing and finite element model updating methodologies developed as part of this work were demonstrated on relatively rigid test cases.

The rest of the dissertation is organized as follows:

- Chapter 2 addresses the first research challenge and discusses the theoretical developments created to account for flexibility and large deflections experienced by very flexible aircraft. It introduces the conventional, established methodologies and then proposes the modifications required to capture the effects of large deflections and geometrical nonlinearities in the GVT and FEM updating process. The GVT methodology is described first and then the FEM updating methodology is presented.

- Chapter 3 addresses the second research challenge and presents the experimental validation of the GVT methodology on multiple test cases with varying levels of structural flexibility. It also discusses how the response of a flexible structure changes as a function of loading (and level of deflection) and identifies various topics of interest that will be later incorporated

into applying the GVT methodology to a very flexible aircraft, the University of Michigan's X-HALE.

- Chapter 4 addresses the third research challenge and introduces the FEM updating methodology to be used on the very flexible test cases. The key topic of interest is to investigate if multiple deformed configurations are definitively needed to capture the two effects present in very flexible structures – first being the geometric nonlinearities due to the nonlinear strain-displacement relation, and second being the 3D effects in the presence of local stiffness and stress concentrations in detailed FEM. This requires to calibrate the FEM using the general FEM updating approach with no load, and also with the modified process proposed in this work. Once the calibrated FEMs are available, a complex load (forces and moments in multiple directions) is applied to the two calibrated FEM and the response of the calibrated FEM is analyzed and compared to the reference data.

- Chapter 5 addresses the fourth research challenge and presents the application of the GVT and FEM updating methodology on a 3D printed swept wing. It provides a discussion on the modifications to the FEM updating process to account for 3D printed structures to better match the experimental results. A discussion on the modeling of the various boundary conditions during the GVT is provided along with results that indicate a good initial match for the structural model. The results also highlight some additional work required to capture the nonlinear boundary conditions.

- Chapter 6 ties all the research challenges together and validates the theoretical developments on a VFA. It introduces the most complex test case used to exercise the GVT and FEM updating methodologies developed as part of this work, the X-HALE. Various GVT are conducted on the VFA, with different boundary conditions and excitation sources. The FEM of the VFA is then updated using the FEM updating methodology and results are provided for all the tests along with a discussion of the problem set up and sources of error. The updated FEM is used to create a prediction for the true free-flying GVT of the aircraft in the absence of a suspension contaminating the response of the structure. A GVT with near free-free boundary conditions is then performed. Results indicate the updated FEM of the X-HALE is able to accurately capture the free-flight response of the as-built VFA structure.

- Chapter 7 provides a summary of the work performed and documented in this dissertation. It provides the key takeaways and contributions resulting from exercising the methodologies developed in this work, both computationally and experimentally, on various test cases. Recommendations for future work to enhance and build upon this work are provided.

CHAPTER 2

Theoretical Developments

This chapter addresses the first research challenge, suspension design and modeling for performing GVT on VFA. It presents the theoretical concepts developed to investigate the key objectives of this thesis. Section 2.1 contains the description of a methodology to model and account for the suspension system and its influence in the suspension of very flexible structures. Section 2.2 provides a methodology to account for multiple deformed configurations representative of operating conditions for very flexible aircraft in the FEM updating process. The computational and experimental strategies developed in this chapter are verified numerically and validated experimentally in subsequent chapters in this dissertation.

2.1 GVT on VFA - Experimental and Numerical Approach

In typical ground vibration tests, the vehicle is suspended on soft elastic supports to simulate free-free boundary conditions [27]. Since the structure needs to be supported either with springs or with a system of bungee cords, free-free boundary conditions can be only approximated [77]. Moreover, the addition of accelerometers, the presence of the shaker and its connection to the structure, and the dynamics of the support system itself add complexity to the test and interpretation of results. To facilitate this process, the support system is typically designed such that its frequencies are much lower than the lowest vehicle frequency to ensure dynamic decoupling from the structure being analyzed.

Consider a 2 DOF system in free vibration as shown in Fig. 2.1, satisfying the equations given by Eq. 2.1,

$$\begin{bmatrix} m & 0 \\ 0 & m \end{bmatrix} \begin{bmatrix} \ddot{x_1} \\ \ddot{x_2} \end{bmatrix} + \begin{bmatrix} c_{sup} + \frac{c_{st}}{2} & -\frac{c_{st}}{2} \\ -\frac{c_{st}}{2} & c_{sup} + \frac{c_{st}}{2} \end{bmatrix} \begin{bmatrix} \dot{x_1} \\ \dot{x_2} \end{bmatrix} + \begin{bmatrix} k_{sup} + \frac{k_{st}}{2} & -\frac{k_{st}}{2} \\ -\frac{k_{st}}{2} & k_{sup} + \frac{k_{st}}{2} \end{bmatrix} \begin{bmatrix} x_1 \\ x_2 \end{bmatrix} = 0 \quad (2.1)$$

where m is the structural mass for each of the components, $\frac{c_{st}}{2}$ its viscous damping coefficient,

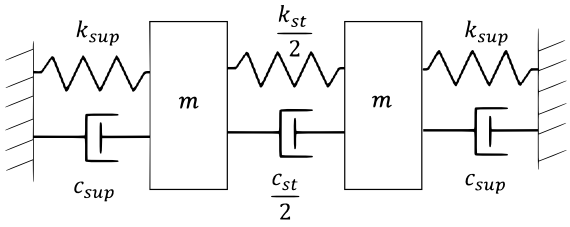

Figure 2.1: Schematic of a simple elastic structure in the presence of a supporting system.

and $\frac{k_{st}}{2}$ its stiffness. The system described in Eq. (2.1) is suspended with a support having its own damping and stiffness characteristics described by c_{sup} and k_{sup}, respectively, while the mass of the support is assumed to be negligible with respect to m.

The setup of the elastic structure with a spring-damper suspension has two undamped natural frequencies given by

$$\omega_{sup} = \sqrt{\frac{k_{sup}}{m}} \qquad \omega_m = \sqrt{\frac{k_{sup} + k_{st}}{m}}, \tag{2.2}$$

where ω_m refers to the frequency of the system including the support. The first mode is the rigid body mode that is now non-zero because of the presence of the support, while the second mode is the elastic mode of the structure which is now contaminated by the support. Similarly, as shown in [34], the damping ratios for the support by itself, and the system composed of the support and the structure are given by

$$\zeta_{sup} = \frac{c_{sup}}{2m\omega_{sup}} \qquad \zeta_m = \frac{c_{sup} + c_{st}}{2m\omega_m}. \tag{2.3}$$

Following Ref. [33] and introducing the true frequency and damping characteristics of the test structure as

$$\omega_{st} = \sqrt{\frac{k_{st}}{m}} \qquad \zeta_{st} = \frac{c_{st}}{2m\omega_{st}}, \tag{2.4}$$

one can combine Eqs. (2.2) and (2.4) to obtain

$$\omega_{st}^2 = \omega_m^2 - \omega_{sup}^2 \tag{2.5}$$

and then

$$\omega_{st}^2 = \omega_m^2 \left(1 - \omega_{sup}^2/\omega_m^2\right). \tag{2.6}$$

This relation allows for identifying the frequency of the test structure if the support system has been experimentally characterized as a separate component. Equations (2.3) and (2.4) yield

$$\zeta_{st}\omega_{st} = \zeta_m\omega_m - \zeta_{sup}\omega_{sup} \tag{2.7}$$

so that the true damping ratio of the structure can then be obtained as

$$\zeta_{st} = \zeta_m \frac{\omega_m}{\omega_{st}} \left(1 - \frac{\omega_{sup}}{\omega_m} \frac{\zeta_{sup}}{\zeta_m} \right). \tag{2.8}$$

Equations (2.6) and (2.8) indicate that the closer the frequency of the support to the structure's elastic frequency, the higher is its impact on the measurements. The impact on the system's damping is even higher compared to the impact on the frequency considering there is no squared term in Eq. (2.8). This process of identifying the impact of the support on a test structure was extended for the MDOF system as described in Ref. [34]. However, this procedure was defined only numerically for the MDOF system and was not verified experimentally. This work expands on experimental verification of the impact of the suspension system(s) on the structure's modal parameters in the context of very flexible structures suspended using multiple suspension systems. Instead of approximating the impact of the added stiffness and damping on individual modes of the test structure, the suspension system is experimentally characterized, numerically modeled and included in the test structure's finite element model.

One of the challenges in GVT on very flexible structures is designing a suspension setup that can support the structure while being decoupled from its dynamics. Specifically, the first natural vibration frequency of a VFA is typically below 1 Hz [7]. Therefore, it can be very difficult to design a support system whose frequencies are separated by an order of magnitude from the structural frequencies of the test structure, so that support and airframe modes do not interact. If the support and airframe dynamics are coupled, then the support must be properly characterized to account for it in the aircraft FEM that is updated based on GVT results. Furthermore, while GVT of moderately flexible aircraft can be conducted in undeformed (jig) shape, a single-point characterization (for a given mass condition) may not be sufficient for calibrating the FEM of a VFA. Indeed, VFA achieve significantly different configurations during normal operations, and these configurations are also significantly different from the undeformed shape on the ground. The effects of these geometry changes needs to be accounted for and characterized by testing the aircraft in different deformed shapes achieved, for instance, by means of multiple suspension points placed at variable locations along the span. However, if variable or multiple suspension points are used, the effect of each suspension point needs to be individually characterized and identified.

As part of identifying a suitable suspension setup, a variety of bungee cords that have very low stiffness were tested to explore their suitability for suspending a VFA. Low stiffness springs were also tested to identify the best compromise where there is minimal interaction between suspension and airframe modes. Different pulleys were tested to see if a system with multiple pulleys used to turn directions for the spring/bungee cords would allow for a longer suspension setup. These tests showed that additional damping from the pulleys causes only the final section of the suspension

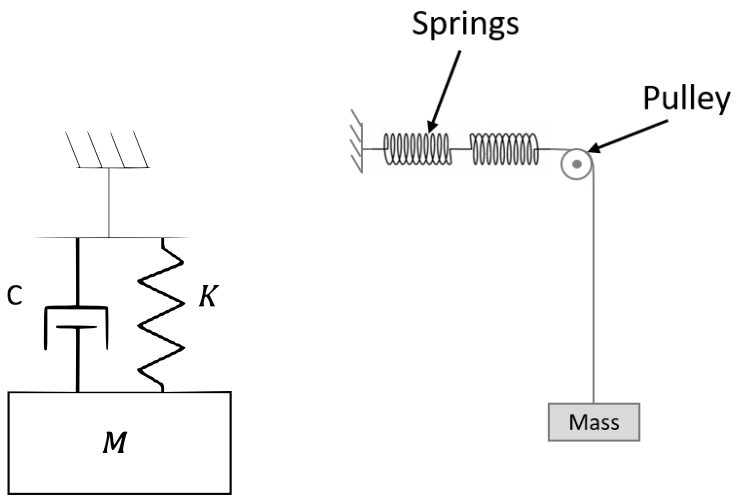

(a) 1 DOF support setup.

(b) Realization based on practical constraints.

Figure 2.2: Schematic of a simple 1 DOF suspension system (left), and a 1 DOF system with a pulley to turn directions (right).

setup to interact with the test structure. This increases the stiffness of the suspension setup, hence reducing the frequency separation between the suspension and airframe modes. For preventing the coupling of these modes during ground vibration testing, the support should be characterized, modeled, and then removed.

This study proposes a methodology for GVT on very flexible structures that addresses the above challenges. A low-frequency elastic support suitable for suspending the structure is designed and built using available materials.

Next, the support is characterized and included in the numerical FEM of two test cases, a very flexible beam exhibiting geometrically nonlinear deformations and an existing VFA test case. The numerical models are used to test various suspension configurations (or deformed shapes) using the experimentally identified suspension setup characteristics. Moreover, it is also used to investigate the support system influence on the modal parameters of the support-structure assembly. Once GVT results are available, the test structure's FEM will be updated as shown in Section 3.2 to match the measured structural modal parameters in any one deformed configuration while keeping the FEM of the support system unchanged. Since the support system is characterized upfront as an isolated component, this results in a correct updating of the FEM such that it is dynamically representative of the actual test structure.

A suspension setup that allows to test the very flexible structure in various deformed shapes can be characterized as follows:

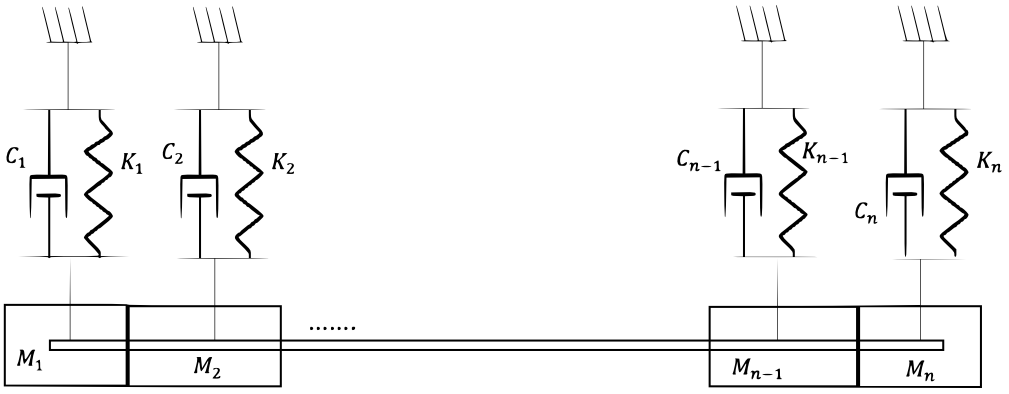

Figure 2.3: Schematic of multiple 1 DOF setups on the structure.

1. For each station of the aircraft that needs to be suspended to achieve a given deformed shape, the mass M_i that the suspension system supports is identified. This can be simplified by having a symmetric suspension setup such that the total mass is divided equally among the stations.

2. For each station, an equivalent mass block that can be assumed to be rigid with respect to the structure is defined. This can be achieved by using a solid block of metal with mass M_i. Figure 2.2a shows the schematic of the 1 DOF system representing each suspension system at a given station.

3. A low-stiffness spring or bungee-cord based suspension system is designed for each suspension point of the structure. The choice of the suspension is affected by practical constraints like height of test facility while still providing the capabilities to sustain the mass without plastic or nonlinear deformations. Figure 2.2b shows the schematic of the 1 DOF suspension system which includes a pulley to turn directions, and allow room for the springs to stretch under loading where the vertical height of the test facility may not be enough to allow for using soft, high-stretch springs or bungee cords.

4. Tests are performed to identify each of the 1 DOF suspension system's parameters. The procedure is repeated for each of the suspension points on the structure as shown in Fig. 2.3.

Each of the 1 DOF blocks representing a suspension point needs to be identified individually. Considering the ith block with mass M_i, stiffness K_i, and viscous damping coefficient C_i, an experimental GVT is performed to identify the fundamental damped frequency ω_{d_i} and the damping ratio ζ_i. Next, the undamped natural frequency ω_{n_i} and the viscous damping coefficient are obtained as

$$\omega_{n_i} = \frac{\omega_{d_i}}{\sqrt{1-\zeta_i^2}} = \sqrt{\frac{K_i}{M_i}} \qquad C_i = 2\,\zeta_i \omega_{n_i} M_i. \tag{2.9}$$

Identifying these modal parameters from experimental data is also a challenge, particularly because of the low frequency and high damping associated with suspension systems of this nature. Peeters et al. [78] demonstrated the use of LMS PolyMAX [79], a polyreference least-squares complex frequency-domain (LSCF) modal parameter estimation method for experimental modal analysis (EMA). This estimator allows for clear stabilization diagrams, which are particularly helpful when the frequency response function (FRF) data are contaminated with noise and are hence difficult to interpret such as for high-order or highly-damped systems with large modal overlap.

Due to the advancements in multiple-input multiple-output (MIMO) sine stepped/swept testing [31, 29], testing software have improved to include mode indicator functions (MIF), which help in characterizing nonlinearities and identifying modes, and PolyMAX, which allows for easier identification of modal parameters. These developments coupled with the proposed method allow for characterizing the suspension system for any number of suspension points. Next, the individual models for each suspension can be used in numerical FE calculations. Figure 2.4 shows the process defined to identify the modal parameters of the very flexible structure in a given configuration, update the model, and use that to validate the FEM in another deformed configuration.

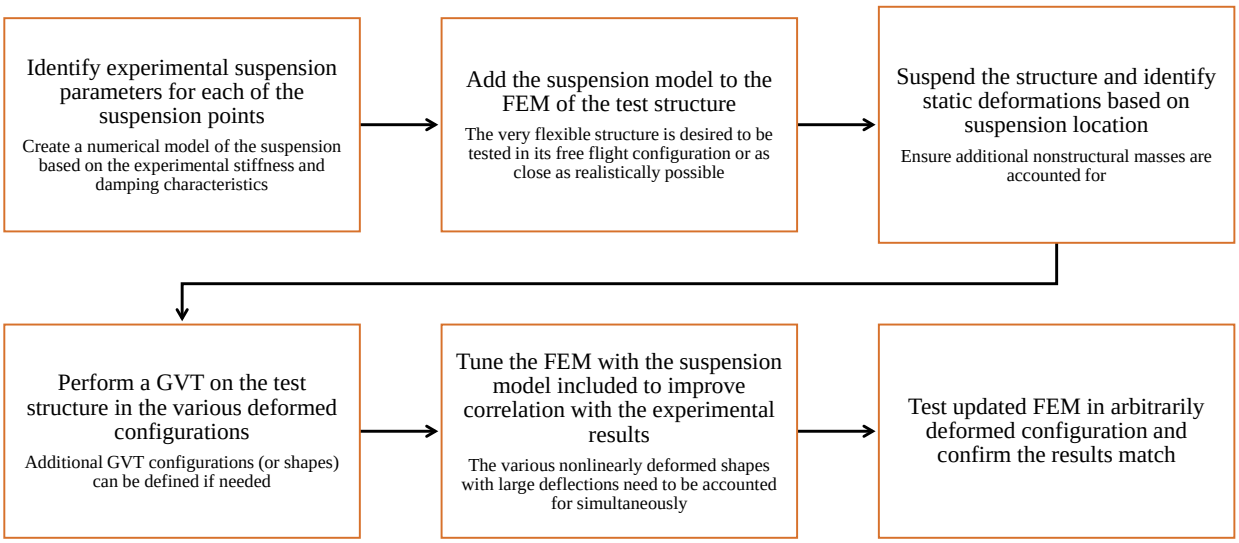

Figure 2.4: Algorithm for testing and updating FEM of very flexible structures.

When conducting GVT of VFA where the deformed configuration varies with the suspension

setup, the suspension points will be displaced after the structure is allowed to statically deform under its own weight. This can be corrected for a priori, by placing the suspension points at locations that minimize the displacement of the suspension around the fixed point (for example, the ceiling the springs attach to) after being loaded with the test structure. Figure 2.5 shows the displaced points of suspension for a sample deformed configuration of a very flexible structure, where the points of suspension are dropping down vertically, but the angle of connection of the suspension to the structure changes based on its deformed shape. This effect needs to be accounted for in the FEM. Even if the suspension setup is modified such that the springs are always connected vertically, the force imparted by the springs on the structure changes based on the connection angle. This force may change the modal parameters of the structure since it affects the deformed shape during GVT.

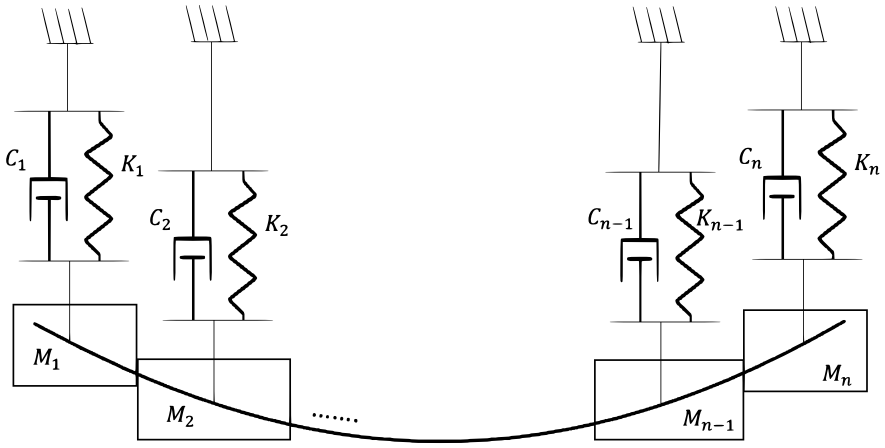

Figure 2.5: Multiple 1 DOF setup for each suspension point on a deformed very flexible structure.

2.2 FEM Updating for VFA

The general finite element model updating problem is typically posed as an optimization problem with the objective of minimizing the difference between the experimental and numerical outputs, with frequencies being the most common function. Various other considerations involving matching mass, inertia, and center of gravity (c.g.) may also be included as constraints along with side constraints on the design variables. This typical optimization problem statement can be written mathematically based on the formulation summarized by [80] and the overall FEM updating process is shown schematically in Fig. 2.6. Here, the "modified FEM" is initialized by the "initial FEM" and updated as the optimizer iterates through the design process.

$$
\begin{aligned}
\textbf{minimize F(x)} \quad = \quad & \left(\frac{m - m_0}{m_0}\right)^2 + \left(\frac{I_{xx} - I_{xx_0}}{I_{xx_0}}\right)^2 + \left(\frac{I_{yy} - I_{yy_0}}{I_{yy_0}}\right)^2 + \left(\frac{I_{zz} - I_{zz_0}}{I_{zz_0}}\right)^2 + \\
& \left(\frac{X_{cg} - X_{cg_0}}{X_{cg_0}}\right)^2 + \left(\frac{Y_{cg} - Y_{cg_0}}{Y_{cg_0}}\right)^2 + \left(\frac{Z_{cg} - Z_{cg_0}}{Z_{cg_0}}\right)^2 + \sum_{i=1}^{N} \left(\frac{\omega_i - \omega_{i_0}}{\omega_{i_0}}\right)^2 \\
\textbf{with respect to:} \quad & \mathbf{x} \\
\textbf{subjected to:} \quad & m^{\ell} \leq m \leq m^{u} \\
& I_{xx}^{\ell} \leq I_{xx} \leq I_{xx}^{u} \\
& I_{yy}^{\ell} \leq I_{yy} \leq I_{yy}^{u} \\
& I_{zz}^{\ell} \leq I_{zz} \leq I_{zz}^{u} \\
& X_{CG}^{\ell} \leq X_{CG} \leq X_{CG}^{u} \\
& Y_{CG}^{\ell} \leq Y_{CG} \leq Y_{CG}^{u} \\
& Z_{CG}^{\ell} \leq Z_{CG} \leq Z_{CG}^{u} \\
& MAC_i \geq MAC_{min}; \quad i = 1, 2, ..., N \\
& \mathbf{x}^{\ell} \leq \mathbf{x} \leq \mathbf{x}^{\mathbf{u}}
\end{aligned} \tag{2.10}
$$

In the optimization problem defined in Eq. 2.10, m is the mass of the structure and ω_i is the i^{th} natural frequency associated with the set of the first N modes. Here, terms with the subscript o refer to the experimental value while the terms without the subscript are the corresponding numerical components. X_{cg} through Z_{cg} refers to the three components of the center of gravity (c.g.) location, while I_{xx} through I_{zz} are the components of the inertia tensor (additional components of the inertia tensor can also be included, but are not shown or investigated here for brevity). The upper and lower bounds in the constraints are denoted by the superscript u and ℓ, respectively, while MAC stands for Modal Assurance Criterion [81], and MAC_{min} corresponds to the desired minimum threshold of acceptable modal correlation.

An interesting modification on the standard FEM updating procedure was proposed by the authors of a study on creating a test validated FEM of the X-56A aircraft [40]. They studied the topic of finite element model updating by posing it as a series of optimization problems dealing with frequency error minimization between the numerical and the experimental models, but added a sub-module that deals with the mass matrix orthogonality using the measured mode shapes. Model tuning of the aircraft was performed in stages, starting with tuning the frequency errors, followed by the cross-orthogonality (mode shape) matrix.

A total of four sequential structural dynamic model tuning runs were conducted focusing on improvement in frequency errors and the off-diagonal terms of the cross-orthogonality matrices

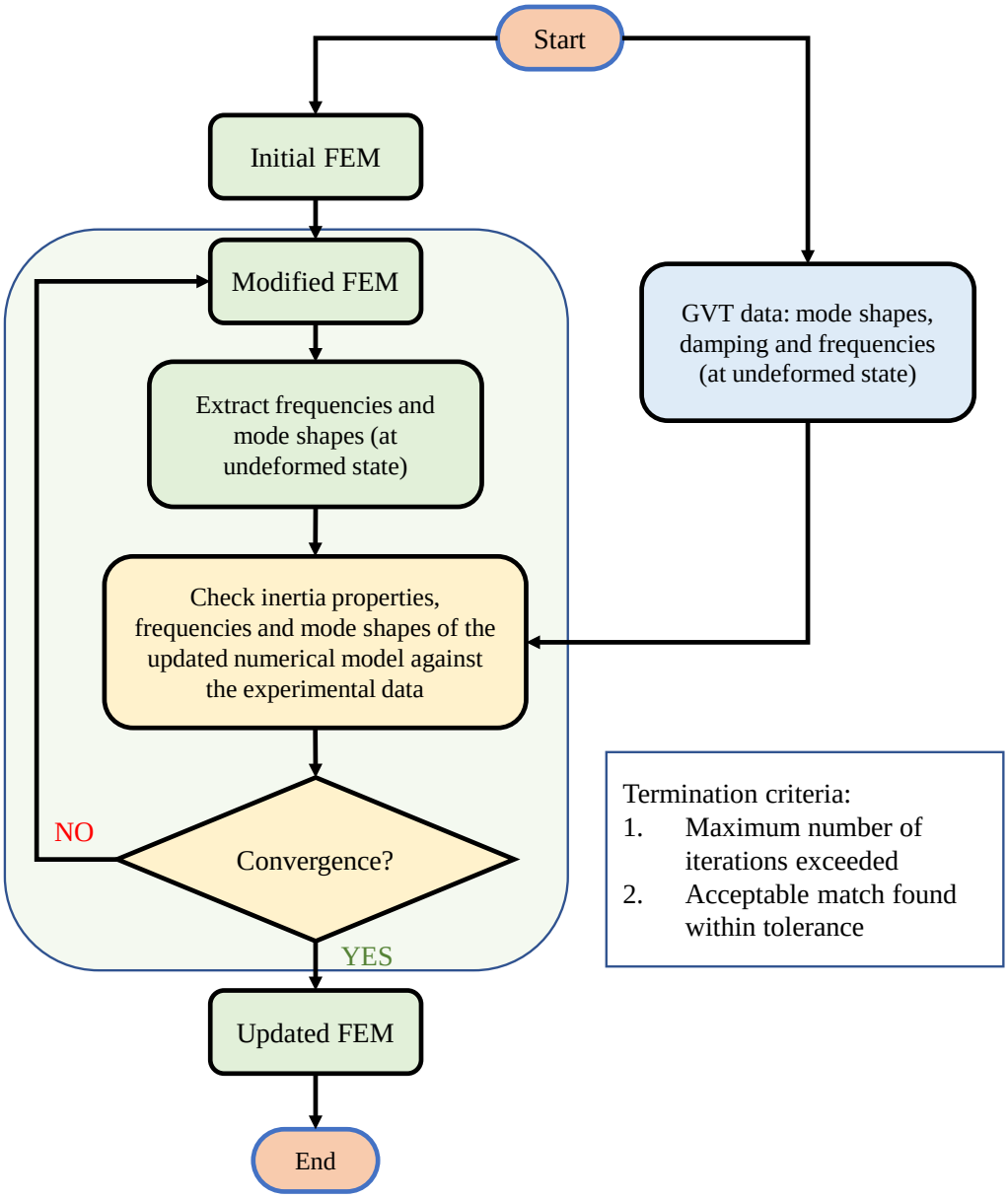

Figure 2.6: Typical finite element model updating process.

with all the mode shapes for the two different weight configurations (empty fuel and water, *and* full fuel and water) of the X-56A aircraft in a single optimization run. The inclusion of orthogonality checks using the analytical mass matrix and the test mode shapes was done to demonstrate accurate mass representation of the test structure and to satisfy NASA and military standards [82, 83]. These standards aim to minimize the difference between specific frequencies and specific entries in the cross-orthogonality matrix to a higher standard than commercial applications. That study provides a good summary of all the objectives for a representative FEM updating problem and defines four

sequential optimization problems that will be used along with the general problem summary shown in Eq. 2.10 as a starting point to modify and apply the problem formulation to very flexible aircraft that exhibit large displacements.

When a very flexible wing undergoes large displacements as a result of loading, there are two main effects that alter its linearized modal characteristics. First, there are the effects of the nonlinear strain-displacement relation that lead to the presence of the additional tangent stiffness matrix. This term, however, is connected with the linear stiffness matrix through the fixed geometry and material properties. Therefore, once the FEM is updated at its unstressed state, the global effects of the deformation are correctly accounted for [84]. The second effect is connected with the actual geometry of the wingbox. Due to the rib separating the upper and lower wingbox skins, significant stresses are developed in the various members during large displacements which lead to local variations in the stiffness of those members (Brazier effect), ultimately affecting the overall modal behavior of the wing around a given deformed state. This local effect primarily impacts the stiffness characteristics and does not have a significant effect on the local inertia (local cross-sectional deformations are small due to the presence of the ribs) [85].

When updating the FEM of a structure, a common first step is to check the stiffness model through a static test validation and updating process. In the case of very flexible structures, loads causing large displacements may also change the mass properties and would be needed for the subsequent vibration (modal analysis) test used to update the mass model. However, in the scope of this work, the objective was to find the most generic FEM updating process that can handle both the mass and stiffness design variables. There can be multiple variations of the problem setup, e.g., one can tune the stiffness model first using multiple deformed cases and then tune the mass model under the same load cases. However, these variations on the problem setup are not studied as part of this work.

Typically, the problem defined in Eq. 2.10 has multiple minima, which implies different combinations of possible values of geometric and material design parameters. This is also true for the FEM updating of the geometrically nonlinear problem when simply modeled as a beam, that is, only capturing the first of the two effects described above: geometric nonlinearity due to the large displacements of the neutral line. However, the second effect (local change in stiffness due to pre-stress) in built-up constructions can provide additional information that can be used to further improve the uniqueness of the combination of geometric and material property adjustments to the FEM. This would lead to testing the structure in multiple deformed configurations and using that information as part of the finite element model updating problem. To generate the modal information about multiple deformed shapes, multiple corresponding load cases causing large displacements on the structure would need to be applied. Therefore, the optimization problem defined in Eq. 2.10 must be augmented to account for the additional entries of frequencies and mode shapes

obtained from the n loading conditions. The new optimization process can then be written as:

$$
\begin{aligned}
\textbf{minimize F(x)} \quad = \quad & \left(\frac{m-m_0}{m_0}\right)^2 + \left(\frac{I_{xx}-I_{xx_0}}{I_{xx_0}}\right)^2 + \left(\frac{I_{yy}-I_{yy_0}}{I_{yy_0}}\right)^2 + \left(\frac{I_{zz}-I_{zz_0}}{I_{zz_0}}\right)^2 + \\
& \left(\frac{X_{cg}-X_{cg_0}}{X_{cg_0}}\right)^2 + \left(\frac{Y_{cg}-Y_{cg_0}}{Y_{cg_0}}\right)^2 + \left(\frac{Z_{cg}-Z_{cg_0}}{Z_{cg_0}}\right)^2 + \\
& \sum_{j=1}^{n}\sum_{i=1}^{N}\left(\frac{\omega_i^j - \omega_{i_0}^j}{\omega_{i_0}^j}\right)^2 \\
\textbf{with respect to:} \quad & \mathbf{x} \\
\textbf{subjected to:} \quad & m^\ell \leq m \leq m^u \\
& I_{xx}^\ell \leq I_{xx} \leq I_{xx}^u \\
& I_{yy}^\ell \leq I_{yy} \leq I_{yy}^u \\
& I_{zz}^\ell \leq I_{zz} \leq I_{zz}^u \\
& X_{CG}^\ell \leq X_{CG} \leq X_{CG}^u \\
& Y_{CG}^\ell \leq Y_{CG} \leq Y_{CG}^u \\
& Z_{CG}^\ell \leq Z_{CG} \leq Z_{CG}^u \\
& MAC_i^j \geq MAC_{min}; \quad i = 1, 2, ..., N \quad \text{and} \quad j = 1, 2, ..., n \\
& \mathbf{x}^\ell \leq \mathbf{x} \leq \mathbf{x}^\mathbf{u}
\end{aligned}
\tag{2.11}
$$

This modified process described in Eq. 2.11 is shown schematically in Fig. 2.7. In this process, the updated FEM obtained from the converged optimization is tested against a new set of GVT results generated within the bounds of deformation used for calibration. If the updated FEM can capture the results of the new load case within predefined tolerances, the updated FEM is retained, and the updating process concluded. If the results do not match, additional GVT are needed for new deformed shapes.

It is important that the problem be solved with all the considerations simultaneously, otherwise the solution will be suboptimal (higher errors). To perform the additional modal analysis about each of the n deformed states adds new requirements. For this, a nonlinear structural solver must be used (e.g., MSC Nastran SOL 400) in a two-step process:

1. Geometrically nonlinear static analysis is performed to capture the structure's deformed shape.

2. Then, modal analysis is performed about the nonlinear statically deformed configuration.

Also, additional measurements are required to create the data sets containing frequencies, damp-

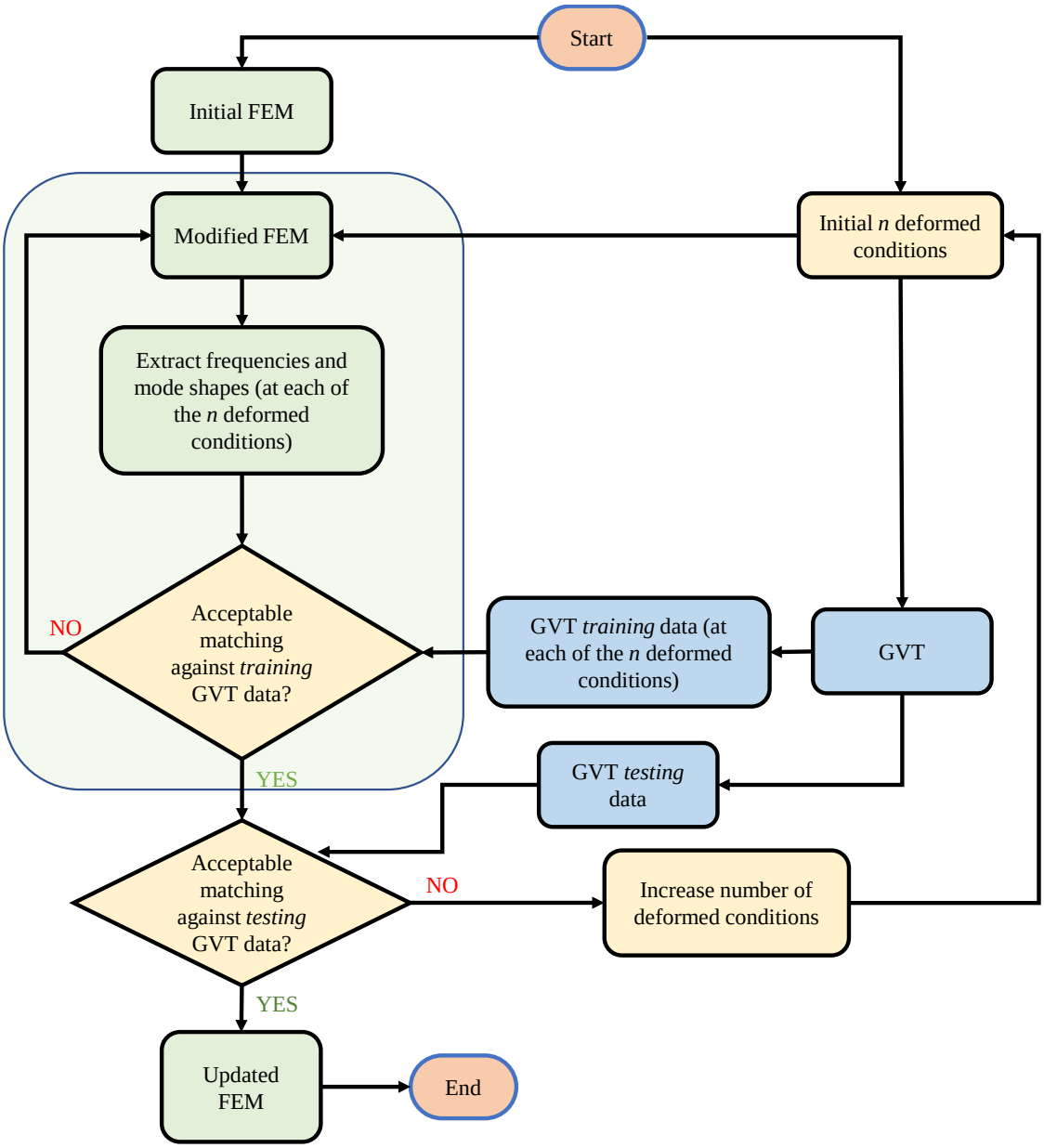

Figure 2.7: Modified process for FEM updating for very flexible structures.

ing, and mode shapes for each deformed shape. Section 4.1 contains a modification on the FEM updating process, to verify the procedure numerically while Chapters 5 and 6 contain applications of the FEM updating process to update the FEMs of structures with varying levels of flexibility and nonlinearities.

CHAPTER 3

Ground Vibration Testing on Very Flexible Structures

As aircraft become more flexible in an effort to reduce fuel consumption or operating costs and improve endurance, structural nonlinearities become more apparent. As a consequence, testing practices that are well established and mature for traditional, linear aircraft need to be re-examined. This chapter investigates the second research challenge, the impact of deformed shapes on modal parameters of very flexible structures. It also provides experimental data to support the first research challenge, suspension design and modeling for VFA. Furthermore, it proposes a method to model the support system's influence when experimentally measuring these parameters. The chapter begins with exercising the available methods of conducting GVT and modeling the effect of the suspension on a flexible Aluminum beam test case. The beam is excited using both an impact hammer and a shaker and is tested under various boundary conditions with varying suspension set ups. Using the knowledge gained from a flexible test case, a more informed GVT was performed on the very flexible test cases.

The studies are conducted on two very flexible test cases. A very flexible beam presented in this chapter, and later, on a very flexible aircraft presented in Chapter 6. The VFA is an experimental testbed developed at the University of Michigan, called the X-HALE [10]. Both test cases exhibit nonlinear deformations under different suspension configurations, thus their modal characterization is performed numerically and experimentally in different deformed configurations. Results are used to assess the impact of deformed shape changes and of the support system influence on the modal characterization of very flexible structures.

3.1 Flexible Aluminum Beam Test Case

This section details the tests conducted to identify the modal characteristics of a flexible aluminum beam with the aim of understanding the best approach to perfrom GVT and FEM updating no

very flexible structures. The beam was studied in different configurations to identify the impact of boundary conditions, the suspension system and the method of excitation. The goal was to develop a numerical and experimental methodology to best match the numerical simulations conducted for the beam (using Nastran) with the experimental results. The impact of the added mass of the accelerometers, the suspension system (springs and pulleys) and the associated effective stiffness and damping values that determine the specific configuration is studied, numerically simulated and experimentally tested.

Modal analysis about a deformed configuration is also performed using SOL 400, a nonlinear solver in Nastran that allows for performing a nonlinear static analysis given a loading (self-weight under gravity in this case) and then perform a modal analysis about that deformed configuration. The results and knowledge gained from the beam tests will be transferred onto the GVT for the very flexible test cases, and eventually to a complex flying wing, the X-HALE. The intention is that once the right experimental boundary conditions (for the beam) are identified, the impact of the suspension system characterized, along with the shaker connection and the associated boundary conditions, a similar methodology can be applied to the more complicated system, the X-HALE.

3.1.1 Overview

The beam tests were conducted on two different Aluminum beams with the dimensions shown in Table 3.1:

Table 3.1: Flexible Aluminum beam properties.

Item	**Beam 1**	**Beam 2**	**Units**
Length	1220.0	1500.0	mm
Width	51.0	51.0	mm
Height	3.1	3.1	mm
Mass	520.0	640.0	g

The beams were tested in six different configurations. Beam 1 was used for configurations one and two, while Beam 2 was used for the other configurations (three through six). An overview of the different configurations is provided below:

1. Beam 1 clamped on one end, mounted on a shaker base, and effect of gravity neglected (see Figs. 3.1 and 3.2)

2. Beam 1 clamped on one end, mounted on a shaker base, and gravity effects included

3. Beam 2 suspended by two springs on both ends and gravity effects included

4. Beam 2 suspended by a system of spring-pulley-spring (pulley in between two springs) on each end and gravity effects included

5. Beam 2 mounted on a shaker connected at the center and suspended with two springs at the ends (springs only)

6. Beam 2 mounted on a shaker connected at the center and suspended with two springs and a pulley at the ends (two springs and then a pulley)

The purpose of configurations 1–4 is to determine the impact of gravity, the effect of the suspension and excitation technique on a simple, moderately flexible isotropic beam, while configurations 5–6 were set up to study and identify the impact of the shaker in terms of the boundary conditions being imparted to the system.

3.1.2 Suspension Impact: Identification on a Flexible Beam

In order to identify the impact of gravity and the boundary conditions (or suspension mechanism) on the flexible beam various configurations were defined. The first configuration involves the beam mounted on a shaker at an orientation where gravity (self-weight) effects can be neglected. The schematic for the beam layout describing the orientation and the accelerometers is shown in Fig. 3.1 while the experimental setup is shown in Fig. 3.2.

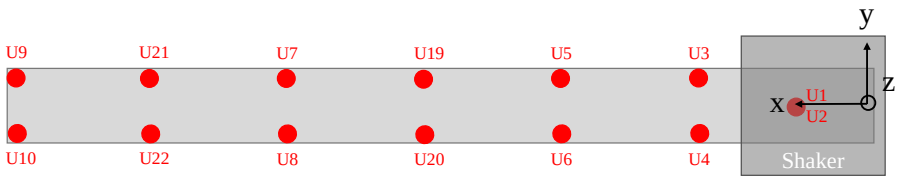

Figure 3.1: Beam configuration 1 schematic.

The beam was excited by the shaker. Configuration 2 was defined such that gravity effects were included both in the numerical and experimental models and the set up is shown schematically in Fig. 3.3. The actual beam set up in the laboratory and mounted on the shaker is shown in Fig. 3.4.

For the simulations of configuration 1 and 2, the beam model is exactly the same. In configuration 1, a simple modal analysis was used, whereas for configuration two; Nastran's SOL400

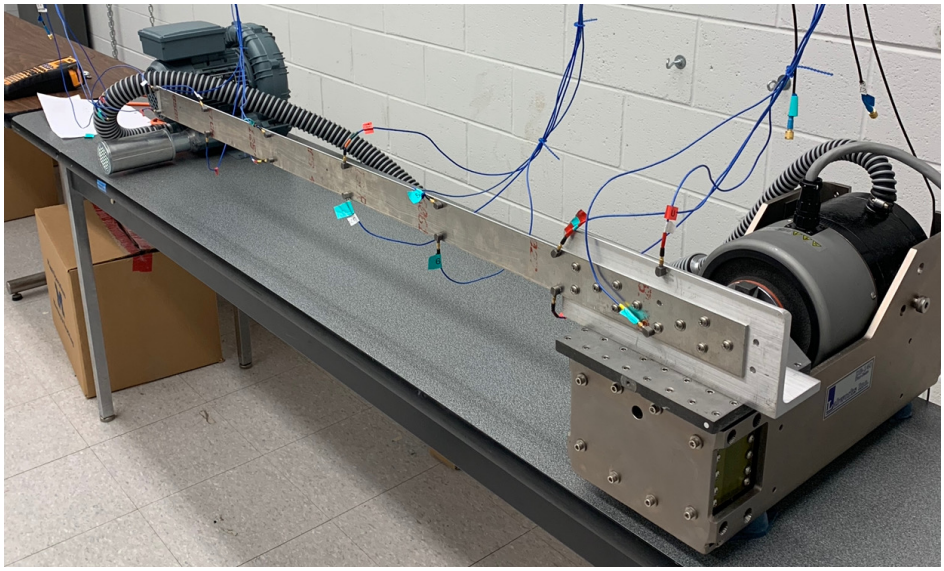

Figure 3.2: Beam configuration 1 experimental setup.

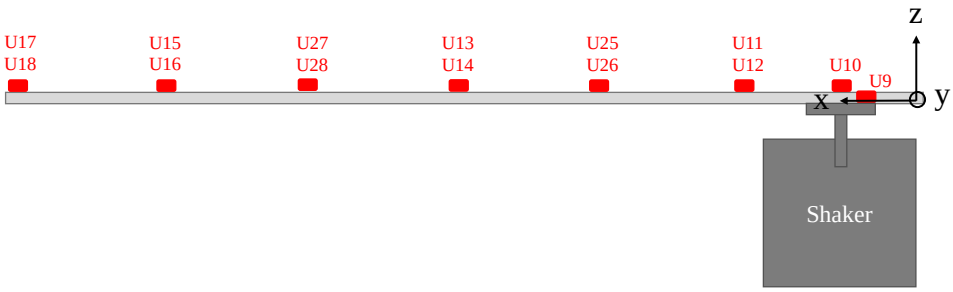

Figure 3.3: Beam configuration 2 schematic.

(nonlinear analysis) was the solver used with a two-step solution. In both cases, all 6 DOFs of the beam were clamped near its root (where it was mounted on the shaker).

1. Nonlinear static deformation under gravity loading.

2. Modal analysis about the statically deformed configuration from step 1.

After the tests with the beam mounted on a shaker, a suspension system was created which offered different boundary conditions than being clamped at one end. This is denoted as configuration 3. Beam 2 was used for the subsequent tests and was suspended from its ends using soft springs. The beam was excited by using an impact hammer. The driving point was the midpoint of

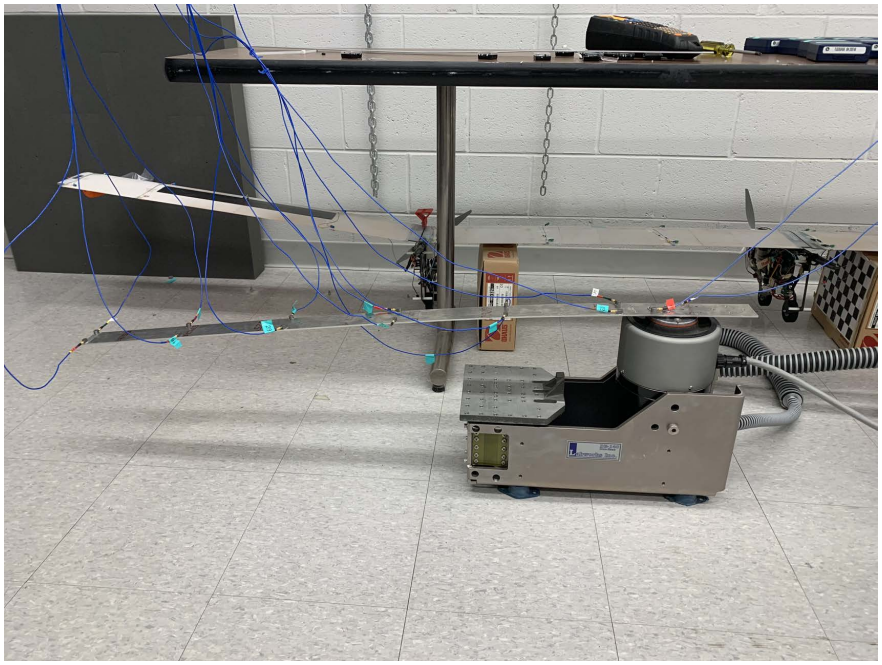

Figure 3.4: Beam configuration 2 experimental setup.

the beam (0.75 m from one end). A schematic detailing the accelerometer layout and a picture of the experimental setup for configuration 3 is provided in Figs. 3.5 and 3.6.

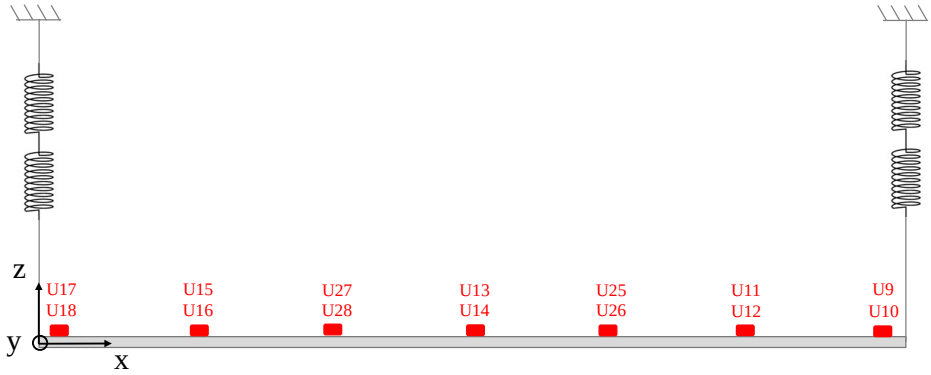

Figure 3.5: Beam configuration 3 schematic.

A soft suspension system was required to isolate the rigid body plunge frequency from the structural frequencies. The softest springs available that could support the weight of the beam and still remain in the linear region when deformed were chosen. The spring geometry and specifications are shown in Table 3.2. A test was done to verify the stiffness of each of the springs used.

Converted to SI units, the spring has a constant of K = 42 $\frac{\text{N}}{\text{m}}$. Two of these springs used in

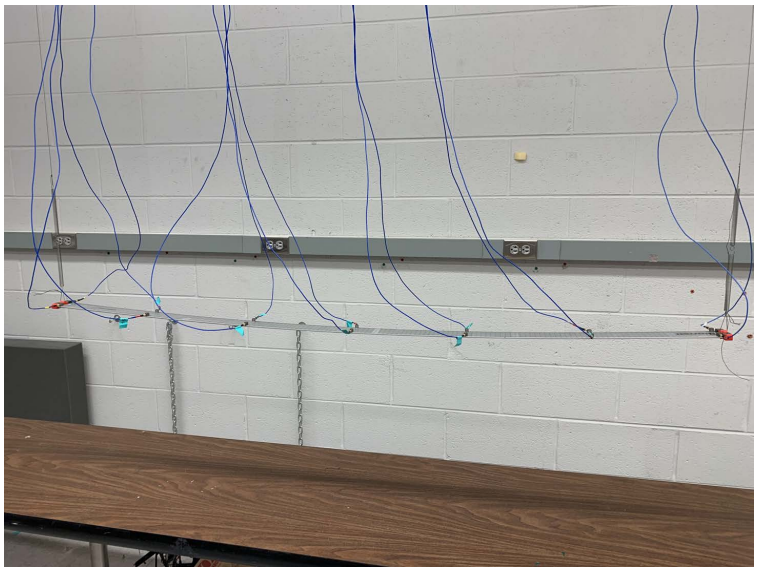

Figure 3.6: Beam configuration 3 experimental setup.

Table 3.2: Specifications of the springs used for the configurations 3 through 6 for the beam GVT.

Item	Qty	Units
Outside diameter	0.343	in
Inside diameter	0.293	in
Overall length	2.50	in
Wire diameter	0.025	in
Rate	0.240	$\frac{\text{lbs}}{\text{in}}$
Load	1.48	lbs
Deflection at load	5.42	in
Initial tension	0.180	lbs
End style	Crossover	-
End type	Loop	-
Material	Music wire	-
Finish	Plain	-

series give a stiffness constant of K = 21 $\frac{\text{N}}{\text{m}}$ which when used in combination with the beam give a plunge frequency of 1.15 Hz. The beam has its fundamental frequency (the first out-of-plane bending mode) at 7 Hz, which means that there does not exist an order of magnitude separation between the plunge frequency coming from the spring and beam interaction and the beam's elastic mode. This would usually be a bad experimental practice, except there is no practical way to isolate the rigid body mode from the interaction of the support/suspension system and the elastic mode for the X-HALE. So, having a similar interaction on a simpler model would allow for better

understanding of the setup and the best method of identifying and implementing the suspension into the numerical model.

For static deformation under gravity, two constraint displacements were added for the first step of the SOL400 solution. For one end, x and y-translations were constrained, while for the other end, only y-translation was constrained. This allows the beam to contract under the loading for static deformation, but not translate in the in-plane direction (y-axis). All other translations and rotations are allowed.

In order to identify the impact of adding a pulley to turn directions (to allow more room for the springs to stretch), configuration 4 was defined. For this configuration, the beam was suspended with one spring, a pulley, and then another spring. The same impact hammer is used to excite the structure. This configuration was designed to study the experimental impact of adding a pulley in between 2 springs. The numerical simulation for both configuration 3 and 4 is the exact same, and the only difference between them is the experimental setup and results.

A schematic showing the accelerometer layout is shown in Fig. 3.7 and the experimental setup is provided in Fig. 3.8.

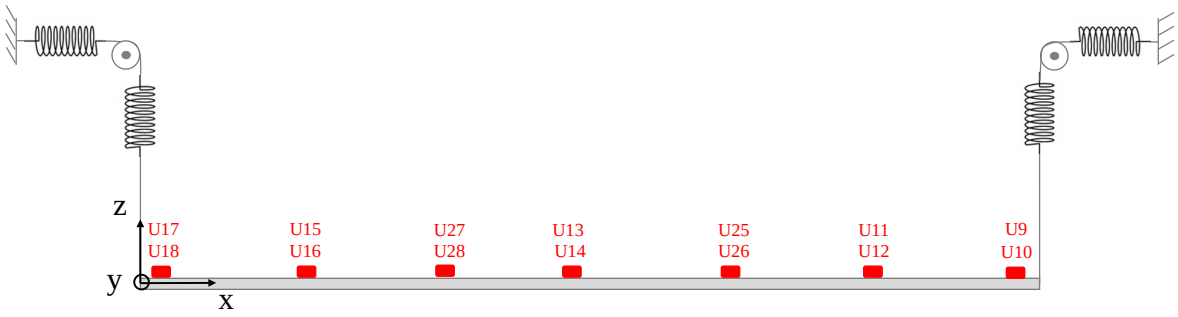

Figure 3.7: Beam configuration 4 schematic.

Inference and conclusions from configurations 1 through 4

- For the first two configurations, the results show strong agreement between the numerical and the experimental values.
- The results show decent agreement between the numerical and the experimental values for configuration 3 (beam with only springs as suspension). However, for configuration 4 (with the addition of the pulley), the numerical results and the experimental results do not show a good agreement, especially for the first three modes. There is increased noise in the frequency response functions, and the pulley adds nonlinearity to the suspension mechanism which impacts the lower modes the most.

Figure 3.8: Beam configuration 4 experimental setup.

- The addition of a pulley increases experimental damping and the discrepancy in frequencies. This indicates that further investigation must be done to identify the spring-damper system that models the addition of the spring and the pulley in combination with the rest of the suspension system including the strings and the attachments.
- This is the topic of interest for the next section and the subsequent configurations of the flexible aluminum beam.

3.1.3 Suspension Design: Identification of Spring and Pulley Suspension Characteristics

Given how the presence of a pulley in the suspension setup impacts the response of the structure, this section describes the tests conducted to identify and model the suspension mechanism. On the X-HALE, the soft support system used to suspend it and the associated boundary conditions will be a system of springs that provide a low stiffness and a pulley (to turn directions) on each side of the craft. The purpose of this support system is to minimize interaction of the plunge frequency of the mass-spring-damper system with the structural frequencies, particularly the first out-of-plane bending frequency which is the first natural frequency of the X-HALE.

Ideally, the tests to characterize the suspension system should be done on a rigid object that weighs the same as the test object. In this case, since there are two sides to the suspension system,

the rigid object should weigh half of the test object. To approximate half the mass of the beam, two steel plates were attached together and suspended from the spring and pulley system (see Fig. 3.9, where the springs are connected to the wall, or, connected with strings to a fixture) and the pulley is connected to the springs. This is the same setup that will be used for the X-HALE, but with different springs.

Figure 3.9: Steel test block (left) and springs and pulley (right).

With this setup, the accelerometers kept getting overloaded with the impact hammer, even with light taps. The impact could be regulated to where the accelerometers would not get overloaded, however the excitation too little energy to excite the bounce frequency of the 1 DOF mass-spring-damper system. This made the characterization of this system very difficult, so another 1 DOF setup was created that had the same mass as half the beam (see Fig. 3.10).

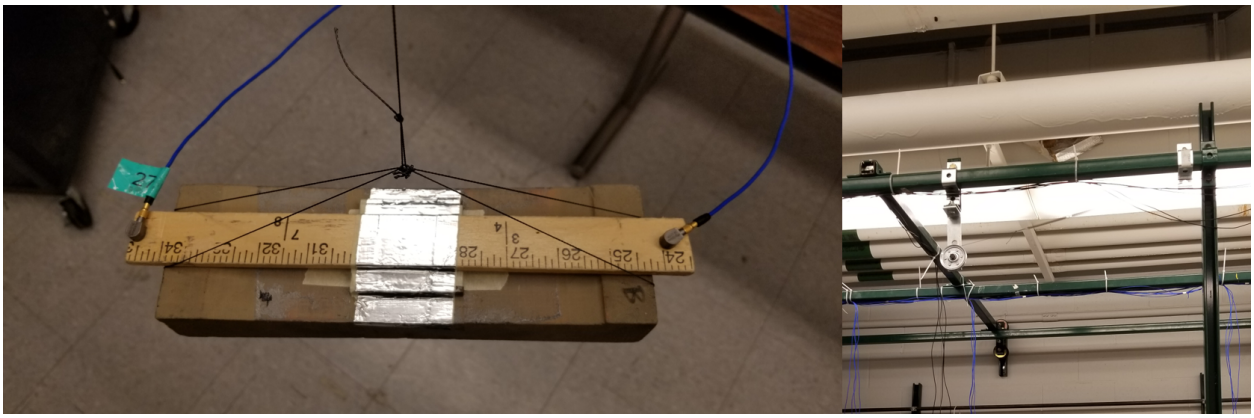

Figure 3.10: Alternate test block (left) and springs and pulley (right).

A Kevlar string is wrapped around the 1 DOF test object and the item is excited by impacting it from below. The beam is attached using the same Kevlar string, except instead of wrapping it around the beam, there is a 3D printed attachment that the beam slides into and which connects with the string. This means that the only significant differences between the connection for the 1

DOF object and the beam are the 3D printed sleeve and the way the Kevlar is attached to them (see Fig. 3.11).

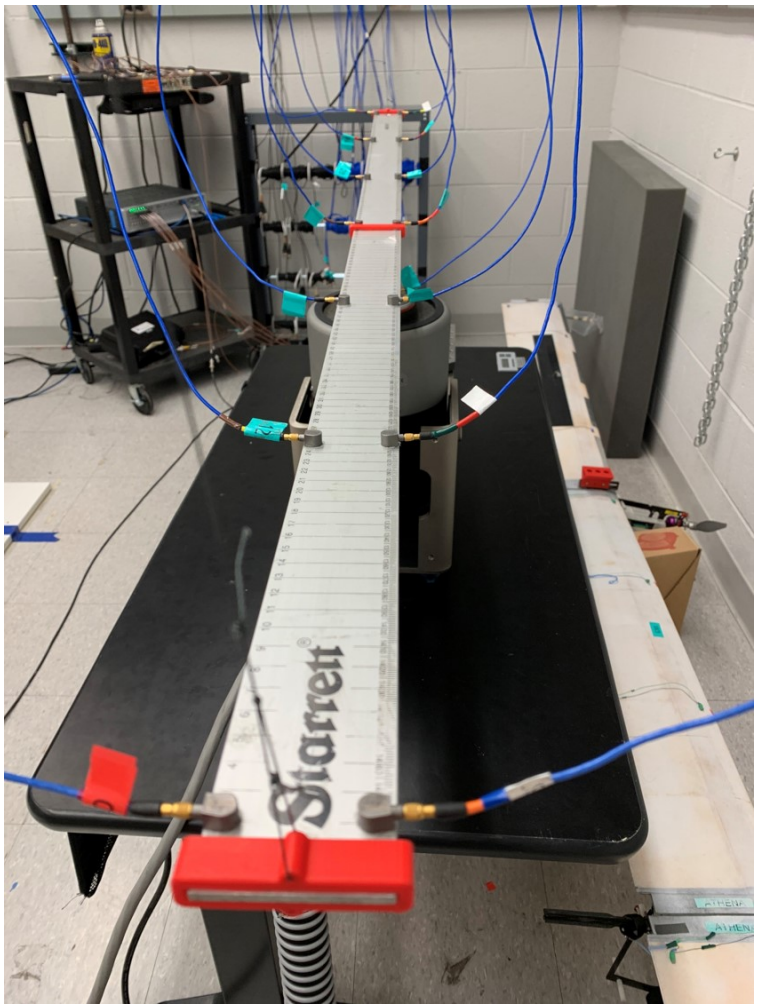

Figure 3.11: 3D printed attachment for beam and string connected to it.

The block of wood shown in Fig. 3.10 is used with the impact hammer to identify the characterize the spring and pulley combination. One test was done using only the springs, while another test was done with both springs and the pulley. For the second test, the last iteration was done with a block representing the mass of half of the X-HALE, and with the springs that will be used for the X-HALE GVT. These are different springs than the ones used for the beam tests, since the mass of the craft is considerably higher than the beam.

The addition of a pulley (as observed previously) increases the damping and increases the difference between the theoretical and experimental frequencies. These findings indicate that there exists a discrepancy between the numerical and experimental results when a pulley is added to the system. There is a need to account for the source of the discrepancy and to model in the numerical

simulation to allow for accurate predictions. This was done in the following way:

Modeling the soft support system in Nastran:

1. Calculating the effective stiffness of the system from the experimental frequency and the known mass. The experimentally identified damping ratio (ζ) is used to calculate the undamped natural frequency, using which the effective stiffness of the system can be calculated since the mass is known.

$$\omega_n = \frac{\omega_d}{\sqrt{1-\zeta^2}} \tag{3.1}$$

$$\omega_n = \sqrt{\frac{k}{m}} \tag{3.2}$$

2. Calculating the viscous damping coefficient from the equation

$$c = 2\zeta\omega_n m \tag{3.3}$$

In the test case, with the block of wood = $\frac{1}{2}$ beam mass = 0.375 kg

$$c = 2 \times 0.0454 \times 6.73 \times 0.375 = 0.229$$

Table 3.3 summarizes the results for both the beam and the X-HALE representative spring-dampers.

Table 3.3: Experimentally identified stiffness and damping coefficients.

Property	Beam block	X-HALE block	Units
ζ: Damping Ratio	0.045	0.047	%
Mass	0.375	5.67	kg
ω_d: Damped natural frequency	6.72	1.76	$\frac{\text{rad}}{\text{s}}$
ω_n: Undamped natural frequency	6.73	1.76	$\frac{\text{rad}}{\text{s}}$
Effective Stiffness	17.0	17.6	$\frac{\text{N}}{\text{m}}$
Viscous Damping Coefficient	19.5	0.30	$\frac{\text{N.s}}{\text{m}}$

3. Defining the model in Nastran: The damping was modeled by a viscous damper element in Nastran. Once the model was tuned to match the experimentally identified effective stiffness and damping for the 1 DOF system, the modal analysis on the 1 DOF system (for both the beam and the X-HALE) gave exactly the values that were being sought. The suspension model's effective stiffness and damping coefficients are shown in Table 3.4).

Conclusions from spring and pulley suspension characterization:

Table 3.4: Suspension system model's effective characteristics.

Suspension	Mass [kg]	Stiffness [$\frac{N}{m}$]	Damp. Coeff. [$\frac{N.s}{m}$]	Theo. Freq. [Hz]	GVT Freq [%]	Error [%]
Beam	0.375	17.0	0.229	1.07	1.07	0.0
X-HALE	5.672	17.6	0.935	0.28	0.28	0.0

- The experimentally identified spring damper model that corresponds to the associated spring and pulleys for both the beams and the X-HALE was tuned to match the results of the 1 DOF (block mass representing half the beam or the X-HALE) case.

- This allows the creation of a spring-damper model that represents the effective stiffness and damping values in the suspension system when an equivalent mass ($\frac{1}{2}$ of the beam or the X-HALE) is suspended from the system. The model can then be used as the suspension system for the input files for both the beam and the X-HALE.

- This does not necessarily mean that the 1 DOF mass-spring-damper model tuned from the 1 DOF impact test would match the effective stiffness when a beam or the X-HALE is used instead of the rigid mass, and some further tuning may be required. This could be due to a variety of reasons including the connections and adapters used to model the mass. To identify the suspension system dynamics, the adapters and connections (during the isolated suspension identification) must be exactly the same as the ones used for the GVT. This was not the case for the 1 DOF systems made for this characterization. The connections used for the characterization presented in this section were similar, but not absolutely the same.

3.1.4 Suspension Modeling: Adding the Spring-Damper Model to the Numerical Solution

The spring-damper model identified in the previous section for the beam was added to the beam's FEM. However, since neither Nastran's SOL400 (nonlinear analysis) nor SOL103 (real eigenvalue analysis) account for damping in their solutions, another solver must be used that can perform complex eigenvalue analysis. SOL107 (complex eigenvalue analysis) was used for this analysis. SOL107 by itself does not have an option for a static deformation solution in order to perform a modal analysis about a deformed configuration, so it was used without accounting for the effects of gravity on the beam.

Conclusions from modeling the suspension:

- The addition of a damper drives down the frequencies in the numerical model as expected. However, the experimental results do not corroborate that. The addition of a pulley (damp-

ing) to the system increases the natural frequencies identified experimentally for configuration 4 (springs and pulley) compared to configuration 3 (only springs).

- The model for the suspension system is the same that was identified experimentally in Section 3.1.3. This model was tuned to match the exact effective stiffness and damping that was identified experimentally, but it does not provide the expected results when used on the beam model. This could be due a variety of reasons ranging from instrumentation to human error, but will be most significantly affected by the imperfect 1 DOF setup used to identify the set of effective damping and stiffness values.

3.1.5 Boundary Conditions: Impact of Shaker Fixture on a Flexible Aluminum Beam

One of the main challenges associated with using a shaker to excite a structure during ground vibration testing is accurately identifying the boundary conditions of the structure. The behavior of a structure subjected to vibration is heavily influenced by the way it is supported, and even small changes in boundary conditions can have a significant impact on the results. In many cases, the boundary conditions of the structure may be unknown or difficult to measure directly. This can make it challenging to design and model an appropriate shaker system that can provide the necessary excitation while also minimizing interference from other sources. In addition, it can be difficult to determine the correct input signals to apply to the shaker system to achieve the desired excitation level and frequency range.

For the X-HALE, impact tests may not deliver enough energy to the structure. The other concern is that it may require a strong impact to get a noticeable reading from the accelerometers. This could cause dents on the wings or the points of impact and may still not be enough energy to excite the frequency range of interest for the very flexible aircraft. This motivates the use of a shaker to provide the excitation. The impact of the shaker attachment and the imposed BCs needs to be identified (initially on the beam) so the best attachment model can be used in the simulation. After these tests, the FEM will be updated with the experimentally identified shaker boundary condition for the configuration(s) with the shaker to better match with the GVT results.

The initial tests to identify shaker attachment BCs were performed on the beam with the intention of using the knowledge acquired from a simple test case to better model the shaker for the X-HALE.

In order to identify the impact of mounting (or rigidly attaching) the beam at its center to a shaker, configuration 5 was created. This configuration is similar to configuration 3 in the sense that it consists of a beam suspended with 2 springs in series at each end. The beam is allowed to deform under its own weight and then a shaker is mounted at the center of the beam without pushing it up

or pulling it down. The accelerometer layout remains the same as previous configurations and the test is intended to be used to identify the shaker's imposed boundary condition to a setup that is already predicted well (Beam + Springs). The schematic of configuration 5 is shown in Fig. 3.12.

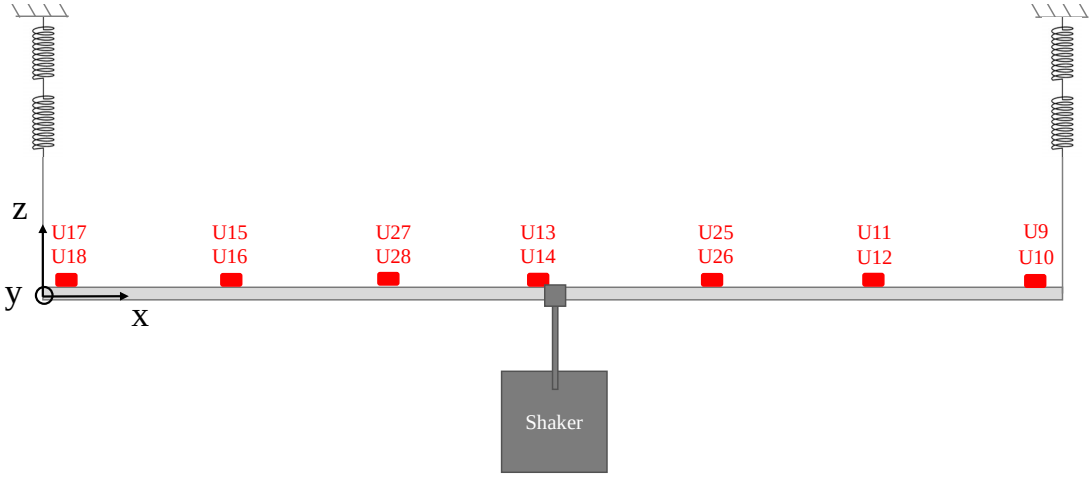

Figure 3.12: Beam with shaker at the center and suspended with two springs at each end.

A configuration 6, similar to configuration 4 was defined to identify the impact of the shaker when a damping element is included in the system (both numerically and experimentally). The suspension system for configuration 6 consists of 2 springs attached in series and a pulley in series with the springs. Like configuration 5, the shaker is attached at the center of the beam. The schematic and experimental setup for configuration 6 are shown in Figs. 3.13 and 3.14.

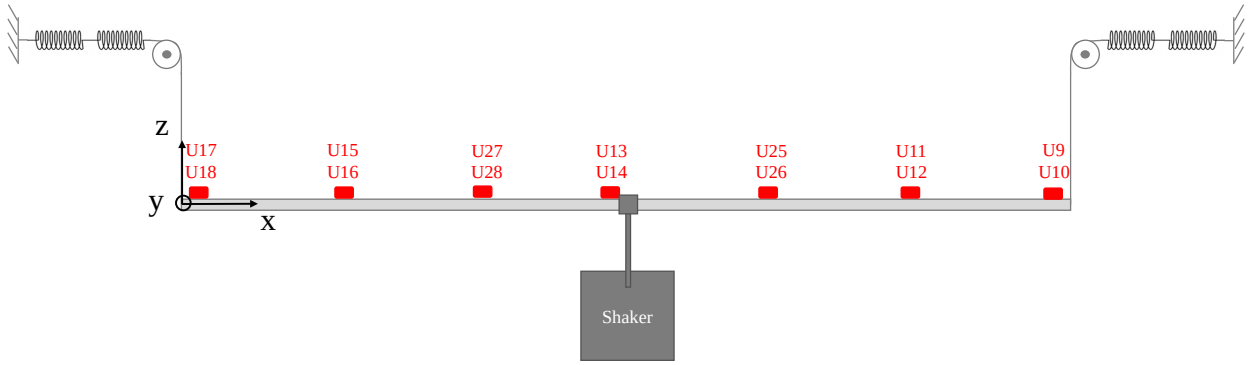

Figure 3.13: Beam with shaker at the center and suspended with a pulley and two springs at each end.

Since the shaker is physically bolted into the 3D printed structure that is attached to the beam, it was decided to model the shaker as a clamp, restricting all 3 translations and rotations. In real

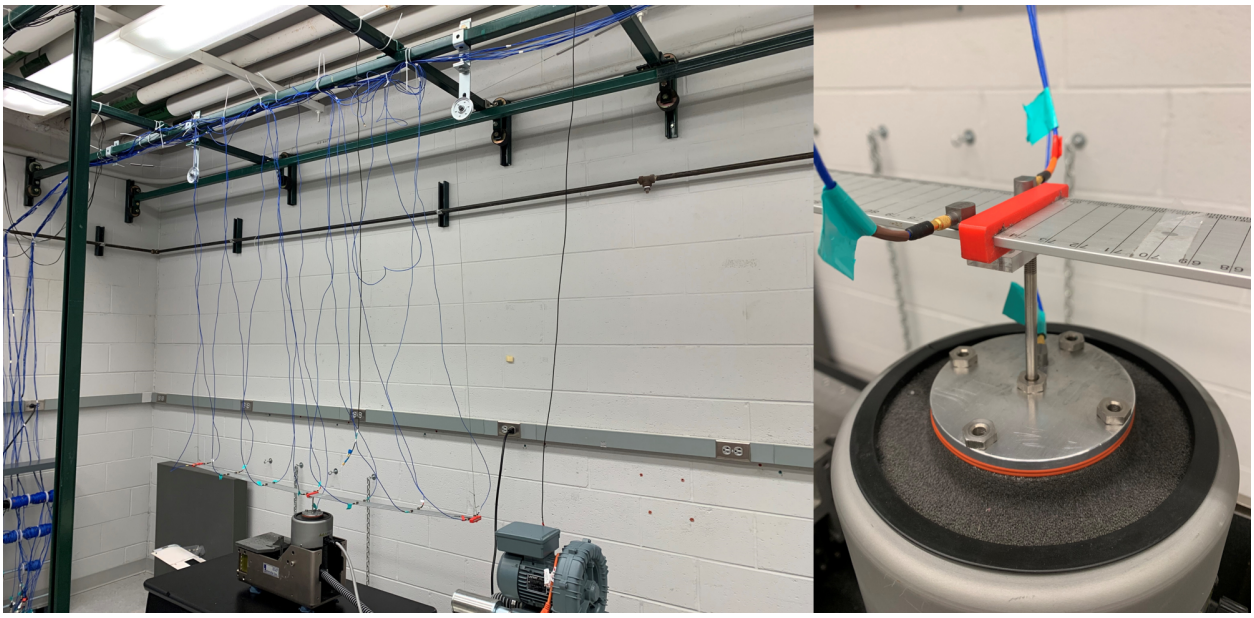

Figure 3.14: 3D printed attachment for shaker attachment (right) and experimental setup of configuration 6 (left).

life, the connection allows for a small degree of roll motion (rotation around y-axis) while all other translations and rotations are constrained as far the stinger and the attachment is concerned. Unreasonable force can cause the stinger to start unscrewing which can be interpreted as rotation around z-axis, however such deflections are neglected and the shaker is modeled as a perfect clamp at the point of attachment on the beam.

Inferences and conclusions on the impact of shaker BC on the beam:

- For the beam, the shaker attachment is best modeled by a clamp at the point of attachment (based on the results from the configuration 5 simulation and experiment). This is case dependant and may not be the best way to model the shaker for something much larger and heavier, like the X-HALE.
- The damping for the first mode with the beam connected to the spring pulley system is significantly higher than when the spring damper system is tested in isolation.

3.1.6 Conclusions from Preliminary Beam Tests

The work done regarding identifying the impact of the various suspension mechanisms on the beam, and in parallel, for the X-HALE allowed for better understanding of the beam model in different configurations. The first two configurations were defined to become familiar with the simple beam problem with and without gravity effects and using an appropriate numerical solver

to model the beam and the associated static deformation.

Configurations 3 and 4 and the associated experimental tests indicated that the addition of a spring was correctly modeled in the FEM and the numerical results matched well with the experimental. However, the addition of a pulley impacted the first few modes of the structure and adds damping to the system. This indicated that a damper must be incorporated in the numerical analysis to better approximate the experimental setup. The most straightforward way is to define a 1 DOF system that has the same mass as the object being tested and identify the impact of the suspension system on the 1 DOF system. This would allow for the characterization of the effective stiffness and damping in isolation and allow for the creation of a spring-damper model that can then be used in the numerical analysis.

However, the characterization of the 1 DOF system is sensitive to the connections, the adapters, the suspension mechanism being used and even the material used to define the 1 DOF system. Initially, a steel plate was being used, but that would overload the accelerometers before the highly damped plunge frequency could be read. An alternative option was to use a wooden block which would not transmit the energy of the impact to the accelerometers unless the impact was very strong (using a rubber tip). This meant that the energy imparted to the wooden block for the identification of the plunge frequency along with the effective stiffness and damping coefficients was higher than the force with which the hammer would be used with the beam (even though the beam is heavier and should require more energy to excite its resonances). Each added component has its own stiffness and damping coefficients, and a combination of structures when joined together to achieve a specific mass adds uncertainties to the model that are difficult to capture numerically. While this study focused on characterizing the suspension setup in isolation and modeling it, there is still work to be done in perfecting the method of characterizing the suspension system in isolation. Experimental characterization requires additional effort. However, to demonstrate the methodology, the procedures defined in this section for the identification of effective stiffness and damping coefficients can be used in the numerical model for a more accurate analysis.

As shown in Section 3.1.3, the physical connection of the beam (or the X-HALE) to the test block needs to be designed better. The FEM with the inclusion of the identified stiffness and damping coefficients does not give results that better agree with the experiment. This indicates that the components used for the 1 DOF test along with all the fixtures add uncertainties in the test that must be minimized to obtain a more accurate isolated suspension model.

Some options to achieve this are:

1. Use a single block of a rigid material (steel, cast iron block etc) that is made or developed into a volume that has the same mass as the object that will be tested in that configuration. By using a single rigid material, the additional stiffness or damping that comes into the picture when multiple items are joined together is eliminated. This could also be achieved by using

something like a dumbbell.

2. For the beam tests, a 3D printed bracket is used. The beam slides into this bracket and then the Kevlar string is looped through the bracket. This was not done for the 1 DOF block tests as this would require the creation of a multiple adapters or would require a block of metal to be milled to have extrusions onto which the same 3D printed bracket will slide. In this scenario, there exist two options of characterizing the springs and pulley combination - either both sides are characterized at once (allowing for 2 points of suspension on the block, which would reduce unwanted rigid body modes from being excited) or using just one side of the suspension system and connecting the fixtures to the cg of the block. This is challenging since any excitation will excite multiple modes and unless there is sufficient energy imparted to the system, the unwanted modes may dominate the FRF.

3. Another method for identifying damping would be to define the right 1 DOF system and time the object as it is excited. If the hammer is overloading the accelerometers or if it is not providing enough energy to the mode to capture the plunge frequency, then the object can be excited by hand and the number of oscillations, the time taken and the rate at which they decay can be recorded. This, along with the amplitude decay would allow for an estimation of the frequency of oscillation and a damping coefficient. Something that can also be explored is identifying how the LMS Test.Lab software works with time data without using an excitation (in the form of an impact hammer, for example). If a manual excitation can be recorded in terms of the time history of the amplitudes of the oscillation, it would give a more accurate way of identifying damping and frequency.

4. A topic that can be explored further is the pulley itself. Pulleys are not designed in general to have oscillatory motion, they are made to enable turning direction and pulling in one direction. More expensive pulleys with higher quality ball bearing were tested and they were worse in terms of how many oscillations the mass would undergo visually compared to the pulley used for these tests. It is possible that a needle or roller bearing sheave/pulley would allow for lower friction/damping when the springs extend and contract causing the pulley to rotate.

The knowledge obtained from the preliminary tests conducted on the beam and identifying and modeling the suspension system as well as the boundary conditions can be transferred to conducting GVT on very flexible structures. The modeling and GVT techniques will be applied on multiple test cases to validate the proposed methodology, and the rest of this chapter is organized as follows. Section 3.2 introduces the first very flexible test case, a very flexible beam and the associated suspension parameters, while Section 3.2.1 presents numerical and experimental results

for the GVT of the beam using the proposed methodology. The process is numerically and experimentally demonstrated on a very flexible beam and later on a VFA test case to identify their modal parameters in different configurations.

While this section focused on identifying and modeling the suspension system and its influence on the test structure, damping is not investigated further in this dissertation. It is a complex phenomenon that is already a significant challenge for simple structures, and becomes a topic of research in itself as the structures get more complex (like built up wings or aircraft). For very flexible structures, damping may not remain constant with deformation.

3.2 Very Flexible Aluminum Beam Test Case

An aluminum beam with dimensions shown in Table 3.5 was tested according to the process described above. The beam was tested in two significantly different deformed configurations suspended under its own weight. Figure 3.15a shows the test setup in MSC Nastran, while the experimental setup is shown in Fig. 3.15b, and the jig shape defined in the test software is shown in Fig. 3.15c. The two configurations shown in Fig. 3.15 are called outboard and inboard configurations. An outboard configuration places the suspension attachments towards the free ends (0.31 m away from the ends) such that the beam bows upward and the free ends point toward the ceiling. In this configuration, the free ends of the beam are vertically displaced 0.6 m from the undeformed jig shape, corresponding to a tip deflection of approximately 33%, which is clearly outside of the linear regime. An inboard configuration places the suspension attachments towards the midspan of the beam so that the beam bows downwards and the free ends point towards the floor.

In each of these configurations, the tests are intended to attain large static deflections and demonstrate how the geometric stiffening effect due to nonlinear deformation and the deformed shape of the structure influence the experimentally observed modal characteristics.

Table 3.5: Aluminum beam dimensions and spring properties.

Property	**Value**	**Units**
Length	3.66	m
Width	50.8	mm
Height	3.20	mm
Mass	1.60	kg
Expected 1st mode	1.20	Hz
Spring stiffness	7.10	$\frac{\text{N}}{\text{m}}$
Expected plunge mode	0.47	Hz

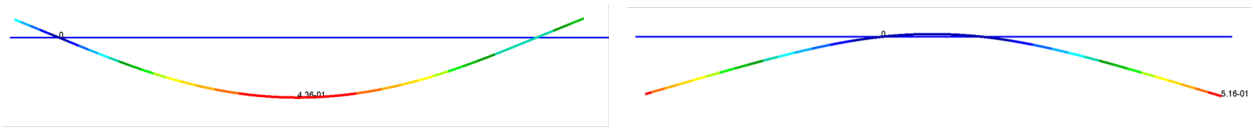

(a) Nonlinear static solution (Nastran SOL400).

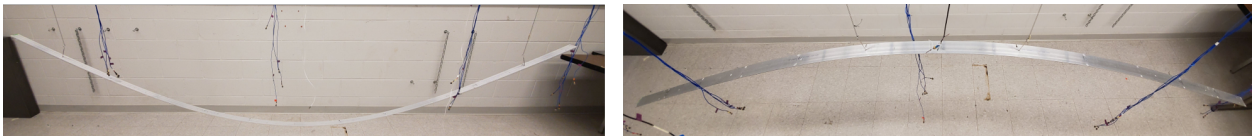

(b) Experimental setup.

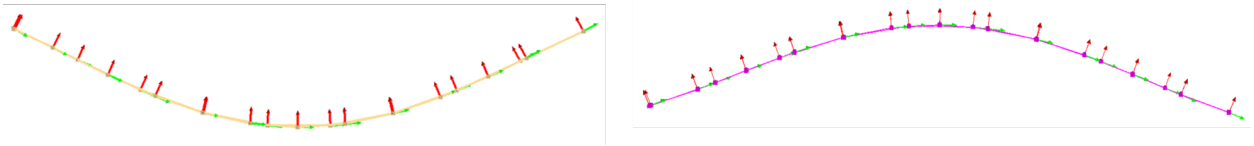

(c) Jig shape in LMS.TestLab

Figure 3.15: Static deformation of the aluminum beam.

A soft spring system was designed such that the rigid body mode with the beam is separated from the fundamental frequency of the beam as much as possible. No single spring would be able to provide even a 2x difference between the plunge frequency of the beam and spring system and the fundamental elastic frequency of the beam. A 3x2 system of springs was used to suspend the beam, 3 serial sections of 2 springs connected in parallel. Since this spring setup is very soft and stretches more than the vertical height of the test facility, a ball bearing, low-friction pulley was used to turn directions and allow the springs room to elongate horizontally under the mass of the beam. The actual experimental setup is similar to the schematic shown in Fig. 2.2b. The parameters of the spring setup used for this are shown in Table 3.6. The experimental stiffness and damping parameters of the support were identified by performing an impact hammer test on a 1 DOF system that contains calibrated weights adding up to half the beam weight. This is done because the beam is suspended using two points and each suspension point thus supports half of the total beam weight. The results of the suspension identification are shown in Table 3.7.

3.2.1 Beam Results

To verify the beam's FEM and the chosen discretization, the natural frequencies are computed about the undeformed configuration with varying finite element discretization and compared to the analytical solution. This also allows for identifying parameters to tune if the beam FE parameters are inaccurate with respect to the experimental results. Results in Table 3.8 show that the FEM

Table 3.6: Spring selection for suspension.

Property	Value	Units	Expected Plunge Freq [Hz]
Max. allowed load	11.10	N	–
Manufacturer's stiffness for single spring	8.75	$\frac{N}{m}$	0.53
Measured stiffness for single spring	10.53	$\frac{N}{m}$	0.58
Three springs in series	3.51	$\frac{N}{m}$	0.33
Three double-parallel springs in series	7.10	$\frac{N}{m}$	0.48

Table 3.7: Effective suspension parameters identification.

Property	Left	Right	Units
Mass	0.80	0.80	kg
Plunge frequency	0.40	0.41	Hz
Effective stiffness	5.06	5.19	$\frac{N}{m}$
Effective viscous damping coefficient	28.17	44.84	$\frac{N.s}{m}$
Damping ratio	7.00	11.00	%
Damped frequency	2.51	2.54	$\frac{rad}{s}$
Undamped frequency	2.52	2.55	$\frac{rad}{s}$

reproduces the analytical frequencies with the chosen discretization. OOP refers to the out-of-plane bending modes, IP refers to in-plane bending modes, and T refers to the torsional modes. The undeformed configuration allows for identifying the initial, uncoupled modes that evolve once the structure deforms.

The beam was numerically tested in various load conditions to identify the impact of deformation on the evolution of modes, particularly on the coupling between in-plane bending and torsional modes. These loading conditions are defined as a distributed load across the beam and as a factor of the gravity load. The load is gradually increased starting from 0 g to 1 g in 45 increments and the effect of loading to the deformation in the structure is shown in Fig. 3.16 for the inboard configuration and Fig. 3.17 for the outboard configuration.

The evolution of modes for the outboard configuration as a function of the load factor is shown in Fig. 3.18. Modes up to 100 Hz are presented in Figs. 3.18 and 3.19. These show that the modes that start out as the out-of-plane bending modes do not show significant evolution as the structure gets deformed. The mode associated with rigid body rotation around the beam axis couples with the first in-plane bending mode and the trend for that mode is shown in Fig. 3.19. An observation that can be made here is that the displacement of the rigid-body mode can be interpreted physically as the displacement of the center of gravity of the vibrating system. For the rigid-body modes associated with pitching along the beam axis and rolling along the chord axis, the center of mass

Table 3.8: Beam FE frequencies vs. analytical frequencies.

	Frequencies (Hz)			Error (%)	
Mode	**SOL103 183 elem**	**SOL103 366 elem**	**Analytical**	**366 vs. 183 elem**	**Anal. vs. 366 elem**
1 OOP	1.23	1.23	1.23	0.03	0.00
2 OOP	3.40	3.40	3.40	0.03	0.00
3 OOP	6.66	6.66	6.66	0.04	0.01
4 OOP	11.00	11.01	11.01	0.04	0.01
5 OOP	16.44	16.44	16.44	0.05	0.01
1 IP	19.71	19.71	19.72	0.03	0.03
6 OOP	22.95	22.97	22.97	0.05	0.01
7 OOP	30.56	30.57	30.58	0.06	0.02
8 OOP	39.25	39.27	39.28	0.06	0.02
9 OOP	49.02	49.05	49.06	0.07	0.02
1 T	51.80	51.81	51.87	0.01	0.12
2 IP	54.27	54.29	54.35	0.03	0.12
10 OOP	59.88	59.92	59.94	0.07	0.03
2 T	103.60	103.61	103.74	0.01	0.12
3 IP	106.24	106.28	106.55	0.04	0.26

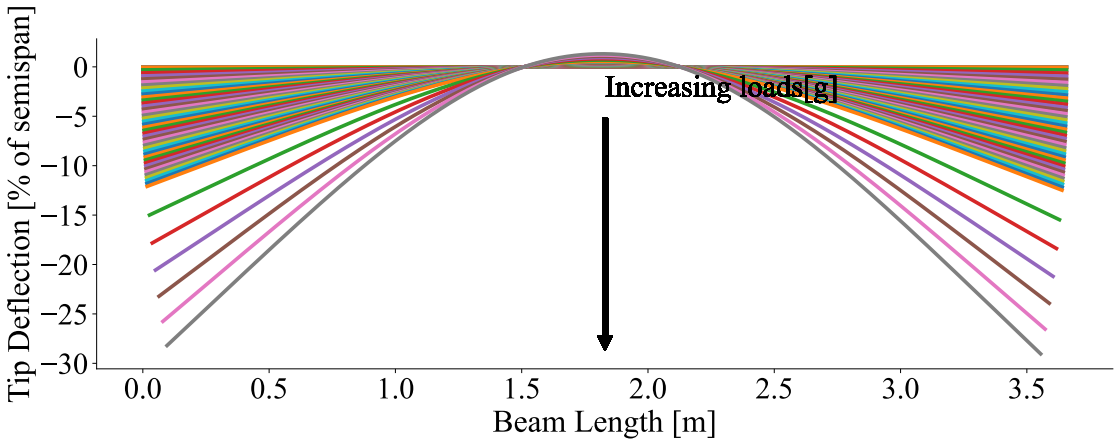

Figure 3.16: Static deformation evolution with loading for the inboard suspension.

of the vibrating system changes when gravity effects are considered. This is not due to flexibility in the structure, but increased flexibility amplifies this effect. The system (beam or any other structure) will change its behavior under loading for those rigid-body modes for which the center of mass no longer remains constant as the structure undergoes displacement.

Consider an arbitrary system with the six rigid-body degrees of freedom. For translational rigid-body modes, the relative position of the deformed structure and its center of mass does not change. i.e., the minimum potential energy for the system has the same value. However, for pitching and rolling rotations, the relative position of the center of mass changes due to the effect

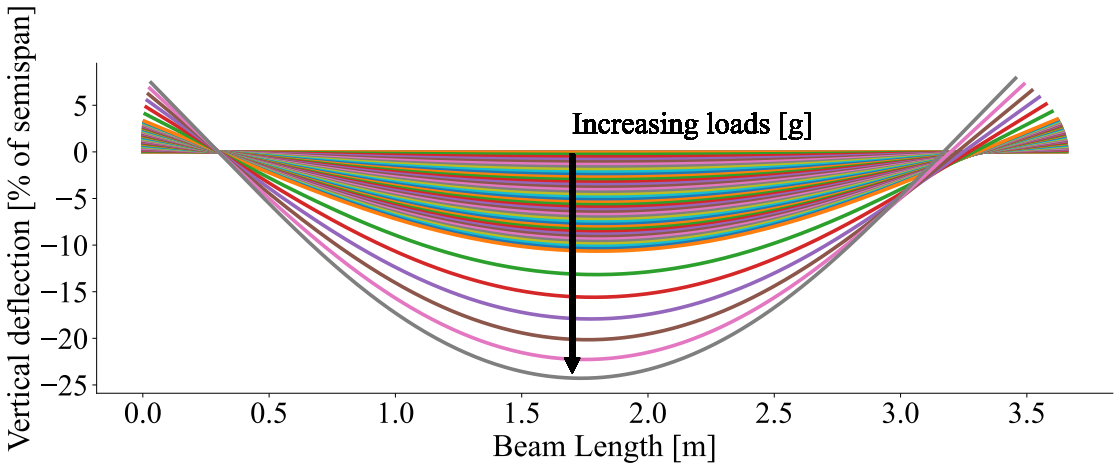

Figure 3.17: Static deformation evolution with loading for the outboard suspension.

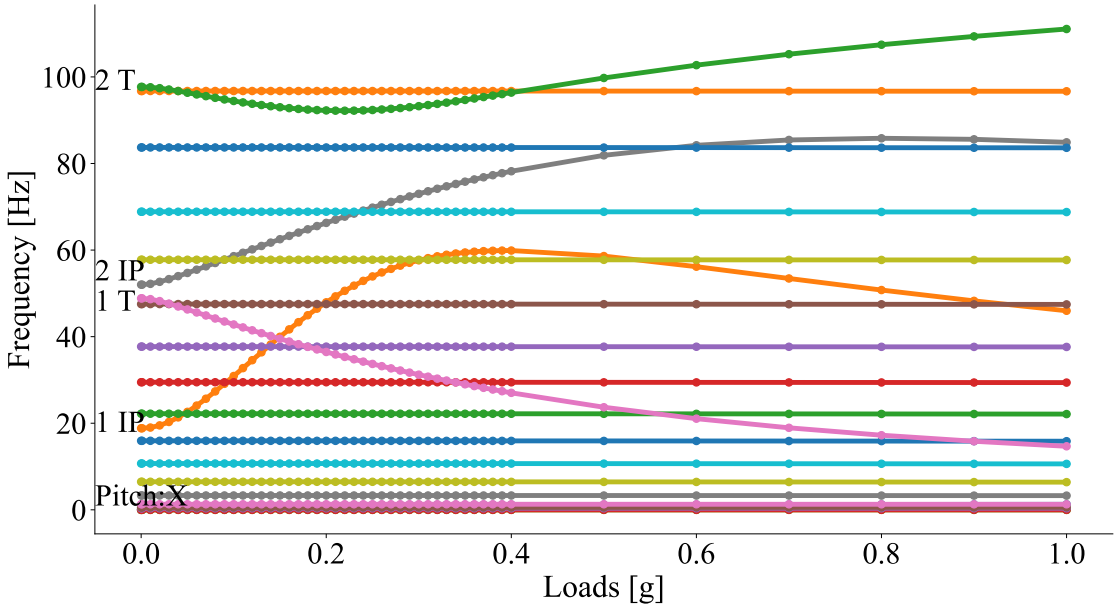

Figure 3.18: Modes evolution with load factor for the outboard suspension.

of the gravity load. The yawing motion preserves the center of mass (stays in the same position). The rigid-body motion frequencies associated with the pitching and rolling rotations are not zero anymore. This is associated to the different value of the center of mass since the configuration of the system has changed with the motion associated to these degrees of freedom. In other words, this change of frequency occurs as a consequence of the variational principle of minimum potential energy. For the very flexible beam, the only modes that show interesting progression with increased deformation are the ones with labels on the left side of Fig. 3.18. For this reason, these modes are the only ones shown in the plots discussing mode evolution for either case. Figure 3.20 shows

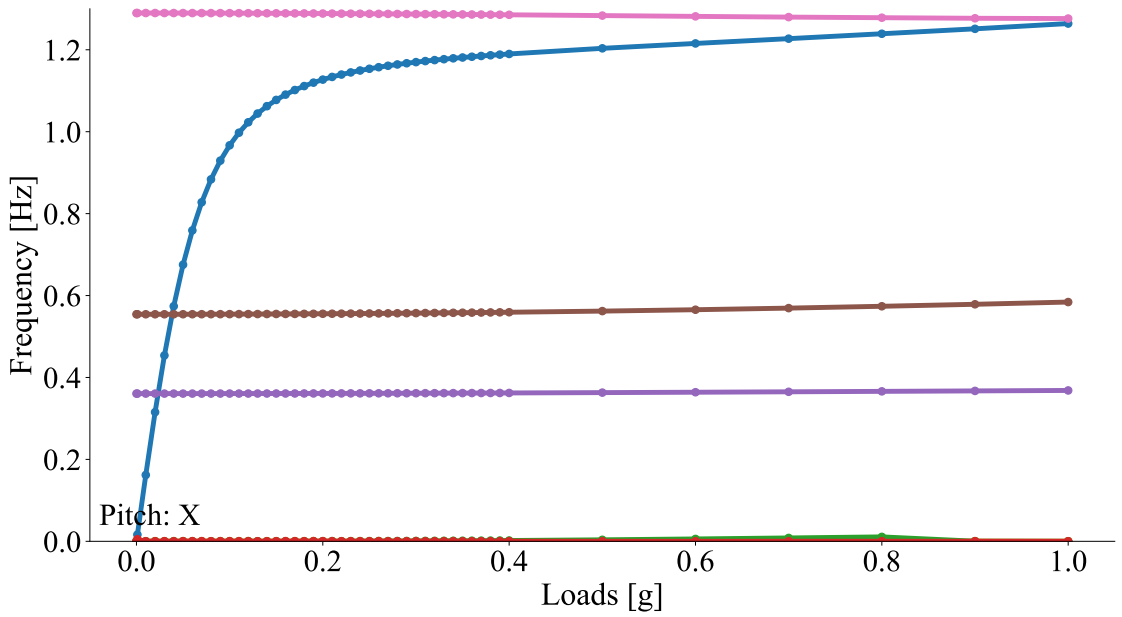

Figure 3.19: Rigid body rotation (pitch around x-axis) couples with first in-plane bending mode.

the selected modes for the outboard configuration evolving with loading and, equivalently, static deformation. The initial, uncoupled modes (in the unloaded case) are indicated by letter markers (A–E) for the mode evolution at 0.1 g loading and at the fully loaded/deformed case at 1 g. The evolution of the modes with loading was tracked using a mode tracking algorithm developed as discussed in [86, 87].

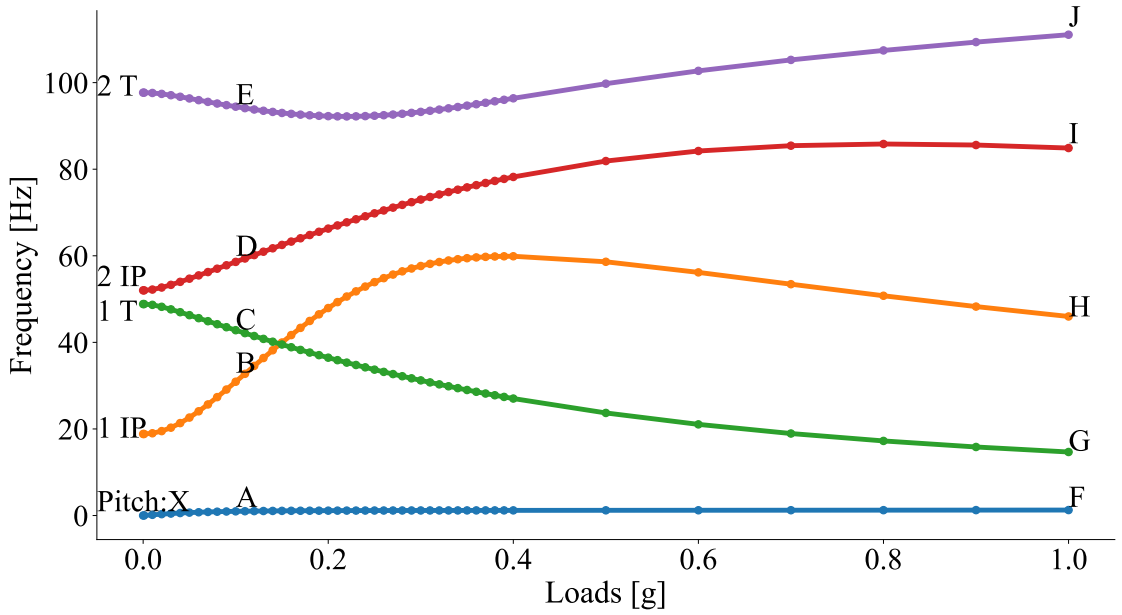

Figure 3.20: Selected modes evolution with loading for the outboard suspension.

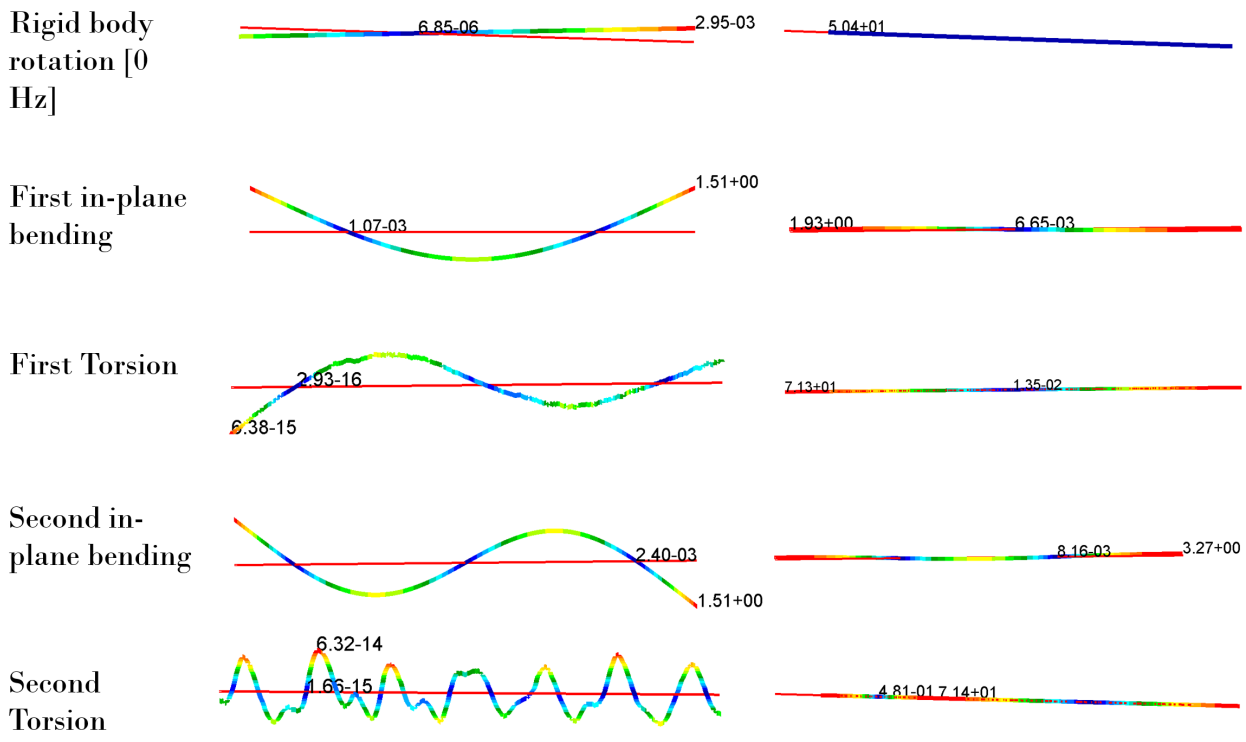

Figure 3.21: Mode shapes translational (left) and rotational (right) components for the unloaded case: outboard configuration.

The mode shapes for the outboard configuration at these three load cases are shown in Figs. 3.21, 3.22, and 3.23. A definitive identification of the modes can only be made from the unloaded/undeformed condition. As the structure starts to deform under incremental loading for the numerical simulations in the outboard configuration, the first in-plane bending mode starts to couple with the second torsion mode and a rigid body rotation mode (pitch mode about the beam axis). Similarly, the second torsion mode interacts with the first in-plane bending and contains components of the rigid body rotation mode. As the loading and deformation increases, the modes also evolve and what started as the second torsion mode goes down in frequency and then around 0.2 g loading, starts increasing. Likewise, the first-in-plane bending mode increases numerically with loading until it reaches an inflection point around 0.4 g, at which point it reduces in frequency with deformation and ends visually looking closer to the third in-plane bending mode as shown in Figs. 3.21, 3.22, and 3.23. At around 50 Hz, the second in-plane mode interacts with the first torsion mode and reduces in frequency as the structure gets progressively more deformed; while what was initially the first torsion mode goes up in frequency. Another coupling that occurs is the rigid body rotation along the beam axis couples with the first in-plane bending mode and increases in

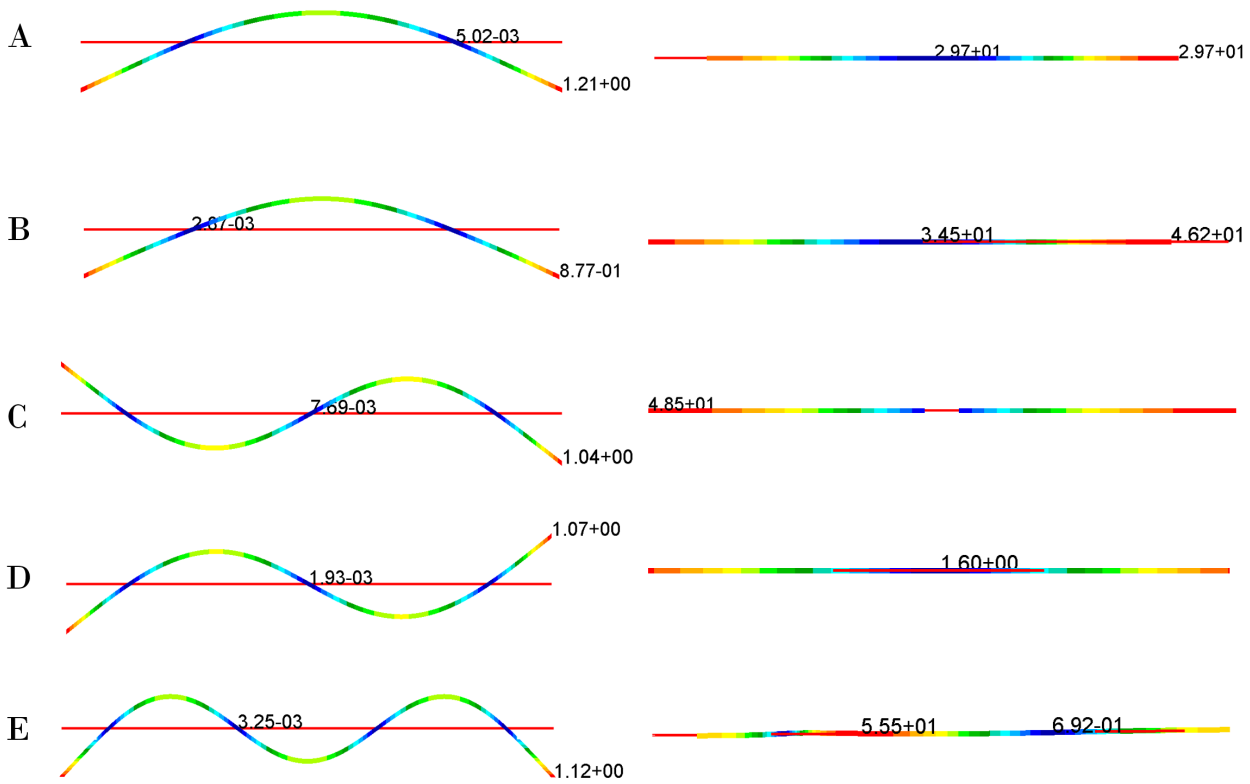

Figure 3.22: Mode shapes translational (left) and rotational (right) components evolution at 0.1g: outboard configuration.

frequency and ends as the first in-plane bending frequency at the 1 g load case as shown in Fig. 3.19 for the outboard suspension configuration. A similar trend is observed for the same modes for the inboard suspension configuration. The results for inboard configuration are shown in Fig. 3.24, with the results for the outboard configuration overlaid. The modes are labelled according to the initial definition at the unloaded case.. The inboard configuration exhibits similar mode evolution and trends as the outboard, but the frequency values and evolution are different. This indicates that as the deformation increases, the couplings in the two different suspension cases change and evolve differently. This is most apparent from the mode that starts out as 2 IP and interacts with 1 T. For the outboard case, this mode increases in frequency, plateaus and shows a small decrease at the fully loaded configuration, whereas in the inboard case it continues to increase with the load. The mode shapes for this mode at the final load case are also different, indicating how the different deformed shapes exhibit different mode evolution with increasing loading or deformation.

Results show significant changes in the natural frequencies based on deformation. As the structure gets progressively more deformed, the in-plane bending-dominated modes reduce in frequency and couple with the torsion modes. While the torsion-dominated modes increase in frequency and also get coupled with the in-plane bending modes. These couplings are multi-mode interactions

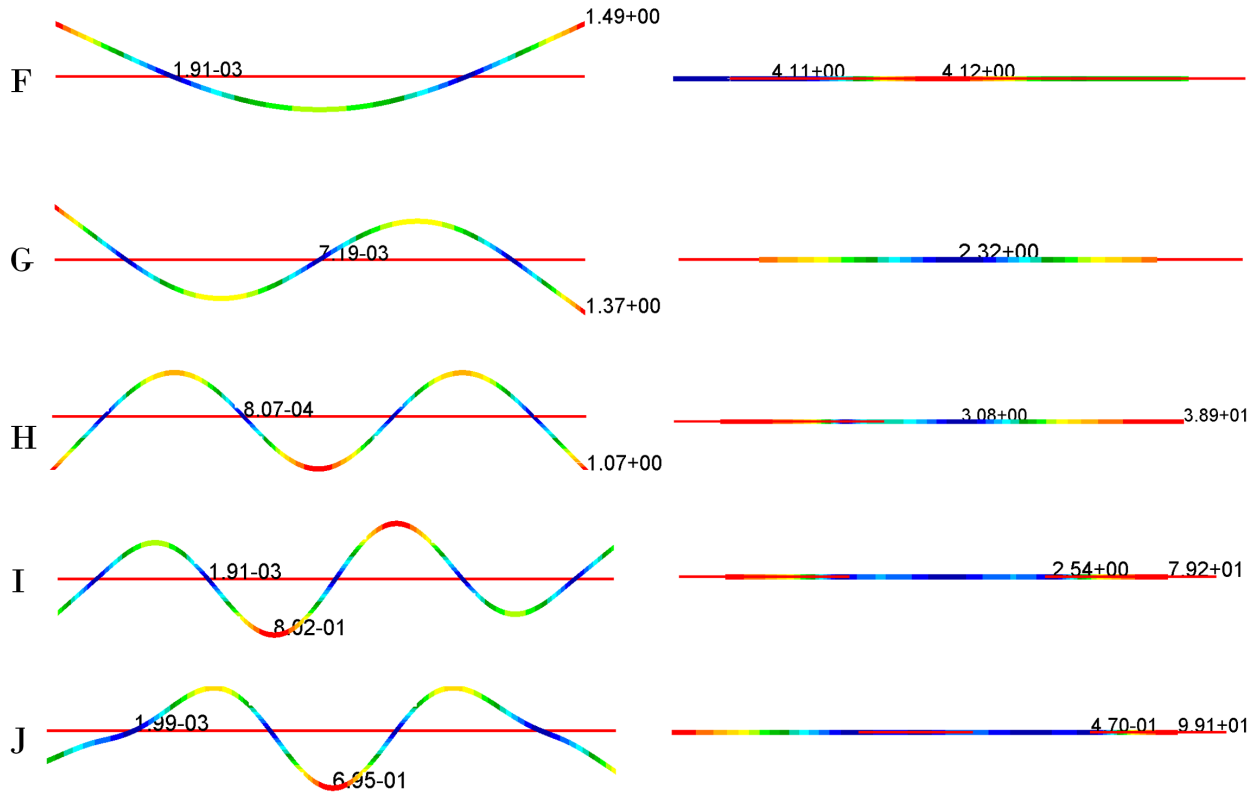

Figure 3.23: Mode shapes translational (left) and rotational (right) components at the final load case (1g): outboard configuration.

and the interactions evolve as the shape of the structure changes under loading.

Once the suspension properties are identified, a numerical model of the suspension system was created and included in the beam FEM. The actual beam structure was instrumented with 26 uniaxial accelerometers across the span in 13 stations. Each span-wise station consists of two accelerometers placed along the chord. The out-of-plane bending and torsional modes are identified using the uniaxial accelerometers, whereas the in-plane bending modes are identified using triaxial accelerometers. All beam experimental tests were conducted with an impact hammer with a soft rubber tip in order to excite the low frequency modes and since most of the modes of interest are under 100 Hz. The test was setup such that a frequency resolution of 0.05 Hz was obtained which allows for finer identification of experimental modes and better estimation of damping. However, the trade-off is that each impact required 20 seconds of measurement time to evaluate the response of the structure.

The initial numerical results of the beam tests conducted with the beam hung in the outboard configuration are shown in Fig. 3.25, with each color representing the different cases showing frequencies in Hz. The numerical results are shown for four cases, “Undeformed” refers to the case

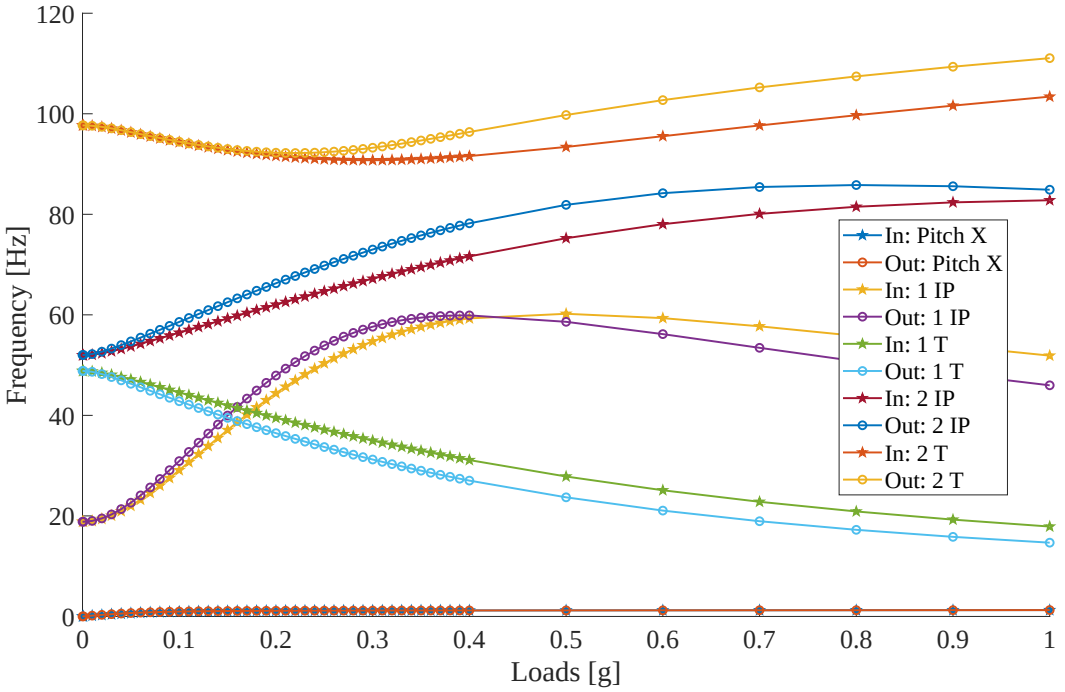

Figure 3.24: Modes evolution with load factor for outboard (*) and inboard (o) configurations.

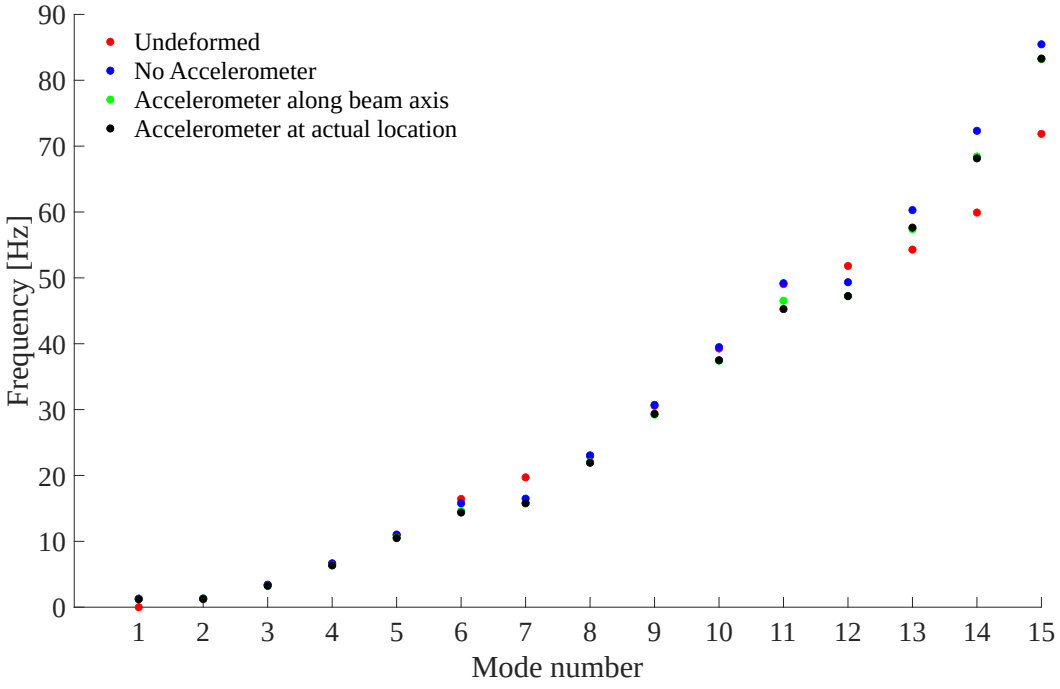

Figure 3.25: Numerical results comparison: outboard configuration.

where the static deformation of the beam under self-weight was not accounted for, "No accelerometer" refers to the case where static deformation of the beam was accounted for, i.e., modal analysis was performed about a deformed condition but accelerometers and their mass not being accounted for in the numerical model. The two following cases both account for the effect of deformation under self-weight in the numerical model. "Accelerometer along beam axis" refers to the FEM incorporating the accelerometer mass at the correct span location and along the beam axis, but not accounting for the chordwise locations, while "Accelerometer at actual location" includes the concentrated masses defined for the accelerometer at an offset from the beam axis to account for the physical location of the accelerometers. These cases are presented here to indicate the difference in the numerical results based on how the accelerometers are accounted for in the numerical model.

The beam was tested experimentally first with the accelerometer cables coming out from the sensor taped to the beam for about 5 cm cable length per accelerometer. This was done to avoid the cables touching the beam and affecting the response as the beam is excited. Another test was conducted with the accelerometer cables pointing out chordwise from the beam, thus reducing the impact of the cables and their mass. It was ensured that no cable is in contact with the beam. The results of these two slightly different experimental setups for the outboard configuration is shown in Fig. 3.26. Case 1 refers to the first cable arrangement where the cable is taped for a short length along the beam, while case 2 refers to the other arrangement where the cable is pointing out away from the beam. All successive experimental tests were conducted with the accelerometer cable arrangement as discussed for case 2.

The initial FE numerical results obtained from a statically deformed modal analysis in MSC Nastran SOL400 match the GVT results relatively well for the higher modes but the in-plane bending modes and the lower out-of-plane bending modes are poorly matched. The location of the accelerometers was measured and updated in the FEM along with tuning the stiffness parameters. The accelerometer cables point out chordwise from the beam and this leads to the center of mass of the accelerometers moving away from the actual location of the accelerometer placement. This would not be a significant concern with a test structure where the accelerometer mass can be neglected, but in the case of the beam, their mass is non-negligible. This effect was incorporated by having the numerical concentrated masses of the accelerometer defined at the very tip of the beam in the chordwise direction. Since the beam dimensions do not exactly match the ones specified by the manufacturer, they were also measured and updated in the FEM. The Young's modulus initially used was slightly different than the modulus of the aluminum alloy listed by the beam's manufacturer, so this was corrected as well. The parameters updated are shown in Table 3.9. After tuning these parameters for the outboard configuration, results from the FEM were compared to the GVT results in both configurations. Once the mass and location of the attachments and accelerometers was measured and added to the FEM, almost all modes of interest are identified

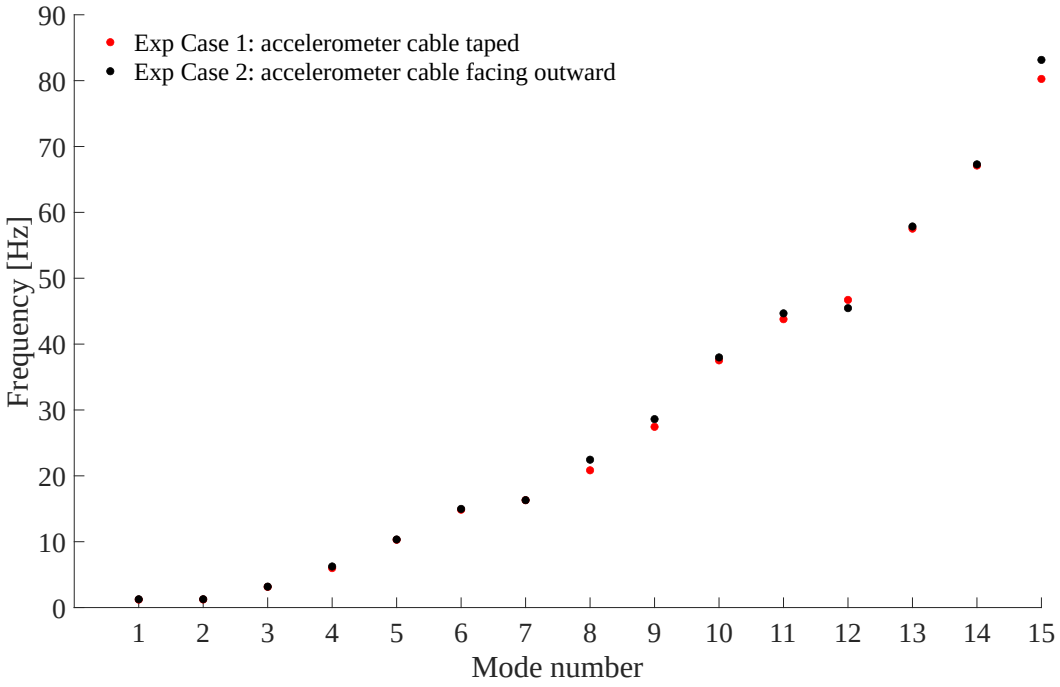

Figure 3.26: Experimental results for the two accelerometer cable arrangements for the outboard configuration.

Table 3.9: Parameters updated for the beam's numerical model.

Beam Properties	**Initial Value**	**Updated Value**	**Units**
Length	3.66	3.66	m
Width/Thickness	0.0508	0.0507	m
Height	0.00318	0.00321	m
Mass	1.60	1.61	kg
Young's Modulus	70.0	68.9	GPa

within 5% error. However, the biggest change is seen in the modes that have in-plane bending or torsional components. Mode 1, which has a strong in-plane component, along with a rigid body rotation component has a reduction in error between the tuned and the un-tuned model as well as mode 6 which contains second in-plane bending coupled with first torsion components. The out-of-plane bending modes do not show significant change since the deformation does not affect them as much as the in-plane bending and torsion modes. Experimental tests were performed on the beam in both configurations (under self weight) and the experimental results compared to the FE numerical results with the updated model are presented in Tables 3.10 and 3.11 for the outboard and inboard configurations respectively. Here, the error compares the undamped experimental

frequencies with the numerical frequencies.

Table 3.10: Experimental vs. tuned numerical results outboard configuration (1 g). Error compares the undamped experimental modes against the numerical.

Mode #	Num. freq. (Hz)	Exp. freq. (Hz)	Exp. damp. (%)	Undamped exp. (Hz)	Error (%)
1	1.26	1.26	3.5	1.26	0.3
2	1.28	1.27	1.9	1.27	0.5
3	3.28	3.18	3.4	3.18	3.1
4	6.39	6.23	4.3	6.24	2.5
5	10.61	10.34	0.7	10.34	2.6
6	14.67	14.98	1.4	14.98	2.0
7	15.85	16.31	0.1	16.31	2.8
8	22.12	22.45	0.1	22.45	1.5
9	29.39	28.61	0.2	28.61	2.7
10	37.62	37.98	0.1	37.98	0.9
11	45.98	44.67	1.3	44.67	2.9
12	47.45	45.46	0.1	45.46	4.4
13	57.70	57.86	0.1	57.86	0.3
14	68.78	67.29	0.2	67.29	2.2
15	83.62	83.15	0.1	83.15	0.6

Table 3.11: Experimental vs. tuned numerical results inboard configuration (1 g).

Mode #	Num. freq. (Hz)	Exp. freq. (Hz)	Exp. damp. (%)	Undamped exp. (Hz)	Error (%)
1	1.25	1.25	2.5	1.25	0.3
2	1.26	1.35	3.6	1.35	7.0
3	3.28	3.35	5.3	3.35	2.1
4	6.37	6.50	0.5	6.50	2.0
5	10.57	10.36	0.5	10.36	1.9
6	15.89	15.30	1.6	15.30	3.9
7	17.88	18.53	1.2	18.53	3.5
8	22.07	21.92	0.2	21.92	0.7
9	29.52	28.60	0.1	28.60	3.2
10	37.70	37.82	0.4	37.82	0.3
11	47.50	45.44	0.1	45.44	4.5
12	51.88	52.23	1.8	52.24	0.7
13	57.93	56.81	0.8	56.81	2.0
14	68.51	69.60	0.4	69.60	1.6
15	82.80	80.62	0.1	80.62	2.7

The most significant differences between the two suspension configurations are modes with in-plane bending and torsional components as expected, whereas the out-of-plane bending modes are not significantly influenced. This is evident when the different deformed configurations are compared against each other numerically and experimentally in Tables 3.12 and 3.13 respectively.

Table 3.12: Numerical results: outboard vs. inboard configuration.

Mode #	Outboard freq. (Hz)	Inboard freq. (Hz)	Difference (%)
1	1.26	1.25	0.9
2	1.28	1.26	1.4
3	3.28	3.28	0.1
4	6.39	6.37	0.4
5	10.61	10.57	0.4
6	14.67	15.89	7.7
7	15.85	17.88	11.4
8	22.12	22.07	0.2
9	29.39	29.52	0.4
10	37.62	37.70	0.2
11	45.98	47.50	3.2
12	47.45	51.88	8.5
13	57.70	57.93	0.4
14	68.78	68.51	0.4
15	84.89	82.80	2.5

Table 3.13: Experimental results: outboard vs. inboard configuration.

Mode #	Outboard freq. (Hz)	Inboard freq. (Hz)	Difference (%)
1	1.26	1.25	1.0
2	1.27	1.35	6.1
3	3.18	3.35	5.1
4	6.23	6.50	4.1
5	10.34	10.36	0.3
6	14.98	15.30	2.1
7	16.31	18.53	12.0
8	22.45	21.92	2.4
9	28.61	28.60	0.0
10	37.98	37.82	0.4
11	44.67	45.44	1.7
12	45.46	52.23	13.0
13	57.86	56.81	1.8
14	67.29	69.60	3.3
15	83.15	80.62	3.1

3.3 Concluding Remarks

This chapter presented a methodology for GVT of very flexible structures exhibiting large deformations under self-weight in different suspension configurations. The impact of the suspension

configuration on the modal characterization was studied using suspensions that do not have the conventional order-of-magnitude separation between the suspension mode and the elastic modes of the test structure. By properly identifying and modeling the suspension/support system in the structure's numerical model, GVT results from a single deformed condition allowed for recovering the true structural modal parameters once the support system's influence is modeled, tuned, and removed from the FEM. The results showed good agreement between the numerical and experimental setup and are within uncertainty bounds associated with the test, which include numerical modeling errors and uncertainties based on the experimental setup.

The GVT methodology proposed in this work was demonstrated on an isotropic, constant cross-section 3.7-m long aluminum beam. The adjusted model can then be used in any deformed configuration to identify its structural modal characteristics. For built-up very flexible structures like a wingbox, all the modal parameters may not be recovered from a single configuration test. This is explored on multiple very flexible test cases, and verified in the following chapters in this dissertation. Development of internal stresses caused by the deformation changes stiffness, altering the frequencies. Moreover, damping may not remain constant with deformation. These effects were not considered in the numerical models used in this study. The impact of deformation on damping should be investigated further in future work with the X-HALE as a potential numerical and experimental test case.

CHAPTER 4

Finite Element Model Updating for Very Flexible Structures

This chapter addresses the third research challenge, FEM updating for VFA. As aircraft wings become more flexible as a result of searching for more fuel efficient and higher performance solutions, structural nonlinearities become more apparent. Geometric nonlinearities make the structure's modal parameters a function of the deformed shape and, therefore, of the loading condition. Modal characterization of very flexible structures is challenging due to these nonlinearities and the very low natural frequencies (the fundamental mode is typically below 1 Hz). In traditional, stiffer structures, a single shape is sufficient to characterize the structure through ground vibration testing and finite model updating due to its linear behavior. However, with very flexible structures, different deformed shapes have different modal parameters (frequencies, damping, and mode shapes). The study in this chapter investigates the impact of large displacements on the modal parameters (frequency and mode shapes) of very flexible structures and introduces a method to update the corresponding finite element model. Results are presented to discuss the impact of deformed shapes and the development and applicability of the procedure to general very flexible wing structures.

This chapter is organized into different sections that discuss the problem setup, verification, and application. Section 4.1 describes a modification on the methodology to study the problem numerically in order to demonstrate and verify the new procedure. Section 4.2 introduces the beam FEM test case which is used to set up and exercise the optimization framework and data handling required to use a nonlinear structural solver with the optimizer. Section 4.3 introduces the built-up FEM test case and a discussion of the application of the proposed methodology to it. Section 4.4 summarizes the work done and outlines the future work that can be conducted to build on this study.

4.1 Verification Approach for New FEM Updating Procedure

To demonstrate and verify the new procedure described in Section 2.2, a numerical-only process is presented with a surrogate of the GVT data. The FEM updating process is studied purely numerically by creating a reference FEM and randomly perturbing its geometric and/or material properties to generate a mistuned model. The mistuned model represents an initial FEM to be tuned, while the reference FEM emulates the actual structure and its results would represent the GVT data in this verification exercise. This surrogate GVT data contains the sets of frequencies and mode shapes for the n loading cases leading to the corresponding deformed shapes.

The 'mistuning' is done through a script that reads the material properties, concentrated mass properties, element properties, and all other properties associated with a FEM. The user can specify what terms should be mistuned as well as the weighting factors for adjusting these terms. With the numerical reference and mistuned models available, the multidisciplinary optimization problem described in section 2.2 is performed on the mistuned model in different loading conditions. The process is adjusted to work within a numerical only environment and is shown in Fig. 4.1.

The process described in section 2.2 requires using a nonlinear structural solver. Nastran's solution 400 was selected to perform the two-step nonlinear static + deformed modal analysis for each of the selected load cases. A natural extension to using Nastran's SOL400 as the structural solver is to evaluate Nastran's built-in optimization toolbox, SOL200, for setting up the problem described in Eq. 2.11. However, upon reviewing the capabilities of SOL200 it was determined that there exist limitations that prevented its utilization in the case of very flexible structures. These are:

1. A nonlinear structural solver is not available within the optimizer.

2. There does not exist the capability to perform a multistep solution within each subcase. This implies that a deformed modal analysis cannot be performed using SOL200.

This leads to the inability to handle multiple objectives (like matching frequencies and static deflection) in the same input file (or objective function) since that calls for having both static and modal results accessible and the optimizer only has access to one solver results in each subcase. Therefore, alternative optimization toolboxes were evaluated, namely OpenMDAO [1] and SciPy's minimize. SciPy [2] was chosen as the optimization framework for this study because of its smaller learning curve, and the ability to use the same optimization algorithms as OpenMDAO. Both a gradient-free (Nelder-Mead (NM)) and a gradient-based (Sequential Least Squares Programming

[1] https://openmdao.org/
[2] https://scipy.org/

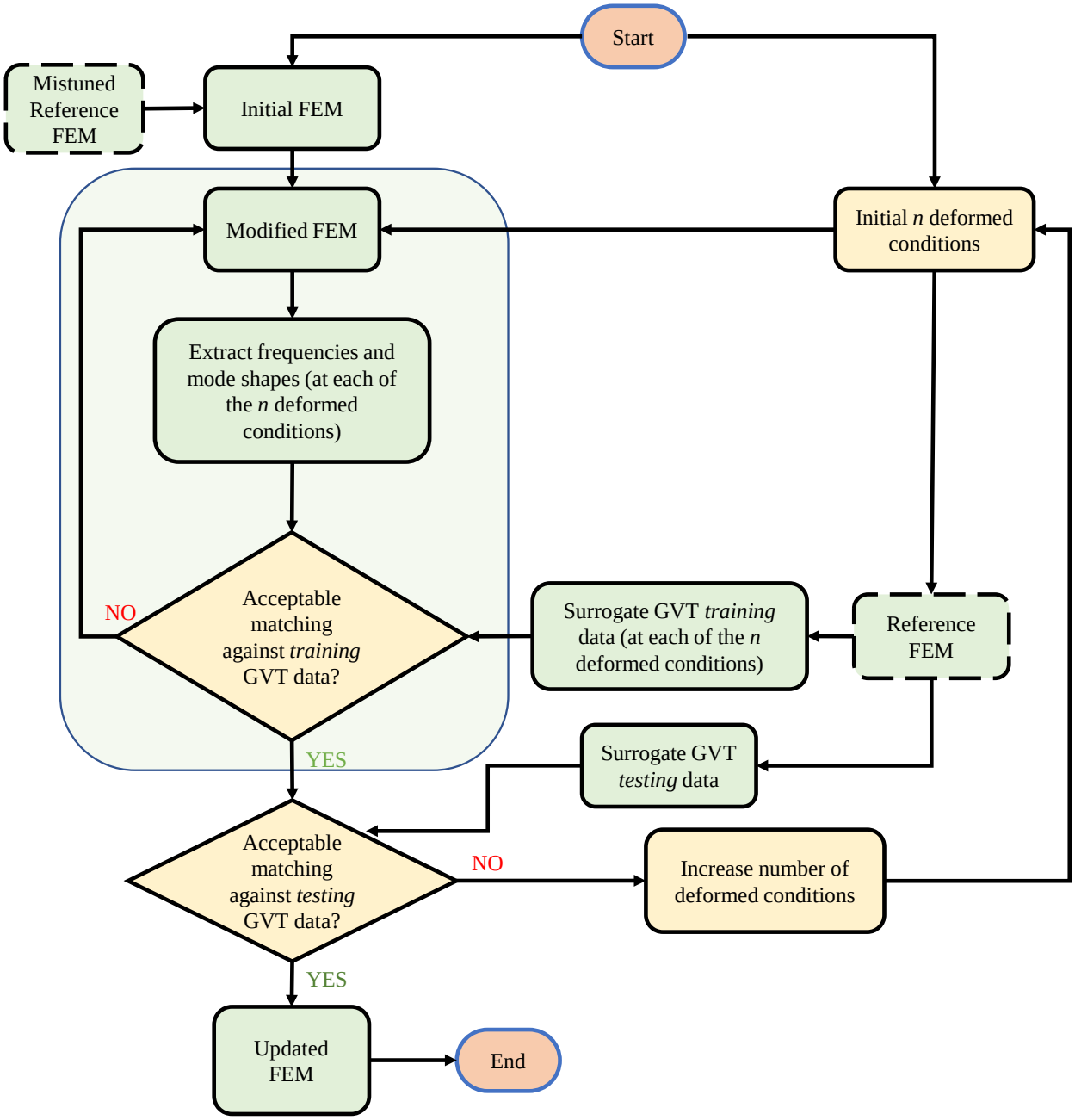

Figure 4.1: Verification process for FEM updating for very flexible structures.

(SLSQP)) algorithms were selected to perform the optimization problem (see Fig. 4.2). Since Nastran is a black box to the external optimizer, only finite differences can be used when evaluating gradients of the outputs with respect to the design variables. The interfacing of SOL400 with SciPy's optimizer was done using an open source Python module called PyNastran [88], which

was used to write an updated input file (with updated design variables) each iteration of the optimizer. Codes were developed to read the output of the SOL400 run and compute each of the metrics in the objective function as well as evaluate the constraints and apply bounds to the design variables. A schematic of the data handling and inputs/outputs (I/O) to the optimizer is shown in Fig. 4.3. The unconstrained, gradient-free Nelder-Mead algorithm was set up first since it does not require gradient evaluation, which makes the problem easier to start. For the gradient-based, constrained SLSQP algorithm, a user-defined function was also provided to evaluate gradients of both the objective and constraint functions with respect to the design variables, but the optimizer's internal gradient evaluation proved faster and had the same accuracy. So user-evaluated gradients were not used for the gradient-based optimizer for this study.

The user can choose the type of optimizer to use within SciPy's minimize, and a description of the differences between them is provided here. Nelder-Mead (also known as the nonlinear simplex) only takes a relative function or design variable value tolerance. It cannot handle constraints or bounds directly, but a penalty method can be used to indirectly account for constraints while forming an unconstrained problem to feed into the optimizer. On the other hand, the constrained, gradient-based SLSQP optimizer treats the objective function as a black box and uses finite differences to compute gradients. SciPy calls Nastran to run the input file and perturbs each design variable to evaluate the sensitivities. The Jacobian(s) evaluated for the objective function are available to the user. Similarly, gradients of the constraint variables are computed internally using finite differencing – but these are not available to the user. An important consideration is the scaling of the design variables and the bounds placed on them.

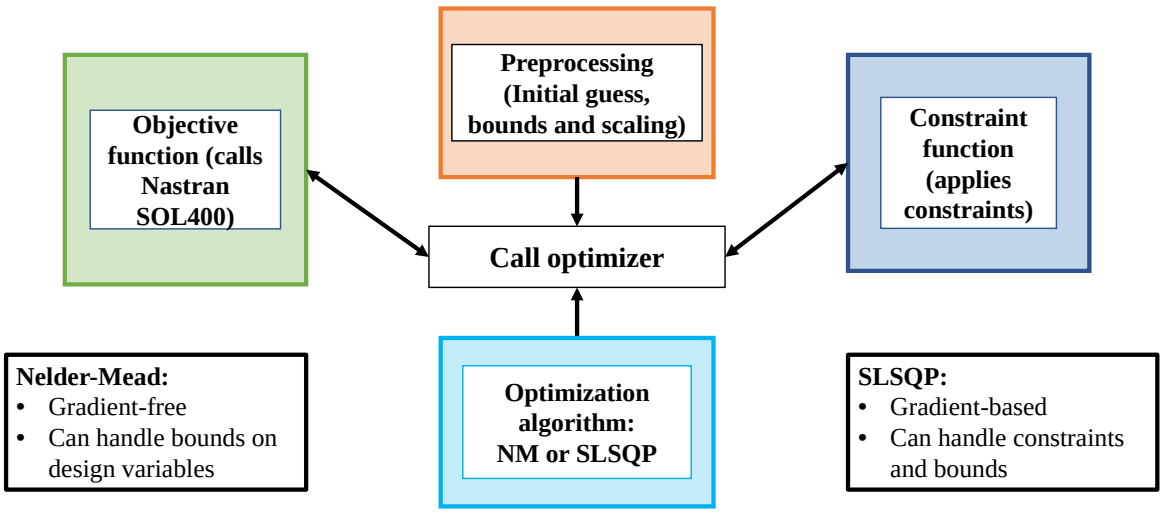

Figure 4.2: Selected optimization algorithms: Nelder-Mead and SLSQP.

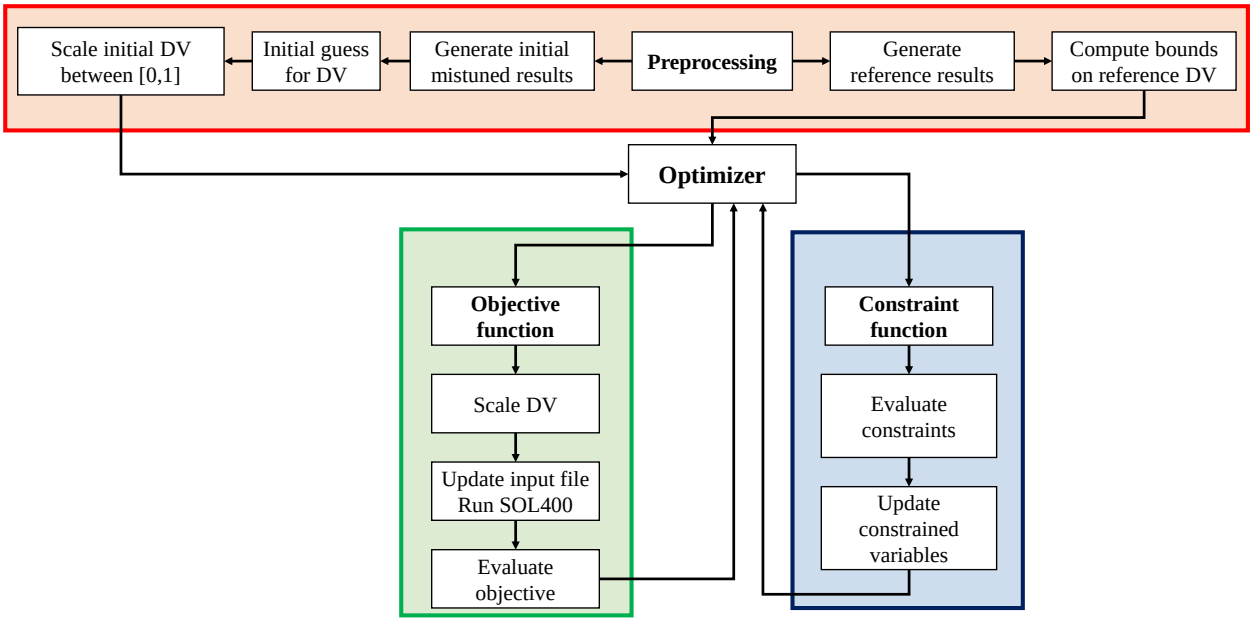

Figure 4.3: I/O for using Nastran's SOL400 with SciPy's optimizer.

To account for the static shape about which the GVT would be conducted, the objective function described in Eq. 2.11 can be augmented with the static deflection of all the different deformed configurations. This can be done easily from the numerical only set up since the two-step nonlinear static and deformed modal solution means that the results of the first step are accessible and can be used by the optimizer. In an actual GVT, this would either be done separately if the measurements are available in order to update the stiffness model of the FEM, or a stiffness update using static deflections is simply not performed independent of the entire FEM calibration. Instead, the frequency and mode shape errors are used to force adjustments on the stiffness design variables. Another topic of interest is to investigate if multiple deformed configurations are definitively needed to capture the two effects described above (geometric nonlinearities due to the nonlinear strain-displacement relation and the 3D effects in the presence of local stiffness and stress concentrations in detailed FEM). This requires calibrating a FEM using the general FEM updating approach with no load as described in Eq. 2.10, and also with the modified process described in Eq. 2.11. Once the calibrated FEMs using the two different techniques are available, a complex load (forces and moments in multiple directions) would be applied to the two calibrated FEMs and their responses would be analyzed and compared to that of the reference FEM. Section 4.3 includes a discussion of such a comparison.

Interestingly, during the initial tests using Nastran's SOL200 and even using the SOL400 and SciPy system developed in this work, doing a sequential optimization (stiffness first, then mass) did not yield any better results (both in terms of accuracy and computational time) than handling

the stiffness and mass design variables all at once. Part of the future work is to refine the objective function, add/subtract design variables and aggregate constraints to speed up the optimization.

The investigations performed as part of this work focus on very flexible wings or wing-like structures. The models were considered clamped at the root and varying loads were applied to get the large displacements under those conditions. This was done to mimic the loads during different flight maneuvers that can cause significant deformation for very flexible wings. The goal is to adjust the model to best capture the elastic behavior within the range of deformations expected under operating conditions. The scheme can be applied *ad hoc* or algorithmically to minimize the error metric (objective function) and improve the quality of the results. In order to capture the basic geometric nonlinear effect associated with large deflections of beam-type motion, a single configuration, under load or not, is sufficient as demonstrated in the scaling study by [84]. However, to capture the local nonlinear effects associated with built-up structures, additional deformed conditions are needed to tune the model. This is problem dependent and will affect the number of deformed states needed to capture the local effects. As long as the metric of error is satisfied, the exit criterion for convergence is reached. Additionally, variations in the model updating procedure and optimization problem definition are discussed in sections 4.2 and 4.3 with the goal of investigating the sensitivity of the test cases to the problem set up and sequence of steps, along with the number of deformed states used.

4.2 Uniform Beam Test Case

A uniform aluminum beam was selected as a simple test case to experiment with the optimization framework and to develop the data handling required to use a nonlinear structural solver (Nastran's SOL400) within an external optimizer. The beam was clamped on one end and free on the other. The beam is studied under different distributed loads that change its shape considerably. Table 4.1 provides the dimensions of the beam, while the results of the two-step nonlinear static and deformed modal solutions of the beam under different loads are provided in Table 4.2; mode types are identified using the unloaded and undeformed configuration. Modes labeled as OOP are out-of-plane bending, IP are in-plane bending, and T are torsion. The difference in the natural frequency values under the different loading conditions can be observed here. The static deformation is shown in Fig. 4.4, which highlights the orders of magnitudes difference in the maximum deflection under the loads applied.

The structure is discretized with 150 beam elements and is subdivided into three regions for mistuning and creating the initial FEM to be tuned. Material and geometry properties were chosen as the design variables for the beam, and randomly varied to within $\pm 5\%$ of the reference values for the initial FEM. Inequality constraints are imposed on the total mass and inertia properties, as

Table 4.1: Solid Aluminum beam properties.

Nominal properties	Value	Units
Length	1.5	m
Width	5	mm
Height	3	mm
Density	2700	$\frac{\text{kg}}{\text{m}^3}$
Young's modulus	70	GPa
Poisson's ratio	0.33	–

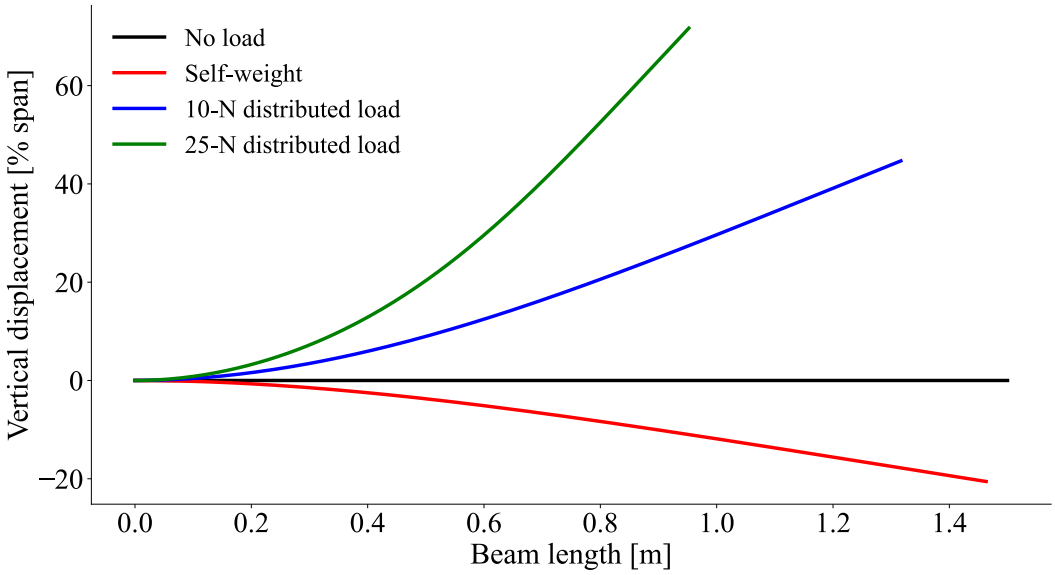

Figure 4.4: Static deformation of the very flexible beam under different loading conditions.

well as the center of gravity. A one-sided MAC inequality constraint was also imposed to ensure the mode shapes also closely match and no mode switching occurs as a result of changes in design variables as the optimizer explores the design space. The bounds on the design variables were set to be $\pm 10\%$ of the reference values. Similarly, the constraint variables had their upper and lower limits set within $\pm 10\%$ of the reference FEM's results. The reference, initial, and converged design variables for the optimization problem using the Nelder-Mead gradient-free, unconstrained optimizer are shown in Table 4.3.

The reduction in error after calibration for the beam test case is illustrated in Fig. 4.5. The results show excellent correlation for the calibrated FEM with the reference FEM for all the load cases. While the initial error in natural frequencies was up to 15% and varied significantly between the different deformed cases, the converged design variables allow to match all the frequencies for all the load cases within 0.5%.

Table 4.2: Beam FE frequencies in Hz for the different load cases. Mode type identified from the unloaded case.

Mode #	Unloaded	Mode Type	−1 g (self-weight)	10 N	25 N
1	1.10	1 OOP	1.12	1.24	1.61
2	6.87	2 OOP	6.85	5.17	3.52
3	18.27	1 IP	9.71	6.76	6.75
4	19.24	3 OOP	19.04	18.36	17.29
5	37.70	4 OOP	37.45	36.61	35.20
6	61.23	1 T	62.02	56.17	40.09
7	62.32	5 OOP	70.68	61.04	59.38
8	93.08	6 OOP	92.76	91.71	89.91
9	113.99	2 IP	120.22	128.54	126.62
10	130.00	7 OOP	129.65	141.54	165.80
11	173.05	8 OOP	172.69	171.53	169.54
12	183.68	2 T	221.86	220.66	218.60
13	222.24	9 OOP	231.50	251.64	273.82
14	277.57	10 OOP	277.17	275.93	305.08
15	306.11	3 T	296.50	337.31	335.16

Table 4.3: Aluminum beam test case design variables.

Region	DV Type	Reference DV	Initial DV	Difference (vs reference), %	Converged DV	Difference (vs reference), %
R1	Material density	2700.0 $\frac{kg}{m^3}$	2715.11 $\frac{kg}{m^3}$	0.6	2734.03 $\frac{kg}{m^3}$	1.3
	Young's modulus	70.0 GPa	70.65 GPa	0.9	70.82 GPa	1.2
	Thickness	5.0 mm	5.1 mm	2.0	4.976 mm	0.5
	Height	3.0 mm	3.10 mm	3.3	2.99 mm	0.3
R2	Material density	2700.0 $\frac{kg}{m^3}$	2634.79 $\frac{kg}{m^3}$	2.4	2783.76 $\frac{kg}{m^3}$	3.1
	Young's modulus	70.0 GPa	73.31 GPa	4.7	78.20 GPa	4.0
	Thickness	5.0 mm	5.1 mm	2.0	5.009 mm	0.2
	Height	3.0 mm	3.10 mm	3.3	2.98 mm	0.7
R3	Material density	2700.0 $\frac{kg}{m^3}$	2619.33 $\frac{kg}{m^3}$	3.0	2711.78 $\frac{kg}{m^3}$	0.4
	Young's modulus	70.0 GPa	71.45 GPa	2.1	73.49 GPa	5.0
	Thickness	5.0 mm	5.1 mm	2.0	4.957 mm	0.9
	Height	3.0 mm	3.10 mm	3.3	2.96 mm	1.4

A similar result was obtained using the gradient-based SLSQP optimization, except the optimizer in this case required fewer function evaluations compared to the gradient-free method, resulting in a 4X speedup (1.25 hrs vs. 5 hrs on a quad-core Intel i7-7700HQ CPU with a base clock speed of 2.80 GHz and a solid state drive). The static displacements for the reference, initial, and calibrated FEM (from the SLSQP run) are shown in Fig. 4.6 and indicate that for all load cases, the converged design variables provide the same static displacement as the reference FEM.

The first three out-of-plane bending modes are shown in Fig. 4.7. The mode shapes look similar (between the initial mistuned, reference, and calibrated FEM) due to small initial variations in

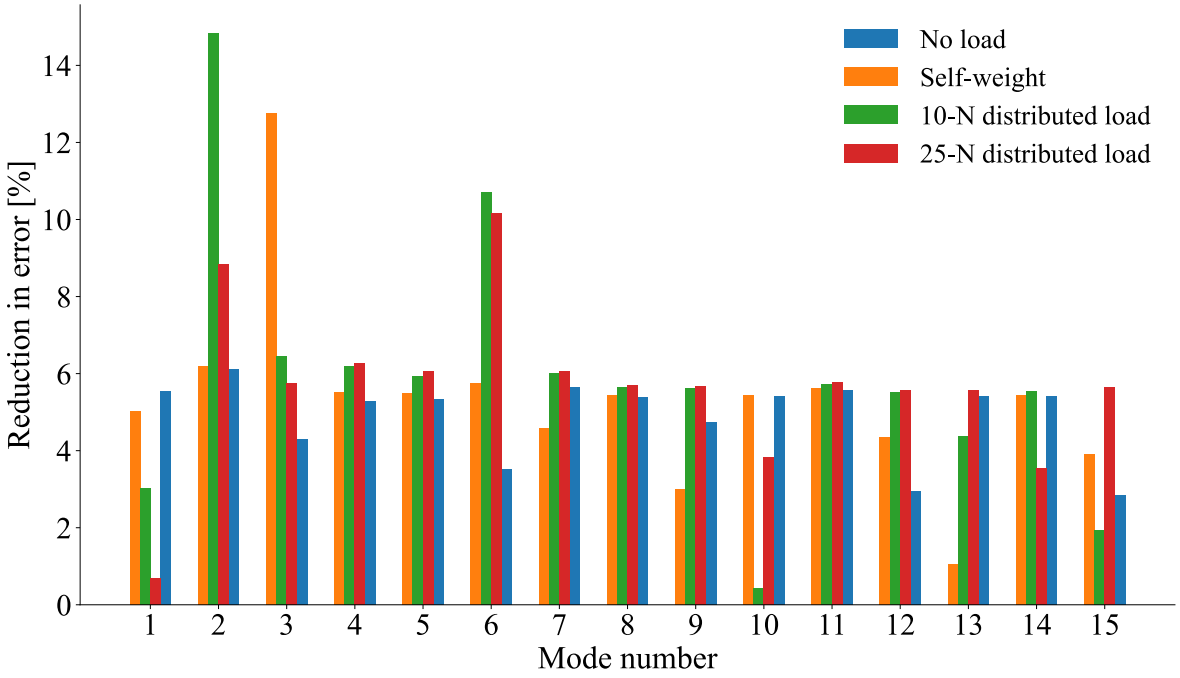

Figure 4.5: Reduction in percent error after calibration compared to the initial FEM (against the reference FEM) for the beam.

the design variables, but the calibrated FEM shows excellent agreement with the reference mode shapes. This indicates that both the eigenvalues and eigenvectors match the reference FEM well, but the problem setup needs to be evaluated carefully in order to ensure the solution is physical. In this case, the bounds and constraints are used to bring the design space closer to what would be expected from a GVT-FEM correlation. Unlike a purely numerical optimization problem, where each element can have its material and geometry variables included in the design variables, and the problem can have hundreds or thousands of design variables, for the test case(s) used in this study, the overall material and geometry properties were selected as the design variables with constraints placed on the structure's overall mass, inertia, and c.g., as well as bounds on the design variables.

The initial and final MAC results for the case under self-weight (-1 g) are shown in Fig. 4.8. MAC is typically used to compare experimental (GVT) and numerical (FEM) mode shapes. Here, while it does show that some modes switched order in the initial FEM and were fixed in the calibrated FEM, it is not as useful since this is a numerical system, and the initial (mistuned) model has the same number of degrees of freedom and minimal initial deviation regarding mode shapes. A closer look at the mode shapes and frequency comparison gives a better sense of the outcome.

As part of the investigations regarding the choice of the objective function and design variables, the beam FEM was also tuned using a modified objective function which included a static deflec-

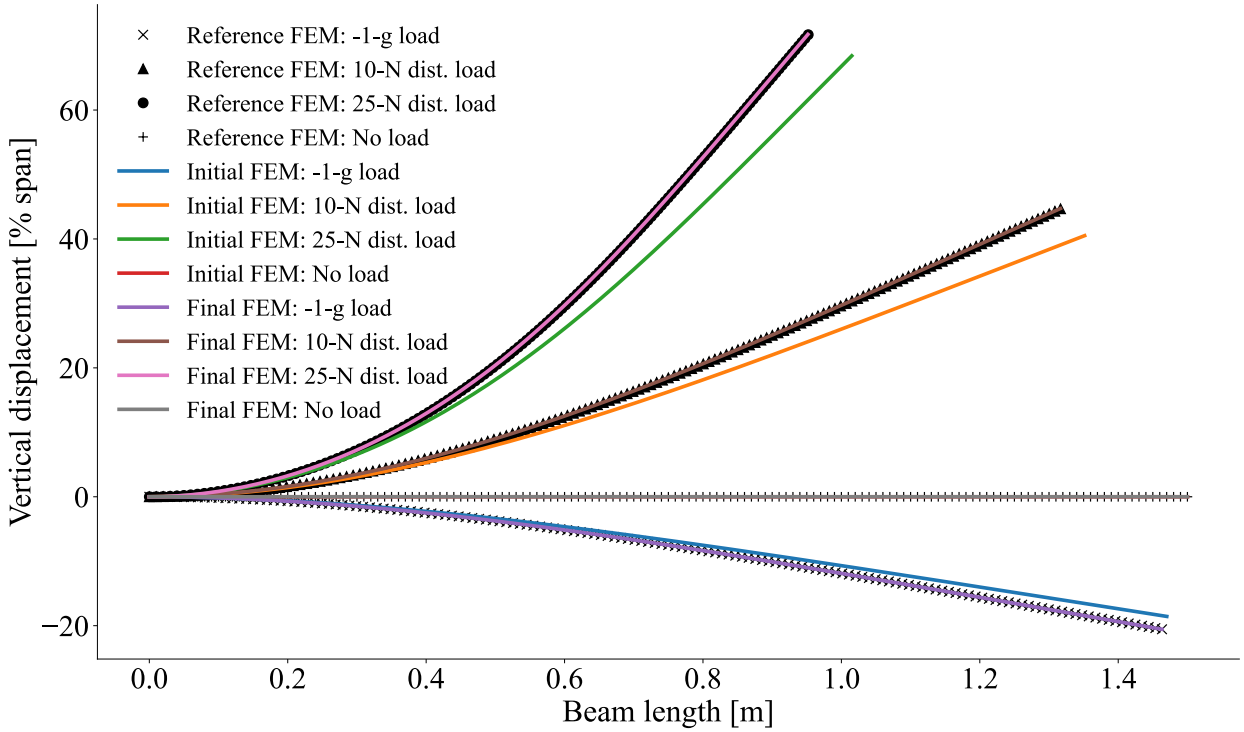

Figure 4.6: Static deformation of the very flexible beam under different loading cases after optimization.

tion component. The term added to the objective function from Eq. 2.11 is shown in Eq. 4.1, where j refers to the j^{th} subcase causing large displacements.

$$\sum_{j=1}^{n}\left(\frac{SD_j - SD_{j_0}}{SD_{j_0}}\right)^2 \tag{4.1}$$

Figure 4.9 shows the static displacement of the reference, initial, and final FEM cases while Fig. 4.10 shows the reduction in error between the natural frequencies of the initial and the final (calibrated) FEM. Interestingly, in this situation, the optimizer was not able to find the global minima and got stuck in a local one, where the process ended because the relative change between two iterations reached the specified tolerance (the same tolerance was used for the optimization problem without static deflection in the objective function). The static deflection in Fig. 4.9 shows excellent agreement between the calibrated and the reference FEM even though some of the natural frequencies show large errors. The results indicate that while the frequency errors between the initial and calibrated models are reduced significantly, just adding a static deflection component to the objective function is not sufficient to improve the optimization problem formulation and additional investigations are needed in how to use this additional component in the multi-objective function.

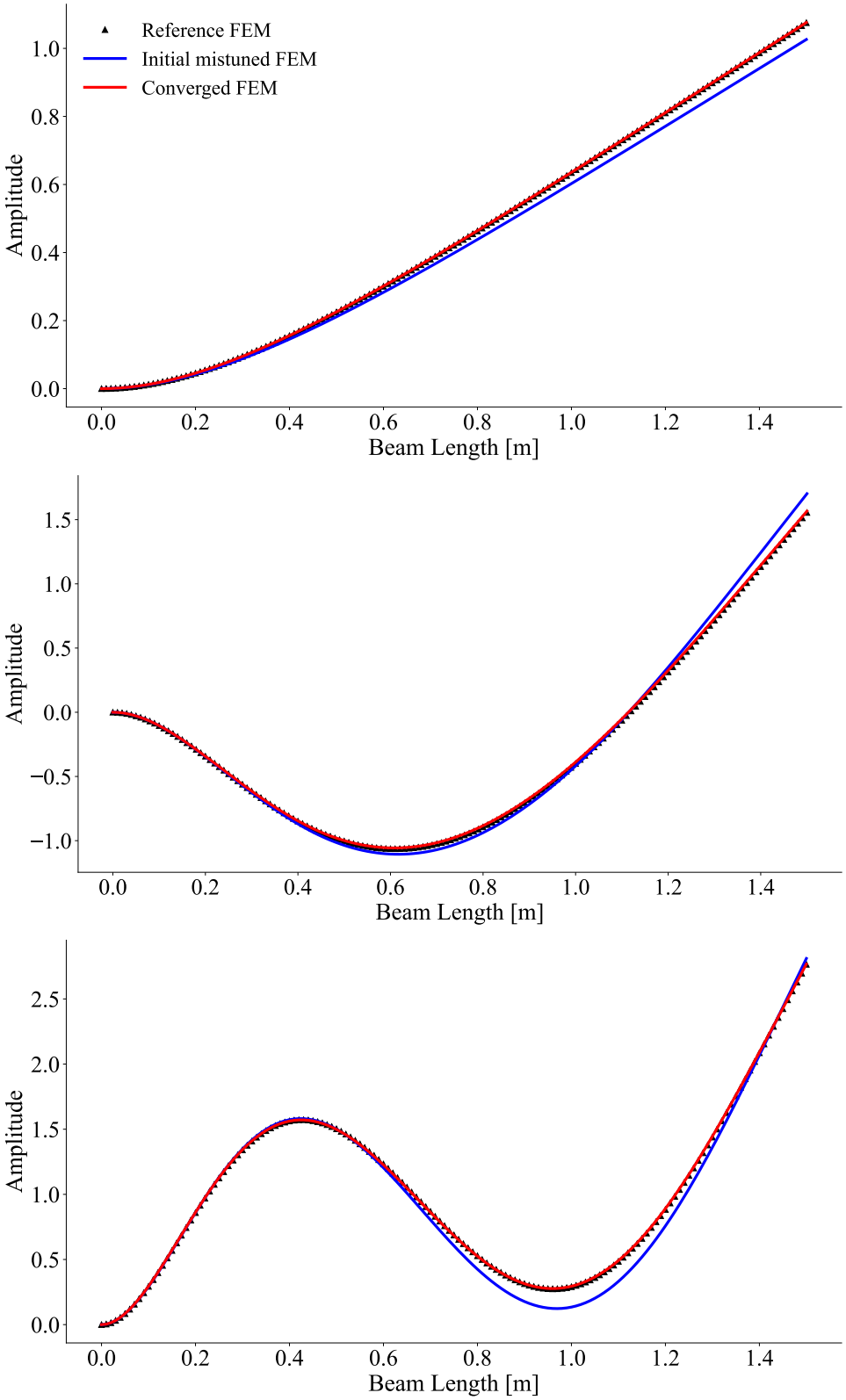

Figure 4.7: First three out-of-plane bending mode shapes.

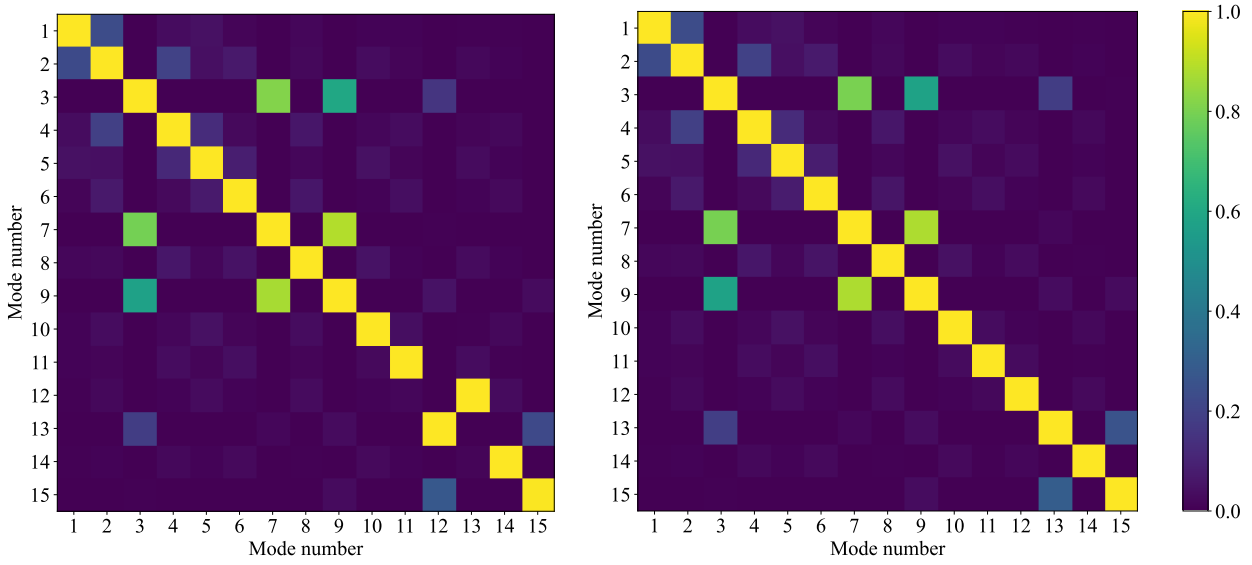

Figure 4.8: Initial (left) and final (right) modal assurance criterion for beam under self-weight.

The random mistuning of the reference properties was done through a script such that each of the design variables gets modified by a different factor, up to $\pm 5\%$ of its corresponding reference value. A larger range of random mistuning, $\pm 10\%$ was also tested, and the converged DV showed no difference in their ability to match the reference FEM's natural frequencies and mode shapes. For this study, there is an assumed confidence in the starting (initial) FEM's material and geometric properties. This is similar to how a comparison with experimental GVT data would have been made; the initial FEM is not a random set of material and geometric properties, but rather an informed model of the original design. The FEM updating is done to tune or calibrate that starting model, representative of the structure. Therefore, a wider variation of the material and geometric properties would not be expected.

4.3 Built-up FEM Test Case

In order to capture the 3D effects related to the geometry of a wingbox, a detailed FEM is needed. These include the stresses developed in the skins during large displacements which lead to local variations in the stiffness of those members, ultimately affecting the overall modal behavior of the wing around a given deformed state. This local effect primarily impacts the stiffness characteristics and does not have a significant effect on the local inertia (local cross-sectional deformations are small due to the presence of the ribs – the Brazier effect) [85]. As described in section 2.2, the local changes in stiffness due to pre-stress can provide additional information that can be used to further improve the uniqueness of the combination of geometric and material property adjustments

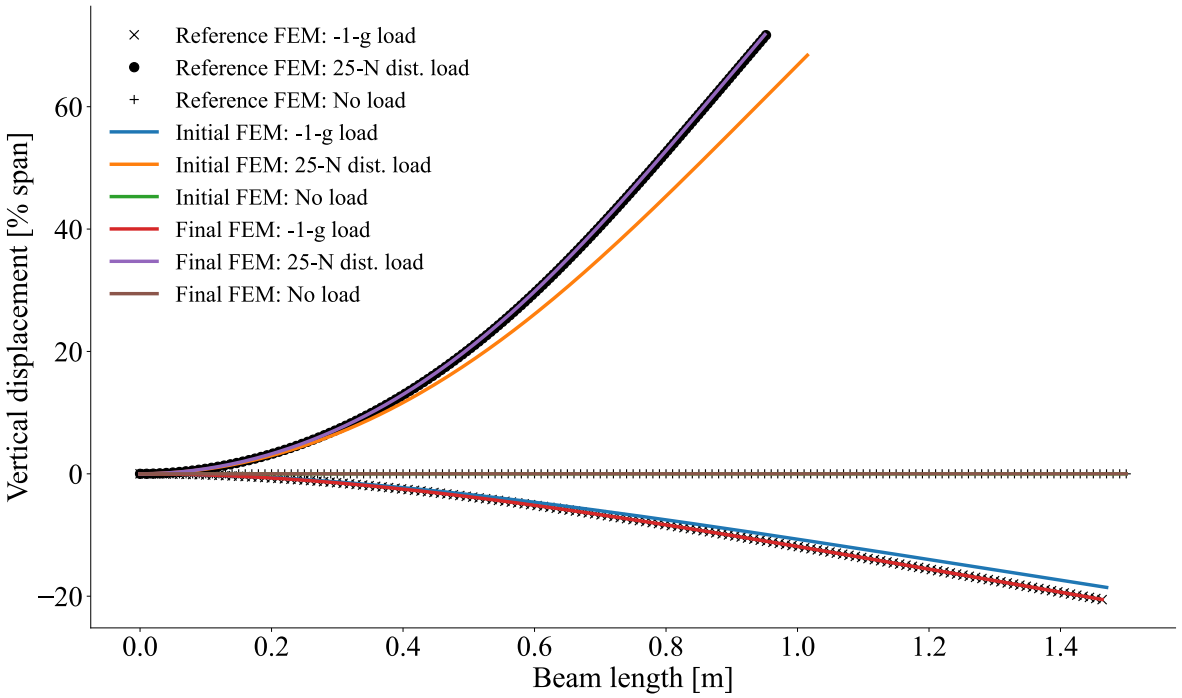

Figure 4.9: Static deformation after optimization with static deflection included in the objective function.

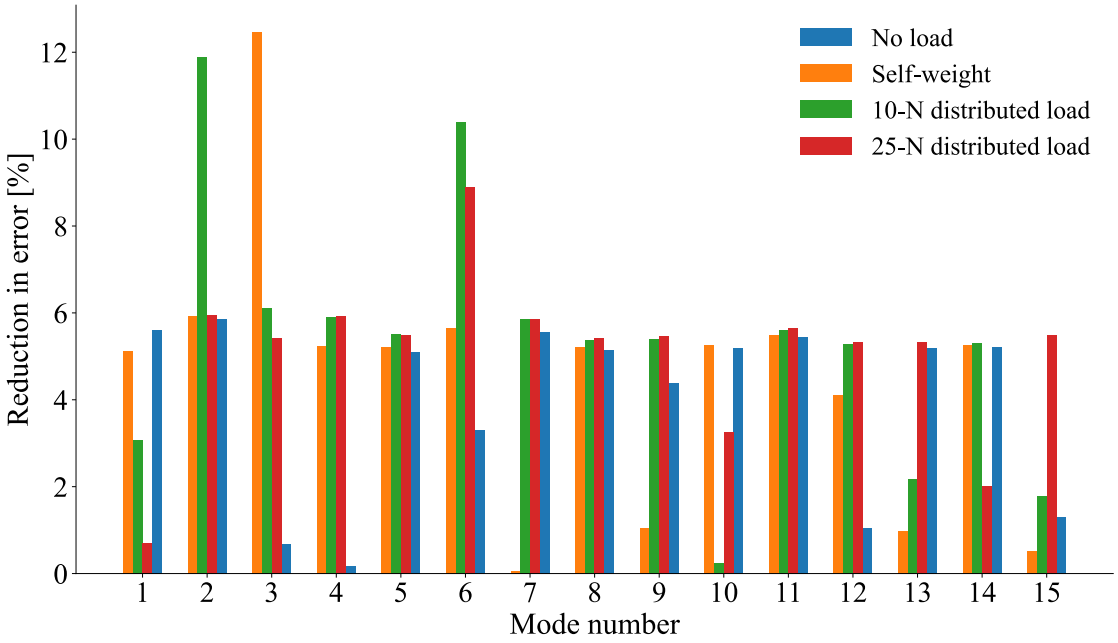

Figure 4.10: Reduction in percent error after calibration with static deflection in the objective function compared to the initial FEM (against the reference FEM) for the beam.

to the FEM. This would lead to testing the structure in multiple deformed configurations and using that information as part of the finite element model updating problem. In order to investigate this effect, the detailed FEM was set with uniform material properties for all the components, which kept the problem tractable (an optimization problem that calls Nastran SOL400 multiple times and does gradient evaluations for each optimizer iteration can become memory and time intensive quite quickly, while requiring substantial file I/O handling). The model uses Aluminum for the material and shell elements for all the components, includes top and bottom spars, ribs, and skin. The FEM under loading and the corresponding effects of the ribs on the skin are shown in Fig. 4.11, while Table 4.4 provides material and geometry properties.

Table 4.4: Wingbox properties.

Property	**Value**	**Units**
Length	16	m
Width	1	m
Height	0.16	m
Density	2,851	$\frac{\text{kg}}{\text{m}^3}$
Young's modulus	69	GPa
Poisson's ratio	0.33	–

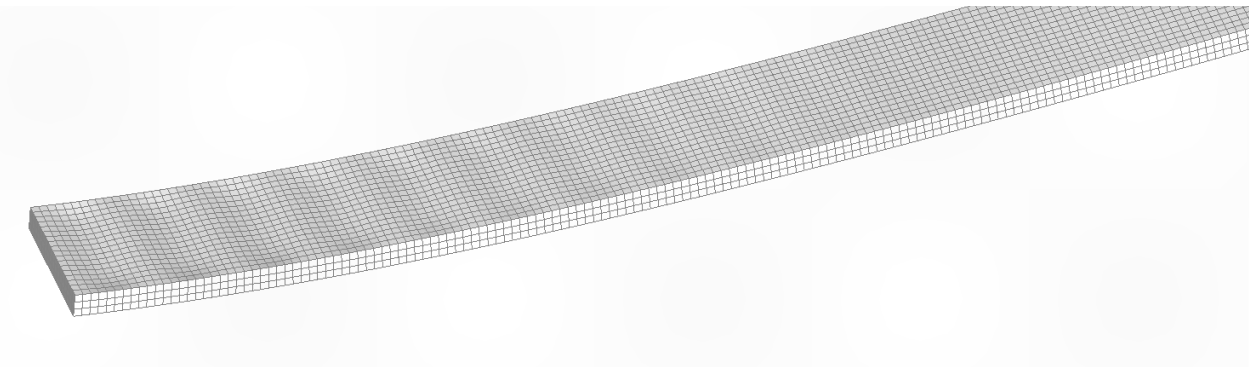

Figure 4.11: Skin effects under loading on the built-up FEM.

The reference wingbox natural frequencies at the different load cases are shown in Table 4.5. Here, EXT refers to an extension mode. As the load changes, the nature of the mode will evolve, and this is particularly evident for the in-plane and torsion dominated modes since they will couple differently under loading causing large out-of-plane displacements [2]. This variation in mode shapes is exemplified in Figs. 4.12 and 4.13. The initial, mistuned FEM for the wingbox was created in the same manner as described in section 4.2, i.e., by a random $\pm 5\%$ variation on the

material and geometry properties. Similarly, constraints and bounds were also applied in the same manner as for the previous case. The wing's reference, initial, and converged design variables employing SLSQP optimization are shown in Table 4.6.

Figure 4.14 shows the reduction in percentage error of the natural frequencies between the different load cases for the initial FEM vs. the calibrated FEM indicating that the converged design variables enable substantial error reduction for all the load cases. Figure 4.15 shows the absolute error between the initial and final (updated) FEM compared to the reference FEM, highlighting the updated FEM's ability to reach $< 0.5\%$ errors for all the modes for all the load cases.

Table 4.5: Natural frequencies (Hz) for the reference wingbox FEM. Mode type identified from the unloaded case.

Mode #	**Unloaded**	**Mode Type**	**-1 g**	**2.5 g**
1	0.717	1 OOP	0.688	0.471
2	2.899	1 IP	2.882	2.571
3	4.412	2 OOP	4.290	3.635
4	12.023	3 OOP	11.775	9.805
5	17.525	1 T	17.228	16.195
6	17.777	2 IP	18.063	18.079
7	22.664	4 OOP	22.270	19.101
8	35.651	5 OOP	34.970	29.533
9	48.181	3 IP	48.019	42.108
10	50.127	6 OOP	48.615	46.059
11	52.183	2 T	52.255	49.839
12	65.201	7 OOP	57.416	51.777
13	66.836	1 EXT	62.476	52.688
14	80.014	8 OOP	63.616	58.441
15	85.557	3 T	70.245	60.957

Table 4.6: Wingbox design variables.

DV Type	**Reference DV**	**Initial DV**	**Difference (vs reference), %**	**Converged DV**	**Difference (vs reference), %**
Density	2851.0 $\frac{\text{kg}}{\text{m}^3}$	2729.0 $\frac{\text{kg}}{\text{m}^3}$	4.3	2803.122 $\frac{\text{kg}}{\text{m}^3}$	1.7
Young's Modulus	69.0 GPa	71.0 GPa	2.9	67.65 GPa	2.0
Ribs Thickness	2.0 mm	2.10 mm	5.0	2.00952 mm	0.5
Skin Thickness	8.0 mm	8.3 mm	3.8	8.0082 mm	0.1
Spar Thickness	5.0 mm	5.1 mm	2.0	5.1825 mm	3.6

A comparison of the static deformation for the 2.5-g load case is provided in Fig. 4.16. The static deformation for the calibrated FEM is practically indistinguishable from the reference FEM. The modal assurance criterion comparison provided in Fig. 4.17 shows how the calibrated FEM is much better able to match the mode shapes of the reference FEM.

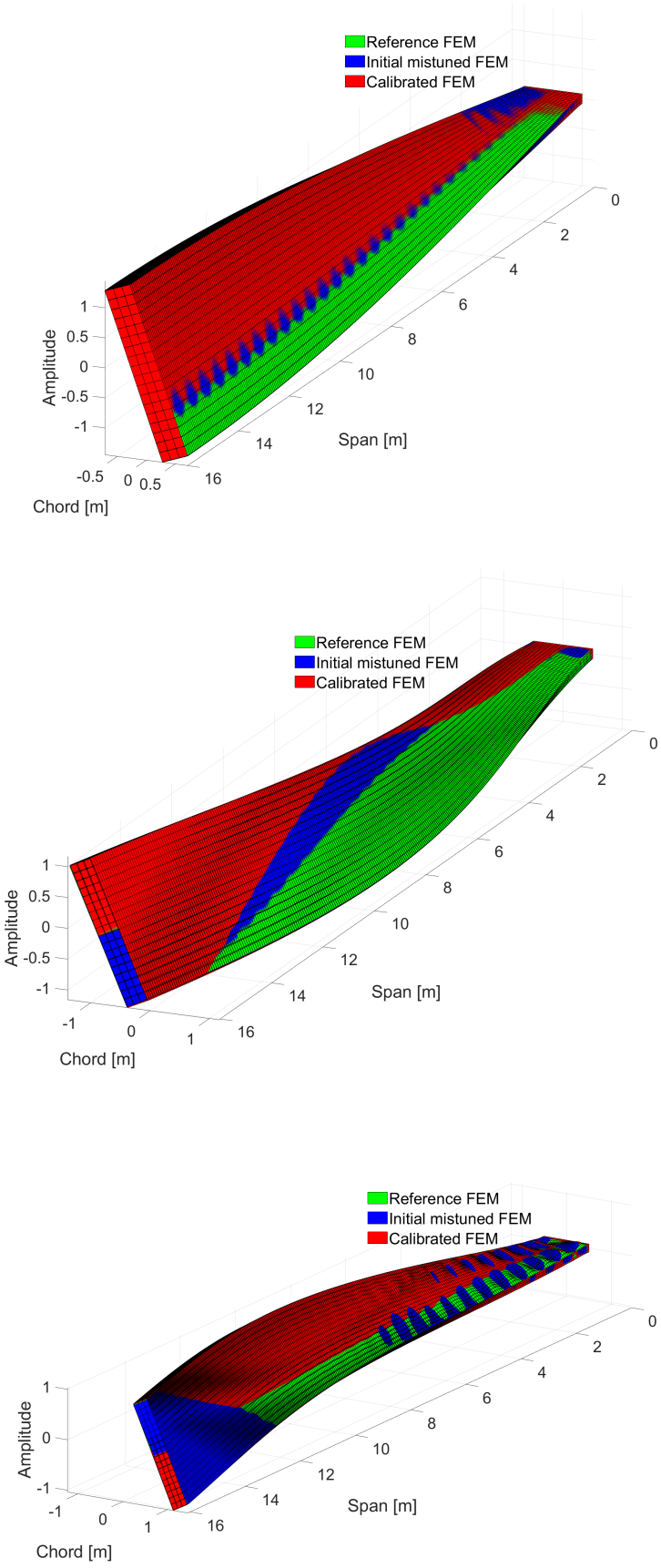

Figure 4.12: Fifth wingbox mode for the three load cases. Unloaded (top), self-weight (middle) and 2.5-g load (bottom).

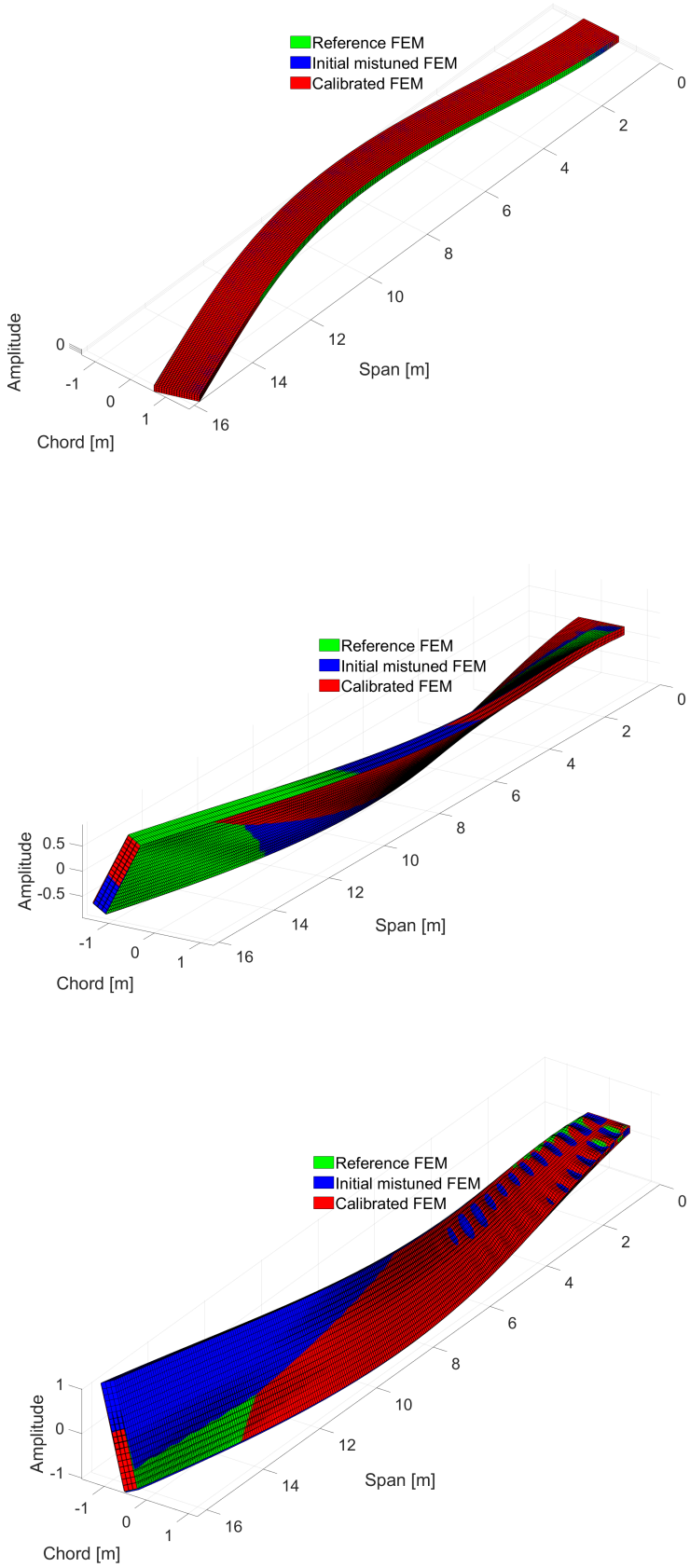

Figure 4.13: Sixth wingbox mode for the three load cases. Unloaded (top), self-weight (middle) and 2.5-g load (bottom).

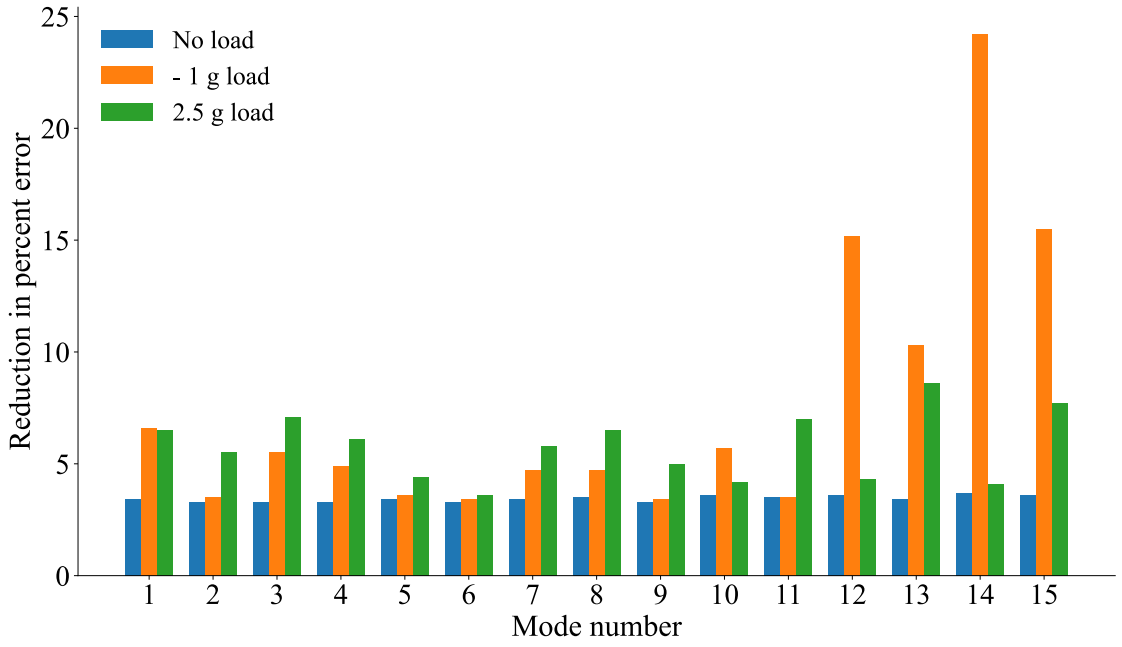

Figure 4.14: Reduction in percent error after calibration compared to the initial FEM (against the reference FEM) for the wingbox.

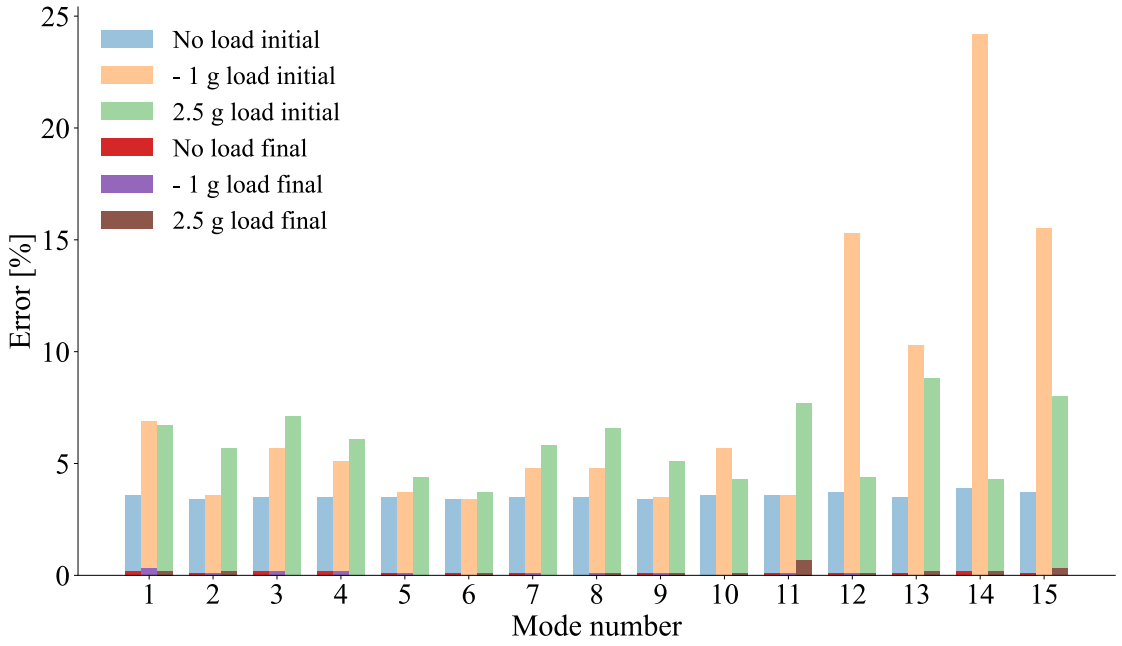

Figure 4.15: Percent error after calibration compared to the initial FEM (against the reference FEM) for the wingbox.

While the MAC in Fig. 4.17 shows that the calibrated FEM is better able to capture the order of modes compared to the reference FEM, the mode shapes shown in Fig. 4.18 indicate that the 3D

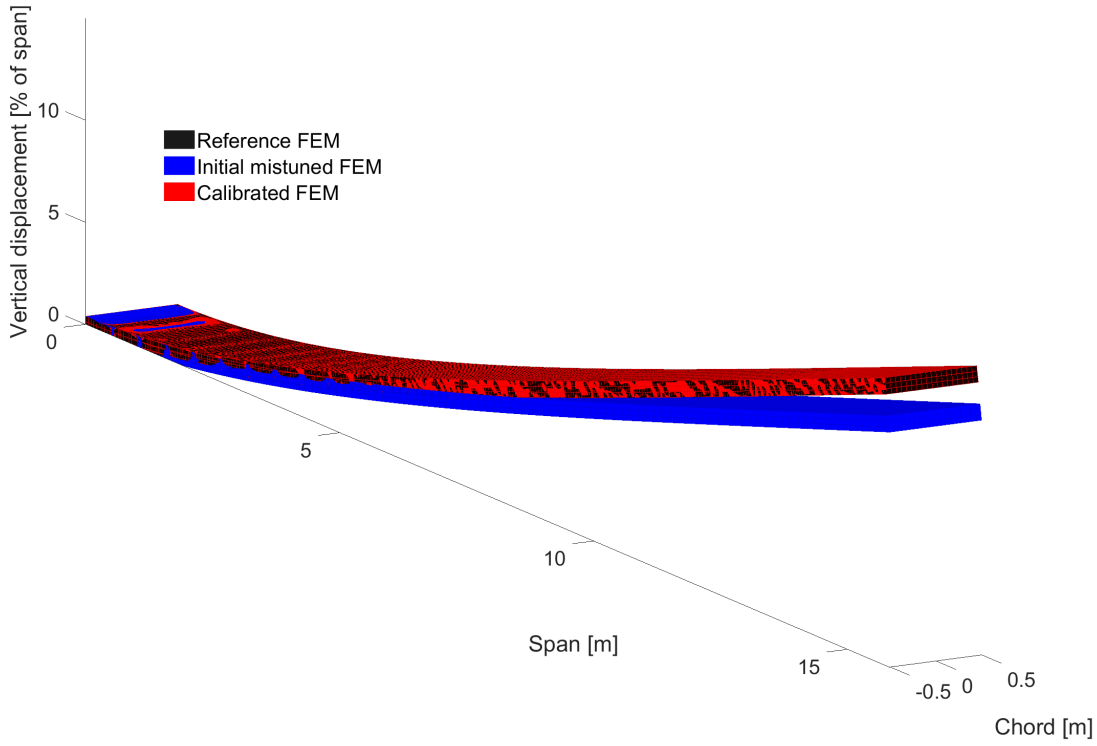

Figure 4.16: Reference, initial, and final (red; on top of black) static deflection for the 2.5-g load case.

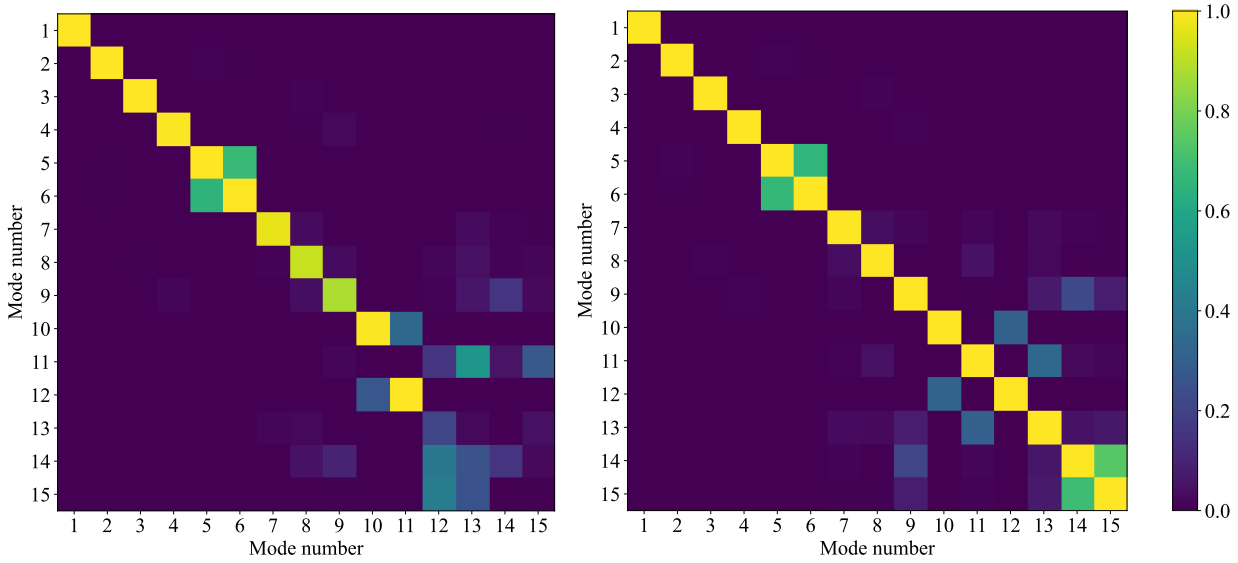

Figure 4.17: Initial (left) and final (right) modal assurance criterion for wingbox under 2.5-g load.

effects coming from the skin and ribs are also captured well by the calibrated FEM, while the initial FEM does not match the reference one. The mode shape plots were generated using the reference FEM data with the root mean square of the error between the reference and the initial FEM used to generate the color bar. This indicates that the calibrated FEM shows very low errors compared to the reference FEM, while the magnitude of the errors for the initial FEM is higher. The variation in the error across the wingbox indicates that the 3D effects coming from skin wrinkling are also corrected by the calibration process.

The wingbox was also calibrated using only the undeformed and unloaded case to investigate the impact of using multiple deformed configurations. This allows to use a linear, undeformed modal solution in order to perform the optimization using SciPy's minimize. The results of this optimization are shown in Fig. 4.19 (percent error in frequency before and after calibration) and Table 4.7 (design variable comparison).

In order to compare the calibrated FEM from the linear single case modal solution against the multi-subcase deformed modal solution, a new load case that excites the structure in multiple directions and causes large displacements was created. This load case contains out-of-plane and in-plane inertial forces, as well as a tip moment, and is shown in Fig. 4.20. It is different than any of the loads used to update the structural model. The goal is to use Nastran SOL400 to nonlinearly deform the structure and investigate if the results of the two calibration procedures exhibit any difference in their ability to match the reference structure under this arbitrary loading case. The comparison of errors in the natural frequencies between the FEM calibrated using the linear, unloaded and undeformed case versus the modified optimization procedure is shown in Fig. 4.21.

The interesting things to note from these results are:

1. As shown in Fig. 4.19, the FEM calibrated using the linear, unloaded and undeformed condition for the optimization matches the unloaded and undeformed linear reference case's natural frequencies within 0.5%. This indicates that the linear, single case optimization works well when not influenced by any loading causing large displacements.

2. From Fig. 4.14, it can be noted that the FEM calibrated using the multi-case deformed optimization matches not only the unloaded and undeformed configuration, but also the other two load cases (which were also used to calibrate it) that cause large displacements.

3. When the natural frequencies of the FEM obtained from the two calibration procedures are compared under a new loading case that they were not subject to during the course of the calibration process, the two FEM show interesting differences in their ability to match the reference FEM under the same load. The calibrated FEM using the new methodology has

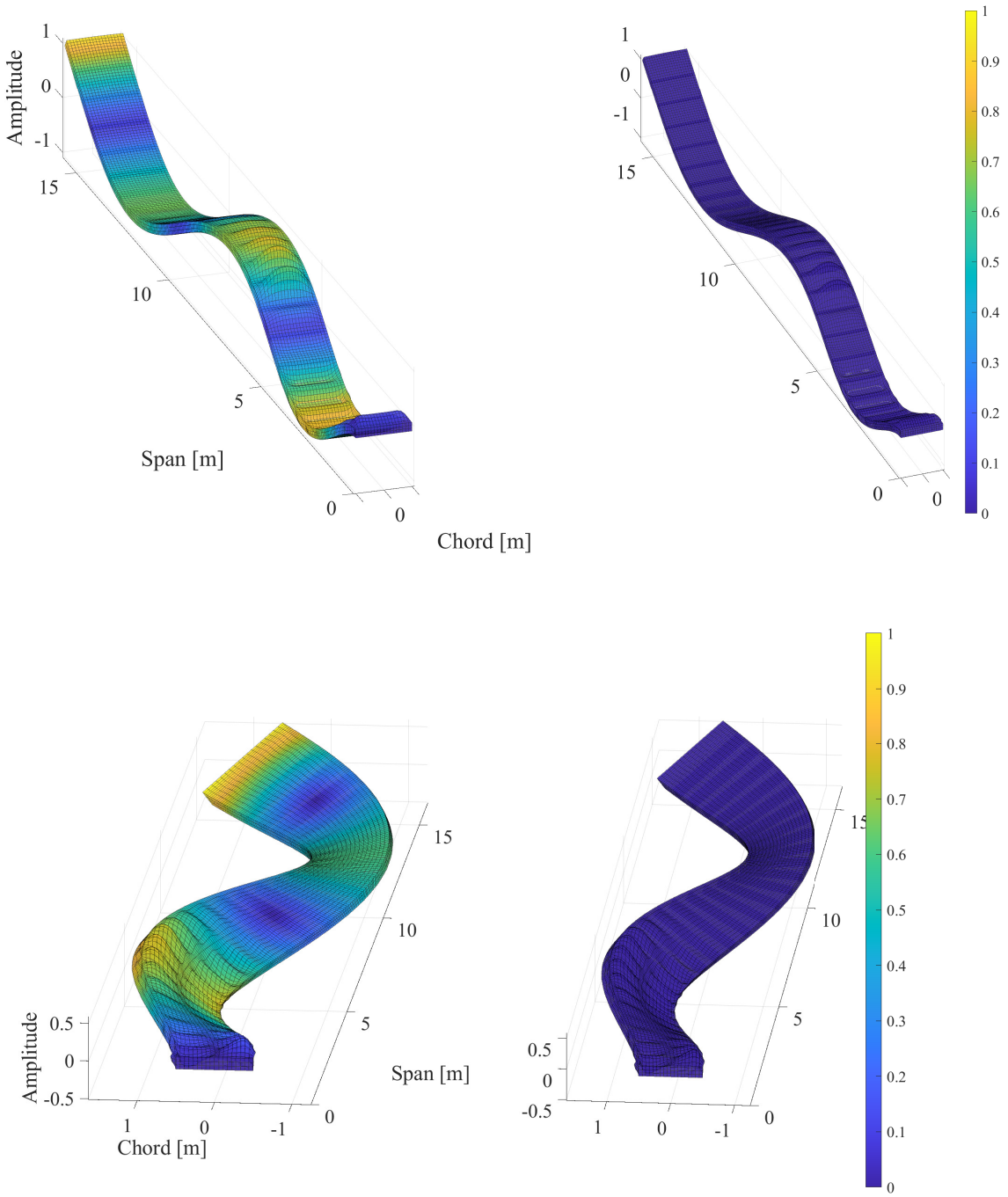

Figure 4.18: Fourth out-of-plane and second in-plane bending modes compared with the reference before (left) and after (right) optimization. Color bar represents the RMS error (normalized by the amplitude of the maximum initial error) with respect to the reference solution.

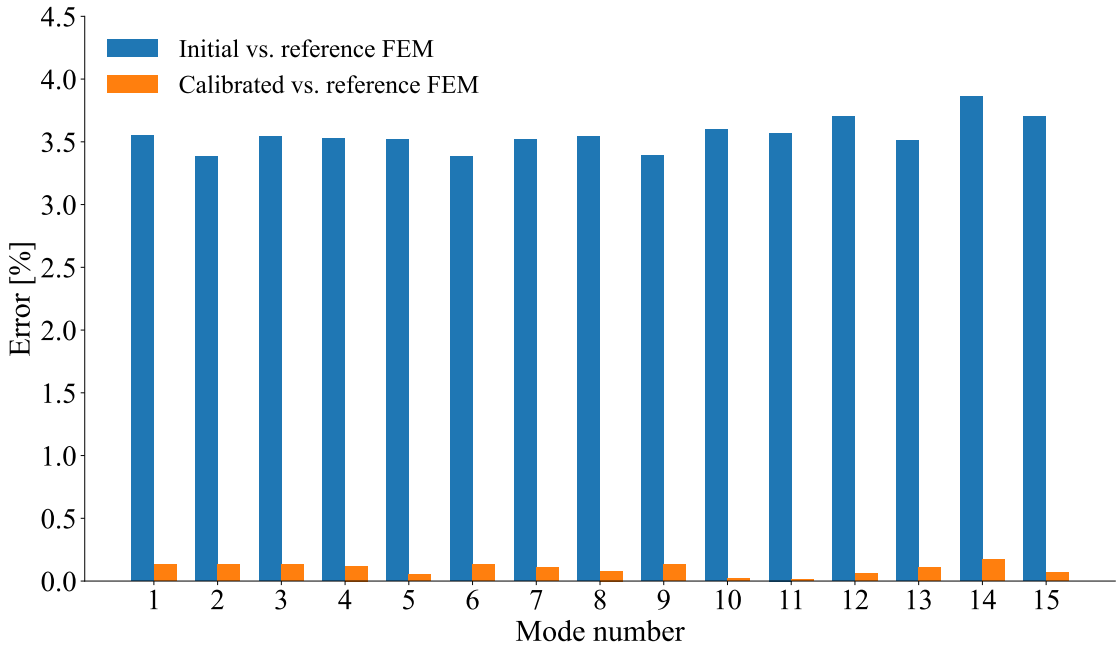

Figure 4.19: Percent error before and after linear, unloaded and undeformed calibration compared to the the reference FEM for the wingbox.

lower errors for all the frequencies, and especially in the higher modes, as can be seen in Fig. 4.21.

4. This difference between the two FEM is present for various combinations of loads, and the error increases as the magnitude of deformation on the structure increases. This indicates that the FEM calibrated using the multi-case deformed optimization captures the effect of flexibility better than the FEM calibrated under only one condition.

The key takeaway is that the typical FEM updating methodology (linear, unloaded, and undeformed optimization) works reasonably well for structures operating in the linear or mildly nonlinear range. However, it fails to capture structural nonlinearities in very flexible wings operating under large deflections, something that the methodology developed in this work is able to accurately capture. The differences become more pronounced as the magnitude of the loads causing large displacement increases. This highlights the need for augmenting and refining the conventional FEM updating procedures when applied to very flexible structures. The results presented indicate that the new methodology proposed and verified as part of this study improves upon the established FEM updating technologies when considering very flexible structures.

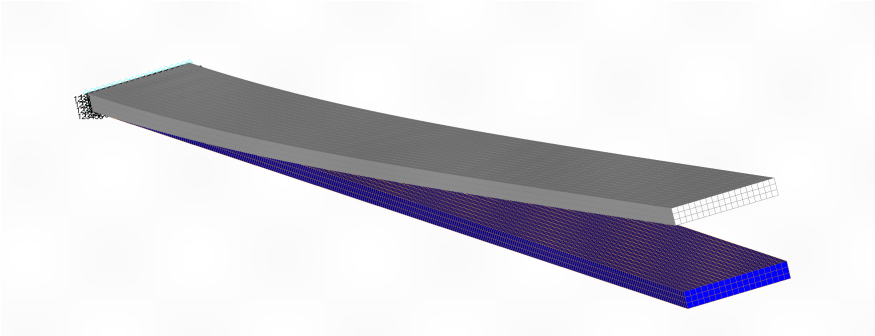

Figure 4.20: Reference wingbox FEM deformed under new loading case (undeformed model shown in blue). Maximum tip displacement is 3.6% of span (magnified in the image to facilitate visualization), smaller than the deflection caused by the 2.5-g load.

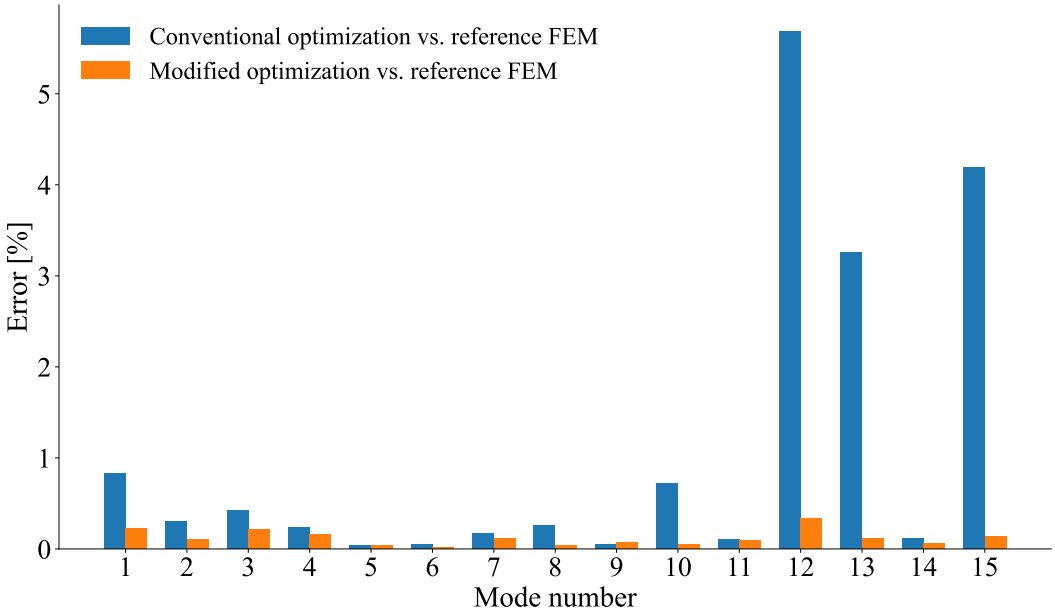

Figure 4.21: Comparison of errors in natural frequencies between the FEM calibrated using the two optimization procedures.

Table 4.7: Design variables before and after optimization using single and multiple subcases.

DV Type	Reference DV	Initial DV	Difference, %	Converged DV - undeformed single	Difference, %	Converged DV - deformed multiple	Difference, %
Density	2851.0 $\frac{kg}{m^3}$	2729.0 $\frac{kg}{m^3}$	4.3	2780.594 $\frac{kg}{m^3}$	2.5	2803.122 $\frac{kg}{m^3}$	1.7
Young's Modulus	69.0 GPa	71.0 GPa	2.9	67.82 GPa	1.7	67.65 GPa	2.0
Ribs Thickness	2.0 mm	2.1 mm	5.0	2.10855 mm	5.4	2.00952 mm	0.5
Skin Thickness	8.0 mm	8.3 mm	3.8	8.1073 mm	1.3	8.0082 mm	0.1
Spar Thickness	5.0 mm	5.1 mm	2.0	5.0723 mm	1.4	5.1825 mm	3.6

4.4 Conclusions

This chapter introduced and verified a new methodology to update the finite element models of very flexible wings. These structures can undergo large displacements during normal operating conditions and the deformation subsequently affects the modal parameters. The study described a way to pose and capture the multiple cases causing large displacements within the optimization problem and provided details on the optimization problem formulation. The impact of the number of load cases and deformed shapes on the optimization procedure is discussed. The study also provided insights gained from exercising the optimization algorithms introduced here. Modifications on the objective function to include additional conditions related to other data that can be collected during a GVT campaign are also investigated and discussed. The techniques were exercised on a very flexible beam and a detailed wing box FEM to evaluate the problem formulation, data handling and I/O, and to improve our understanding of the effect of flexibility and large displacements in the finite element model updating procedure, respectively. The results showed that the procedure developed in this study is capable of accurately updating their FEM for geometrically nonlinear conditions. Limitations of optimization techniques and the problem set up are highlighted since the nonlinear structural solver along with the large number of function calls and gradient evaluations can quickly make the problem intractable. Post-processing tools developed as part of this work are used to take a reference model for a very flexible structure and visualize it in different deformed configurations, along with analyzing and visualizing the outcome of the FEM updating starting from multiple deformed configurations. The subsequent chapters include using the algorithm and the codes developed as part of this work and applying them to a GVT of very flexible structures. Ways to further refine the terms that can be added to the objective function, additional design variables, and/or smarter ways of constraining the optimization problem formulation are investigated. Finally, future work can focus on stress-testing the algorithm and the FEM updating process to ensure the procedure is robust to different initial conditions and models of varying complexity.

CHAPTER 5

Ground Vibration Testing and Finite Element Model Updating of a 3D-Printed Swept Wing

This chapter addresses the fourth research challenge, FEM updating considering increased uncertainties and material property variabilities coming from novel manufacturing techniques. The chapter presents the numerical and experimental tests performed on a 3D-printed wing designed for aeroelastic studies. This effort is part of a collaborative project to exercise the methods and solutions to evaluate the flutter behavior of tail-sitter, swept-wing unmanned aerial vehicle configurations.

The structural dynamics characterization of the model was conducted both in and out of the wind tunnel in order to build towards the aeroelastic model that will be used for flutter analysis. Wind tunnel testing is an indispensable tool for verification and validation of existing and emerging computational tools [89]. It also provides support to the flight test campaign – to identify and characterize the aircraft and improve confidence in the numerical models before its first flight. A variety of instrumentation are used to identify the characteristics of the model during such tests, *e.g.*, sensors installed on-board the test article, or measurement devices located in and out of the wind tunnel [90]. Technological advances allow for instrumenting structures with high-density strain-sensing optical fibers for characterizing their structural dynamics and aeroelastic response [91]. This chapter describes the wind tunnel test article and the corresponding characterization tests on a full-scale, half model of the Active Aeroelastic Aircraft Testbed (A3TB) unmanned aerial vehicle (UAV) developed for flutter identification and control studies [92].

Building upon past work consisting of numerical flutter analyses of the A3TB with different methodologies to help assess the accuracy of those formulations and the ability to capture the observed flutter behavior [93], the current study details the experimental tests performed to characterize the 3D-printed wind tunnel model (denoted as A3TB-WT) designed at the Technion (Israel Institute of Technology) and assembled and instrumented at the University of Michigan. Once the A3TB-WT model was assembled and instrumented, GVT were performed to characterize the structural dynamics and identify the modal parameters of the as-built structure [37, 39] and deter-

mine how it deviates from the as-designed model. While GVT on the wing were conducted both in the laboratory and in the wind tunnel, the aeroelastic or aerodynamic model correlation from the variety of wind tunnel tests is beyond the scope of this thesis.

The wing, inspired by the X-56A "Mutt" [94], was instrumented using different sensors to support data collection for structural dynamics and aeroelastic analyses, i.e.,

1. High-resolution strain sensing optical fibers,
2. High-senstivity vibration accelerometers and,
3. An external motion recovery system (MRS) using multiple cameras and infrared (IR) reflective markers on the wing.

A variety of numerical [93] and experimental [95, 96] studies were performed on the structure to characterize it. A key topic of interest was to predict flutter [97], both computationally, as well as experimentally, by performing wind tunnel tests below the flutter boundary [98]. In order to improve confidence in the ability of the numerical model to accurately predict flutter for this type of wing [99, 100], an accurate FEM representing the as-built model needed to be developed. This was done through updates of the originally designed model. Previous work involved performing GVT on the 3D printed wing, and comparison with the initial FEM of the A3TB-WT yielded discrepancies between the experimental and numerical results [96]. These discrepancies arise not only from idealization and simplification in the modeling, but also from uncertainties in material properties and boundary conditions.

Using common FE modeling techniques, the study examines the model updating procedure's ability to account for the dynamic behavior of a 3D printed swept wing in the presence of uncertainties associated with 3D printing. Accounting for manufacturing variability and material property uncertainties is crucial for ensuring precision in creating and updating the FEM of 3D printed or composite parts. This chapter proposes a method to update the FEM of 3D printed structures while considering uncertainties without characterizing the printing process itself. The focus of the study is on the dynamic behavior of the wing, with no emphasis on the chemistry or manufacturing techniques.

This chapter is organized as follows. Section 5.1 provides an overview of the A3TB-WT model and presents results obtained from the various GVT. Section 5.3 provides a discussion on the updates to the finite element model updating process to account for 3D printed structures to better match the experimental results. Section 5.4 discusses the preliminary model adjustments and additional tests conducted to minimize uncertainties. Section 5.5 provides the set up and results from the FEM updating process applied to the A3TB-WT and provides a discussion on some of the Section 5.6 summarizes the work done and provides a brief discussion of the lessons learned from the GVT and FEM updating on the A3TB-WT, along with describing future work.

5.1 The A3TB-WT, a 3D-printed Swept Wing

This section presents the A3TB-WT model and provides a description of the FEM. This baseline numerical model was used as the starting point for the numerical investigations performed in this work, and was updated based on the FEM updating process for 3D printed structures.

5.1.1 A3TB Model Description

The A3TB-WT contains basic features that are encountered in blended wing-body vehicles. The full vehicle has a wingspan of 3 m and weighs approximately 11 kg. The rectangular wings are swept back by 22 degrees and twisted linearly by negative 3 degrees (wash-out) from the wing root to the tip. A symmetric NACA 0012 airfoil provides sufficient thickness for the structural elements and a zero aerodynamic pitching moment coefficient. The 3D printed wings are fitted with 8 trailing-edge flaps for control, and wing-tip fins for increased lateral stability. Figure 5.1 shows the A3TB geometry. The half-vehicle replica, the A3TB-WT wing, is also 3D printed in segments from PA-12 Nylon material. The segments are connected via a 20×5-mm graphite spar that is clamped at the root. The wing is wrapped in Polyester film, providing the aerodynamic shape and additional structural stiffness.

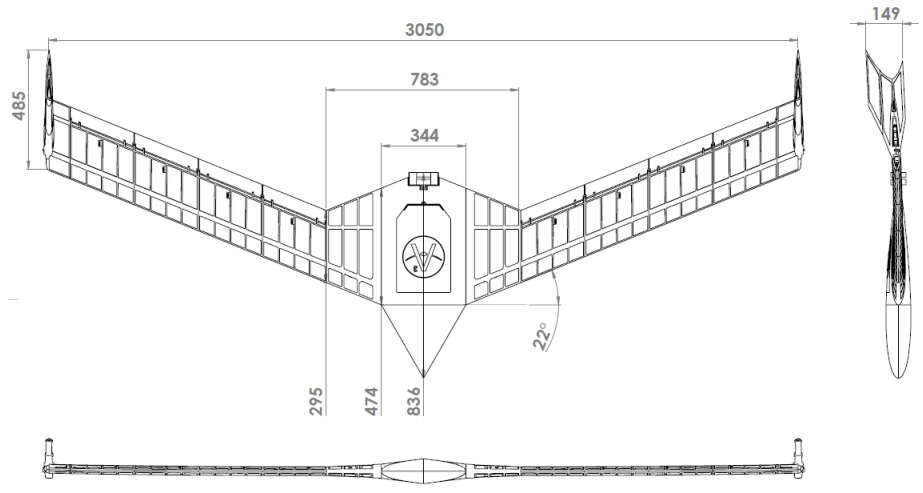

Figure 5.1: Original A3TB UAV geometry [measurements in mm]. Half of it formed the geometry of the A3TB-WT.

5.1.2 Baseline Numerical Model

A detailed Nastran FEM was originally created during the design of the A3TB [92]. The FEM has approximately 14000 nodes and 15700 elements. The main spar of the wing is made of a carbon

fiber beam, modeled as a laminate plate which is inserted into the 3D printed, PA-12 sleeve. The rear spar of the wing is modeled as a beam and the control surfaces attach to this beam. Each wing segment has a combination of rigid and spring elements defining the connection between them. The root section is modeled as plate elements for the profile, while the ribs are modeled as beams with a thicker cross section than the rest of the wing. Further details on the FEM can be found in [101] and [92]. This FEM was adapted for the A3TB-WT and is shown in Fig. 5.2. Two configurations were defined for the A3TB-WT:

1. Configuration 1: Baseline A3TB-WT wing. This includes both a skin-on and a skin-off case.
2. Configuration 2: A3TB-WT wing with a small shaker mounted at the wingtip.

Results from the modal analysis on the two configurations are given in Table 5.1. Modes labeled as OOP are out-of-plane bending, IP are in-plane bending, T are torsion, and CS are control surface modes.

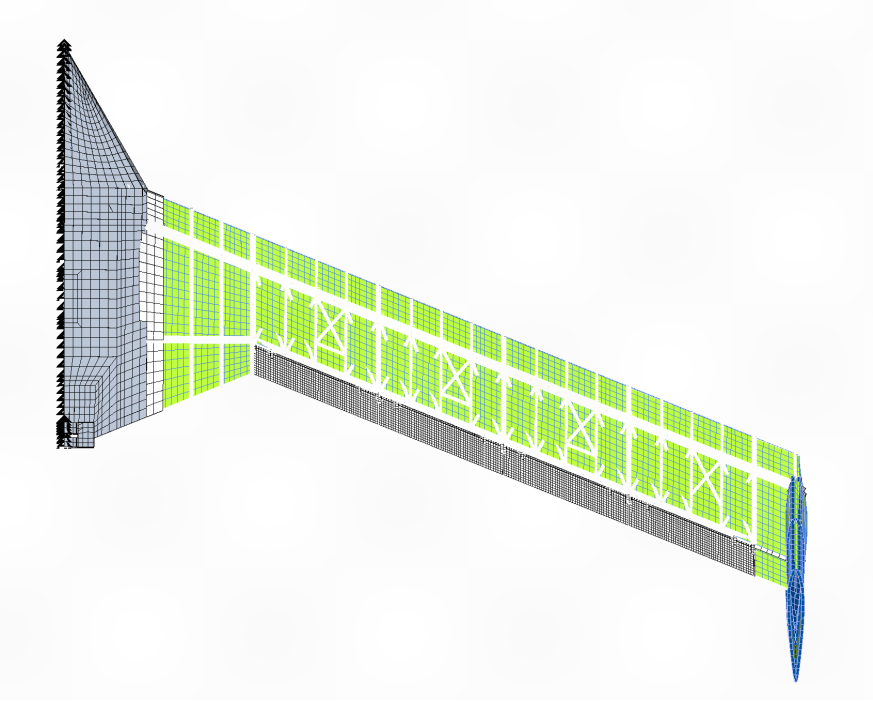

Figure 5.2: Overview of the A3TB-WT FEM.

5.2 Ground Vibration Tests

This section describes the GVT set up for the A3TB-WT and presents the results. GVT is typically conducted using vibration accelerometers to record the response of the structure to an external

Table 5.1: Natural frequencies (Hz) for configuration 1 with and without skin and configuration 2 of the A3TB-WT FEM.

	Configuration 1				Configuration 2	
Mode #	**Skin-off**	**Mode type**	**Skin-on**	**Mode type**	**Skin-on**	**Mode type**
1	3.25	1 OOP	3.29	1 OOP	2.96	1 OOP
2	10.09	1 T	11.02	1 T	9.54	1 T
3	12.38	1 IP	13.76	1 IP	12.22	1 IP
4	17.05	2 OOP	17.76	2 OOP	17.62	2 OOP
5	27.57	Wingtip	31.48	3 OOP	31.13	3 OOP
6	30.55	3 OOP/CS	35.17	T 2/CS	33.97	T 2/CS
7	34.30	T 2/CS	36.28	T 2/CS	36.15	T 2/CS
8	35.01	CS	37.28	T 2/CS	37.17	CS
9	36.25	CS	50.40	CS	50.53	CS
10	44.89	2 IP	52.21	CS	51.50	CS
11	49.12	CS	52.89	2 IP	52.53	2 IP

source of excitation. Typical excitation sources lead to approaches like impact test (using an impact hammer with a built-in load cell) or shaker test, where the test article is excited by a shaker.

The wing was tested in both the skin-off and skin-on states to determine the impact of the skin on the natural frequencies and mode shapes as well as the ability of the detailed FEM to capture the effects of the skin. Another configuration was defined for GVT that takes advantage of the small shaker mounted at the wingtip to excite the wing for flutter prediction during wind tunnel tests (see [95]). Figure 5.3 shows the A3TB-WT wing set up for GVT in the different configurations.

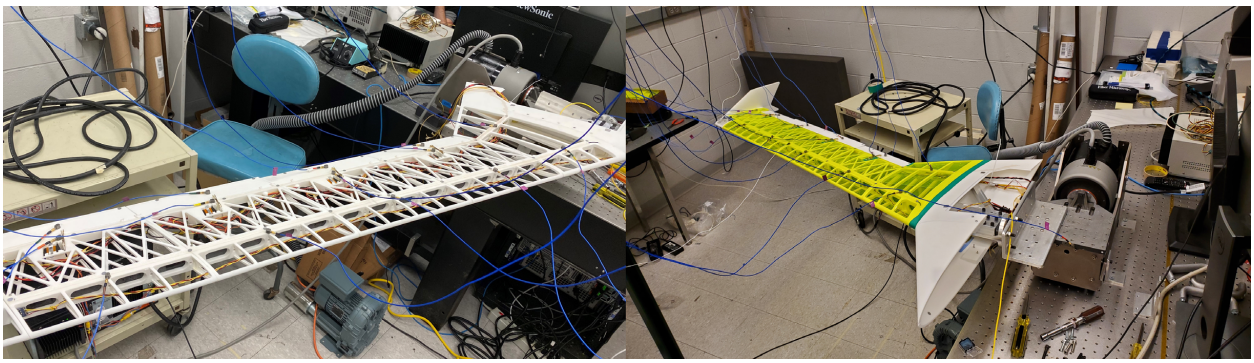

Figure 5.3: Overview of the A3TB-WT model without skin (left) and with skin (right) during GVT.

The different data collected during GVT are:

1. Acceleration data from high-sensitivity vibration accelerometers, shown in Section 5.2.1;

2. Strain data from fiber optic strain (FOS) sensors;

3. Displacement data from motion capture system (MCS).

In this work, only data from the vibration accelerometers were used to evaluate experimental results and compare with the numerical models. The FOS and MCS systems were deployed during the GVT and some of the results presented here contain data coming from those sources. However, for the GVT and FEM updating processes described in this chapter, only the vibration accelerometer results were used.

5.2.1 Accelerations from High-Sensitivity Vibration Accelerometers

During GVT, the wing was instrumented with 16 uniaxial and 2 triaxial accelerometers. The uniaxial accelerometers were uniformly spaced over 6 stations along the span and each station had one accelerometer near the front spar and another near the rear spar to capture both out-of-plane bending and torsional vibrations. One uniaxial accelerometer was placed on each of the control surfaces to resolve the contribution of the control surfaces' resonances to the overall structural response. The triaxial accelerometers were set up along the front spar in order to resolve the in-plane bending vibrations. The process of installing the accelerometers involves using wax to stick the accelerometer on the wing surface and routing the cable overhead using a strut to support the accelerometer cable weight to minimize its interference with the structure. It also involves setting up the geometry of the test article in the Siemens LMS Test.Lab[1] software along with creating a connection between the nodes of the geometry and measurement points. It was observed that the accelerometers do not stick to the rough 3D-printed Nylon 12 surface as well as they do to metals and oven-cured composite materials. This is a potential source of error in the data collected from these sensors. Figure 5.4 shows the layout of the vibration accelerometers along with the fiber optic cables and IR markers installed on the wing to capture data during GVT.

The wing was tested using both an impact hammer excitation and a shaker excitation where it (the wing) was mounted on the shaker table – to allow for base excitation, as shown in Fig. 5.5. The impact hammer test was conducted with a soft rubber tip for excitation. The test software was configured to resolve frequencies up to 100 Hz. Similarly, the shaker excitation was set up as a stepped sine excitation from 2.0 Hz to 100.0 Hz with increments of 0.1 Hz and 10 cycles at each increment. The results for the natural frequencies identified using the Siemens LMS.TestLab software and the vibration accelerometers for configuration 1 with and without skin are given in Table 5.2. The corresponding results for configuration 2 but with skin only are given in Table 5.3.

The results shown in Table 5.2 corresponding to configuration 1 without skin are from the first round of GVT performed as a shakedown on the fully assembled wing (without the tip shaker) and

[1] https://www.plm.automation.siemens.com/global/en/products/simcenter/testlab.html

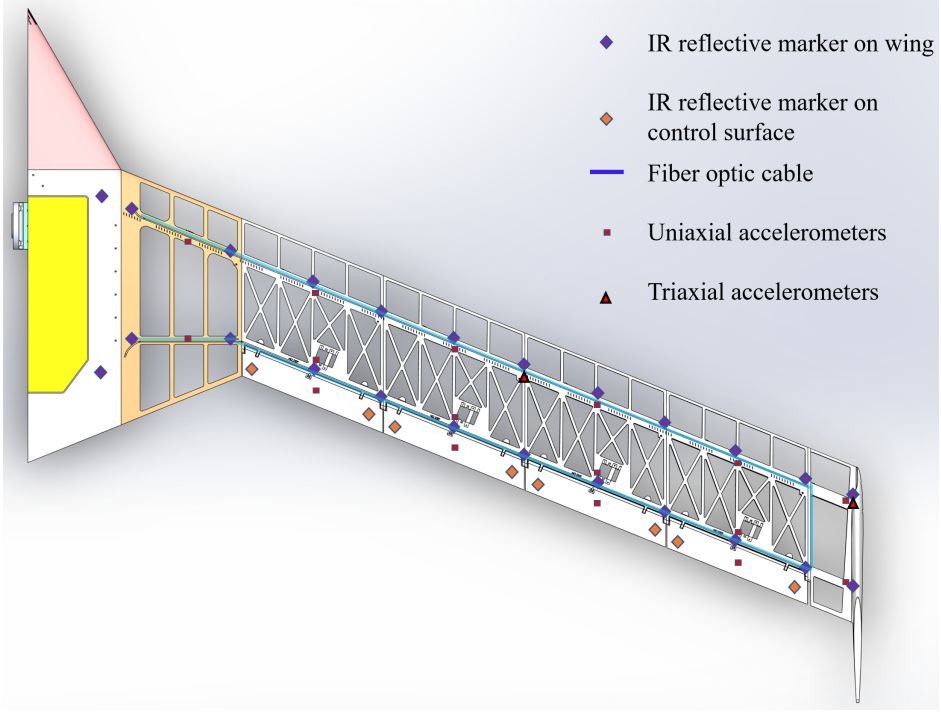

Figure 5.4: FOS layout (blue line), vibration accelerometers (red markers), and IR markers (purple and orange markers) over the A3TB-WT CAD model.

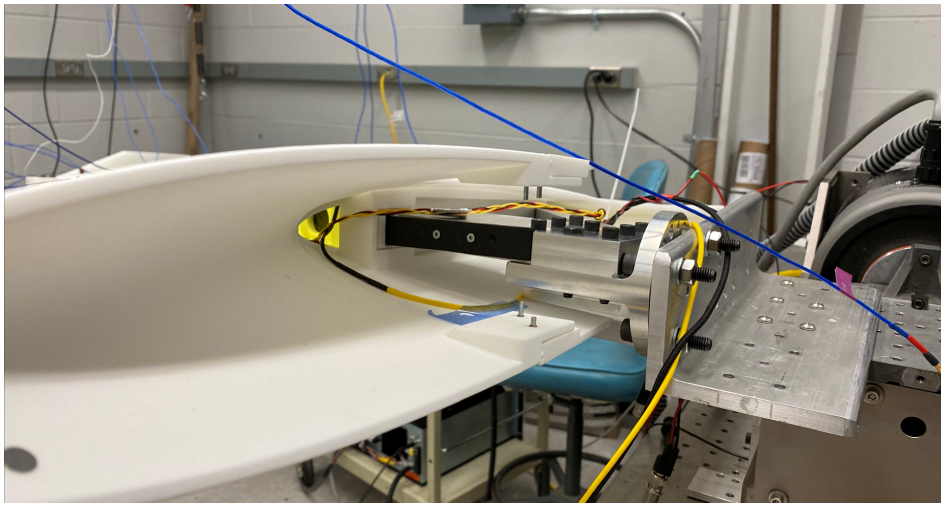

Figure 5.5: The A3TB-WT model clamped to the shaker table during GVT.

did not include accelerometers measuring the in-plane response of the wing. However, all subsequent GVT performed with the LMS Test.Lab system and the vibration accelerometers included accelerometers measuring the in-plane response. Interestingly, even without accelerometers measuring the in-plane response, there was a resonant mode identified at 6.78 Hz in this test using shaker excitation. This mode was also visually apparent as the shaker swept through the range of

Table 5.2: GVT results (frequencies in Hz) using the vibration accelerometers for configuration 1 with and without skin.

	Configuration 1 without skin				Configuration 1 with skin			
	Impact Hammer		Shaker		Impact Hammer		Shaker	
Mode #	Frequency	Mode type	Frequency	Mode type	Frequency	Mode type	Frequency	Mode type
1	2.46	1 OOP	2.47	1 OOP	2.48	1 OOP	2.49	1 OOP
2	–	1 IP	6.78	Unknown	–	1 IP	7.10	1 IP
3	11.40	1 T	11.44	1 T	12.10	2 OOP/1 T	12.04	2 OOP/ 1 T
4	13.20	2 OOP	13.18	2 OOP	14.70	1 IP/1T	14.80	1 IP/ 1 T
5	25.20	3 OOP	25.44	3 OOP	26.85	3 OOP	25.75	3 OOP
6	45.26	4 OOP/2 T	45.48	4 OOP/2 T	43.17	4 OOP/2 T	45.27	4 OOP/2 T
7	47.96	2 T/4 OOP	47.57	2 T/4 OOP	49.10	2 T/4 OOP	46.44	2 T/4 OOP
8	–	2 IP	–	2 IP	53.50	2 IP	51.79	2 IP

frequencies. Once the in-plane accelerometers were added, a first in-plane mode was identified at 7.1 Hz for the configuration 1 with skin.

Table 5.3: GVT results (frequencies in Hz) using the vibration accelerometers for configuration 2 with skin only.

	Impact Hammer		Shaker	
Mode #	Frequency	Mode type	Frequency	Mode type
1	2.3	1 OOP	2.32	1 OOP
2	–	1 IP	6.78	1 IP
2	11.86	1 T/ 2 OOP	11.81	1 T
3	12.98	1 IP/1T	12.64	2 OOP
4	26.72	3 OOP	26.52	3 OOP
5	44.86	4 OOP/2 T	45.67	4 OOP/2 T
6	47.04	2 T/4 OOP	50.5	2 T/4 OOP
7	53.39	2 IP	52.11	2 IP

Table 5.4 shows the comparison of the numerical against the experimental modal analyses performed on configuration 1 of the A3TB-WT outside the tunnel.

These results indicate that, in general, the as-built A3TB-WT was stiffer than the as-designed one. This is due in part to the uncertainties in the material properties used in manufacturing the model and the variability of the resulting pre-stress caused by the skin applied to the wing (using hot air to stretch the film). Another interesting takeaway was that the first in-plane mode, which was resolved experimentally, was not being captured by the finite element model of the A3TB-WT.

Table 5.4: Comparison of natural frequencies (Hz) between the as-designed model and the as-built structure outside the wind tunnel.

Mode #	FEM	Mode type	GVT	Mode type	Error [%]
1	3.29	1 OOP	2.49	1 OOP	32.3
2	–	–	7.10	1 IP	–
3	11.02	1 T	12.04	2 OOP/ 1 T	−8.5
4	13.76	1 IP	14.8	1 IP/ 1 T	−7.0
5	17.76	2 OOP	12.04	2 OOP/ 1 T	47.5
6	31.48	3 OOP	25.75	3 OOP	22.3
7	36.28	T 2/CS	45.27	4 OOP/2 T	−19.9
8	37.28	T 2/CS	46.44	2 T/4 OOP	−19.7
9	50.40	CS	–	–	–
10	52.21	CS	–	–	–
11	52.89	2 IP	51.79	2 IP	2.1%

5.2.2 Initial FEM updates

After reviewing the A3TB-WT GVT experimental set up and comparing it to the numerical model and the FEM boundary condition, an effort was made to identify the sources of error. The significant mismatch between the initial finite element model and the GVT was attributed to:

1. Imperfect clamped condition at the wing root, that is, not truly clamped experimentally and not well modeled numerically.

2. Variability in the manufacturers' reported properties of the 3D printed and composite materials.

3. Unknown pre-stress caused by the skin installation and shrinkage process.

The following adjustments were made to the FEM to improve the modeling of the boundary conditions and update the material properties to better match the experimental results:

1. The wing frame is made of Nylon 12. Its Young's modulus was adjusted from 1.65 GPa to 1.8 GPa (material specs provided from the 3D-printing company were different than the baseline material specs used in the initial FEM).

2. Nylon 12 material density changed from 950 $\frac{\text{kg}}{\text{m}^3}$ to 890 $\frac{\text{kg}}{\text{m}^3}$. This was done based on the measured weight of the parts.

3. In the original FEM, all nodes on the symmetry plane were clamped (see Fig. 5.6a). This was changed to using a spring connected with rigid body elements to the nodes between the spar on the fuselage and the first segment's interface plane, as shown in Fig. 5.6b.

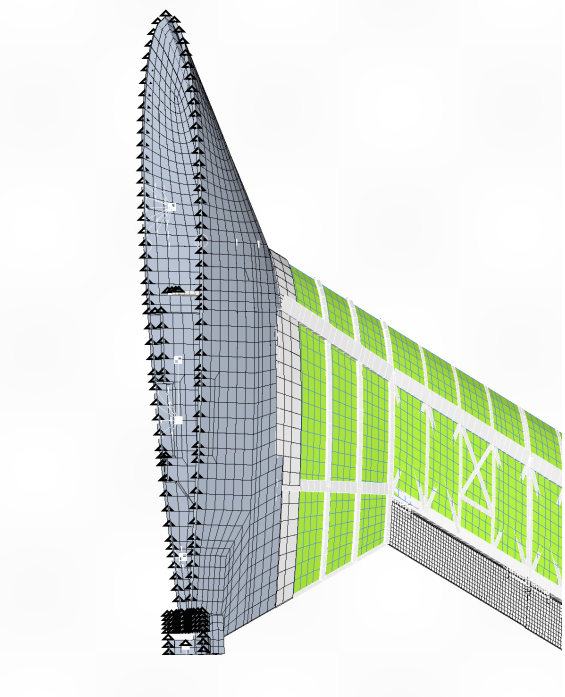

(a) Initial A3TB-WT root boundary condition. Black triangles represent nodes clamped on the symmetry plane.

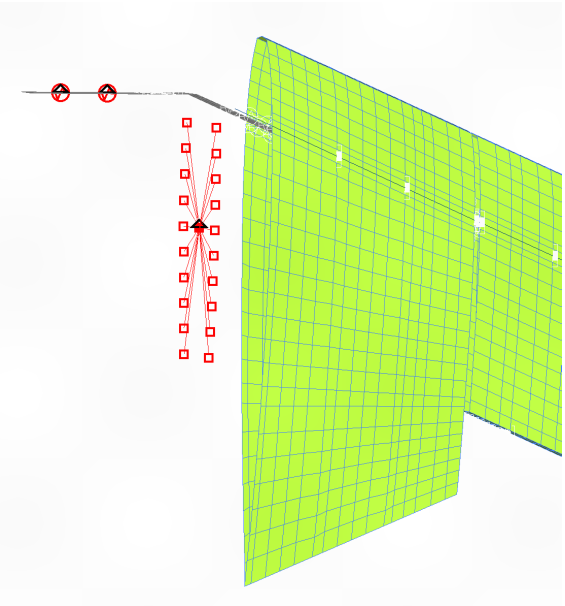

(b) Modified A3TB-WT root boundary condition. Black triangles represent clamped nodes, red-colored elements represent the rigid body elements connected to clamped nodes using springs.

Figure 5.6: Original A3TB-WT root boundary condition (left), and initial modification (right).

4. This root spring only allows motion in the out-of-plane direction. Another modification was to clamp the two nodes on the spar that actually connect to the load cell adapter (see the two screws on the carbon fiber spar near the root of the A3TB-WT in Fig. 5.5).

After these modifications were done, the updated FEM's modal results were compared to the experiment and the results are summarized in Table 5.5 for configuration 1 without skin and Table 5.6 for configuration 1 with skin. These data include the results from the MCS and the FOS systems for a quick comparison between the different experimental systems used to record data during GVT. Here, the data from the MCS and FOS was obtained from an impact hammer excitation to the structure. 'Impact GVT' refers to modes resolved using vibration accelerometers under an impact hammer excitation, while 'Shaker GVT' refers to modes resolved from the vibration accelerometers using a shaker excitation.

As discussed previously, the GVT for configuration 1 without skin did not have accelerometers measuring the in-plane response, thus, neither the impact nor the shaker tests conducted with the vibration accelerometers were able to identify the first in-plane mode. However, since the mode measured at 6.8 Hz was later identified, it is listed as the first in-plane mode here. It is interesting

Table 5.5: Comparison of updated FEM (frequencies in Hz) with GVT for A3TB-WT configuration 1 without skin.

Type	MCS	FOS	Impact GVT	Shaker GVT	FEM
1 OOP	2.3	2.5	2.5	2.5	2.4
1 T	11.3	11.4	11.4	11.4	10.1
1 T/1 IP	–	6.8	–	6.8	11.7
2 OOP	13.1	13.4	13.2	13.2	15.1

Table 5.6: Comparison of updated FEM (frequencies in Hz) with GVT for A3TB-WT configuration 1 with skin.

Type	MCS	FOS	Impact GVT	Shaker GVT	FEM
1 OOP	2.8	2.6	2.5	2.5	2.6
1 T	12.2	11.9	12.1	12.0	11.1
1 T/1 IP	–	6.9	–	7.1	13.4
2 OOP	15.0	15.1	14.7	14.8	15.9

to note that even with the updates to the FEM and a better match between the first out-of-plane and torsion modes, the FEM is not able to capture the first in-plane dominated mode. It captures a torsion dominated mode which is coupled with in-plane motion.

Further investigation of the FEM boundary conditions revealed that the root spring boundary condition to represent the imperfect clamping boundary condition (only two points on the carbon fiber spar were clamped in the experiment) could be modified further to capture the first in-plane dominated mode. This is discussed in Section 5.4.2.

5.3 Modified FEM Updating Process for 3D Printed Structures

A FEM updating procedure developed by Sharqi and Cesnik [38] was chosen as the starting point for this study, and was adjusted in a two-step process to account for the uncertainties coming from the 3D printed structure. First, the FEM updating process is modified to handle 3D printed structures by introducing different bounds on the design variables associated with the different parts of the structure. Second, experimental tests are conducted to inform the values of the as-built component properties. These are used as a center value in the adjustment of the FEM of the 3D printed structure to the experimental GVT results. The model updating process is posed as an optimization problem with the objective of minimizing the difference between the numerical model and the experimental measurements. In this optimization problem, various modules involving

frequencies, mass, inertia, and center of gravity are available and can be activated based on which data are accessible and what differences need to be minimized.

The optimization problem is given by:

$$
\begin{aligned}
\textbf{minimize F(x)} \quad = \quad & \left(\frac{m - m_0}{m_0}\right)^2 + \left(\frac{I_{xx} - I_{xx_0}}{I_{xx_0}}\right)^2 + \left(\frac{I_{yy} - I_{yy_0}}{I_{yy_0}}\right)^2 + \left(\frac{I_{zz} - I_{zz_0}}{I_{zz_0}}\right)^2 + \\
& \left(\frac{X_{cg} - X_{cg_0}}{X_{cg_0}}\right)^2 + \left(\frac{Y_{cg} - Y_{cg_0}}{Y_{cg_0}}\right)^2 + \left(\frac{Z_{cg} - Z_{cg_0}}{Z_{cg_0}}\right)^2 + \sum_{i=1}^{N} \left(\frac{\omega_i - \omega_{i_0}}{\omega_{i_0}}\right)^2 \\
\textbf{with respect to:} \quad & \mathbf{x} \\
\textbf{subjected to:} \quad & m^\ell \leq m \leq m^u \\
& I_{xx}^\ell \leq I_{xx} \leq I_{xx}^u \\
& I_{yy}^\ell \leq I_{yy} \leq I_{yy}^u \\
& I_{zz}^\ell \leq I_{zz} \leq I_{zz}^u \\
& X_{CG}^\ell \leq X_{CG} \leq X_{CG}^u \\
& Y_{CG}^\ell \leq Y_{CG} \leq Y_{CG}^u \\
& Z_{CG}^\ell \leq Z_{CG} \leq Z_{CG}^u \\
& MAC_i \geq MAC_{min}; \quad i = 1, 2, ..., N \\
& \mathbf{x}^\ell \leq \mathbf{x} \leq \mathbf{x}^\mathbf{u}
\end{aligned}
\tag{5.1}
$$

and the overall FEM updating process is shown schematically in Fig. 5.7. Here, the "modified FEM" is initialized after performing the model adjustments on the "initial FEM" and updated as the optimizer iterates through the design process.

In the optimization problem defined in Eq. 5.1, $\mathbf{x}$ are the set of design variables, m is the mass of the structure and ω_i is the i^{th} natural frequency associated with the set of the first N modes. Here, terms with the subscript 0 refer to the experimental value while the terms without the subscript are the corresponding numerical components. X_{cg} through Z_{cg} refers to the three components of the center of gravity (c.g.) location, while I_{xx} through I_{zz} are the components of the inertia tensor (additional product of inertia terms can also be included, but are not shown or investigated here for brevity). The upper and lower bounds in the constraints are denoted by the superscript u and ℓ, respectively, while MAC stands for Modal Assurance Criterion, and MAC_{min} corresponds to the desired minimum threshold of acceptable modal correlation.

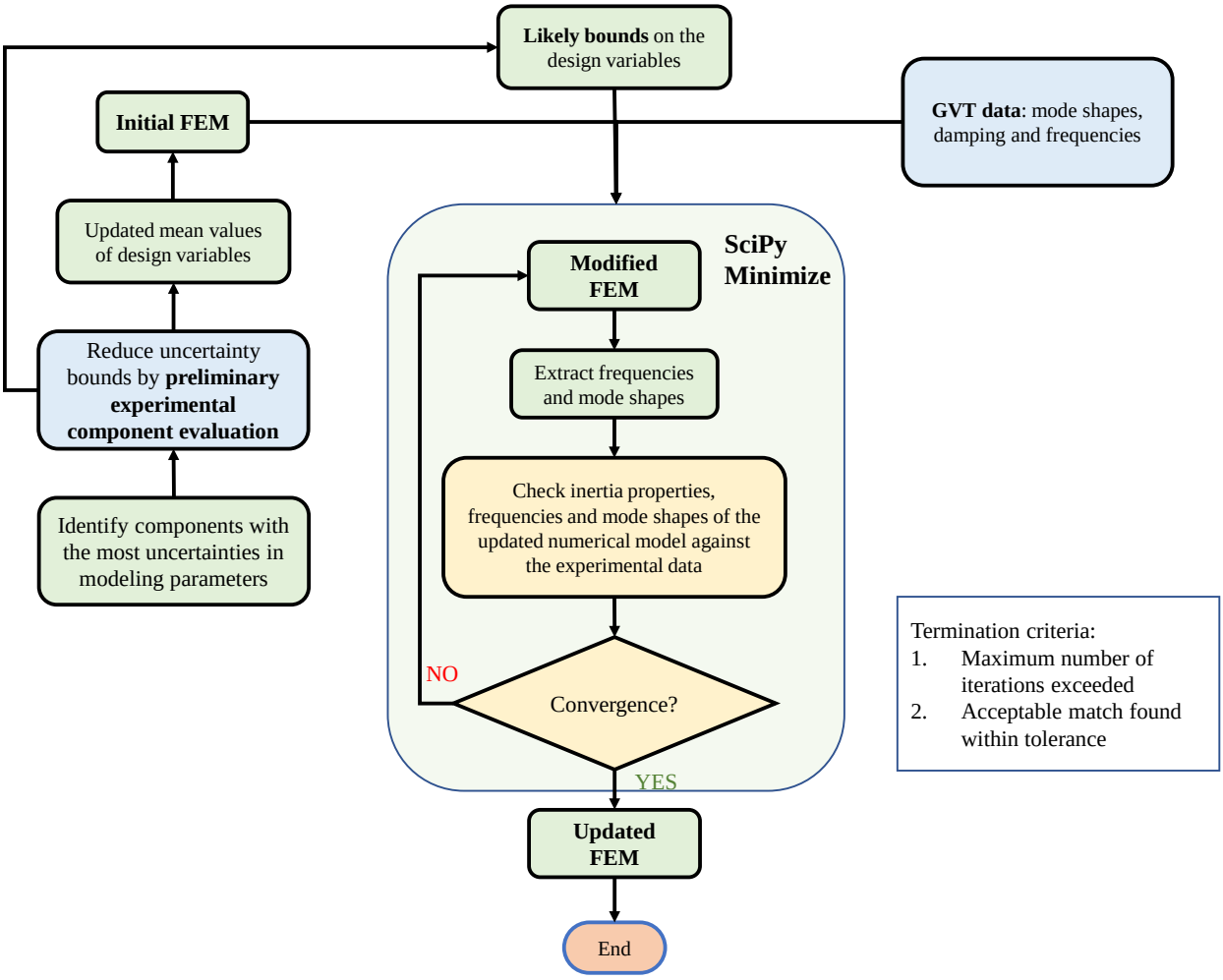

Figure 5.7: Finite element model updating process modified for 3D printed structures.

5.4 Preliminary Adjustments

This section describes the preliminary adjustments made to the numerical model of the A3TB-WT before the FEM updating process was applied to it. There were discrepancies between the modeling of the boundary conditions compared to the actual test setup that are addressed here. Another topic addressed here is the modeling of the main spar; tests indicate that it was modeled wrongly in the FEM. Once these adjustments were performed, the FEM was updated in Section 5.5 using the process described in Section 5.3.

5.4.1 Finite Element Models

The initial FEM of the A3TB-WT was created from the full-vehicle FEM of the flight test article. It was modified by introducing the new fixture at its (plane of symmetry) root for the wind-tunnel

assembly. Once the A3TB-WT parts were manufactured, assembled, and instrumented, adjustments to the FEM model were necessary to capture the as-built configuration more closely. These adjustments are presented before the FEM updating process takes place.

Past work indicated that there were large errors (greater than 10%) between the results of the GVT and the FEM [96]. Previous *ad hoc* attempts to improve the FEM focused on updating the mass model based on weighing the structure and adjusting the density of the material properties to attain the target mass. Another change to the FEM included removing the fully clamped boundary condition on its symmetry plane and replacing it with multiple root springs to represent the imperfect boundary condition, particularly at the wind tunnel wall mount. A key conclusion from past work [96] was that even with the updates to the FEM and a better match between the first out-of-plane and torsion modes, the FEM was not able to capture the first in-plane dominated mode that occurred around 7 Hz. It captured a torsion dominated mode which is coupled with in-plane motion, but this mode occurs close to 12 Hz. This was not sufficient to capture flutter since the flutter mechanism for this wing indicates participation of both the first in-plane bending and the first torsion mode [93].

The significant mismatch between the FEM and the GVT results was summarized in Section 5.2.2, and will be focus of the adjustments made to the FEM to better match with the experimental setup and results. The A3TB-WT has different boundary conditions for the GVT conducted in the laboratory (mounted to a shaker table) and the one conducted in the wind tunnel, attached to a Pitch-and-Plunge apparatus (PaPA). Even though PaPA allows to 'fly' a wing during a wind tunnel test by unlocking the pitch and plunge degrees of freedom, no rigid-body degree of freedom was allowed in tests related to this study. The shaker table and wind tunnel boundary conditions can be seen in Fig. 5.8. The red circle in the image on the right highlights the single pin used to lock the pitch rotation in the PaPA, which is a source of uncertainty since it allows some flexibility in that degree of freedom.

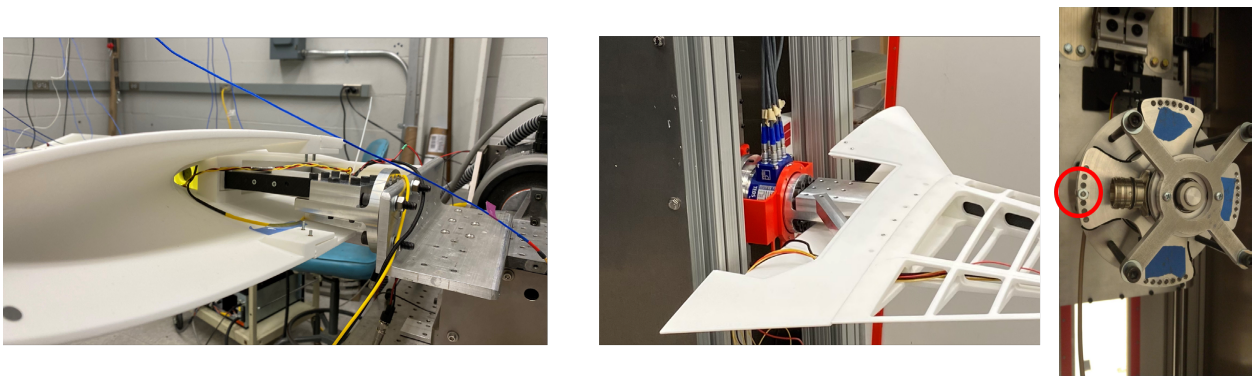

Figure 5.8: Shaker table boundary condition (left) and wind tunnel boundary condition (center and right).

5.4.2 Boundary Condition Modeling Updates

Further investigation of the modeling of the boundary conditions revealed that the root spring used to represent the imperfect clamping boundary condition (only two points on the carbon fiber spar were bolted to the clamp adapter in the experiment), along with the spring used to represent the root clamp adapter mounting to either the shaker table or the PaPA, could be modified further to capture the first in-plane dominated mode. Adjusting the in-plane and out-of-plane bending moment components of the spring element allowed capturing the first in-plane mode around 7 Hz without affecting the out-of-plane and torsion dominated modes. This modification required making the following changes to the FEM:

1. The location of the hole in the center of the PaPA clamp adapter (see the root section of the wing in the center image in Fig. 5.8) was measured and a grid point was created in the FEM at that location. The different rigid body elements representing the bolts on the spar as well as the other metallic struts that represent the set up of the root segment connect to this point (see right side of Fig. 5.9). The central point has a 6-DOF spring that is clamped.

2. The points on the spar that represent the root area of the spar bolted to the clamp adapter were adjusted after measurement (the two points on the spar shown on the left in Fig. 5.8). These root spar points were initially modeled in the FEM as fully clamped and were adding additional stiffness to the FEM that is not representative of the actual experimental set up. These points are now connected to the grid point representing the center of the clamp adapter using rigid body elements.

The modifications allow for an improved characterization of the struts connecting the fuselage/body section to the rest of wing (center image in Fig. 5.8) along with a more realistic model of the connection between the root section of the spar and the root clamp adapter. The CAD model showing the root area along with a view of the FEM showing the spar, the clamped grid, and the rigid body element connections that represent the physical setup are shown in Fig. 5.9.

5.4.3 Updating the Carbon Fiber Spar Material Stiffness

Upon inspection of the composite spar and its stiffness properties defined in the FEM, it was observed that the material representing the spar was listed as T300 woven fabric. This has a manufacturer's specified fiber tensile modulus of 230 GPa and a composite (ply) tensile modulus of 130 GPa [2]. However, the ply modulus of elasticity defined in the FEM was 64.75 GPa. This represents a significant discrepancy between the manufacturer's specified material properties and

[2] https://www.toraycma.com/wp-content/uploads/T300-Technical-Data-Sheet-1.pdf.pdf

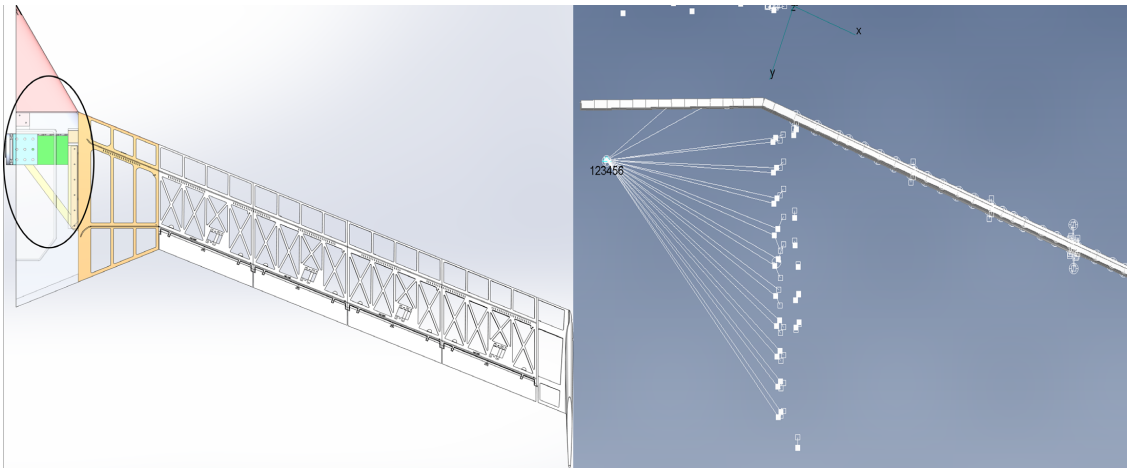

Figure 5.9: CAD layout of the A3TB-WT (left) with the root area highlighted in black. Spar FEM with modifications to the root spring representing the updated boundary condition is shown to the right.

the initial properties in the FEM. Another mismatch was that the spar was modeled as having a constant cross section of 20×5 mm; however, measurements of the cross section indicated deviations of up to 10% from the expected geometry. Increasing the ply-level elastic modulus in the FEM to the manufacturer specified modulus made the FEM stiffer by up to 20%, which was a trend in the wrong direction for comparison against the GVT results.

Further investigation was required in order to characterize the spar by itself and improve the material properties associated with the spar to increase confidence in both the component model as well as the overall FEM. The spar was characterized by applying various tip loads and measuring the resulting displacements. Using the simplified relation for tip displacement for an isotropic beam (Eq. 5.2), an equivalent stiffness of the composite spar can be estimated experimentally. In this expression, δ is the tip displacement, F the tip load, L the length of the spar, E the equivalent composite tensile modulus, and I is the area moment of inertia of the spar.

$$\delta = \frac{FL^3}{3EI} \implies E = \frac{FL^3}{3\delta I} \tag{5.2}$$

The experimentally measured composite tensile modulus was used to obtain a ply-level elastic modulus for the FEM that better approximates the estimated composite modulus when the plies are stacked/assembled in the FEM. This improves the stiffness property associated with the spar such that the FEM becomes more representative of the actual structure and the match between experimental results for both static deflections and GVT to the FEM is improved. A plot of the out-of-plane tip deflections comparing the original and the updated ply elastic modulus against the experimental results is shown in Fig. 5.10. The updated spar stiffness allows for a closer match

for the tip deflection than the original stiffness. Another interesting takeaway is that the actual spar material is not T300 woven carbon fiber fabric. The measured stiffness was lower than the initial value defined in the FEM. The updated spar material property in the FEM allows for a more informed starting point for the optimizer as well as better definition on the bounds placed on the optimizer during the finite element update process.

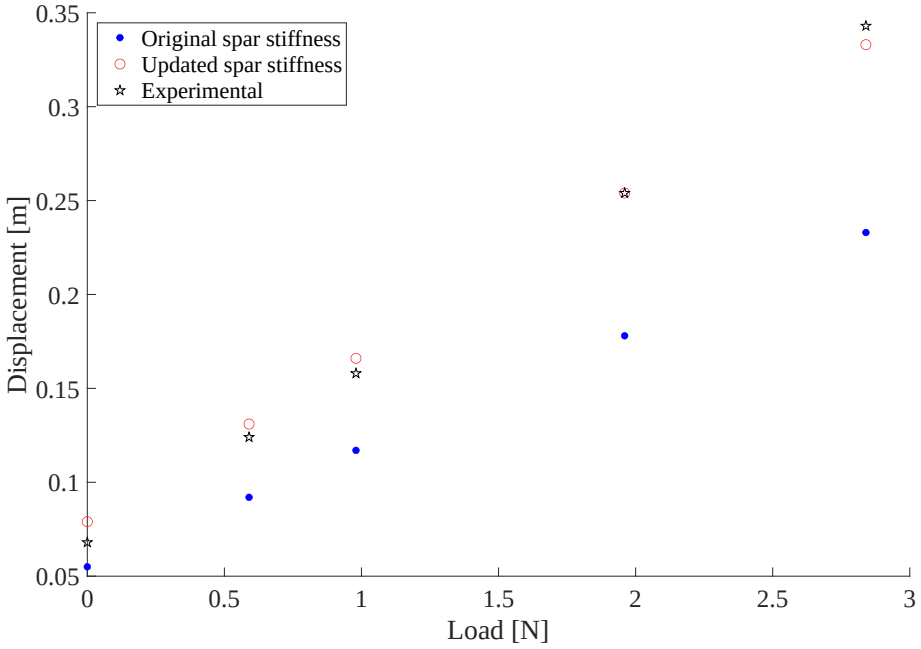

Figure 5.10: Comparison of the tip displacements for the updated spar stiffness against the original.

5.5 A3TB-WT FEM Updating

The FEM updating process described in Section 5.3 is applied to the the A3TB-WT after the initial model adjustments performed in Section 5.4. The details of the optimization problem along with the results are presented here. Two calibration cases were considered, based on the different boundary conditions in the shaker table GVT (left image in Fig. 5.8) and in the wind tunnel GVT (right image in Fig. 5.8). The GVT results are detailed in past work related to the structural characterization of the A3TB-WT [96], and summarized in Section 5.2. The difference between the optimization process for the shaker table GVT associated FEM update versus the wind tunnel GVT associated FEM update is the selection of design variables. The first FEM update used the data collected from the shaker table GVT and has all the design variables (material properties and root spring) shown in Table 5.7 available to the optimizer for exploring the design space. The

second FEM update, associated with the wind tunnel GVT, builds upon the first FEM update and only uses the root spring design variables in the FEM updating process.

5.5.1 Design Variables, Bounds and Constraints

Material properties of the different components and the root spring's stiffness coefficients were chosen as the design variables for the A3TB-WT. In this study, the material properties are defined as being constant along the entire structure for the respective component, but future work will include an exploration of splitting the structure's FEM into segments (based on how the wing was 3D printed and then assembled in segments). This will allow for identifying and fine tuning the differences between the different segments as well as the nonlinearities that come from the junction or the segment interfaces (the segments are glued together and represent an imperfect contact patch). Inequality constraints are imposed on the total mass, inertia and center of gravity properties. The design variables had variable bounds placed on them based on the level of uncertainty on their original values. The mass or density related design variables have the tightest bounds since mass of individual components and the entire structure can be measured. The bounds on the carbon fiber spar related design variables were restricted after the spar was characterized separately and greater confidence was obtained for its stiffness. The design variables related to the 3D printed material's and the skin stiffness were the most relaxed since those material properties are the least certain. The spring related design variables had their bounds defined based on which spring component showed the highest sensitivity to the minimization of the objective function (i.e., improved the match with the experimental results). The constraint variables had upper and lower limits set within $\pm 10\%$ of their original values. The design variables chosen for the optimization problem are shown in Table 5.7, along with their values before and after the FEM updating process.

5.5.2 FEM Updating Using Shaker Table GVT

The results from the shaker table GVT and FEM updating are shown in Table 5.8. The updated FEM has very good agreement with the experimental GVT with less than 0.5% error for the first three modes (the modes that participate in flutter for this wing model [93]) and less than 2% error for the first five modes.

5.5.3 Wind Tunnel FEM Updating

The second FEM update was performed starting from the FEM obtained from the laboratory (shaker table mounted) GVT FEM update (shown in Table 5.8). This FEM update used only the root spring components as the design variables, in order to capture the imperfect boundary

Table 5.7: Design variables for the A3TB-WT FEM updating using shaker table GVT results.

DV Type	Component	Normalized bounds	Initial DV	Final DV	Units	Difference (vs. initial) %
Density	3D printed	0.95, 1.05	890.00	889.11	$\frac{kg}{m^3}$	0.1
Density	Composite spar	0.95, 1.05	1471.50	1465.61	$\frac{kg}{m^3}$	0.4
Density	Fin	0.95, 1.05	824.41	788.96	$\frac{kg}{m^3}$	4.3
Density	Fuselage	0.95, 1.05	950.00	950.48	$\frac{kg}{m^3}$	0.1
Young's Modulus	3D printed	0.75, 1.25	1.80	1.36	GPa	24.5
Young's Modulus	Skin	0.5, 5.0	1.83	5.84	GPa	220.
E_1 or E_2	Composite spar	0.8, 1.2	45.00	54.00	GPa	20.0
G_{12}	Composite spar	0.8, 1.2	2.01	2.07	GPa	2.8
Young's Modulus	Fuselage	0.75, 1.25	1.65	1.49	GPa	10.0
K_x	Root spring	0.75, 1.5	1.0×10^{12}	1.0×10^{12}	$\frac{N}{m}$	0.0
K_y	Root spring	0.75, 1.5	1.0×10^{12}	1.0×10^{12}	$\frac{N}{m}$	0.0
K_z	Root spring	0.75, 1.5	1.0×10^{12}	1.0×10^{12}	$\frac{N}{m}$	0.0
M_x	Root spring	0.75, 2.0	1.0×10^{3}	2.0×10^{3}	$\frac{Nm}{rad}$	100.0
M_y	Root spring	0.75, 1.5	1.0×10^{12}	1.0×10^{12}	$\frac{Nm}{rad}$	0.0
M_z	Root spring	0.75, 1.5	5.0×10^{3}	7.05×10^{3}	$\frac{Nm}{rad}$	41.0

Table 5.8: Results from the FEM update using the shaker table GVT data.

	GVT on shaker base		Initial FEM		Updated FEM	
Mode #	Mode type	Frequency [Hz]	Frequency [Hz]	Difference (vs. GVT) %	Frequency [Hz]	Difference (vs. GVT) %
1	OOP 1	2.49	2.21	−11.4	2.50	0.5
2	IP 1	7.15	6.31	−11.7	7.15	0.0
3	T 1	11.78	10.58	−10.2	11.79	0.1
4	OOP 2	14.83	13.04	−12.1	14.55	−1.9
5	OOP 3	33.03	30.68	−7.1	33.37	1.0

condition imposed during the wind tunnel GVT (mounted on a pitch and plunge apparatus, see right image in Fig. 5.8). The results from this FEM updating are shown in Table 5.9.

Table 5.9: Results from the FEM update using wind tunnel GVT data.

	GVT in wind tunnel		FEM updated from shaker table GVT		Updated FEM (constant segment properties)	
Mode #	Mode type	Frequency [Hz]	Frequency [Hz]	Difference (vs. GVT) %	Frequency [Hz]	Difference(vs. GVT) %
1	OOP 1	2.62	2.50	−4.5	2.62	−0.1
2	IP 1	7.1	7.15	0.7	7.12	0.2
3	T 1	12	11.79	−1.7	11.89	−0.9
4	OOP 2	15.1	14.55	−3.7	15.23	0.9
5	OOP 3	35.5	33.37	−6.0	35.13	−1.0

5.5.4 Discussion Regarding FEM Updating of the A3TB-WT

The FEM of the A3TB-WT was updated using the GVT data coming from the shaker table GVT and then the wind tunnel GVT, however this updating was done in the unloaded and undeformed condition. When the A3TB-WT was tested in the wind tunnel with the air blowing, the aeroelastic

frequencies of the structure change (as expected), but even at the lowest airspeed that it was tested, the torsional frequency did not match the one coming from the updated FEM. The aeroelastic model of the A3TB-WT used for this comparison was developed in [93]. In other words, the updated FEM was not capturing the experimental aeroelastic frequencies observed in the wind tunnel testing campaign conducted on the A3TB-WT [96, 95]. The aeroelastic frequencies were estimated from wind tunnel test data using the methodology developed by [4] and are shown in Fig. 5.11. Vibration accelerometers were not used during the wind-on wind tunnel tests, so the frequencies and dampings are estimated from the FOS data.

The estimated parameters (aeroelastic frequencies and dampings) are presented over the whole range of tested airspeeds. It should be noted that they belong to two separate tests with slightly different boundary conditions:

1. Test 1 with airspeeds ranging between 16–26 m/s and one pin used to lock the pitch rotation of the PaPA (see right image in Fig. 5.8).

2. Test 2 with airspeeds ranging between 28–39 m/s, with strain data available up to 34 m/s [96] and two pins used to lock pitch rotation of the PaPA. Strain data beyond 34 m/s was not collected due to a malfunction with the strain data acquisition system.

The estimated frequencies vary smoothly with airspeed. The stable mode (OOP bending) frequency slightly increases, while the unstable mode (first torsion) frequency decreases with airspeed. In the tested airspeed range, both aeroelastic modes are stable, with an increasing damping trend. This indicates that the flutter of this configuration might be explosive, with damping that switches from positive to negative only very close to flutter onset.

Since the A3TB-WT only exhibits small deflections under the airspeeds it was tested in, there do not exist multiple configurations with large deflections that would improve the FEM updating process' ability to capture the as-built structure. Indeed, the primary source of discrepancy between the FEM and the physical wing tested in the wind tunnel is the nonlinear boundary condition. The root connection between the PaPA and the wing presents a boundary condition that varies with loading, and the effect of this is visible from Fig. 5.11 where the torsional mode has a different frequency than expected even at the lowest airspeed (where the aerodynamic loading and damping should be minimal). As demonstrated in Chapter 4, the FEM updating procedure developed in this work has the ability to capture the effects of large displacements, and local changes in stiffness due to pre-stress that can provide additional information that can be used to further improve the uniqueness of the combination of geometric and material property adjustments to the FEM. However, that is not useful in updating the FEM of the A3TB-WT, since the mismatch comes from the root boundary condition, and not the structure. The variety of wing root connections

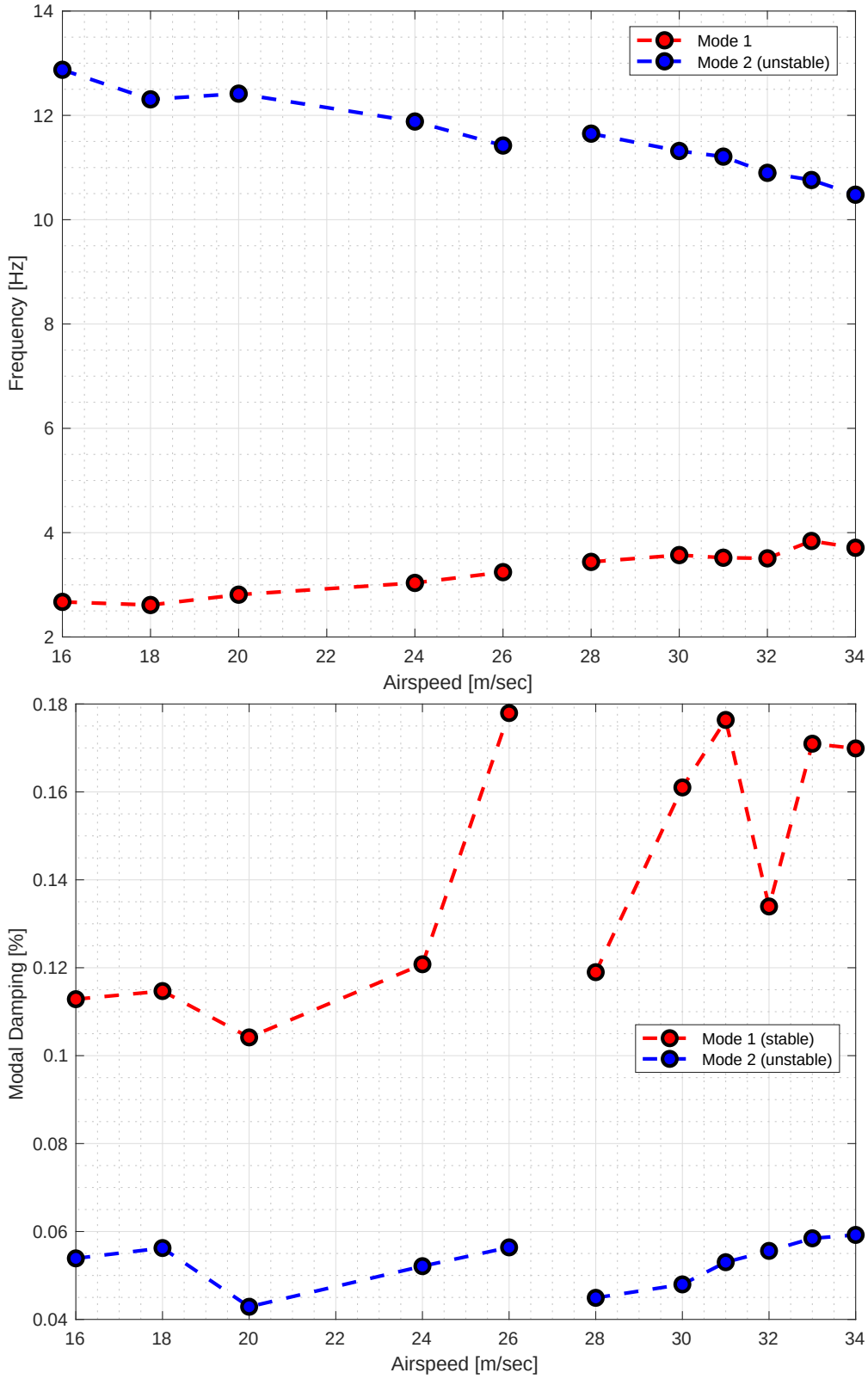

Figure 5.11: Estimated aeroelastic frequencies and damping values [4] based on experimental strain data collected during the wind tunnel tests of the A3TB-WT.

used for the GVT of the A3TB-WT require a characterization of the boundary condition(s) and its nonlinearities under loading.

The solution is to identify the stiffness characteristics of PaPA used for attaching the test article during wind tunnel testing. The PaPA has a connection mechanism that allows wings to be mounted on it and allows the pitch and/or plunge rigid body degree of freedom to be unlocked. This helps in simulating some of the rigid body DOFs associated with free-flying aircraft and gets us closer to the flight-testing environment. However, when the rigid body DOFs are locked (to have a fixed vertical height or angle of attack (AoA)), the mechanism used to hold the AoA or the vertical height constant presents an imperfect boundary condition. This influences the structural and aeroelastic frequencies of the test article and the impact of the nonlinear and imperfect boundary condition needs to be characterized. The expectation is that the stiffness of the boundary condition changes as the PaPA root attachment point gets loaded – this can be experimentally identified and quantified. This characterization will enable the extraction of the equivalent spring constants associated with the PaPA root attachment connection mechanism and improve modeling of the connection and boundary conditions as a nonlinear spring that changes its spring constant with loading.

5.6 Concluding Remarks

This chapter presented the GVT and FEM updating of the A3TB-WT, a 3D-printed blended wing body half-model developed for aeroelastic studies in the University of Michigan's 5-ft by 7-ft wind tunnel. The structure was characterized using a series of GVT conducted both in and out of the wind tunnel. They provided experimental characterization to refine the model in support of flutter onset prediction. Then the FEM of the A3TB-WT was updated using a modification on the FEM updating methodology developed as part of this work.

The FEM updating process devised for 3D printed structures that present significant uncertainty in their properties was presented and the methodology was applied to the 3D printed swept wing, which was inspired by the X-56A experimental aircraft and developed at the Technion for flutter identification and control studies. Using the data collected from GVT in the laboratory (mounted on a shaker table) and in the wind tunnel (mounted on a pitch-and-plunge apparatus, but without enabling free rigid-body degrees of freedom), the FEM was tuned and results indicate good agreement between the experimental GVT and numerical model. It was found that the updated FEM was able to match the results from the structural characterization, however, it failed to capture (or get closer) to the aeroelastic frequencies observed during wind tunnel testing. This indicates the need for better characterization of the boundary condition and incorporating the ability to handle such a nonlinear, load-varying boundary condition within the FEM will allow for an improved match for the GVT performed in the wind tunnel.

CHAPTER 6

Ground Vibration Testing and Finite Element Model Updating of a Very Flexible Aircraft

This chapter focuses on the application of the GVT and the FEM updating methodologies on a very flexible aircraft. Being very flexible and made of lightweight composite materials, the airframe presents the ideal structure to exercise all of the developments and findings from the previous chapters. The chapter contains a discussion of the research challenges posed in this dissertation as they apply to the X-HALE, and addresses them – both numerically and experimentally. Section 6.1 discusses the X-HALE airframe characteristics while Section 6.1.1 presents the preliminary tests conducted to characterize the GVT rig and suspension setup and discusses the experimental identification of the stiffness and damping coefficients associated with the suspension system. Section 6.1.2 presents a preliminary comparison of numerical and experimental results for the X-HALE in different deformed configurations while Section 6.2 provides details of the GVT campaign on the aircraft. Section 6.3 discusses the application of the finite element model updating methodology on the VFA. Section 6.4 contains a description of the setup and results of the free-free GVT performed on the X-HALE to validate the GVT and FEM updating methodology applied to the airframe. Section 6.5 summarizes the work done and outlines the future work that will be conducted towards improving GVT techniques for very flexible structures.

6.1 The University of Michigan's X-HALE

The University of Michigan's X-HALE is an experimental testbed for identifying areas of improvement needed in design, analysis and control of VFA [10]. The X-HALE was designed to:

1. Be aeroelastically representative of VFA and exhibit nonlinear couplings between flight dynamics and structural dynamics;

2. Be capable of large static deflections, with a tip deflection greater than 30% of the semi-span during operation;

3. Enable studying control design methodologies for VFA.

The X-HALE is a very flexible, remote-piloted aircraft developed with the primary objective to collect experimental aeroelastic data and to serve as a platform to evaluate control strategies. It is a wing-boom-tail type of aircraft with a 6-meter span, divided into six sections of 1-meter long each, with the tip sections set at a dihedral angle of 10 deg. The wing has an EMX-07 airfoil profile with chord of 0.2 m, while the tails have a NACA 0012 airfoil profile with a chord length of 0.12 m. There are eleven control effectors available on board the VFA: two roll spoilers located at the dihedral sections, four elevators situated at each outboard tail, and five motors providing distributed electric propulsion. The center tail is not used as a control surface.

The configuration is being experimentally studied both on the ground (GVT – discussed here) and in flight. These tests are building up a unique set of coupled nonlinear aeroelastic-flight dynamics data to support validation of numerical modeling, analysis and simulation tools. The X-HALE configuration can be seen both on the ground and in flight in Fig. 6.1, highlighting the level of deformation attained by the aircraft in flight. Its main physical characteristics are listed in Table 6.1.

Figure 6.1: X-HALE airframe on the ground and in flight.

Table 6.1: Main X-HALE airframe characteristics.

Wing span	6	m
Wing chord	0.2	m
Planform area	1.2	m^2
Aspect ratio	30	-
Propeller diameter	0.3	m
Gross take-off weight	11.35	kg

6.1.1 Preparatory Tests for GVT on X-HALE

To characterize the system supporting the X-HALE during GVT, the following tests, further detailed below, were conducted:

1. Characterization of the GVT rig built to be used for suspending the X-HALE.
2. Tests on different spring setups to identify a soft spring system for suspending the aircraft while minimizing the coupling of support and airframe modes.
3. Experimental identification of the stiffness and damping characteristics of the system that defines the overall suspension setup.

6.1.1.1 X-HALE GVT Rig Characterization

In order to ensure the GVT set up did not substantially impact the aircraft's dynamic behavior, the rig built for suspending and testing the X-HALE was characterized. This was done by a series of impact tests. The rig consists of P1000 Unistruts [1] connected along the length of the testing facility with a damper at the ends where they connect to the walls. The overall dimensions of the setup are 7-m long by 2-m deep, with a floor to ceiling height of 2.2 m. The first test layout consisted of a single roving accelerometer moved to 4 points over the rig and the second test layout consisted of 11 accelerometers mounted on different struts of the rig facing different directions. Figure 6.2b shows the rig schematic for the first test and Fig. 6.2a shows the actual rig along with the accelerometer locations for the second test. These tests were conducted to identify the modal characteristics of the rig itself and to evaluate their potential impact on the GVT on the X-HALE. Results from the impact testing are shown in Table 6.2. The lowest frequency of the rig is approximately 16 Hz. Depending on the suspension mechanism from the rig to the X-HALE, and the frequency range of interest for the structural modes of the X-HALE, the fundamental frequency of the rig could be a source of interference to the airframe's resonance frequencies. One way of resolving this would be by stiffening the GVT rig itself. For the studies presented in this work, the range of interest for the structural modes of the X-HALE is limited to < 10 Hz such that the impact of the rig on the structure can be neglected. As discussed in Ref. [25], the effects of the rig can be captured in the FEM by including the rig structure in the system. Characterizing the rig allows one to identify its contribution to the system and eventually to update the FEM of the aircraft once GVT results are available.

[1] https://www.atkore.com/About-Us/Brands/Unistrut

(a) GVT Rig.

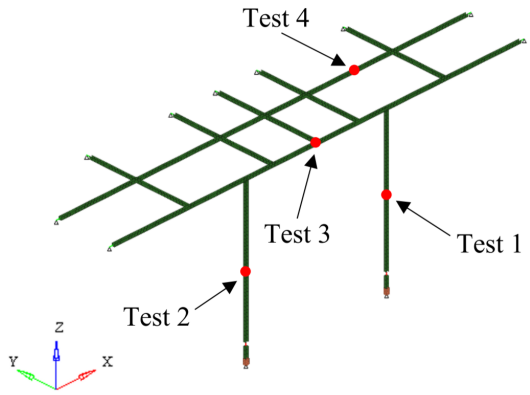

(b) Accelerometer locations for the tests.

Figure 6.2: X-HALE GVT Rig Characterization.

Table 6.2: Natural vibration frequencies of the test rig.

	Frequency (Hz)	
Mode #	Test 1	Test 2
1	16.64	16.58
2	19.76	19.18
3	20.2	21.27
4	20.88	22.18
5	21.52	28.7
6	29.36	29.75
7	35.24	32.75
8	42.96	35.21
9	55.12	45.17
10	59.08	51.75

6.1.1.2 Selection of Suspension Springs

In order to suspend the X-HALE, it was hypothesized that a system of springs could be used, connected either to the inboard (first wing junctions away from the center) or the outboard (second wing junctions away from the center) locations on the aircraft. The reality was that the all the springs available in the laboratory that could be ideal for achieving the low plunge frequency needed to stay clear of the X-HALE's first bending mode (< 1 Hz), started deforming plastically at a load smaller than the mass of the X-HALE. This was predominantly the issue faced in the support system selection. Sets of springs and elastic cords were investigated as potential suspension elements for the X-HALE GVT and both exhibited poor performance when loaded to the expected

load levels. Springs soft enough to avoid coupling with the first bending mode of the airframe (< 1 Hz) exhibited plastic deformation and therefore were not suitable. Alternatively, soft elastic cords would reach their stretching limit and would act as inextensible ropes, which also renders then unsuitable. Another concern was the lack of information available for the materials available on hand, either in the lab, or from common vendors. The sellers did not know the stiffness properties for the elastic or bungee cords they had in stock. Vendors and manufacturers were unable to provide detailed material property information for their products that were used in this study. Eventually, it was decided to test all bungee cords on hand and to select whichever one was the best compromise. Bungee cords were purchased from local stores and tested. A variety of consumer-grade springs and elastic cords were procured and tested. None would provide the exact support conditions needed to stay clear of the fundamental structural mode of the X-HALE.

Since free-free boundary conditions need to be approximated using a spring-based suspension system, springs selected should be soft enough to have a low plunge frequency with the airframe suspended but stiff enough to not extend plastically when loaded. A complete decoupling of the suspension and airframe modes cannot be achieved in practice for VFA due to the difficulty in having one order of magnitude of frequency separation while ensuring sufficient spring stiffness to support the load. However, spring stiffness should be as low as possible to minimize the interaction between suspension and airframe mode. A moderately stiff spring with a spring constant of 195 N/m was selected for the laboratory GVT and ten of these springs were used in series for each side of the suspension (for a net stiffness value of 19.5 N/m per set of springs). Since the total extension experienced by the ten springs is greater than the vertical height of the test rig, a single low-friction, ball-bearing pulley was used to allow the springs to extend horizontally along the length of the test rig and then turn directions (to drop vertically) in order to suspend the X-HALE. Figure 6.3 shows the aircraft suspended from the GVT rig with the ten springs in series in a deformed state.

6.1.1.3 Identification of Suspension Setup

The majority of the suspension setup and characterization for the X-HALE is similar to the beam suspension setup and characterization described in Section 3.2. The addition of a pulley in order to accommodate the springs in the setup shown in Fig. 6.3 adds damping and inertia to the system. In order to identify the experimental spring-damper setup, a 1 DOF rigid block was created that has half the mass of the X-HALE, and suspended from one side of the two-sided suspension system. This setup was characterized using impact testing, with data being recorded using both accelerometers and a high frame rate video camera, and the experimental frequency and damping values were used to create a model for the spring-damper setup. The experimental plunge frequency and damping coefficient values identified from the suspension system are shown in Table 6.3.

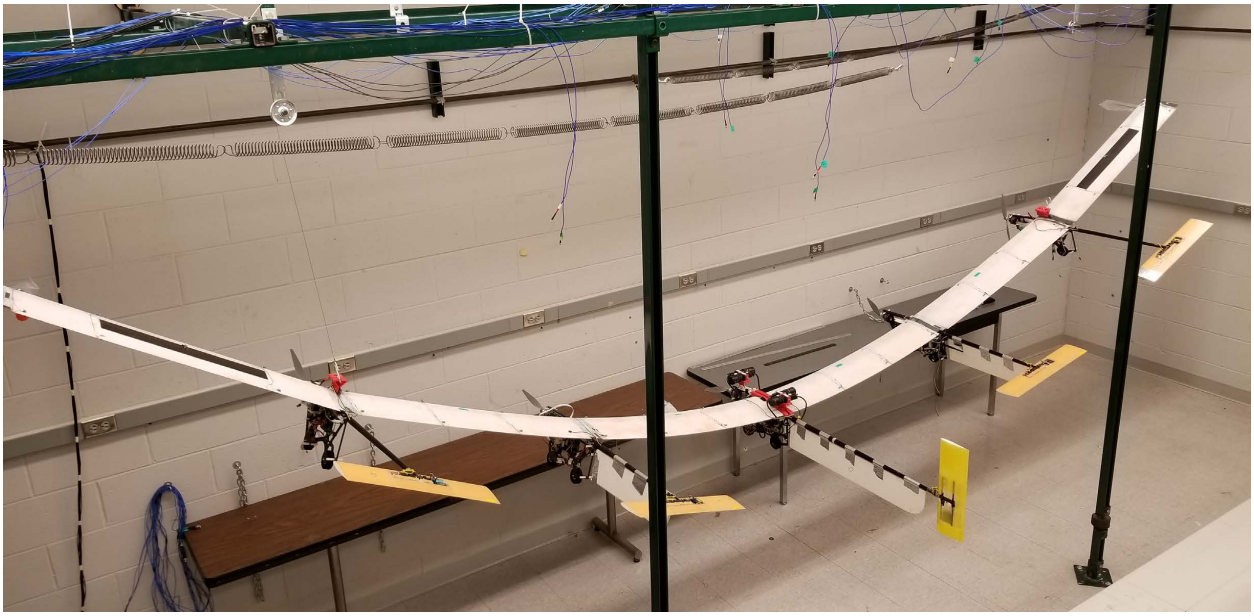

Figure 6.3: X-HALE suspension setup.

Table 6.3: Experimental natural frequency and damping for the 1 DOF block representing the suspension system

Mass (kg)	Stiffness (N/m)	Analytical freq. (Hz)	GVT freq. (Hz)	GVT damping (%)	Error (%)
5.672	19.5	0.30	0.28	4.68	3.83

6.1.1.4 Suspension System Modeling

Table 6.4 shows the results for the X-HALE representative spring-damper obtained from the experimental frequency and damping ratios. With these preliminary tests and their results, the numerical model can be updated to simulate the experimental suspension conditions.

Table 6.4: Experimentally identified stiffness and damping coefficients for the X-HALE suspension system

Property	**Left**	**Right**	**Units**
Mass	5.67	5.67	kg
Effective stiffness	17.59	18.01	$\frac{N}{m}$
Viscous damping coefficient	0.94	1.35	$\frac{N.s}{m}$
Damping ratio	4.70	6.70	%
Damped frequency	1.76	1.78	$\frac{rad}{s}$
Undamped frequency	1.76	1.78	$\frac{rad}{s}$

6.1.1.5 Tests Definition

For the GVT on the X-HALE, the following configurations are defined:

1. X-HALE suspended from the outboard wing junctions as shown in green in Fig. 6.4 (the joints between the outermost wings and the ones adjacent to it)

2. X-HALE suspended from the inboard wing junctions as shown in red in Fig. 6.4 (the joints between the wings at center and 1 m away from the center)

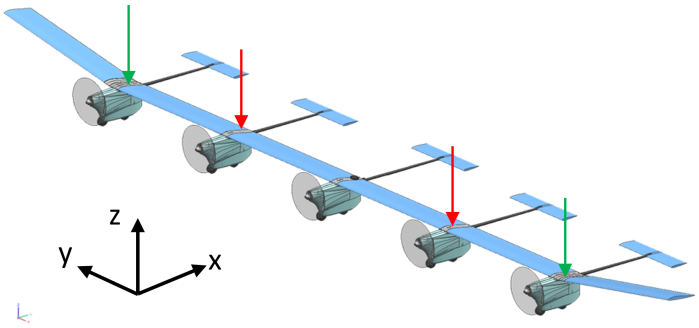

Figure 6.4: X-HALE configurations for GVT based on suspension location. Red and green arrows represent inboard and outboard suspensions respectively.

These two configurations are defined because the joint between the wings is a connection point from which the aircraft can be suspended. Moreover, using a combination of the two suspension configurations allows to recover most of the vehicle in-flight shapes. These two suspension configurations are at the extremes of the deformations the aircraft normally experiences in flight. Within the two suspension configurations, multiple accelerometer setups are defined to enable capturing out-of-plane bending and torsional modes. Uniaxial accelerometers are used to capture out-of-plane bending and the difference in amplitude and phase between the accelerometers at the leading edge and at the trailing edge of the wing allows for capturing torsion. Triaxial accelerometers are used to improve the discretization along the span as well as aid in capturing in-plane modes.

The X-HALE configurations corresponding to the two suspension setups defined in the Siemens PLM Test.Lab software are shown in Fig. 6.5. This is the jig shape (deformed initial shape) defined in the test software and it allows to capture the mode shapes about the deformed configuration. The accelerometer layout constitutes the geometry of the aircraft as represented in the test software. This accelerometer layout was fixed and is shown in Fig. 6.10. The point of suspension was varied (outboard or inboard), while the accelerometer layout was kept constant for the sake of consistency in test data collection.

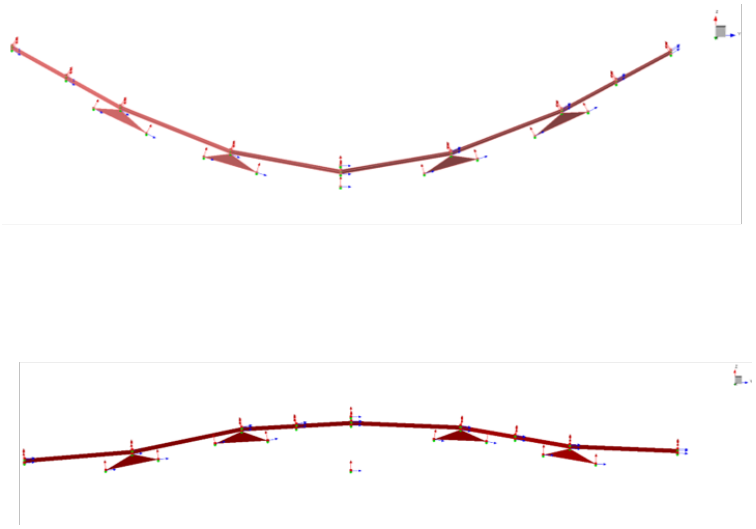

Figure 6.5: Jig shapes for the outboard (top) and inboard (bottom) X-HALE configurations defined in the LMS Test.Lab software.

6.1.2 Initial (shakedown) X-HALE GVT and Results

The suspension setup defined above was included in the X-HALE FE model using the experimentally identified spring values. Numerical statically deformed modal analysis was performed using the MSC Nastran SOL400 in the following steps:

1. Nonlinear static analysis to compute the deflection of the structure under self-weight based on the suspension configuration. This step is done to capture the aircraft's deformed shape as it is suspended from the rig and consider the tangent stiffness in the subsequent modal step.

2. Pre-stressed modal analysis about the nonlinear statically deformed configuration.

For static deformation under self-weight, two constraint displacements were added for the first step of the SOL400 solution. The coordinate system defined for the numerical model is defined such that the span of the aircraft is in the y-axis with the center being the origin of the system. The chord is along the x-axis and x is positive towards the trailing edge of the aircraft while y is positive towards the right side from the center and z is positive upwards. For one side of the suspension, the x and y translations were constrained, while for the other side, only the x translation was constrained. This allows the aircraft structure to translate laterally when subject to large deflections due to self-weight (shortening effect), but not translate in the in-plane direction (x-axis). All other translations and rotations are allowed. Once the nonlinear static deflection under self-weight is obtained, modal analysis is performed about the deformed configuration considering the tangent

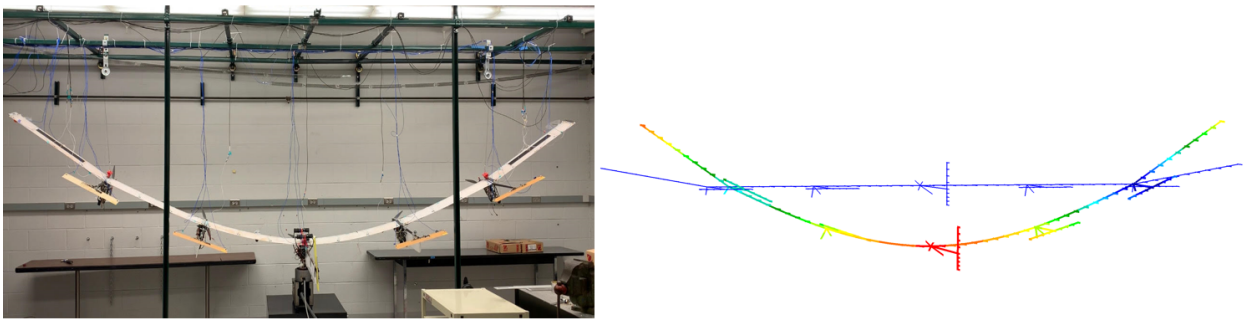

(a) Static deformation outboard

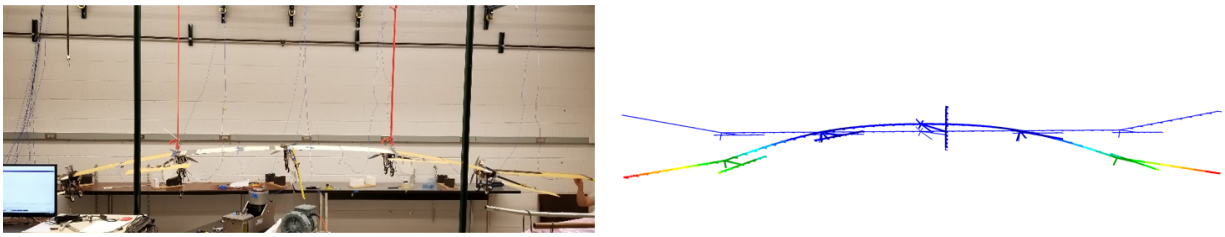

(b) Static deformation inboard

Figure 6.6: Static deformation in the outboard (a) and inboard (b) configuration

stiffness. Figures 6.6a and 6.6b show the results from the static analysis and the comparison with the aircraft suspended from the experimental rig.

In order to get familiar with the test structure and the instrumentation used to perform the testing, recording, and postprocessing of data, an initial GVT was conducted on the airframe. The shaker was used for excitation for these tests. This GVT was intended as a shakedown test of the equipment and connections as well as to identify possible sources of error before the main laboratory GVT was conducted on the X-HALE. This set of GVT were conducted in 2019 and the results were published in [2]. An experimental test was defined in the LMS Test.Lab environment using a stepped sine signal for the shaker from 0.5 Hz to 10 Hz, with a step size of 0.1 Hz and dwelling for 10 periods at each step. The aircraft was suspended as shown in Fig. 6.6a. Once deformed under its own weight, the shaker was connected to the structure using a stinger. During this initial test it was discovered that the boundary condition between the airframe and stinger was not adequately fixed and therefore introduced motion during operation which affected the modal results. This source of error was addressed in future tests as discussed in Section 6.2.2 and the updated connection is shown in Fig. 6.19. The results from the statically deformed modal analysis conducted in SOL400 are compared with the experimental results in Tables 6.5 and 6.6.

The Siemens LMS TestLab software resolves mode shapes based on the accelerations and phase differences between the accelerometers. Mode shapes for the fourth and fifth out-of-plane bending

Table 6.5: X-HALE experimental vs. numerical frequencies in outboard configuration

Mode #	**Numerical freq. (Hz)**	**Exp. freq. (Hz)**	**Error (%)**	**Damping (%)**
Plunge	0.27	–	–	–
Roll	0.43	–	–	–
1 OOP	0.96	1.04	8	1.20
2 OOP	2.55	2.6	2	0.90
Central tail bending	2.97	–	–	–
1 T	3.39	3.4	0	1.15
2 T	4.34	4.64	6	3.10
3T/1 IP	4.61	5.08	9	1.70
3 OOP/2 T	4.27	4.12	4	0.94
4 OOP	7.32	6.9	6	1.90
5 OOP	8.41	8.06	4	1.30

Table 6.6: X-HALE experimental vs. numerical frequencies in inboard configuration

Mode #	**Numerical freq. (Hz)**	**Exp. freq. (Hz)**	**Error (%)**	**Damping (%)**
Plunge	0.28	–	–	–
Roll	0.23	–	–	–
1 OOP	0.93	0.98	5	3.54
2 OOP	2.67	2.74	3	1.49
Central tail bending	2.98	–	–	–
1 T	3.56	3.39	5	0.55
3 OOP/ 2 T	4.39	4.36	1	1.92
3 OOP/ 3 T	4.66	4.93	5	2.45
1 IP	6.05	5.96	2	2.01
4 OOP	7.81	6.86	14	2.91
5 OOP	8.75	8.23	6	1.34

modes obtained from the GVT software are shown in Fig. 6.7. Due to the presence of a suspension system, some of the overall airframe modes have low, but non-zero frequencies. The plunge mode and the roll mode frequencies can be numerically identified and, given the right test setup, identified experimentally as well. The presence of the springs further away from each other in the outboard suspension configuration enables the roll mode to be of a higher frequency. This is because the aircraft has a large static deflection in that setup which causes higher stiffness. The first in-plane mode is also noticeably different in the two tested configurations. This is an example of the nonlinear behavior exhibited by the X-HALE where different deformed configurations lead to different modal characteristics. The presence of springs closer to each other stiffens the first in-plane mode for the inboard configuration. The coupling between in-plane, torsion and out-of-

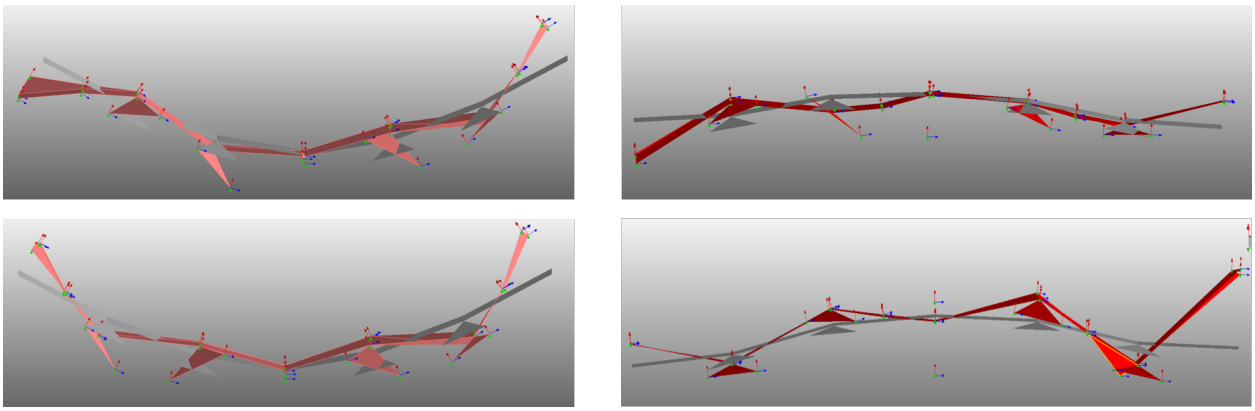

Figure 6.7: X-HALE experimental 4th and 5th OOP bending modes for outboard (left) and inboard(right) suspension.

plane modes also changes as a function of loading/deformed configuration. This is the same trend observed in the nonlinearly deformed beam test structure. However, the X-HALE mode shapes exhibit more complex couplings and requires the usage of the FEM updating procedure developed in this work for FEM update based on the GVT results.

6.2 Laboratory GVT

Between the initial shakedown GVT and the tests conducted for this study, the X-HALE went through a few years of ground and flight testing, which involved modifications to the airframe's electronics and instrumentation. Outdated or damaged mechanical and electrical components were removed and new ones were installed as part of maintenance of the airframe. These changes caused the mass and c.g. to be significantly different than during the initial shakedown GVT. An updated laboratory GVT was needed to better characterize the current system in the laboratory, and to exercise the GVT and FEM updating methodology on the current airframe.

Before the GVT were conducted, preliminary mass and c.g. measurements were recorded to identify the difference in the airframe's mass and c.g. and update the mass model of the aircraft. An interesting observation was made during these measurements. The airfame's flexibility would cause it to deform and adhere to small imperfections in the ground it was sitting on. The aircraft's mass is measured by putting a weighing scale aligned with each of the wheels (five weighing stations along the span corresponding to each pod, and each station consists of a scale under the front and rear wheels, for a total of 10 scales). The ground on which the scales were sitting was not flat and would cause erroneous readings for the mass and c.g.. A simple rig made of various Unistrut bars bolted together was created to serve as the 'level' ground and minimize the uncertainty in the mass and c.g. measurements. Figure 6.8 shows the set up of the Unistrut rig and

the aircraft sitting behind it before the measurements were taken.

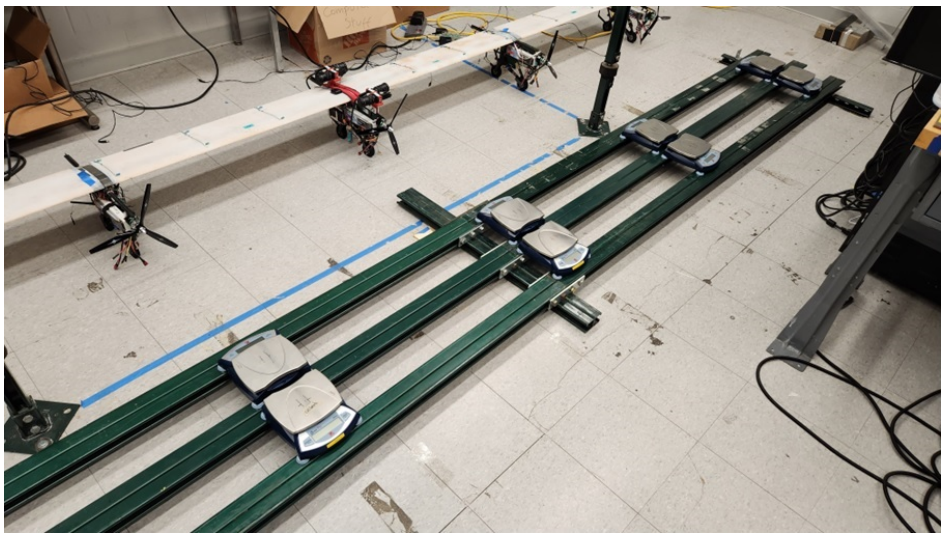

Figure 6.8: The Unistrut-based rig created to measure the mass and c.g. of the X-HALE.

After measuring the mass of the airframe using the new rig, it was found that the mass had increased by $< 5\%$, however the change in mass was not symmetric about the center of the aircraft. This lack of symmetrical mass adjustment was observed both in the spanwise and chordwise mass distributions. Figure 6.9 shows the difference in the chordwise c.g. for the original X-HALE airframe (defined in 2019) compared to the current one (as of 2023). The individual pods have different c.g. and that c.g. position as a percentage of chord length is shown for each pod (along with standard deviation around the mean, taken from 10 samples) in Fig. 6.9.

Once the X-HALE FEM's mass model was updated based on the actual mass and c.g. distribution, the aircraft was prepared to undergo GVT in the laboratory. This GVT used the same springs as the shakedown tests in Section 6.1.2. Another addition was the inclusion of a DC accelerometer to measure the very low-frequency rigid body plunge mode coming from the spring-pulley suspension system. Further discussion on the usage and importance of the DC accelerometer for the X-HALE GVT can be found in Section 6.4.1. The accelerometer layout for the laboratory GVT was fixed and is shown in Fig. 6.10. Here, names starting with 'U' refer to uniaxial ICP accelerometers, 'T' refer to triaxial ICP accelerometers and 'DC' refer to DC accelerometers. Figure 6.11 shows the Kevlar string connected to the spring, with the other end connected to a 3D printed adapter on the X-HALE as well as the DC accelerometer attached at the center of the aircraft. The X-HALE was excited using both an impact hammer and a shaker, and the results of both of these GVT are shown in Sections 6.2.1 and 6.2.2.

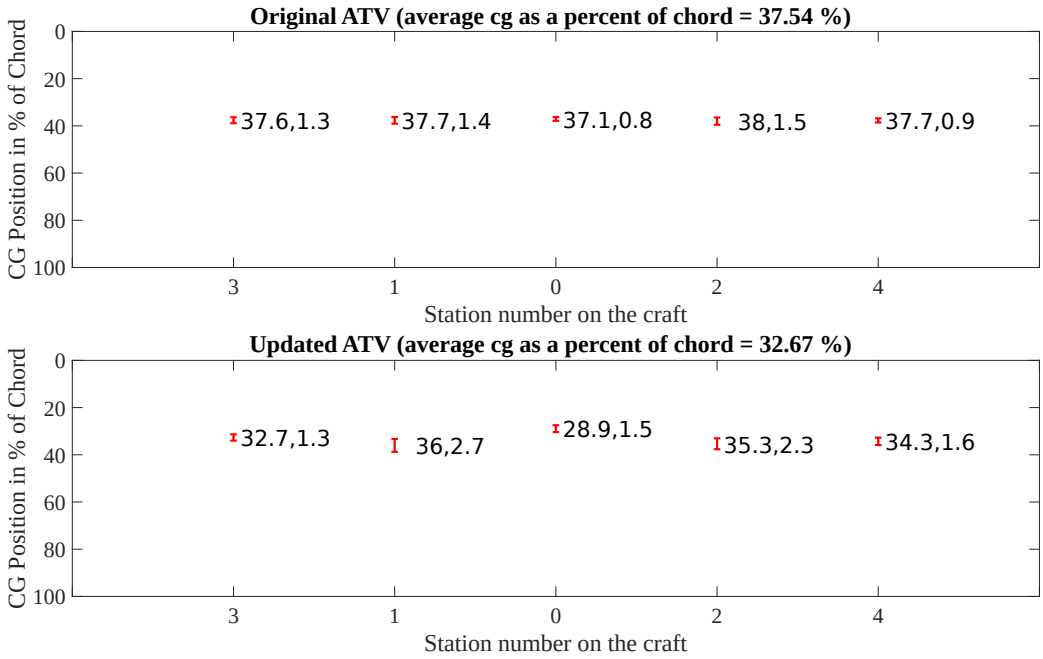

Figure 6.9: Change in chordwise c.g. for the updated X-HALE airframe. Red error bars represent standard deviation around the mean.

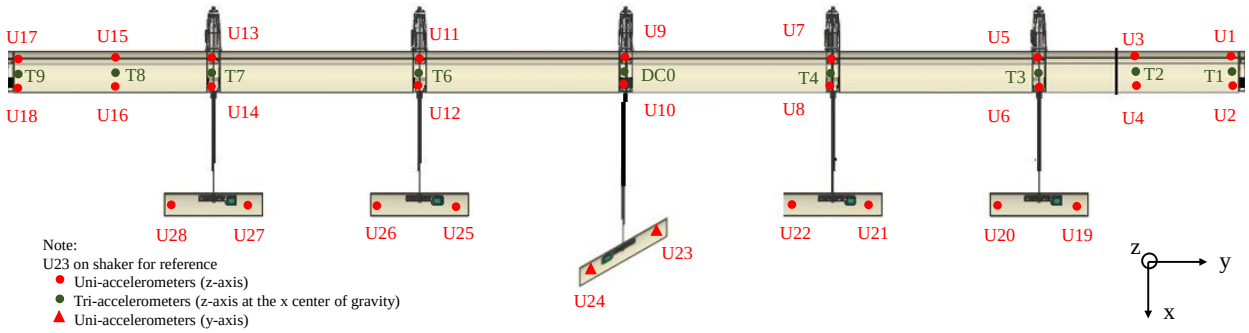

Figure 6.10: X-HALE lab GVT accelerometer layout.

6.2.1 Impact Hammer GVT

The impact hammer test was conducted by suspending the X-HALE from the suspension rig and impacting it with a soft rubber hammer tip. The soft rubber tip works best for exciting the low-frequencies of the structure and does not damage the foam-filled fiberglass composite construction of the wing sections. Multiple impact tests were conducted for both the outboard and inboard

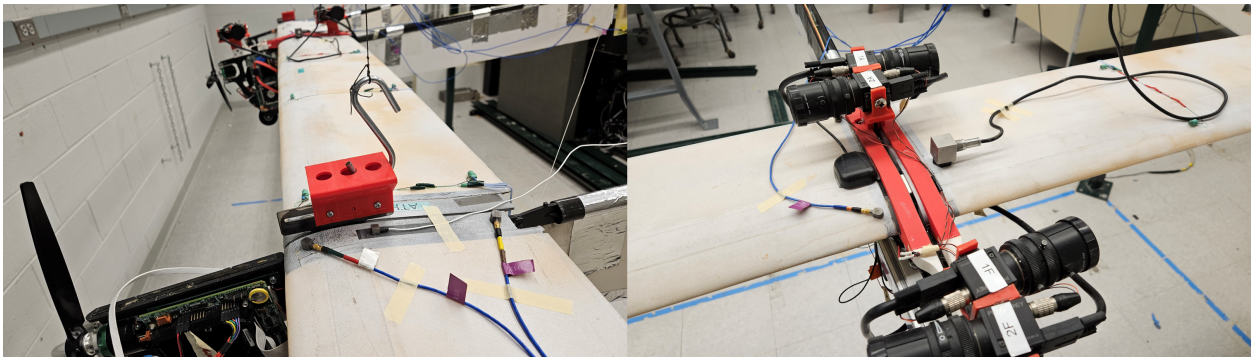

Figure 6.11: Kevlar string connecting the springs to the aircraft using a 3D printed adapter (left) and DC accelerometer to measure low frequency modes accurately (right).

configurations and these tests were conducted using a combination of roving hammer over the span (multiple impacts conducted over different wing sections) or fixed impact points on a single wing. Another test type was defined with the impact hammer where a pulse or push was given with the hammer and the results (FRF) computed from the pulse as the input. This is not a good impact or impulse, but since the frequency range of interest is between 0 and 10 Hz, it provides sufficient energy to excite the modes in that range of frequencies. The aircraft setup in the outboard configuration is shown in Fig. 6.12, while the setup for the inboard configuration is shown in Fig. 6.13.

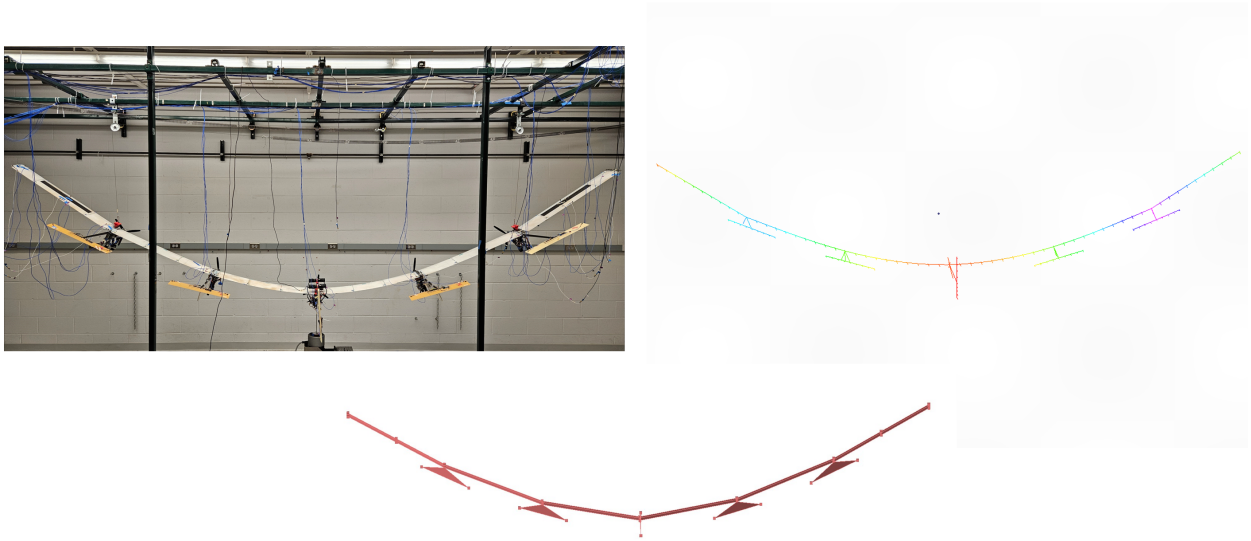

Figure 6.12: The X-HALE set up for GVT in the outboard configuration (top left), the nonlinear static deformation under self weight (top right) and the jig shape used in LMS Test.Lab to define the initial geometry based on the accelerometer layout (bottom).

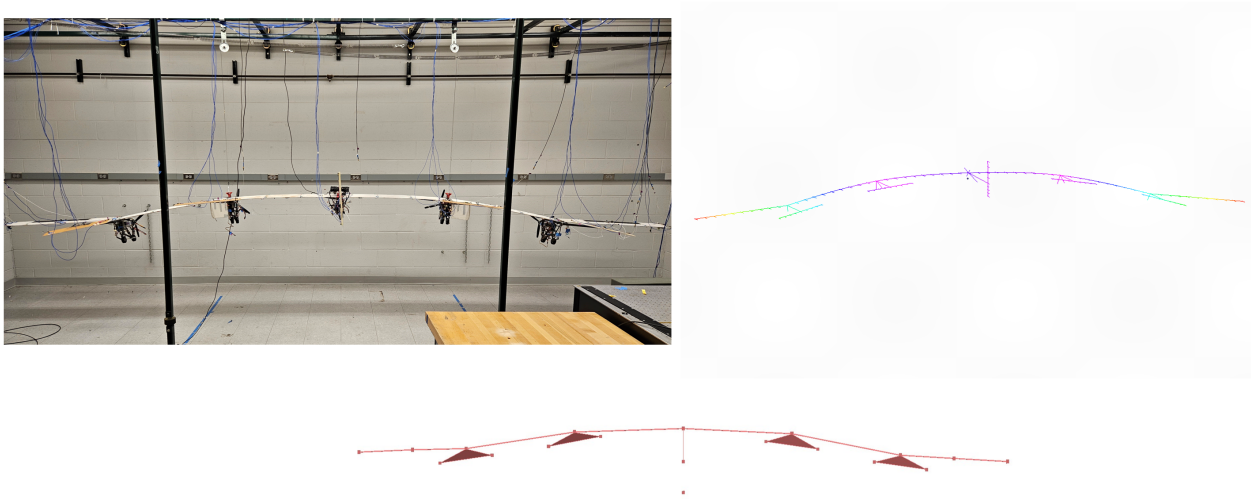

Figure 6.13: The X-HALE set up for GVT in the inboard configuration (top left), the nonlinear static deformation under self weight (top right) and the jig shape used in LMS Test.Lab to define the initial geometry based on the accelerometer layout (bottom).

The results from the various impact tests (different driving/impact points) showed little variation ($<$ 10 % standard deviation around the mean), and for each test, data was averaged over five impacts using the impulse hammer. This indicates that the results between the different impact tests were consistent with each other. Figures 6.14 and 6.15 show the comparison (between the GVT and the initial FEM) of the first 7 modes for the outboard and inboard configurations respectively. Results presented are averaged over the various impact tests, with the error bars representing the standard deviation around the mean.

These results show the difference in natural frequencies between the two differently deformed configurations as well as how the initial FEM is closer to capturing some modes while further apart for others. Another interesting observation is that the difference between the FEM and the experimental results is smaller for the inboard configuration than the outboard. The first seven mode shapes are shown in Figs. 6.16 and 6.17. FEM mode shapes are on the left, while the experimental ones are on the right.

6.2.2 Shaker GVT

For the X-HALE GVT with shaker excitation, a shaker mount was created that would hold the shaker rigidly and be bolted to the ground. This was done to ensure a stable base for the shaker to operate from, and to minimize the impact of any shaker motion exciting the base and affecting the energy being transferred to the aircraft. This base, made of Unistruts bolted to an assembly of

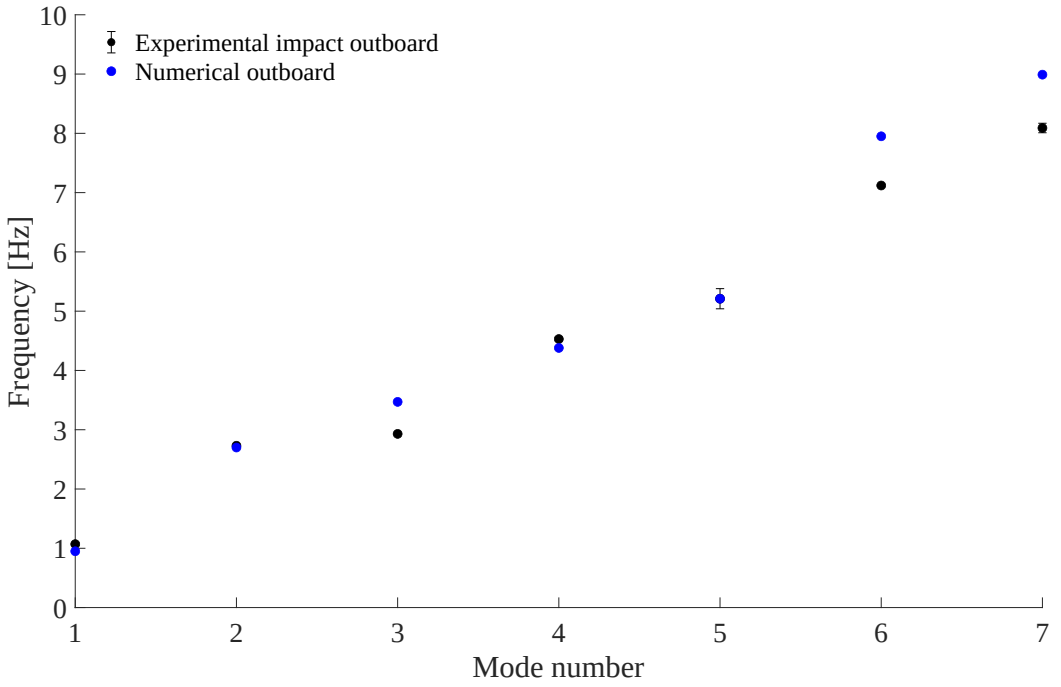

Figure 6.14: Comparison of the first 7 modes from the impact test GVT vs. the initial FEM for the outboard configuration.

80/20s [2] is shown in Fig. 6.18. Since flexibility of the base can influence the X-HALE's structural dynamics response, the base was characterized using an impact hammer GVT with and without the shaker. The base's fundamental mode without the shaker is over 100 Hz, and its fundamental mode with the shaker mounted on it is greater than 70 Hz. This indicates that the resonance modes of the shaker mount itself will not be a significant source of noise or influence the X-HALE's response during GVT.

A stinger was used to connect the shaker to the aircraft and one end of the stinger was screwed in directly to the shaker while the other end was screwed into a 3D printed adapter that bolts into the center pod of the X-HALE. Since the shaker is physically bolted into the 3D printed structure that is attached to the aircraft, it was initially decided to model the shaker as a clamped boundary condition, restricting all 3 translations and rotations. However, the actual connection allows for a small degree of rotation (around the roll, pitch and yaw axes) while the translations are constrained as far the stinger and the attachment is concerned. Since the perfect clamp connection did not accurately capture the shaker stinger connection to the X-HALE shown in Fig. 6.19, the attachment model was adjusted to act as a constraint on the three translations, while the rotational DOFs were unconstrained. Unreasonable force can cause the stinger to start unscrewing which can be inter-

[2] https://8020.net/product-basics

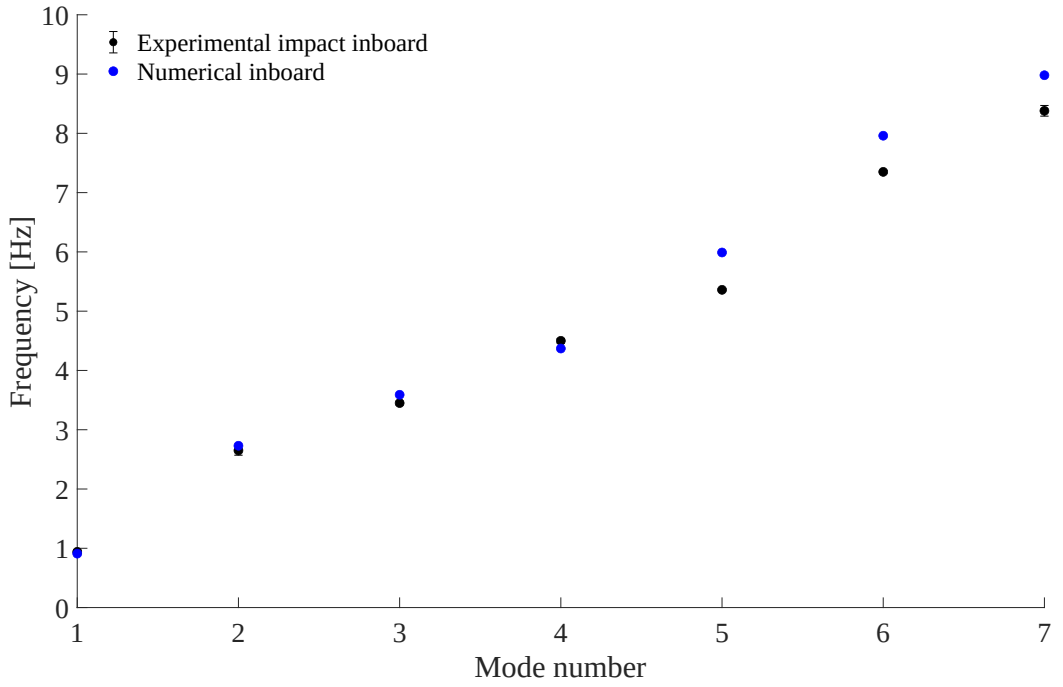

Figure 6.15: Comparison of the first 7 modes from the impact test GVT vs. the initial FEM for the inboard configuration.

preted as an imperfect boundary condition regarding vertical translation, however such deflections are neglected. An interesting observation is that this boundary condition prevents vertical translation, essentially eliminating the plunge mode coming from the suspension set up. The impact hammer GVT does not restrict this degree of freedom.

Some notes from the shaker tests:

1. It was observed that a swept sine excitation was not providing good results, particularly at lower frequencies (< 20 Hz). The swept sine test jumps from the low (0.5 Hz) frequency to 10 Hz in an instant. However, the stepped sine input test provided the expected excitation.

2. Another observation was that the frequency response function plots were noisy. So much so that it was difficult to confidently identify structural resonances. Peters, et al. and LMS international [79, 78] discussed using the PolyMAX modal parameter estimation method. This method allows analyzing large frequency band containing a high number of modes in a single analysis run and was helpful in identifying resonances from the FRFs.

3. The LMS software has a warning that it cannot accurately detect very low frequency modes (< 3.7 Hz), for the current excitation setup. Understanding and resolving this warning is ongoing, however, it does resolve some of the very low frequency modes, just not very clearly.

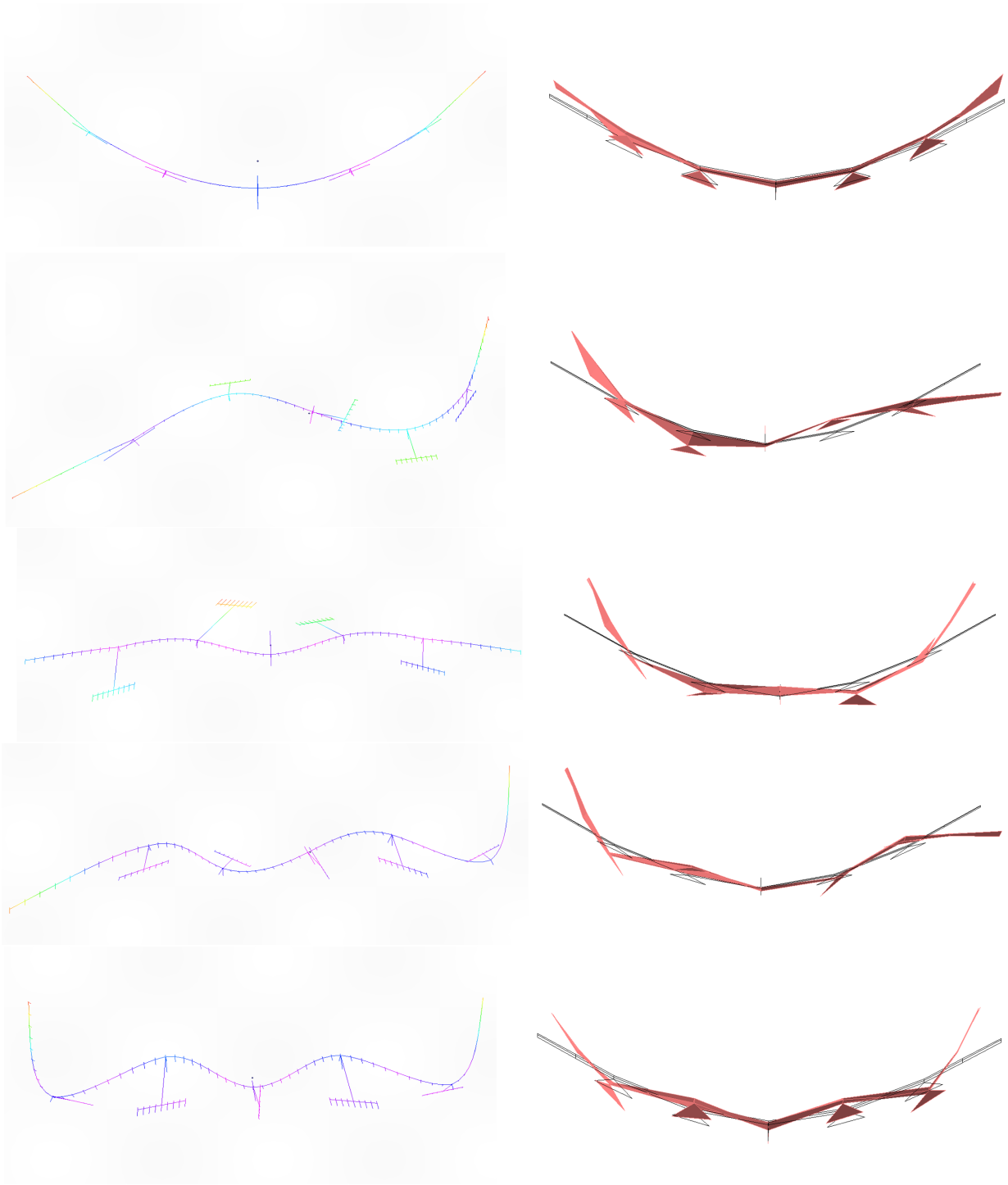

Figure 6.16: First five out-of-plane bending mode shapes. Numerical (FEM) modes on the left, GVT (experimental) modes on the right.

The resolution of the low frequency modes can be improved by using DC accelerometers, which are particularly good at capturing very low frequency resonances.

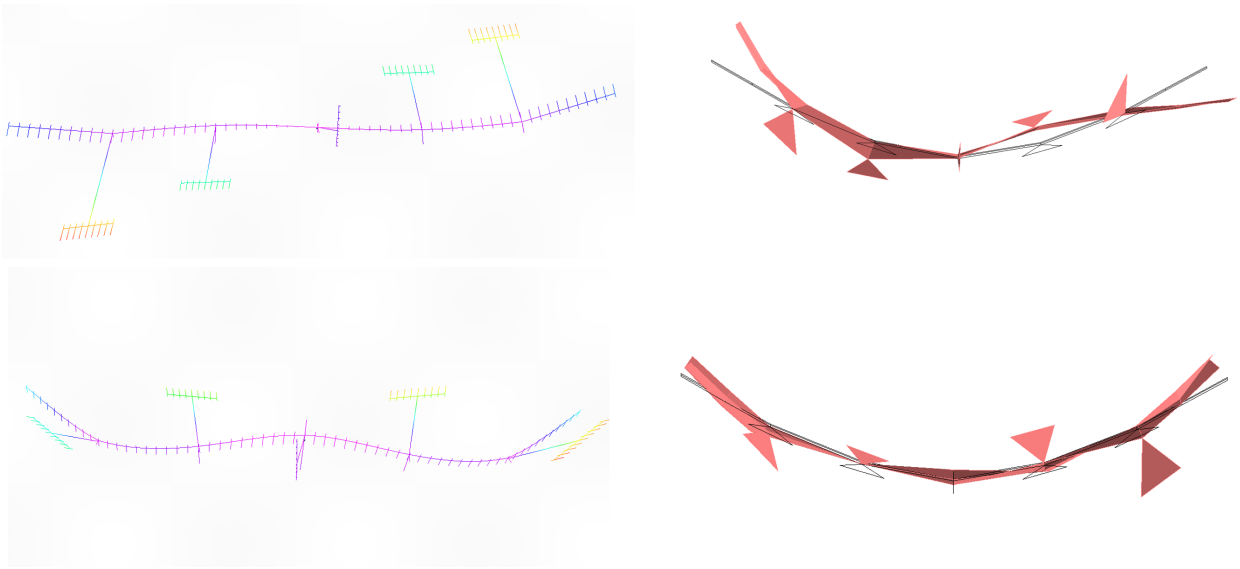

Figure 6.17: First and second torsion coupled with in-plane bending modes. Numerical (FEM) modes on the left, experimental on the right.

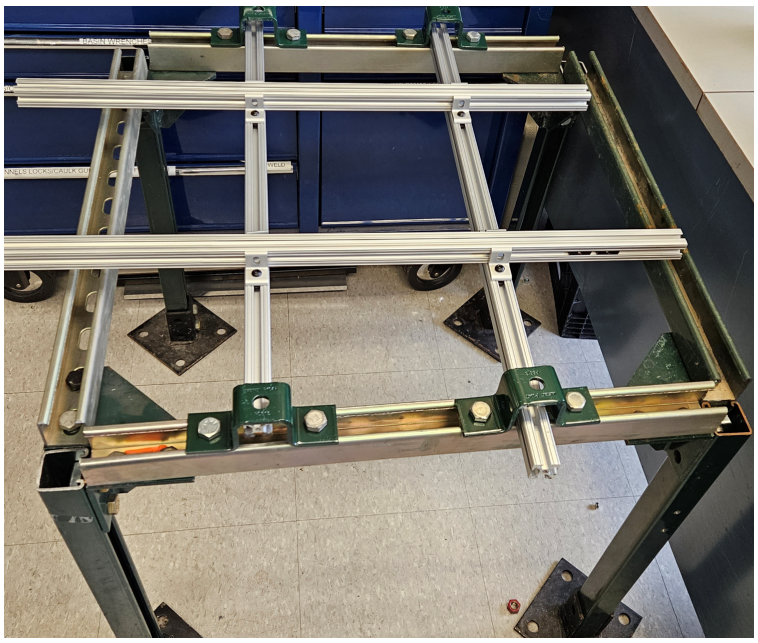

Figure 6.18: Shaker mount rig created to hold the shaker when performing shaker GVT on the X-HALE.

4. While identifying resonance modes and shapes from the FRF plots for a complicated system like the X-HALE is somewhat subjective (due to uncertainties coming from user error, instrumentation errors and nonlinearities associated with the various adapters and connections), multiple runs were performed for each configuration, and the results presented are

averaged over the runs.

5. When viewing mode shapes in the LMS software, an animated mode shape can be seen and saved as a gif.

6. All stepped sine tests were conducted from 0.5 – 10 Hz, with steps of 0.1 Hz and 10 cycles at each step.

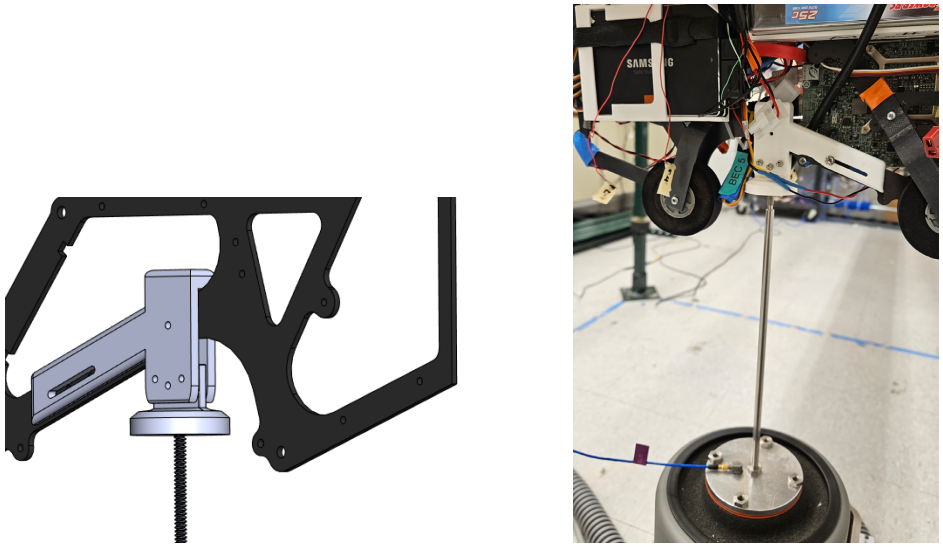

Figure 6.19: Shaker stinger attachment to the X-HALE.

The results from the shaker GVT on the X-HALE are shown in Figs. 6.20 and 6.21.

There are significant differences between the two excitation mechanisms and the largest source of uncertainty is the attachment of the shaker to the airframe. Interestingly, the impact test results generally have a smaller spread (over multiple tests) and are closer overall to the initial numerical model. This can be observed when the results of the two experimental tests (impact hammer excitation and shaker excitation GVT) are compared together as in Figs. 6.22 and 6.23.

6.3 FEM Updating on the X-HALE

With experimental GVT data now available, the FEM updating problem was formulated and applied to the X-HALE. The goal for GVT of aircraft is to approximate free-flying conditions in order to mimic the structural dynamic response of the vehicle in flight. These conditions are typically approximated by using a soft suspension model whose natural frequency is significantly lower than the fundamental natural frequency of the test structure. As discussed in [2], it may be very challenging or impossible to create a suspension system that does not interfere with the elastic

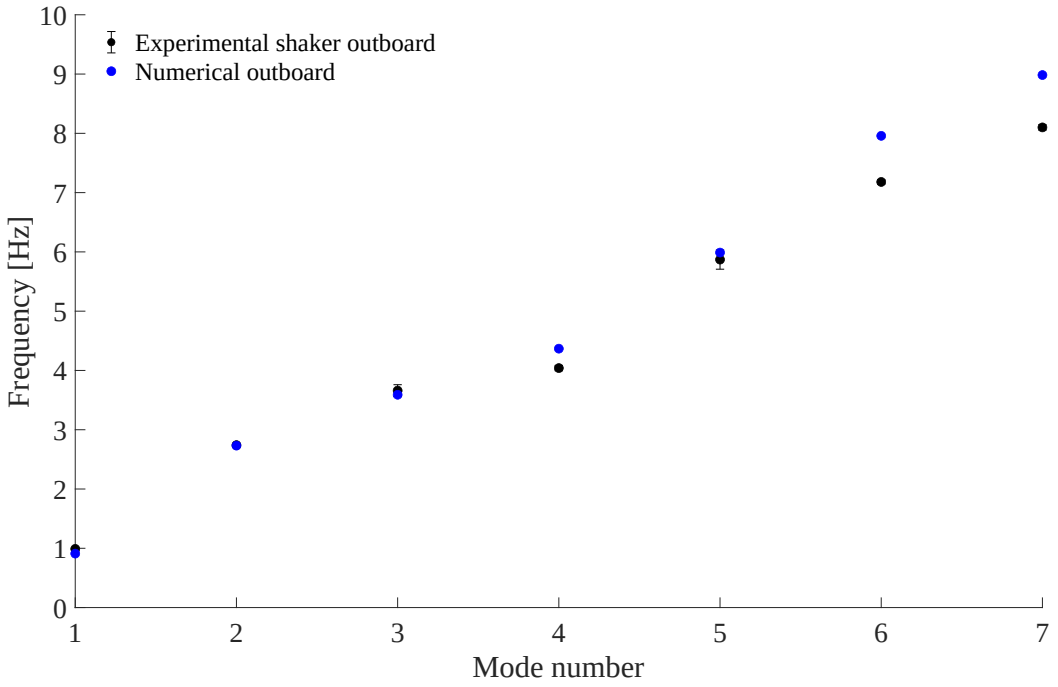

Figure 6.20: Comparison of the first 7 modes from the shaker GVT vs. the initial FEM for the outboard configuration.

frequencies of very flexible structures. So far, to generate the modal information about multiple deformed shapes, multiple corresponding load cases causing large deformations on the structure were used. During GVT of the X-HALE (Section 6.2) or the very flexible beam presented in Chapter 3, the deformed shape for the structure was achieved by changing the location of the suspension. In both cases, the gravitational loading (self-weight) for the very flexible structures causes the deformation. However, the placement of the suspension (i.e., boundary conditions applied to the structure) affect the loading and therefore the deformed shape.

In the FEM updating process demonstrated and verified in Chapter 4, the deformed shapes were obtained purely from changing the inertial loads acting on the structure and not by adjusting the suspension location (or boundary conditions). Moving the point of suspension affects the shape as well as the modal parameters in a similar manner as the loads being applied to the very flexible test cases. The FEM updating process needs to be augmented to handle multiple deformed configurations simultaneously resulting from different boundary conditions (as opposed to the deformations coming from a load factor applied to the gravitational loading). The optimization framework developed as part of this thesis will be used to update the FEM of the X-HALE as it undergoes large deformations under gravitational loading, as a result of the different boundary conditions applied during suspension.

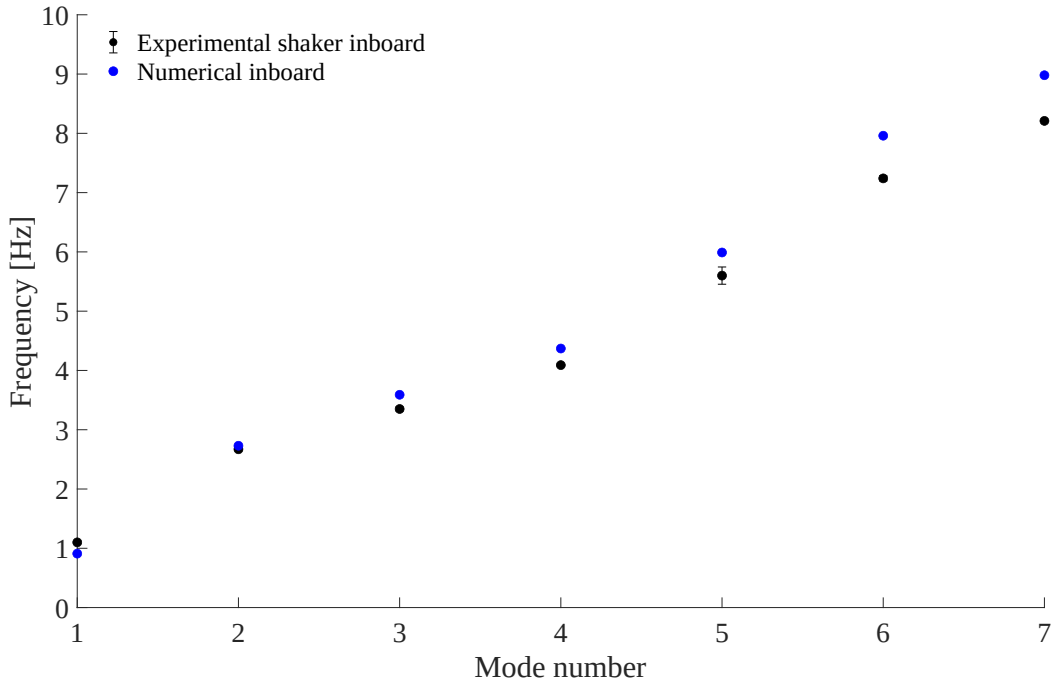

Figure 6.21: Comparison of the first 7 modes from the shaker GVT vs. the initial FEM for the inboard configuration.

6.3.1 Problem Setup

The FEM updating process presented in Chapters 2 and 4 and shown schematically in Fig. 2.7 was used to set up the FEM updating problem for the X-HALE. The GVT training data used came from the impact GVT conducted on the airframe in the outboard and the inboard configurations. The input file provided to Nastran's SOL400 to run the subcases corresponding to different configurations required creating a set up where for one subcase, the set of boundary conditions pertaining to the outboard configuration would be active. For the other subcase, the set of boundary conditions pertaining to the inboard configuration would be active. Changing boundary conditions between subcases of SOL400 is not challenging (just requires calling the constraint condition specifying the set of nodes and DOFs to be constrained). However, changing the location of the grid points that the springs connect to for the subsequent deformed modal analysis in the presence of the suspension required creating a multi-point constraint equation (MPC) that changed the "active" spring based on the desired configuration. The steps to achieve this switching are shown below:

1. Create a boundary condition pertaining to each of the configurations.

2. Create a grid point coincident to the existing set of grid points to which the springs would connect to for each configuration.

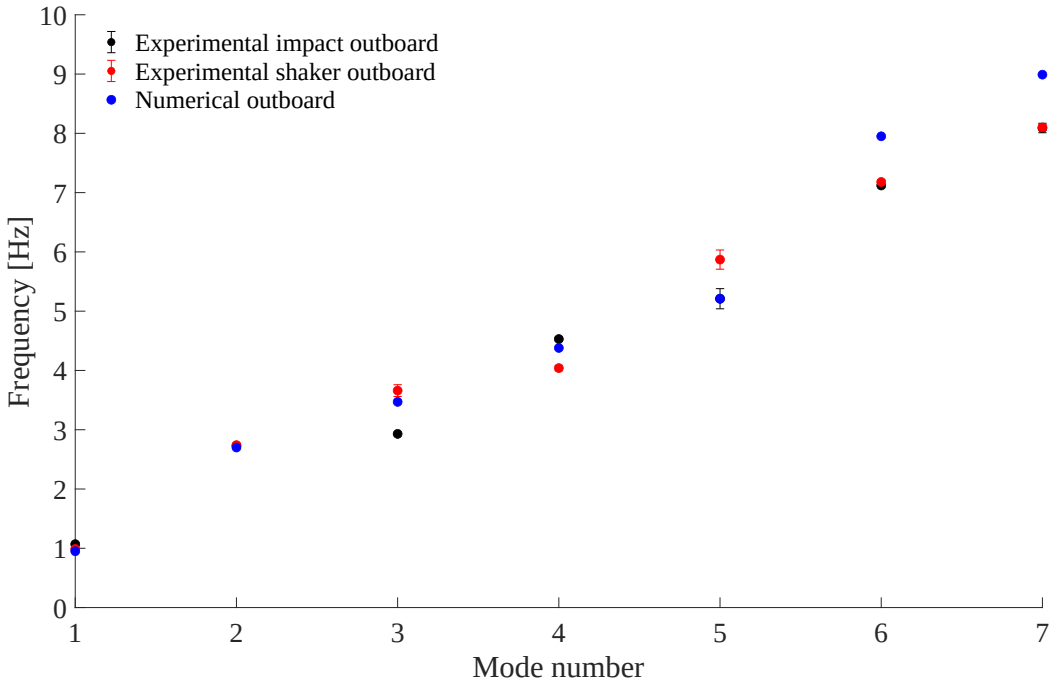

Figure 6.22: Comparison of the first 7 modes from the shaker and impact hammer GVT vs. the initial FEM for the outboard configuration.

3. Create a multi-point constraint equation of the form $\sum_j A_j u_j = 0$ where A_j represents the coefficient or scaling factor for u_j, which represents the DOF C_j at grid point. The index j represents the number of grid points in the MPC. This MPC will connect the grid point defined in the step above to the structural grid point.

4. Based on which configuration is active (i.e., the subcase within the single input file), the constrained boundary condition(s) will be called to obtain the nonlinear statically deformed condition.

5. Based on which configuration is active, the relevant MPC will be called in the deformed modal analysis after the nonlinear static analysis.

6. This allows switching the configuration, and therefore, changing the boundary conditions and spring connection point(s) within the same input file that is used by the optimizer to run and work with all the deformed conditions simultaneously.

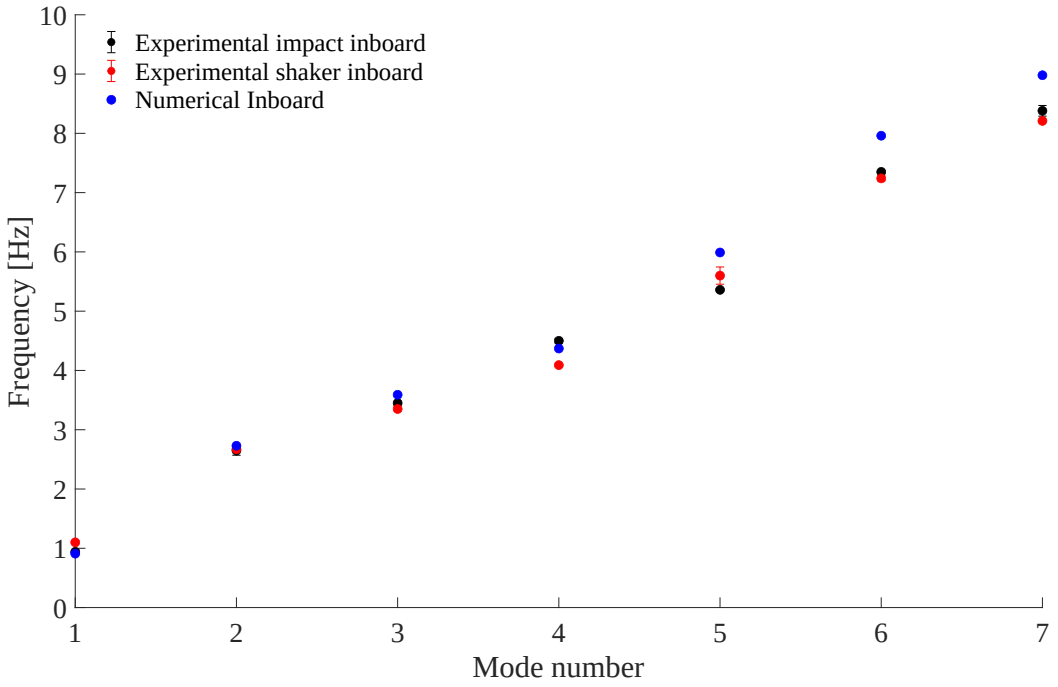

Figure 6.23: Comparison of the first 7 modes from the shaker and impact hammer GVT vs. the initial FEM for the inboard configuration.

6.3.2 Design Variables

Material properties of the different wings and joiners (the pieces that connect two wings) were chosen as the design variables for the X-HALE. Originally, the material properties were defined as constant along the entire structure for all the wings and joiners, but that is not representative of the actual construction. Different wing segments were constructed at different times and have been used differently (i.e., damaged wings have been repaired or replaced after flight tests). This leads to the wings having noticeable differences between their sitffnesses - including differing tension on the skin. The joiners currently on the airframe were not manufactured in the same batch and have different wall thicknesses, this causes their stiffness to be variable between wing junctions. No attempt was made to individually characterize each component, rather this was handled by allowing larger bounds on the design variables pertaining to these components.

This will allow for identifying and fine tuning the differences between the different segments as well as the nonlinearities that come from the junction or the segment interfaces (some of the components are glued together and represent an imperfect contact patch, while some other have Aluminum brackets connecting different components and are fastened by hand). Inequality constraints are imposed on the total mass, inertia and center of gravity properties. The design variables had variable bounds placed on them based on the level of uncertainty on their original values. The

mass or density related design variables have the tightest bounds since the mass of individual components and the entire structure can be measured. The bounds on the wings and joiner related design variables were larger since the age, connection imperfectness and manufacturing tolerances create both nonlinearities and uncertainties. The design variables related to wing and tail connections were the most relaxed since those material properties are the least certain. The constraint variables had upper and lower limits set within $\pm 10\%$ of their original values.

The design variables chosen for the optimization problem are shown in Table 6.7, along with their values before and after the updating process. Here, WR1 refers to the first wing to right of the center of the X-HALE, while WL1 refers to the first wing to the left. Similarly WR2 and WL2 refer to the second wings to the right and left of the center respectively. The joiners are machined pieces milled out of Aluminum stock that connect two wings to each other, and their naming reflects the two wings they connect to. The tail boom is the relatively rigid rod that connects the pitch elevators to the wings. The Wing-Tail spring refers to the spring that is used to model the connection between the tail boom and the wing. On the X-HALE, the wing-tail connection is accomplished by sliding the tail boom onto a tail boom connector. This connector is fastened to the pods attached at each wing junction. The tail boom is not screwed in, but after sliding on to the connector, is held into place by using metal tape to wrap around the end of the boom and the adapter installed on the wing. This connection presents a large uncertainty (or bounds in an optimization problem) during the FEM creation and updating process.

6.3.3 Results and Discussion

The resonance modes that are identified most clearly in the GVT are the first seven structural modes of the X-HALE. These are the first five out-of-plane bending modes and the first two torsion-in-plane coupled modes. These modes were used in the FEM updating process and the outcome of the update is presented and discussed here. The rigid body plunge mode coming from the spring-based suspension set up in the laboratory was identified using the DC accelerometer. Interestingly, the triaxial ICP accelerometers also resolved the sub 0.5 Hz plunge mode, but the noise levels were of the same order as the accelerations read by the accelerometers. This highlighted the value of the DC accelerometer in such a GVT, and a discussion of the data recording and comparison between DC accelerometers and conventional ICP accelerometers is provided in Section 6.4.1.

From the design variables presented in Table 6.7, it can be observed that the updated FEM has different values of stiffnesses for the different wing sections and joiners. This is expected because there is no uniformity in the wings and/or joiners in the as-built structure. The uncertainties in the actual structure are reflected in the spread of material properties in the updated FEM. The natural frequencies of the X-HALE before and after updating the FEM, and compared to the

Table 6.7: Design variables for the FEM update of the X-HALE using laboratory GVT results.

DV Type	Component	Normalized bounds	Initial DV	Final DV	Units	Difference (vs. initial) %
Young's Modulus	WR3	0.75, 1.25	4.32	5.02	GPa	16.3
Young's Modulus	WR2	0.75, 1.25	4.32	3.57	GPa	17.4
Young's Modulus	WR1	0.75, 1.25	4.32	4.51	GPa	4.5
Young's Modulus	WL1	0.75, 1.25	4.32	4.94	GPa	14.5
Young's Modulus	WL2	0.75, 1.25	4.32	3.78	GPa	12.5
Young's Modulus	WL3	0.75, 1.25	4.32	3.28	GPa	24.0
Young's Modulus	WL1-WR1 joiner	0.75, 1.25	4.32	4.64	GPa	7.5
Young's Modulus	WR1-WR2 joiner	0.75, 1.25	4.32	4.33	GPa	0.4
Young's Modulus	WL1-WL2 joiner	0.75, 1.25	4.32	4.41	GPa	2.1
Young's Modulus	WR2-WR3 joiner	0.75, 1.25	4.32	4.06	GPa	5.9
Young's Modulus	WL2-WL3 joiner	0.75, 1.25	4.32	4.17	GPa	3.4
Young's Modulus	Tail Boom	0.75, 1.25	5.00	4.99	GPa	0.3
Shear Modulus	WR3	0.75, 1.25	1.71	1.69	GPa	1.1
Shear Modulus	WR2	0.75, 1.25	1.71	1.70	GPa	0.5
Shear Modulus	WR1	0.75, 1.25	1.71	1.75	GPa	2.1
Shear Modulus	WL1	0.75, 1.25	1.71	1.67	GPa	2.1
Shear Modulus	WL2	0.75, 1.25	1.71	1.71	GPa	0.3
Shear Modulus	WL3	0.75, 1.25	1.71	1.79	GPa	4.8
Shear Modulus	WL1-WR1 joiner	0.75, 1.25	1.71	1.72	GPa	0.8
Shear Modulus	WR1-WR2 joiner	0.75, 1.25	1.71	1.76	GPa	2.7
Shear Modulus	WL1-WL2 joiner	0.75, 1.25	1.71	1.77	GPa	3.7
Shear Modulus	WR2-WR3 joiner	0.75, 1.25	1.71	1.78	GPa	3.8
Shear Modulus	WL2-WL3 joiner	0.75, 1.25	1.71	1.77	GPa	3.6
Shear Modulus	Tail Boom	0.75, 1.25	1.88	1.98	GPa	5.3
K_x	Wing-Tail spring	0.5, 2.0	1.0×10^8	1.10×10^8	$\frac{\text{N}}{\text{m}}$	10.3
K_y	Wing-Tail spring	0.5, 2.0	1.0×10^8	1.12×10^8	$\frac{\text{N}}{\text{m}}$	11.8
K_z	Wing-Tail spring	0.5, 2.0	1.0×10^8	1.13×10^8	$\frac{\text{N}}{\text{m}}$	13.1
M_x	Wing-Tail spring	0.5, 2.0	1.0×10^8	1.09×10^8	$\frac{\text{Nm}}{\text{rad}}$	9.4
M_y	Wing-Tail spring	0.5, 2.0	1.0×10^8	1.02×10^8	$\frac{\text{Nm}}{\text{rad}}$	2.0
M_z	Wing-Tail spring	0.5, 2.0	1.0×10^8	1.09×10^8	$\frac{\text{Nm}}{\text{rad}}$	8.9

GVT conducted in the laboratory are provided in Tables 6.8 and 6.9 for the outboard and inboard configurations respectively. As noted above, the FEM updating was conducted considering both the configurations simultaneously. The errors between both inboard and outboard configurations compared to the experimental GVT data are highlighted in Fig. 6.24, indicating that the first seven computational elastic modes match the experimental under 2% error.

Another interesting takeaway is that like the numerical-only verification performed in Chapter 4, the different configurations (inboard or outboard) yield different reductions in percent errors. The in-plane bending and torsional modes show the largest difference between the two configurations, while the out-of-plane bending modes remain similar between the differently deformed configurations. Figure 6.25 shows the reduction in error between the initial and final FEM for both the configurations.

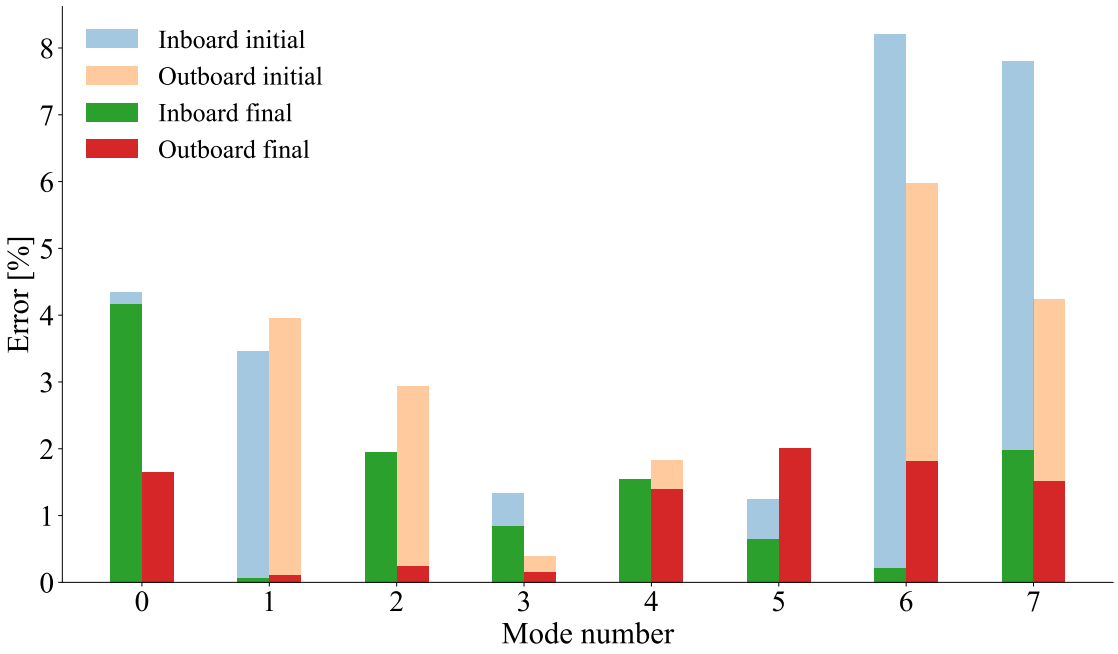

Figure 6.24: Percent error after updating using GVT results compared to the initial FEM of the X-HALE for the inboard and outboard configurations. Mode 0 is the plunge mode related to the suspension.

Table 6.8: Results of FEM updating for the X-HALE: outboard configuration.

		Laboratory GVT	**Initial FEM**		**Updated FEM**	
Mode #	**Mode type**	**Frequency (Hz)**	**Frequency (Hz)**	**Difference (vs. GVT) %**	**Frequency (Hz)**	**Difference (vs. GVT) %**
0	Plunge	0.28	0.27	−4.3	0.27	−4.2
1	1 OOP	0.99	0.96	−3.5	0.99	0.1
2	2 OOP	2.74	2.76	0.6	2.69	−1.9
3	1 T/2 IP	4.24	4.30	1.3	4.28	0.8
4	3 OOP	4.53	4.60	1.5	4.46	−1.5
5	2 T/3 IP	6.23	6.15	−1.2	6.27	0.7
6	4 OOP	7.18	7.77	8.2	7.20	0.2
7	5 OOP	8.10	8.73	7.8	8.26	2.0

Table 6.9: Results of FEM updating for the X-HALE: inboard configuration.

		Laboratory GVT	**Initial FEM**		**Updated FEM**	
Mode #	**Mode type**	**Frequency (Hz)**	**Frequency (Hz)**	**Difference (vs. GVT) %**	**Frequency (Hz)**	**Difference (vs. GVT) %**
0	Plunge	0.28	0.28	−1.7	0.28	−1.7
1	1 OOP	0.95	0.91	−4.0	0.95	−0.1
2	2 OOP	2.70	2.78	2.9	2.71	0.2
3	1 T/2 IP	4.75	4.77	0.4	4.76	0.1
4	3 OOP	4.50	4.58	1.8	4.44	−1.4
5	2 T/3 IP	6.90	7.03	1.8	7.04	2.0
6	4 OOP	7.35	7.79	6.0	7.22	−1.8
7	5 OOP	8.38	8.74	4.2	8.26	−1.5

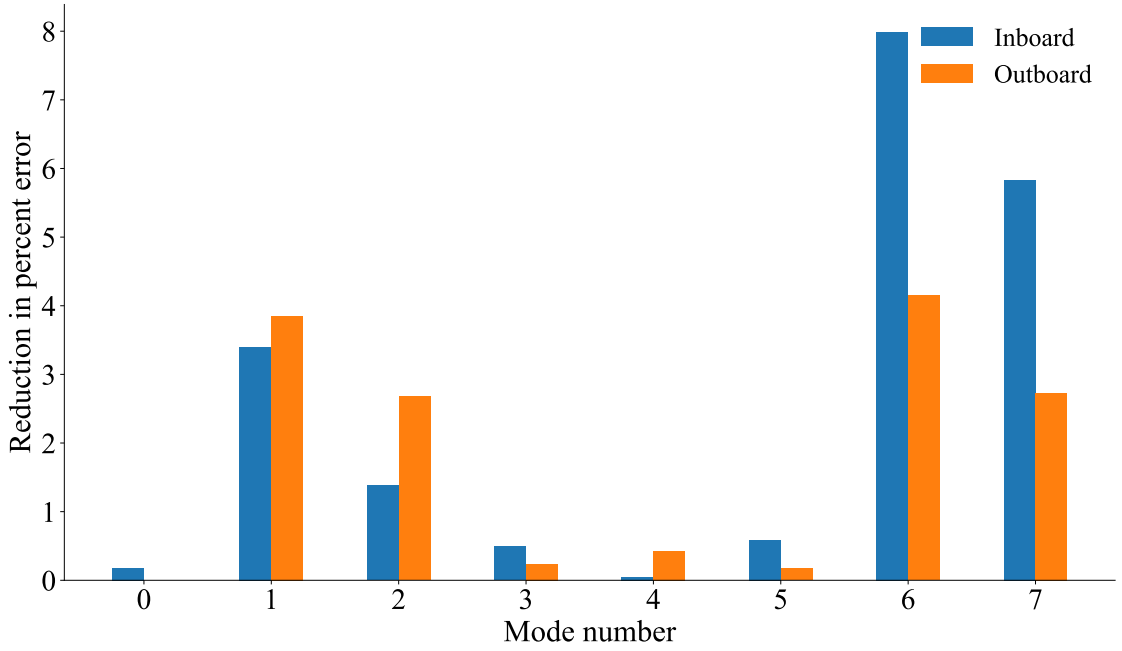

Figure 6.25: Reduction in percent error after updating using GVT results compared to the initial FEM of the X-HALE for the inboard and outboard configurations.

6.4 Free-free GVT on the X-HALE

As part of characterizing the very flexible structure and validating the methodologies both for conducting GVT and updating its FEM, an experiment was designed to conduct a free-free GVT on the X-HALE. The objective is to identify true free-free modal parameters of the VFA by eliminating the effect of the support. However, it is impossible to conduct a true free-free GVT because the presence of a support influences the test article. The updated objective is to create an experiment that can get as close as possible to the one order of magnitude separation between the suspension related modes and the fundamental elastic mode of the structure. This presents two challenges which are addressed in this section.

1. Challenges related to the measurement of very low frequencies. These frequencies come both from the test structure as well as the suspension itself.

2. Challenges related to the suspension, i.e., obtaining a soft enough suspension to minimize interaction between the suspension modes and the aircraft's elastic modes.

6.4.1 Measurement of Very Low Frequencies

In order to capture low-frequency vibrations, identifying and obtaining a sensor capable of measuring vibrations lower than 1 Hz was required. DC accelerometers are DC-coupled, and can respond

down to zero Hertz. They therefore can be used to measure static, as well as dynamic acceleration. Tests were conducted to ensure the data acquisition system used for the GVT can interface with (provide power and appropriate conditioning) and read data from the DC accelerometers. Regular ICP (integrated circuit piezoelectric) uniaxial and triaxial accelerometers were used for comparison. These ICP accelerometers are typically used for shock and vibration testing, and are the standard accelerometers used for GVT in industry. The accelerometers were assembled on the shaker base and tested at different excitation frequencies ranging from 10 to 0.5 Hz. The time and frequency responses of the accelerometers were recorded and used to evaluate the ability of the ICP and DC accelerometers to measure very low frequencies coming from a real world excitation. Figure 6.26 shows the various accelerometers connected to the shaker base for testing.

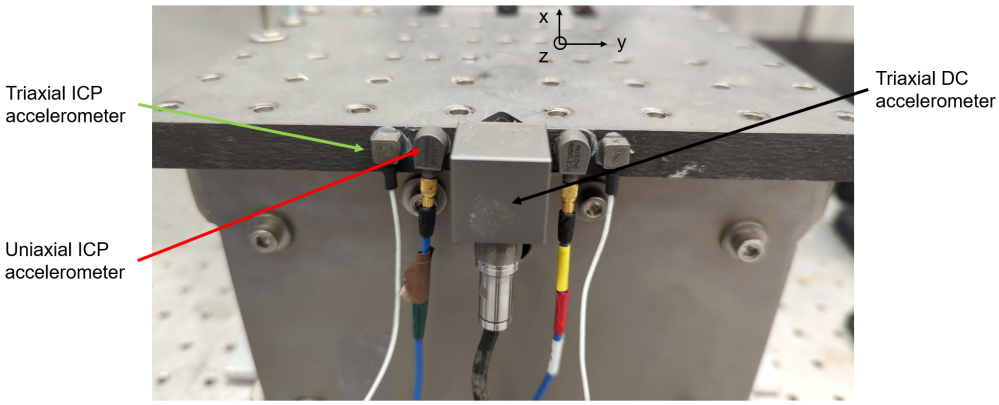

Figure 6.26: Set up of various accelerometers to measure very low frequency vibrations.

After connecting the DC and ICP accelerometers to the DAQ and ensuring the system could interface with all accelerometers properly, it was observed that for frequencies below 5 Hz, the DC accelerometer recorded a cleaner response than the regular vibration accelerometers. Figures 6.27, 6.28 and 6.29 show the plots of the time and frequency domain responses from the accelerometers at 10, 1 and 0.5 Hz respectively.

The key takeaways from the tests conducted to measure vibrations of very low frequencies are:

- Both accelerometers indicate the same acceleration amplitudes for the same signal (within sensor bandwidth).
- The DC accelerometer detects the system dynamics at low frequencies better than a regular accelerometer.
- The DC accelerometer can detect frequencies lower than can be excited with the shaker during GVT.

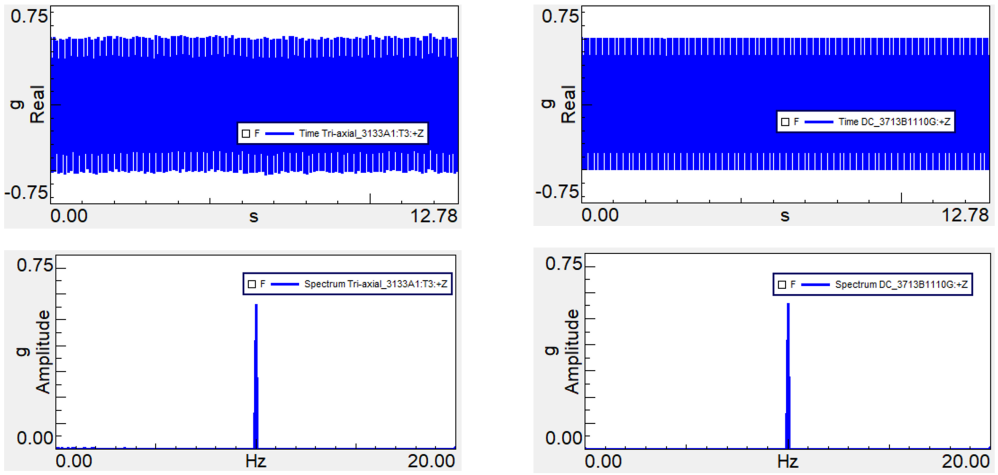

Figure 6.27: Comparison of the time (top) and frequency (bottom) domain responses for the ICP (left) and DC (right) accelerometers at 10 Hz.

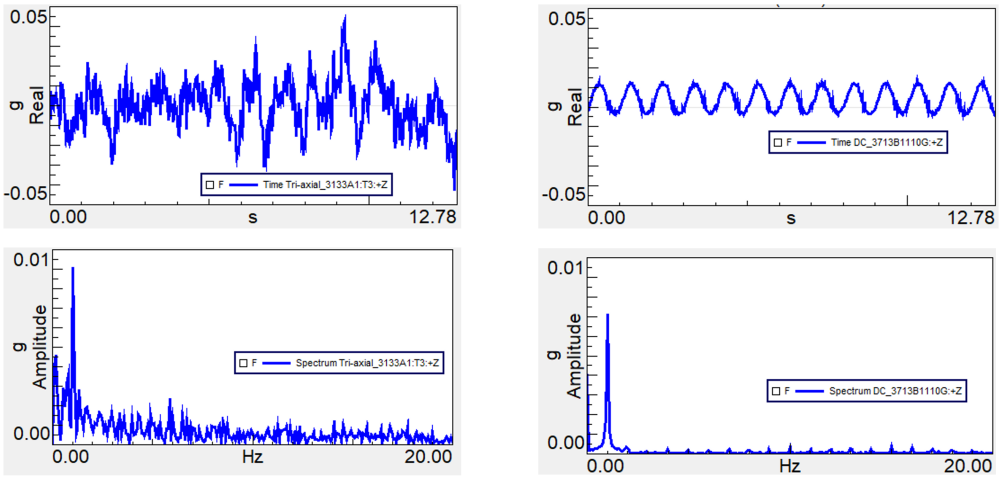

Figure 6.28: Comparison of the time (top) and frequency (bottom) domain responses for the ICP (left) and DC (right) accelerometers at 1 Hz.

- The accelerometers are picking up nonlinearities (harmonics) – this can be adjusted by lowering the amplitude of excitation, but is not the subject of interest here.

The tests conducted with the DC accelerometer indicate that they are successfully able to capture the low frequencies expected from the GVT. This will enable identifying the rigid-body plunge and roll modes of the X-HALE that will be of non-zero frequency because of the presence of the suspension system. The remaining challenge of creating a sufficient separation between the suspension related modes and the aircraft's elastic modes is discussed in Section 6.4.2.

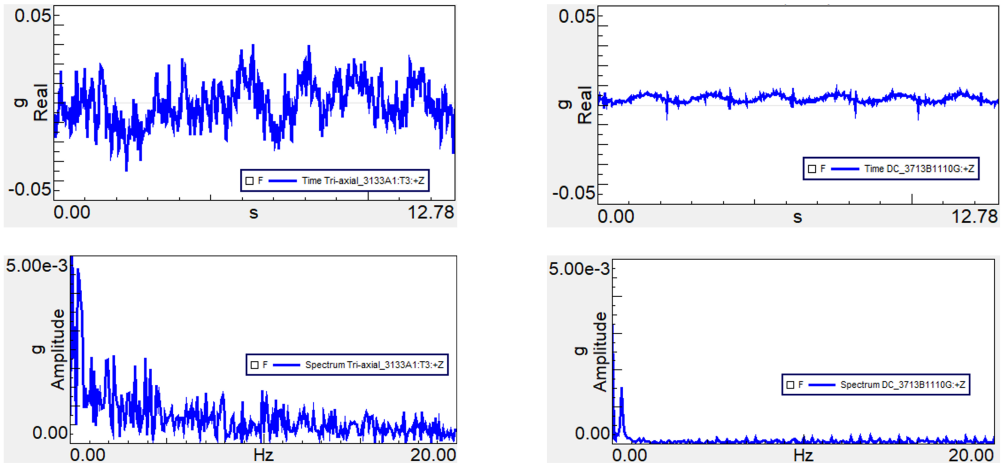

Figure 6.29: Comparison of the time (top) and frequency (bottom) domain responses for the ICP (left) and DC (right) accelerometers at 0.5 Hz.

6.4.2 Soft Suspension for Free-Free GVT

In order to minimize the influence of the support, the aircraft should be connected to a suspension system that offers an order of magnitude of separation between the suspension related rigid body modes and the structural modes associated with the aircraft. To accomplish this separation, a suspension setup made of long, low-stiffness bungee cords that would sustain the weight of the aircraft and remain in the linear region of deformation was designed.

A 1 m long segment of the spool of the bungee cord was tested under various loads to obtain a relation between for the equivalent stiffness per unit length of the bungee cord. The mathematical relation used to create the equivalent stiffness per unit length is shown below.

$$
\begin{aligned}
&\sigma = E\epsilon \\
&\sigma = \frac{F}{A} \\
&E\epsilon = \frac{F}{A} \implies F = EA\epsilon = EA\frac{\Delta l}{l} \\
&F = (\frac{EA}{l})\Delta l
\end{aligned} \tag{6.1}
$$

Since the bungee cord can be considered as an equivalent spring where the load-extension relation $F = kx$ applies in the linear region (where k is the spring constant), the term $\frac{EA}{l}$ in Eq. 6.1 is an analogous expression to the spring constant. For a 1 m long bungee cord, it would just be EA. The stiffness constant of the bungee cord varies inversely with its initial length. The equivalent bungee cord stiffness per unit length was verified by testing cords with varying initial lengths and

identifying the slope of the load vs. extension curves. Based on the stiffness tests, for the bungee cord, a prediction can be obtained for the plunge frequency as a percentage of the fundamental free-free elastic mode of the X-HALE. A sample of this is shown in Table 6.10.

Table 6.10: Bungee cord assessment and prediction.

Initial length [m]	Stiffness [N/m]	Plunge frequency [Hz]	Extension under ½ X-HALE [m]	Total extension [m]	Fundamental elastic mode [Hz]	Difference from true free-free 1st mode [%]	Plunge freq. as a % of fundamental free elastic mode
0	0	-	-	-	0.921	-	-
10	9.03	0.2	1.79	10.79	0.938	1.85	21.7
20	4.51	0.14	4.32	24.32	0.929	0.87	15.2
30	3.01	0.12	7.59	37.59	0.927	0.65	13.0

In order to keep the total height of the facility where the bungee cord would be deployed within reasonable limits, it was decided that a bungee cord of approximately 20 m would provide a sufficient separation between the suspension related plunge resonance mode and the fundamental elastic mode of the X-HALE. As can be observed from Table 6.10, there are diminishing returns to increasing the bungee length. The increase in the separation between the suspension mode and the aircraft's elastic mode does not justify the exponential increase in both the initial bungee length and the displacement under loading. Two bungee spools of 75 ft each (22.86 m) were acquired and set up to be used with the X-HALE, with each side of the aircraft connected to one bungee cord. Even though these spools were the same part and manufactured by the same company, upon testing, it was observed that their stiffness per unit length were quite different. These differences and predicted total lengths at the desired initial length are shown in Table 6.11, while a plot of the bungees' initial lengths versus cumulative extensions under the mass of the X-HALE is provided in Fig. 6.30. It can be observed that the plotted cumulative extensions under the load are slightly nonlinear. This is because the mass of the bungee cord is considered in the predictions - as the initial length of the bungee cord increases, the load increases slightly because of the mass of the cord. Bungee cords may have non-uniform stiffness along their lengths, and exhibit some change in stiffness as they are used (repeated cycles of stretching). In order to account for these concerns, there needs to be a mechanism to align their stretched lengths to have the X-HALE under 1 g (self-weight) in the outboard/inboard configuration. This is required to prevent the airframe from being lopsided once connected to the bungee cords (i.e., the vertical lengths of the bungee cords need to align).

A prediction for the true free-free natural frequencies of the X-HALE after FEM updating is provided in Table 6.12. Predictions are provided for both the "no spring" case, as well as the very soft bungee cord suspension used to approximate the free-free set up. The largest difference between case with no spring and the case with the very soft bungee cords is for the first elastic mode. It should also be noted that the plunge mode with this set up is predicted to be between 0.13

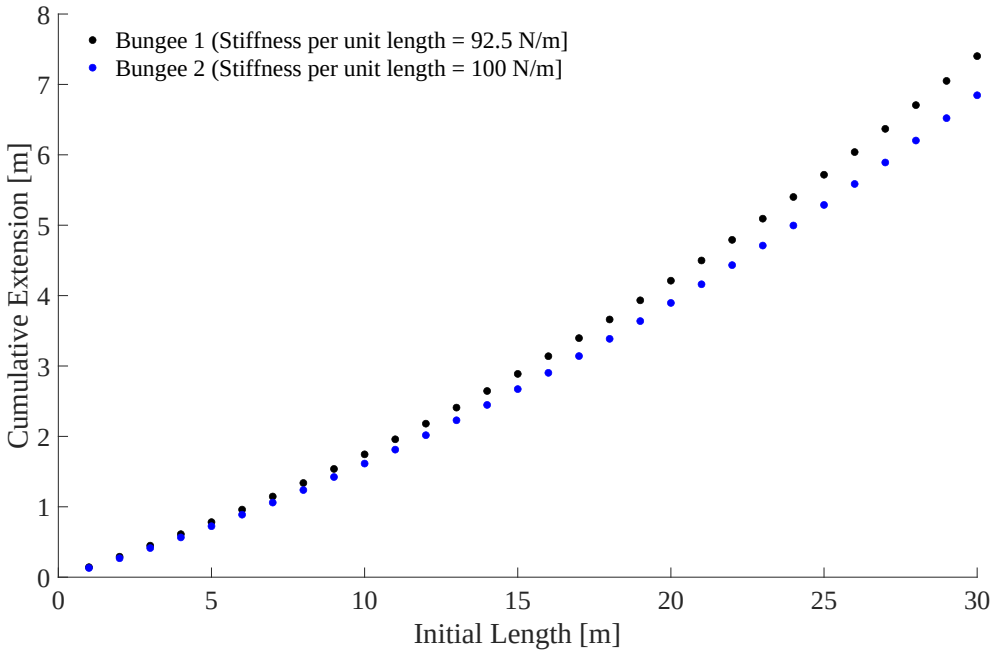

Figure 6.30: The two bungee cords' initial lengths versus predicted extensions under the mass of the X-HALE.

Table 6.11: Differences between, and predictions for the X-HALE bungee cords.

Bungee ID	**Initial length [m]**	**Stiffness per unit length [N/m]**	**Predicted plunge frequency [Hz]**	**Predicted extension under X-HALE [m]**	**Predicted total length under X-HALE [m]**
Bungee 1	20	92.5	0.129	4.2	24.2
Bungee 2	20	100	0.134	3.9	23.9
Bungee 1	23	92.5	0.119	5.1	28.1
Bungee 2	23	100	0.123	4.7	27.7

and 0.14 Hz for the outboard and inboard configurations respectively. This means that the plunge frequency is around 14 % of the fundamental free-free elastic mode (first out-of-plane bending).

6.4.3 Test Setup

The X-HALE was suspended from a crane bucket which was elevated to around 100 ft. The crane bucket was connected to the airframe using two bungee cords. A winching mechanism was used to attach one end of the bungee cord and allow cranking the winch to adjust the length (or height) of the bungee cord as needed. A pulley was used with a Kevlar string to turn directions such that the operator can easily access the cranking mechanism and adjust the height of each bungee individually. The layout of the crane, X-HALE and bungee cords to create the soft suspension

Table 6.12: Predicted natural frequencies for the free-free GVT after updating the FEM.

		Frequency (Hz)				Difference (%)	
		No springs		Free-free bungee		Bungee vs. No springs	
Mode #	**Mode type**	**Inboard**	**Outboard**	**Inboard**	**Outboard**	**Inboard**	**Outboard**
0	Plunge	–	–	0.14	0.13	–	–
0	Roll	–	–	0.15	0.27	–	–
1	1 OOP	0.94	0.96	0.94	0.96	−0.2	−0.8
2	2 OOP	2.68	2.69	2.68	2.69	−0.3	0.0
3	1 T/2 IP	4.76	4.28	4.76	4.28	0.0	0.0
4	3 OOP	4.43	4.46	4.43	4.46	0.0	0.0
5	2 T/3 IP	7.04	6.27	7.04	6.27	0.0	0.0
6	4 OOP	7.21	7.19	7.21	7.19	0.0	0.0
7	5 OOP	8.25	8.26	8.25	8.26	0.0	0.0

to approximate the free-flying conditions is shown in Fig. 6.32, while the actual crane with the X-HALE suspended from it is shown in Fig. 6.33. A schematic with the components used in the set up is shown in Fig. 6.31.

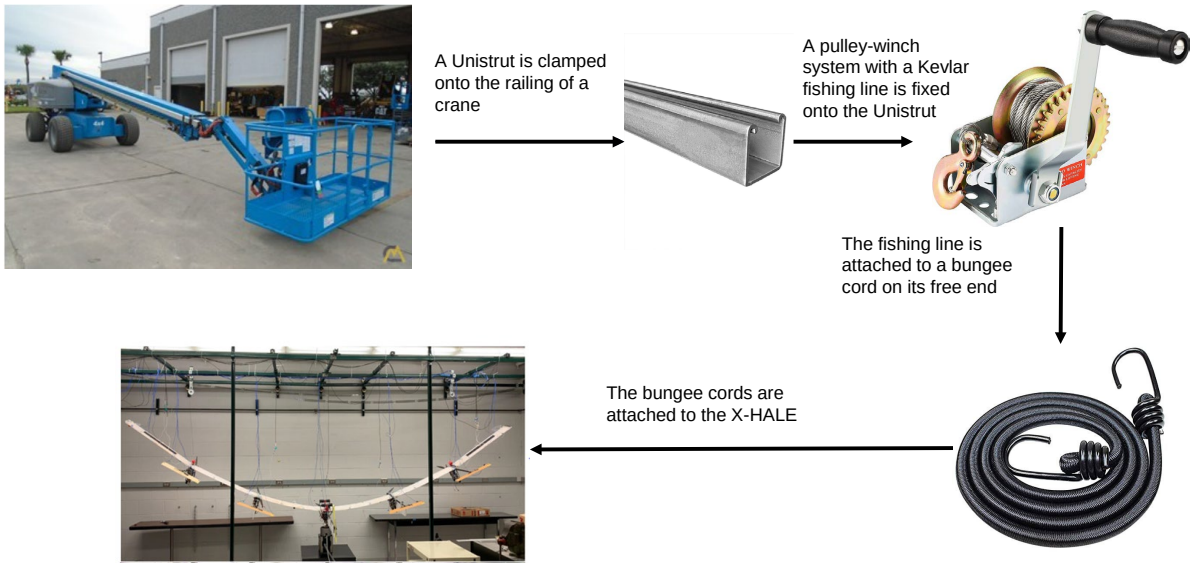

Figure 6.31: Components used in the X-HALE free-free GVT.

The Unistrut and pulley arrangements attached to the crane were set up in a way that allowed changing the location of the bungee connections on the X-HALE, by adjusting which pulley the bungee cords dropped down from. This way, the inboard and outboard configurations could easily

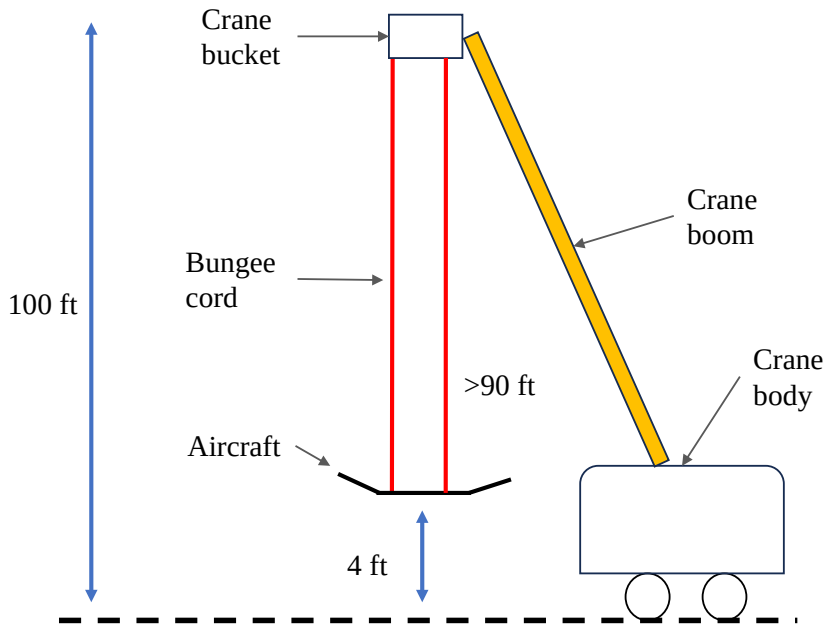

Figure 6.32: Schematic of the aircraft, bungee and crane set up to perform free-free GVT.

be swapped out, by adjusting the pulley location on the crane side, and changing the adapter position the bungee cords connect to, on the aircraft side. The X-HALE suspended from the bungee cords in the outboard configuration during the free-free GVT is shown in Fig. 6.34.

The goal was to conduct multiple rounds of tests in both configurations – both for statistical averaging data (and to have additional data in case of connection stiffness related nonlinearities), as well as collect data in both configurations as the bungee cord gets stretched and used over the course of the experiment. The initial concern of the bungee cord not having uniform stiffness along their lengths and exhibiting change in their stiffness as they are used could then by accounted for by conducting these multiple configuration swaps over time, as the bungee cord gets used. The accelerometer layout for these tests included two DC accelerometers located 1.5 m away from the center of the X-HALE to measure the plunge and roll frequencies, expected to be < 0.5 Hz for both configurations. Triaxial ICP accelerometers were installed along the quarter-chord of the wing to measure in-plane and out-of-plane bending motion, and uniaxial accelerometers were installed at multiple stations along the span. Each uniaxial station consisted of one accelerometer at the leading and trailing edges of the wing, to capture both bending and torsional motions. The accelerometer layout used for the free-free GVT on the X-HALE is shown in Fig. 6.35.

A ground station was set up on the field for data acquisition and as the center point for all the accelerometers and instrumentation cabling to connect to. Since it was not possible to bring a shaker out to the field where the GVT was being conducted (due to the high voltage and power

Figure 6.33: The crane with the X-HALE suspended from it during the free-free GVT.

requirements on the shaker and amplifier, along with the requirement to create a stable mount to bolt the shaker to the ground), only impact tests were conducted on the X-HALE during the free-free GVT. The laboratory GVT performed prior and described in Section 6.2 indicated that impact tests provided sufficient energy to excite the modes of interest on the X-HALE. An overview of the ground station as seen from the crane is shown in Fig. 6.36.

6.4.4 Results of the Free-Free GVT

In order to test the plunge frequency of the bungee cords with a rigid mass representative of the X-HALE (or half of the aircraft per bungee cord), a block mass was connected to the bungee cord and tested. This was done by pulling down the mass and timing the oscillations using two separate timers (operated by two people). This mass was created by using a set of adjustable dumbbells and the independent bungee excitation with this mass is shown in Fig. 6.37. In order to identify if the bungee exhibited a varying stiffness with use and being stretched, these tests were conducted multiple times over the course of the free-free GVT. Table 6.13 shows the plunge mode identified

Figure 6.34: The X-HALE suspended in the outboard configuration during the free-free GVT, connected to the bungee cords dropped from the crane.

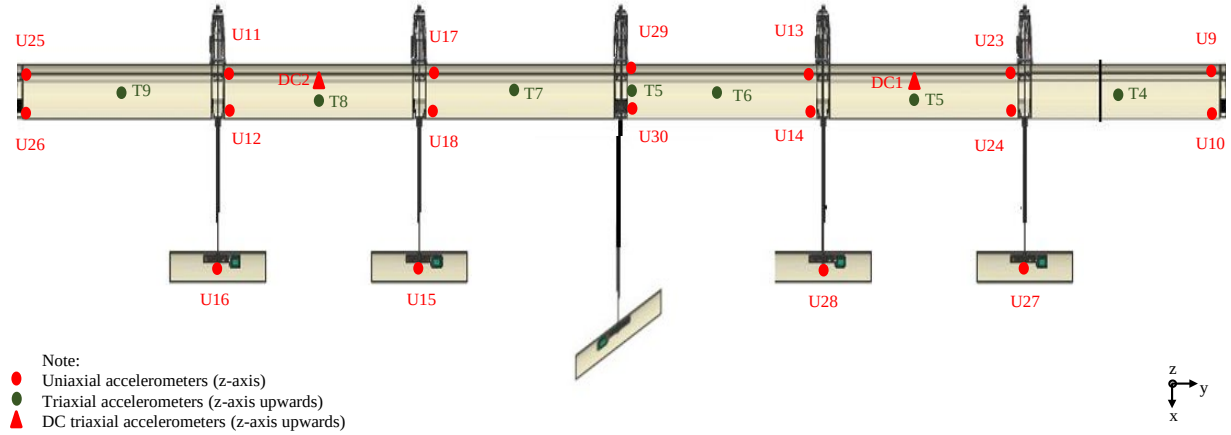

Figure 6.35: Accelerometer layout for the free-free GVT on the X-HALE.

from the different bungees over the course of the test. The tests were done at each configuration change, so some of the entries are dashes, meant to represent the lack of that configuration's plunge mode being tested at that time. A similar test was done when the aircraft was suspended in both inboard and outboard configurations to measure its rigid body modes. The rigid body modes of the aircraft were tested at each configuration swap as well. The modes are the result of the bungee stiffnesses interacting with the mass/inertia of the aircraft. It is desirable to have the effect well separated from the first elastic mode — ideally the rigid body modes converge to zero Hz, but

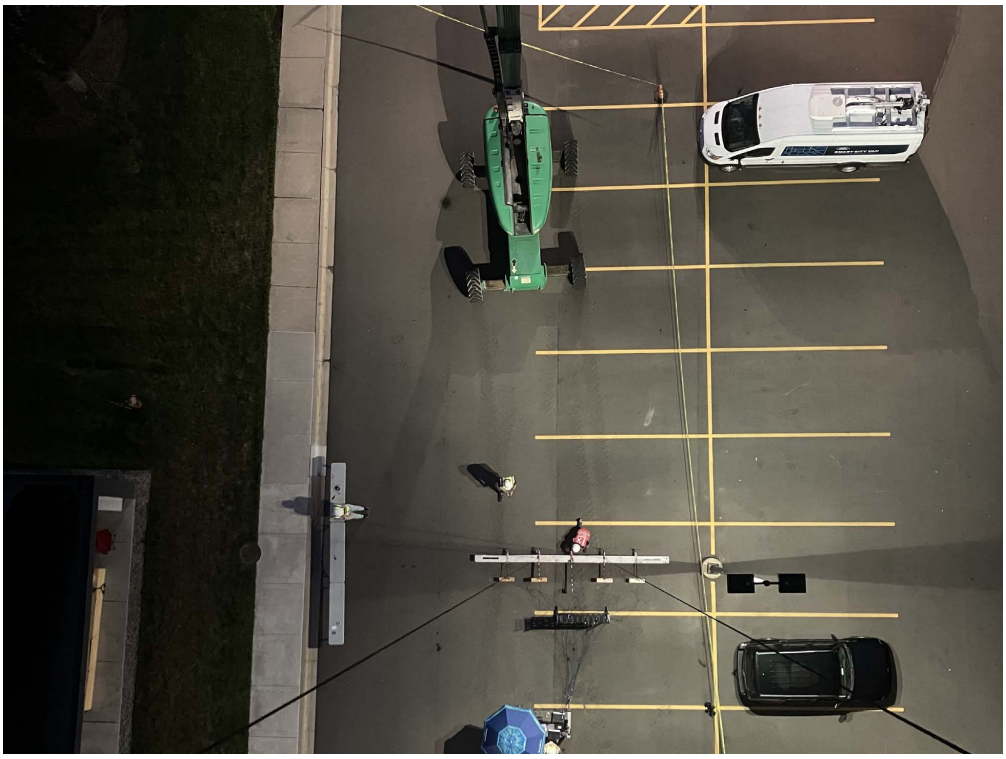

Figure 6.36: The X-HALE during the free-free GVT, as viewed from the crane.

the fact that the suspension has a non-zero stiffness prevents that from being realized. Table 6.14 shows the plunge and roll modes of the aircraft with the bungee suspension. An observation that was made at this point was that the bungees were significantly stiffer than the initial prediction shown in Table 6.12, while being more uniform or consistent between each other. The increased uniformity comes from the fact that the bungees were characterized in the laboratory by unspooling a small segment of each of them and testing their stiffness. The full-length bungees are close to each other, but random segments of the bungee cords might exhibit different stiffnesses.

Table 6.13: Plunge frequencies with the block mass representing $\frac{1}{2}$ the X-HALE mass. Frequencies measured at various points during the free-free GVT to check if, and how the bungee stiffnesses change over the course of the GVT.

	Plunge frequencies in Hz		
Bungee location	**Beginning**	**Middle**	**End**
Inboard right	0.18	–	0.17
Inboard left	0.18	–	0.18
Outboard right	–	0.17	–
Outboard left	–	0.17	–

Figure 6.37: The calibrated mass (dumbbell suspended from bungee cord, middle of the image) used to measure the bungee plunge frequency.

Table 6.14: Rigid body modes of the X-HALE realized because of the interaction of the bungee stiffness with the aircraft's mass/inertia. Frequencies in Hz measured at various points during the free-free GVT to check how the bungee stiffnesses change over the course of the GVT.

Bungee location	**Beginning**	**Middle**	**End**
Inboard plunge	0.21	–	0.22
Inboard roll	0.22	–	0.23
Outboard plunge	–	0.20	–
Outboard roll	–	0.31	–

Since the plunge and roll tests conducted on the block mass or the X-HALE were recorded or measured using handheld timers, there are numerous sources of error associated with them. Some of them are discussed below:

- The times recorded between the different people observing the rigid body modes varied by up to 10%. This is due to multiple reasons – the manual nature of turning on or off the stopwatch, the lag or delay in response time between people as well as the subjectivity associated with counting the peaks and valleys of the block or aircraft as it plunges or rolls.
- The block mass was created based on the weight of the aircraft divided by two (one block mass supported by each bungee). However, the aircraft's mass is not symmetrically dis-

tributed along its span, and this can cause a difference between the rigid body modes coming from the isolated block mass attached to the bungees compared to the X-HALE.

- The mass of the accelerometers on the aircraft was not modeled in the FEM. This creates modeling errors regarding the impact of the accelerometer mass and their cables on the aircraft.

- The summer weather melted the wax used to connect the accelerometers to the airframe. This was resolved by taping the accelerometers to the airframe, which is different than how they were attached during the laboratory GVT.

- The accelerometer wires leading away from the accelerometers (i.e., the cables in contact with the airframe) were not handled properly and were interfering with the motion of the aircraft during the rigid-body tests. The wires were holding the plane in a non-resting position, introducing additional stiffness to the system. However, even with this increased stiffness (which is only relevant during the rigid body modes where there are large displacements of the structure), the suspension related plunge mode is sufficiently far away from the fundamental elastic mode of the X-HALE.

The results of the free-free GVT on the X-HALE, and the comparisons with the predicted data from the updated FEM are shown in Table 6.15. The outboard configuration was observed to have lower damping in the rigid body modes (more oscillations could be observed visually before reaching equilibrium). Another observation was that the in-plane and torsion dominated modes are harder to identify in the inboard configuration. This can be improved by exciting the structure in the in-plane direction, but since some of the modes were not easily identifiable in the current tests, they are listed as missing here, represented by dashes.

While it can be observed that the bungees were much stiffer than initially predicted (the plunge mode is around 30% higher than predicted, and approximately 20% of the first elastic mode), the elastic results indicate a good match between the GVT and the updated FEM, highlighting the FEM updating process's ability to accurately predict the behavior of the X-HALE in different deformed configurations and under different suspension setups than used to tune the FEM. This demonstrates the ability of the updated FEM to closely match the experimental results, even with significant uncertainties in the bungee stiffness, as well as errors in timing the rigid body modes, or modeling errors regarding the impact of the accelerometer cables on the aircraft. For reference, the initial FEM before being updated was notably worse in predicting the behavior of the X-HALE under the free-free suspension conditions. While some modes were predicted within 3% error, others had errors exceeding 5% between the FEM and the experimental results. Table 6.16 shows

Table 6.15: Results of the X-HALE free-free GVT compared with updated FEM.

		Frequency (Hz)				Difference (%)	
		Updated FEM		GVT		Predicted Num. vs Exp.	
Mode #	**Mode type**	**Inboard**	**Outboard**	**Inboard**	**Outboard**	**Inboard**	**Outboard**
0	Plunge	0.14	0.13	0.21	0.20	−51.7	−45.7
0	Roll	0.15	0.27	0.22	0.31	−43.7	−14.2
1	1 OOP	0.94	0.96	0.95	0.98	−1.0	−1.3
2	2 OOP	2.68	2.69	2.71	2.67	−1.0	0.5
3	1 T/2 IP	4.76	4.28	–	4.22	–	1.3
4	3 OOP	4.43	4.46	4.49	4.46	−1.3	0.0
5	2 T/3 IP	7.04	6.27	7.04	6.36	0.0	−1.5
6	4 OOP	7.21	7.19	7.43	7.32	−3.0	−1.8
7	5 OOP	8.25	8.26	8.38	8.44	−1.5	−2.3

the results of the predicted modes from the initial FEM before the FEM updating compared to the experimental results from the free-free GVT.

Table 6.16: Results of the X-HALE free-free GVT compared with initial FEM.

		Frequency (Hz)				Difference (%)	
		Initial FEM		GVT		Predicted Num. vs Exp.	
Mode #	**Mode type**	**Inboard**	**Outboard**	**Inboard**	**Outboard**	**Inboard**	**Outboard**
0	Plunge	0.14	0.13	0.21	0.20	−51.8	−45.8
0	Roll	0.15	0.28	0.22	0.31	−43.8	−12.2
1	1 OOP	0.91	0.93	0.95	0.98	−5.0	−5.2
2	2 OOP	2.76	2.76	2.71	2.67	1.7	2.9
3	1 T/2 IP	4.77	4.30	–	4.22	–	1.8
4	3 OOP	4.58	4.60	4.49	4.46	1.9	3.0
5	2 T/3 IP	7.03	6.15	7.04	6.36	−0.2	−3.4
6	4 OOP	7.79	7.77	7.43	7.32	4.6	5.7
7	5 OOP	8.74	8.73	8.38	8.44	4.1	3.3

Another point of consideration is that while the bungees were not characterized at their full lengths, the plunge frequencies associated with the bungees allows inferring the stiffness of the actual support setup (bungees hung from the crane with the pulley and winch system). This provided an updated value of the bungee cord stiffnesses, and the numerical results were generated again with the updated bungee stiffness values. The results from the FEM with the updated bungee stiffness compared with the GVT are shown in Table 6.17.

Table 6.17: Results of the X-HALE free-free GVT compared with updated FEM, after modifying the support stiffness in the FEM. The measured bungee stiffnesses at their full lengths were used to run the numerical analysis again.

		Frequency (Hz)				**Difference (%)**	
		Updated FEM		**GVT**		**Predicted Num. vs Exp.**	
Mode #	**Mode type**	**Inboard**	**Outboard**	**Inboard**	**Outboard**	**Inboard**	**Outboard**
0	Plunge	0.17	0.18	0.21	0.20	−18.0	−9.1
0	Roll	0.18	0.32	0.22	0.31	−19.2	2.5
1	1 OOP	0.94	0.97	0.95	0.98	−0.8	−0.6
2	2 OOP	2.69	2.69	2.71	2.67	−0.8	0.5
3	1 T/ 2 IP	4.76	4.28	–	4.22	–	1.3
4	3 OOP	4.43	4.46	4.49	4.46	−1.3	0.0
5	2 T/3 IP	7.04	6.27	7.04	6.36	0.0	−1.5
6	4 OOP	7.22	7.19	7.43	7.32	−2.9	−1.8
7	5 OOP	8.25	8.26	8.38	8.44	−1.5	−2.3

The results in Table 6.17 show a better match for the plunge and the roll modes of the aircraft, and a minor improvement in the matching of the first few elastic modes. The experimental fundamental elastic mode, which was already matching the predicted numerical one quite well, also matches better. The rest of the elastic modes show minor or no improvement. A major source of error here that prevents a better match particularly for the rigid body modes is the fact that the accelerometer wires were interfering with the motion of the aircraft during the rigid-body and impact tests. The wires were holding the plane in a non-resting position, introducing additional stiffness to the system. This impacts both the rigid body and the elastic modes of the X-HALE. This is consistent with the observation in Section 3.2.1 about accelerometer cables from two sets of GVT on the same structure with different wire configurations and how they can influence the results for very flexible structures. A key takeaway from this set of tests is that cable management of the accelerometers can have a non-negligible impact on the response of very flexible structures. In order to obtain more accurate results, the impact of the cables needs to be properly accounted for, by either modeling it in the FEM or by minimizing the contact between the cables and the test structure.

6.5 Concluding Remarks

This chapter presented the application of the GVT and FEM updating methodology on a very flexible aircraft, the University of Michigan's X-HALE. The aircraft was tested in both:

1. Laboratory conditions with a soft suspension using a set of springs and pulleys, and

2. Outside the lab, suspended from a crane in a 'free-free' condition, with a very soft suspension meant to get closer to the free-flying aircraft.

After preliminary characterization of the laboratory GVT rig in order to identify how close the rig's resonance frequencies were to the X-HALE's, a set of springs were selected that provided a soft suspension for the aircraft. A complete decoupling of the suspension and airframe modes cannot be practically achieved for the VFA due to the difficulty in having an order of magnitude of frequency separation while ensuring sufficient spring stiffness. This required modeling the spring and suspension dynamics in the FEM and accounting for the suspension effects during FEM updating. Various GVT were conducted on the airframe in multiple deformed shapes achieved using different suspension locations on the X-HALE. These suspension configurations allow capturing airframe deflections that are at the extremes of the deformations the aircraft normally experiences in flight.

In the lab, the aircraft was excited using both an impact hammer and a shaker. While the shaker is a stronger and cleaner excitation source, the boundary condition imposed by the shaker on the aircraft is difficult to model. There are significant differences between the results from the two excitation mechanisms and the largest source of uncertainty is the shaker attachment to the airframe. Interestingly, the impact test results have a smaller spread (over multiple tests) and generally provide a cleaner FRF, resolving the initial concern of the impulse hammer not providing enough energy to excite the modes of interest on the structure. The aircraft's FEM was updated using results from the laboratory GVT, and a prediction was obtained for the behavior of the aircraft under a free-free configuration. Since it is not possible to have a zero-stiffness suspension in a real GVT, a very soft set of bungee cords suspended from a 100-ft tall crane were used to perform this GVT.

The experimental results from the free-free GVT indicated that the updated FEM was able to match (or predict) the elastic modes of the actual structure within 2% for the first 5 modes. This is promising, especially considering that such an experiment is a substantial effort that had many sources of errors. The following conclusions can be drawn from the set of experiments and computational work performed on the X-HALE:

1. For a VFA, it may not be feasible to create a suspension that allows an order of magnitude separation between the rigid body modes and the fundamental elastic mode of the structure. This requires accounting for the suspension in the FEM. This can be achieved by characterizing the suspension upfront as an isolated component, and adding the suspension characteristics in the FEM of the VFA. The GVT of the X-HALE followed the methodology

proposed in this work, and was successfully able to characterize and model the suspension dynamics for the multiple degree of freedom suspension setup.

2. Since VFA undergo large deflections in their flight regime, the linear, unloaded and undeformed shape is not sufficient to capture the various nonlinearities exhibited by the structure within its operating conditions. The various deformed shapes change the stiffness characteristics of the structure. Due to the ribs separating the upper and lower wingbox skins, significant stresses are developed in the various members during large displacements which lead to local variations in the stiffness of those members (Brazier effect), ultimately affecting the overall modal behavior of the wing around a given deformed state. While the X-HALE does not contain stiffening ribs as part of its construction, the large displacements still cause local variations in the skin and other stiffening elements present in the wings. The FEM updating methodology applied to the X-HALE was modified to account for nonlinearities and local effects coming from the presence of the myriad parts used in its construction.

3. The FEM updating process applied to the X-HALE was performed using the suspension setup from the laboratory GVT and after updating the FEM in the presence of the lab suspension, the springs were removed from the FEM. This FEM was used to create a prediction for the free-free GVT performed on the X-HALE. Figure 6.38 shows the aircraft set up during the free-free GVT. The accelerometer wires' stiffnesses or masses were not accounted for in the computational model and during the tests, the wires were holding the plane in a non-resting position, introducing additional stiffness to the system. These, among others, are sources of error during the one-off experiments performed on the X-HALE and introduce uncertainties on both the experimental and numerical sides.

A free-free GVT on a VFA is a substantial effort and requires more resources than a conventional GVT on a relatively rigid (or moderately flexible) structure. An important consideration is that if such an experimental test can be avoided, it would save time and money. This work demonstrated that by properly characterizing the suspension and structure in a laboratory setting, with a suspension mechanism that does not provide the desired order of magnitude separation between the rigid body and elastic modes, we can recover enough information to truly characterize the VFA structure. Given that the behavior of the structure changes as it undergoes large deflections, different deformed shapes are needed to capture the structural dynamics behavior of such very flexible structures. The FEM updating methodology that allows to simultaneously consider multiple large deformed shapes was applied to update the FEM of the X-HALE, and even with significant sources of error, the updated FEM was able to predict the behavior of the X-HALE within 2% error for the first five modes. This is promising, and the results highlight the ability of the GVT and FEM

Figure 6.38: Side view of the X-HALE and the ground station during the free-free GVT. The accelerometer wires introduced additional stiffness to the system.

updating methodology to sufficiently capture the structural dynamics behavior of the VFA without needing to plan for and conduct a full-scale free-free GVT.

CHAPTER 7

Concluding Remarks

This chapter summarizes the findings from the previous chapters along with highlighting the key takeaways and insights obtained from the various numerical and experimental investigations performed as part of this work. The key contributions of this dissertation are presented based on the challenges posed at the beginning and the supporting results provided throughout the previous chapters. Finally, new research questions that arose throughout the course of this work and recommendations for future work are provided to wrap up the work and leave behind pointers for the next set of tasks to improve upon it.

7.1 Summary and Takeaways

This work investigated the processes of ground vibration testing and finite element model updating, with a focus on very flexible structures and identifying the impact of flexibility and geometric nonlinearities in the process. The studies were conducted on various numerical and experimental test cases with varying levels of flexibility and complexity. The methodologies were demonstrated on linear, conventional structures to confirm compatibility with current, established processes and then extended and applied on unconventional or very flexible structures.

A methodology for GVT of very flexible structures exhibiting large displacements under self-weight in different suspension configurations was introduced, numerically verified and experimentally validated. The impact of the suspension configuration on the modal characterization was studied using suspensions that do not have the conventional order-of-magnitude separation between the suspension mode and the elastic modes of the test structure. Results indicate that once the suspension system is well-characterized experimentally and included in the FEM, the influence of the suspension on the structure is known and can be removed after model updating.

A new methodology was developed to update the finite element models of very flexible wings. These structures can undergo large displacements during normal operating conditions and the deformation subsequently affects the modal parameters. The work described a way to pose and cap-

ture the multiple cases causing large displacements (for instance, cases representing different flight conditions) within the optimization problem and provided details on the optimization problem formulation. The updated models can predict the free-flying response of an aircraft while capturing the effects of both geometric nonlinearities and local effects present in built-up structures.

A 3D-printed swept wing was used as a test case that exhibited low flexibility, but exhibited interesting nonlinearities and challenges regarding modeling and experimental characterization. A series of ground vibration and wind tunnel tests using both conventional and novel instrumentation were performed on the wing. This was one of the first detailed experimental characterization of a 3D-printed swept wing and highlighted significant mismatches between the FEM, the as-designed model, and the as-built structure due to uncertainties in both numerical models and experimental tests. The work performed as part of this dissertation included minimizing the discrepancies and improving confidence in the ability to model 3D-printed structures with large uncertainties in their properties.

A very flexible flying wing, the University of Michigan's X-HALE was used as the most substantial test case. The X-HALE is a structure that exhibits nonlinearities due to its construction and design choices. Its high flexibility, the various complex interconnections present between different segments, and the composite construction are all sources of uncertainty in the structural dynamics characterization process. A series of GVT were performed on the aircraft in the laboratory. These GVT were performed with the aircraft suspended using a suspension system that does not exhibit an order of magnitude difference between the suspension mode and the first elastic mode of the structure. This required characterizing the suspension system and including its model in the FEM. Once this was done, the X-HALE's FEM was updated using the experimental data while considering more than one nonlinearly deformed configuration in the model updating process. After updating the FEM, a prediction was obtained for the 'free-flying' aircraft under a very soft bungee cord based suspension. This suspension did offer nearly an order of magnitude separation between the fundamental elastic mode and the rigid-body suspension mode. The experimental results of this free-free GVT matched the prediction from the updated FEM well (within 2% for the first five elastic modes) indicating that the methodology for both performing the GVT and updating the FEM of very flexible structures works well to accurately capture structural nonlinearities in very flexible wings operating under large deflections and improves upon the established FEM updating technologies when considering very flexible structures.

The following topics were posed as challenges associated with performing GVT and FEM updating and the key conclusions to them are listed here.

1. Suspension design and modeling for approximating free-free boundary conditions: The methodology developed as part of this work involves performing a characterization of the MDOF suspension setup used to suspend very flexible structures. This work expands on

experimental verification of the impact of the suspension system(s) on the structure's modal parameters in the context of very flexible structures suspended using multiple suspension systems. Instead of approximating the impact of the added stiffness and damping on individual modes of the test structure, the suspension system is experimentally characterized, numerically modeled and included in the test structure's finite element model. The approach was verified computationally and validated experimentally on multiple test cases of varying flexibility. Results indicate that the methodology developed as part of this works well to account for the design and modeling of a realistic suspension setup for VFA where a conventional order of magnitude separation is not feasible between the suspension mode and the elastic modes of the test structure.

2. Large deflections experienced based on loading and boundary conditions: This work posed a way to account for large deflections experienced by VFA as a consequence of loading (during flight testing) or as a consequence of boundary conditions (during laboratory tests) in the GVT process. This was theoretically studied, and a methodology for its implementation was developed. Multiple test cases were experimentally studied under various large, nonlinearly deformed configurations and the difference in their response based on level of deformation was investigated, both computationally and experimentally.

3. Finite element model updating for VFA: When a very flexible wing undergoes large displacements as a result of loading, there are two main effects that alter its linearized modal characteristics. First, there are the effects of the nonlinear strain-displacement relation that lead to the presence of the additional tangent stiffness matrix. This term, however, is connected with the linear stiffness matrix through the fixed geometry and material properties. Therefore, once the FEM is tuned at its unstressed state, the global effects of the deformation are correctly accounted for [84]. The second effect is connected with the actual geometry of the wingbox. Due to the rib separating the upper and lower wingbox skins, significant stresses are developed in the various members during large displacements which lead to local variations in the stiffness of those members (Brazier effect), ultimately affecting the overall modal behavior of the wing around a given deformed state. This local effect primarily impacts the stiffness characteristics and does not have a significant effect on the local inertia (local cross-sectional deformations are small due to the presence of the ribs) [85]. It was shown how the developed FEM updating methodology can better capture structural nonlinearities in very flexible wings operating under large deflections and has lower errors for all frequencies compared to the conventional linear, unloaded, and undeformed FEM updating process. Illustrated how the new methodology improves upon the established FEM updating technologies when considering very flexible structures.

4. Finite element model updating considering nonlinearities and novel manufacturing techniques: Adjacent to the FEM updating methodology developed for VFA in this dissertation, the linear, unloaded and undeformed configuration of a low-flexibility wing was used to study the changes needed in the FEM updating process to account for nonlinearities coming from boundary conditions and novel manufacturing techniques. A 3D-printed swept wing was studied both computationally and experimentally. First, the FEM updating process was modified to handle 3D printed structures by introducing different bounds on the design variables associated with the different parts of the structure. Second, experimental tests are conducted to inform the values of the as-built component properties. The FEM was updated using the modified methodology and results indicate good agreement between the experimental GVT and numerical model. It was found that the updated FEM was able to match the results from the structural characterization, however, it failed to capture (or get closer) to the aeroelastic frequencies observed during wind tunnel testing. This indicates the need for better characterization of the boundary condition and incorporating the ability to handle such a nonlinear, load-varying boundary condition within the FEM updating process is a topic left for future work.

7.2 Key Contributions

This work resulted in several contributions that advance the state-of-the-art in the fields of GVT and FEM updating for very flexible structures, with a focus on VFA. A methodology for accounting for the suspension mechanism during GVT and the associated deformed shapes was developed, both during the experimental tests as well as in the computational analyses. Following the modal analyses, a FEM updating process to update the computational models to better reflect the as-built structure's characteristics was developed. The key contributions are highlighted below:

1. Introduced and verified methodology for performing GVT of very flexible structures exhibiting large displacements under normal operation. GVT are typically conducted under an undeformed condition and without accounting for the impact of the suspension in the FEM. In the case of VFA, this conventional strategy does not sufficiently capture the in-flight behavior of the structure, and there is no practical way to decouple the suspension dynamics from the structural dynamics of the test structure. This work introduced and verified a methodology for performing GVT of very flexible structures exhibiting large displacements under self-weight. It also demonstrated how low-stiffness suspension configurations impact the modal characterization of very flexible structures using suspension systems that do not have the conventional order-of-magnitude separation between the suspension mode and the elastic modes of the test structure. A methodology was developed to account for such MDOF

suspension systems by experimentally characterizing, numerically modeling, and including them in the test structure's FEM.

2. Developed, verified and validated a new methodology to update the FEM of very flexible wings. Conventional FEM updating is performed in an undeformed jig shape for the structure and seeks to match the experimental response obtained from a GVT (also performed in an undeformed shape). For VFA, their modal paramenters change based on the deformation, which happens as a consequence of loading or applied boundary conditions. A single undeformed, unloaded condition may no longer sufficient to characterize the structural dynamics of such very flexible structures. This work developed and verified a new methodology to update the FEM of very flexible wings that can undergo large displacements during normal operating conditions, which affects their modal parameters. Described a way to pose and capture the multiple cases causing large displacements within the FEM updating optimization problem and provided details on the optimization problem formulation. Demonstrated applicability of the FEM updating methodology on a very flexible isotropic beam and a complex, built-up FEM of a wing box. Showed how the developed methodology can better capture geometric nonlinearities in very flexible wings operating under large deflections and has lower errors for natural frequencies compared to the conventional linear, unloaded, and undeformed FEM updating process. Illustrated how the new methodology improves upon the established FEM updating technologies when considering very flexible structures. Validated on a very flexible aircraft, the X-HALE, using experimental GVT data collected on the aircraft in multiple deformed configurations.

3. Enhanced the FEM updating process to account for increased uncertainties and material property variabilities coming from the manufacturing process. Performed a detailed experimental characterization of a 3D-printed swept wing. Results highlighted significant mismatches between the FEM, the as-designed model, and the as-built structure due to uncertainties in both numerical models and experimental tests. Proposed and implemented changes in the FEM and experimental setup to minimize the uncertainties for structural dynamics characterization.

4. Validated the GVT and FEM updating methodology on an experimental very flexible aircraft by performing a free-free GVT. A free-free GVT on a VFA is a substantial effort and requires more resources than a conventional GVT on a relatively rigid (or moderately flexible) structure. If such an experimental test can be avoided, it would save time and money. This work demonstrated that by properly characterizing the suspension and structure in a laboratory setting, with a suspension mechanism that does not provide the desired order of magnitude separation between the rigid body and elastic modes, we can still recover enough

information to truly characterize the VFA structure. This was demonstrated by conducting a free-free GVT on the VFA. Even with significant sources of errors during this GVT, and higher suspension stiffness than initially predicted, this work provided results that highlight the ability of the GVT and FEM updating methodology to sufficiently capture the structural dynamics behavior of the VFA without needing to plan for and conduct a full-scale free-free GVT.

7.3 Recommendations for Future Work

During the course of this work, new research questions arose that were beyond the scope of study. Some pertain to improving the quality of the experimental and computational analyses performed as part of this work, while others involve exploring novel ways of collecting experimental data or using multidisciplinary optimization techniques. Recommendations for future work are provided to wrap up the work and leave behind pointers for the next set of tasks to improve upon it.

1. Inclusion of damping in the numerical and experimental studies: Damping may not remain constant with deformation. These effects were not considered in the numerical or experimental models used in this study. The impact of deformation on damping should be investigated further in future work with the X-HALE as a potential numerical and experimental test case.

2. Focus on the optimization part of the FEM updating process: Build on the optimization problem by refining the terms that can be added to the objective function, additional design and/or constraint variables. Stress-testing the algorithm and the FEM updating process to ensure the procedure is robust to different initial conditions and models of varying complexity. Other topics to be explored are file I/O, gradient evaluations, and considering other optimization algorithms (only Nelder-Mead and SLSQP were considered in this work).

3. Handling of boundary conditions in the FEM updating process: Using the data collected from GVT of the relatively rigid, 3D printed A3TB-WT in the laboratory (mounted on a shaker table) and in the wind tunnel (mounted on a pitch-and-plunge apparatus, but without enabling free rigid-body degrees of freedom), the FEM was tuned and preliminary results indicate good agreement between the experimental GVT and numerical model. It was found that the updated FEM was able to match the results from the structural characterization, however, it failed to capture (or get closer) to the aeroelastic frequencies observed during wind tunnel testing. This indicates the need for better characterization of the boundary condition and incorporating the ability to handle such a nonlinear, load-varying boundary condition within the FEM updating process is a topic left for future work.

4. GVT using various novel sensors that can enhance capturing local behaviors: Improve upon the setup, data acquisition and the postprocessing techniques for high-density distributed fiber optic and motion capture systems to better capture the structural dynamic behavior during GVT and aeroelastic behavior during wind tunnel tests for very flexible structures. Sensor fusion — how can we use the fact that we have strains, accelerations and displacements being captured simultaneously from the different instrumentation to improve structural dynamics characterization?

5. Using continuous shape sensing techniques for recovering static and dynamic behavior during GVT of very flexible structures: Development of optimal fiber placement strategy for structural dynamics characterization using distributed strain sensing optical fibers. Define feasibility of (and demonstrate experimentally) recovering modal parameters from a GVT conducted using distributed strain sensing optical fibers.

BIBLIOGRAPHY

[1] Noll, T. E., Brown, J. M., Perez-davis, M. E., Ishmael, S. D., Tiffany, G. C., and Gaier, M., "Investigation of the Helios Prototype Aircraft Mishap," *Volume I Mishap Report*, Vol. I, No. January, 2004, pp. 100.

[2] Sharqi, B. and Cesnik, C. E. S., "Ground Vibration Testing on Very Flexible Aircraft," *AIAA Scitech Forum*, Orlando, FL, Jan. 2020.

[3] Böswald, M., Govers, Y., Vollan, A., and Basien, M., "Solar impulse - How to Validate the Numerical Model of a Superlight Aircraft with A340 Dimensions!" *Proceedings of ISMA 2010 - International Conference on Noise and Vibration Engineering*, Leuven, Belgium, Oct. 2010, pp. 2451–2466.

[4] Ben-Asher, T. and Raveh, D. E., "Improvements to Wind-Tunnel Flutter Prediction with Application to the Active Aeroelastic Aircraft Testbed Wind-Tunnel Model," *AIAA Scitech Forum*, Maryland, Jan. 2023.

[5] Hall, D. W., Fortenbach, C. D., Dimiceli, E. V., and Parks, R. W., "A Preliminary Study of Solar Powered Aircraft and Associated Power Trains," Tech. rep., NASA CR 3699, Dec. 1983.

[6] Zerweckh, S., von Flotow, A., and E. Murray, J., "Flight Testing a Highly Flexible Aircraft - Case Study on the MIT Light Eagle," *Journal of Aircraft*, Vol. 27, No. 4, May 1990, pp. 342–349.

[7] van Schoor, M. and von Flotow, A., "Aeroelastic Characteristics of a Highly Flexible Aircraft," *Journal of Aircraft*, Vol. 27, No. 10, Oct. 1990, pp. 901–908.

[8] Covioli, J. V. and Coppotelli, G., "Experimental and Operational Modal Analysis in Support of Modal Model Updating - A Test Case," *8th IOMAC - International Operational Modal Analysis Conference, Proceedings*, Oct. 2019, pp. 283–293.

[9] Mezzapesa, S., Arras, M., Coppotelli, G., Miller, J., Valyou, D. N., and Marzocca, P., "Correlation and Updating of an Unmanned Aerial Vehicle Finite Element Model," *56th AIAA/ASCE/AHS/ASC Structures, Structural Dynamics, and Materials Conference*, Kissimmee, FL, Jan. 2015.

[10] Cesnik, C. E. S., Senatore, P. J., Su, W., Atkins, E. M., and Shearer, C. M., "X-HALE: A Very Flexible Unmanned Aerial Vehicle for Nonlinear Aeroelastic Tests," *AIAA Journal*, Vol. 50, No. 12, 2012, pp. 2820–2833.

[11] Koksal, S., Yildiz, E. N., Yazicioglu, Y., and Ozgen, G. O., "Minimization of Ground Vibration Test Configurations for F-16 Aircraft by Subtractive Modification," *Shock and Vibration*, Vol. 2019, 2019.

[12] Herbut, A., Rybak, J., and Brząkała, W., "On a sensor placement methodology for monitoring the vibrations of horizontally excited ground," *Sensors (Switzerland)*, Vol. 20, No. 7, 2020.

[13] Nedoma, J., Stolarik, M., Kepak, S., Pinka, M., Martinek, R., Frnda, J., and Fridrich, M., "Alternative approaches to measurement of ground vibrations due to the vibratory roller: A pilot study," *Sensors (Switzerland)*, Vol. 19, No. 24, 2019, pp. 1–17.

[14] Pickrel, C. R., "Airplane Ground Vibration Testing - Nominal Modal Model Correlation," *Sound and Vibration*, Vol. 36, Nov. 2002, pp. 18–23.

[15] Peeters, B., Debille, J., and Climent, H., "Modern Solutions for Ground Vibration Testing of Small, Medium and Large Aircraft," *SAE International Journal of Aerospace*, Vol. 1, No. 1, 2008, pp. 732–742.

[16] Göge, D., Lubrina, P., Böswald, M., and Füllekrug, U., "Ground Vibration Testing of Large Aircraft - State-of-the-Art and Future Perspectives," *Proceedings of IMAC XXV*, Orlando, FL, Feb. 2007.

[17] Lo, W., Shih, C., and Hinote, G., "Ground Vibration Test of a Commercial Aircraft," *Proceedings of SPIE*, Vol. 4359, Society of Photo-Optical Instrumentation Engineers, Feb. 2001, pp. 92–97.

[18] Pickrel, C. R., Foss, G. C., Phillips, A., Allemang, R. J., and Brown, D. L., "New Concepts in Aircraft Ground Vibration Testing," *Sound and Vibration*, Vol. 40, Oct. 2006, pp. 12–18.

[19] Chang, C.-S., Hodges, D. H., and Patil, M., "Flight Dynamics of Highly Flexible Aircraft," *Journal of Aircraft*, Vol. 45, No. 2, March 2008, pp. 538–545.

[20] Charmbalis, G. and Cooper, J. E., "Vibration Testing of Aeroelastic Structures Containing Geometric Stiffness Nonlinearities," *54th AIAA/ASME/ASCE/AHS/ASC Structures, Structural Dynamics, and Materials Conference*, April 2013.

[21] Xie, C., Liu, Y., Yang, C., and Cooper, J., "Geometrically Nonlinear Aeroelastic Stability Analysis and Wind Tunnel Test Validation of a Very Flexible Wing," *Shock and Vibration*, Vol. 2016, Jan. 2016, pp. 1–17.

[22] Britt, R., Ortega, D., Mc Tigue, J., and Scott, M., "Wind Tunnel Test of a Very Flexible Aircraft Wing," *53rd AIAA/ASME/ASCE/AHS/ASC Structures, Structural Dynamics and Materials Conference*, AIAA, Honolulu, HI, April 2012.

[23] Kehoe, M. W., "Aircraft Ground Vibration Testing at NASA Ames-Dryden Flight Research Facility," Tech. rep., NASA TM-88272, July 1987.

[24] Woehrle, T. G., Costerus, B. W., and Lee, C. L., "Modal Analysis of PATHFINDER Unmanned Air Vehicle," *Proceedings of IMAC XIII*, Nashville, TN, Feb. 1995.

[25] Whitney, M. J., Panza, J. L., and Brillhart, R. D., "GVT Suspension Effects On Correlation Of The Predator B Vehicle," *Proceedings of IMAC XX*, Los Angeles, CA, Feb. 2002.

[26] Chang, C.-S. and Hodges, D., "Modeling of Ground Vibration Testing for Highly Flexible Aircraft," *47th AIAA/ASME/ASCE/AHS/ASC Structures, Structural Dynamics, and Materials Conference*, AIAA, Newport, Rhode Island, May 2006.

[27] Chang, C.-S. and Hodges, D. H., "Parametric Studies on Ground Vibration Test Modeling for Highly Flexible Aircraft," *Journal of Aircraft*, Vol. 44, No. 6, Nov. 2007, pp. 2049–2059.

[28] Böswald, M., Vollan, A., Govers, Y., and Frei, P., "Solar Impulse – Ground Vibration Testing and Finite Element Model Validation of a Lightweight Aircraft," *International Forum of Aeroelasticity and Structural Dynamics*, Paris, France, June 2011.

[29] Goege, D., Fuellekrug, U., Sinapius, M., Link, M., and Gaul, L., "Advanced Test Strategy for Identification and Characterization of Nonlinearities of Aerospace Structure," *AIAA Journal*, Vol. 43, No. 5, May 2005, pp. 974–986.

[30] Masri, S. and K. Caughey, T., "A Nonparametric Identification Technique for Nonlinear Dynamic Problems," *Journal of Applied Mechanics*, Vol. 46, No. 2, June 1979, pp. 433–447.

[31] Dossogne, T., Noël, J., Grappasonni, C., Kerschen, G., Peeters, B., Debille, J., Vaes, M., and Schoukens, J., "Nonlinear Ground Vibration Identification of an F-16 Aircraft - Part II Understanding Nonlinear Behaviour in Aerospace Structures Using Sine-sweep Testing," *Proceedings of IFASD 2015*, Saint Petersburg, Russia, June 2015.

[32] Böswald, M., Schwochow, J., Jelicic, G., and Govers, Y., "New Concepts for Ground and Flight Vibration Testing of Aircraft based on Output-Only Modal Analysis," *Proceedings of the 7th International Operational Modal Analysis Conference (IOMAC)*, Ingolstadt, Deutschland, May 2017.

[33] Wolf, J. A., "The Influence of Mounting Stiffness On Frequencies Measured In a Vibration Test," *SAE Technical Paper Series*, SAE International, Feb. 1984.

[34] Carne, T. G., Griffith, D. T., and Casias, M. E., "Support Conditions for Experimental Modal Analysis," *Sound and Vibration*, Vol. 41, No. 6, June 2007, pp. 10–16.

[35] Brillhart, R., Napolitano, K., Morgan, L., and LeBlanc, R., "Advanced GVT testing of the Gulfstream G650," *Sound and Vibration*, Vol. 45, No. 8, 2011, pp. 6–9.

[36] Jones, J. and Cesnik, C. E. S., "Preliminary Flight Test Correlations of the X-HALE Aeroelastic Experiment," *Aeronautical Journal of The Royal Aeronautical Society*, Vol. 119, No. 1217, July 2015, pp. 855–870.

[37] Ewins, D. J. and Saunders, H., "Modal Testing: Theory and Practice," *Journal of Vibration and Acoustics*, Vol. 108, No. 1, Jan. 1986, pp. 109–110.

[38] Sharqi, B. and Cesnik, C. E. S., "Finite Element Model Updating for Very Flexible Wings," *Journal of Aircraft*, Vol. 60, No. 2, March 2023, pp. 476–489.

[39] Peeters, B., Debille, J., and Climent, H., "Modern Solutions for Ground Vibration Testing of Small, Medium and Large Aircraft," *SAE International Journal of Aerospace*, Vol. 1, No. 1, Aug. 2008, pp. 732–742.

[40] Pak, C. G. and Truong, S., "Creating a Test Validated Structural Dynamic Finite Element Model of the X 56A Aircraft," *15th AIAA/ISSMO Multidisciplinary Analysis and Optimization Conference*, June 2014.

[41] Ereiz, S., Duvnjak, I., and Fernando Jiménez-Alonso, J., "Review of Finite Element Model Updating Methods for Structural Applications," *Structures*, Vol. 41, July 2022, pp. 684–723.

[42] Li, D. and Zhang, J., "Finite Element Model Updating Through Derivative-Free Optimization Algorithm," *Mechanical Systems and Signal Processing*, Vol. 185, Feb. 2023.

[43] Giclais, S., Lubrina, P., Stéphan, C., Böswald, M., Govers, Y., Ufer, J., and Botargues, N., "New Excitation Signals for Aircraft Ground Vibration Testing," *International Forum on Aeroelasticity and Structural Dynamics*, Paris, France, June 2011.

[44] Rizzo, D. and Blackburn, M., "The History of a Decision: A Standard Vibration Test Method for Qualification," *Journal of the IEST*, Vol. 60, Jan. 2017, pp. 9–20.

[45] Plevris, V. and Markeset, G., "Educational Challenges in Computer-Based Finite Element Analysis and Design of Structures," *Journal of Computer Science*, Vol. 14, No. 10, 2018, pp. 1351–1362.

[46] Inman, D. J. and Minas, C., "Matching Analytical Models with Experimental Modal Data in Mechanical Systems," *Control and Dynamic Systems*, Elsevier, 1990, pp. 327–363.

[47] Lung, S.-F. and Pak, C.-G., "Updating the Finite Element Model of the Aerostructures Test Wing Using Ground Vibration Test Data," *50th AIAA/ASME/ASCE/AHS/ASC Structures, Structural Dynamics, and Materials Conference*, Palm Springs, CA, May 2009.

[48] Živanović, S., Pavic, A., and Reynolds, P., "Finite Element Modelling and Updating of a Lively Footbridge: The Complete Process," *Journal of Sound and Vibration*, Vol. 301, No. 1-2, March 2007, pp. 126–145.

[49] Jin, S. S., Cho, S., Jung, H. J., Lee, J. J., and Yun, C. B., "A New Multi-Objective Approach to Finite Element Model Updating," *Journal of Sound and Vibration*, Vol. 333, No. 11, 2014, pp. 2323–2338.

[50] Mottershead, J. E. and Friswell, M. I., "Model Updating in Structural Dynamics: A Survey," *Journal of Sound and Vibration*, Vol. 167, No. 2, 1993, pp. 347–375.

[51] Girardi, M., Padovani, C., Pellegrini, D., Porcelli, M., and Robol, L., "Finite Element Model Updating for Structural Applications," *Journal of Computational and Applied Mathematics*, Vol. 370, May 2020, pp. 112675.

[52] Cecrdle, J., "Updating of Dynamic Model of Aircraft Structure with Wing Tip-tanks According to Results of Ground Vibration Test," *AIAA Scitech Forum*, San Diego, CA, Jan. 2019.

[53] Gupta, A., Moreno, C. P., Pfifer, H., Taylor, B., and Balas, G. J., "Updating a Finite Element Based Structural Model of a Small Flexible Aircraft," *AIAA Modeling and Simulation Technologies Conference*, Kissimmee, FL, Jan. 2015.

[54] Schedlinski, C., Wagner, F., Bohnert, K., Frappier, J., Irrgang, A., Lehmann, R., and Müller, A., "Test-Based Computational Model Updating of a Car Body in White," *Sound and Vibration*, Vol. 39, No. 9, 2005, pp. 19–23.

[55] Chen, H.-P. and Ni, Y.-Q., "Finite Element Model Updating," *Structural Health Monitoring of Large Civil Engineering Structures*, John Wiley & Sons, Ltd, Feb. 2018, pp. 123–154.

[56] Sabatini, M., Gasbarri, P., Palmerini, G. B., and Monti, R., "Operational Modal Analysis via Image Based Technique of Very Flexible Space Structures," *Acta Astronautica*, Vol. 89, 2013, pp. 139–148.

[57] Pai, P. F., *Highly Flexible Structures : Modeling , Computation , and Experimentation*, AIAA Education Series, AIAA, 2007.

[58] Gold, R. R., Friedman, I. P., Reed III, W. H., and Hallauer, W. L., "Suspension Systems for Ground Testing Large Space Structures," Tech. rep., NASA-CR-4325, Oct. 1990.

[59] Cooley, V. and Giunta, A., "Laboratory Evaluation of Two Advanced Suspension Devices for Ground Vibration Testing of Large Space Structures," *AIAA/ASME/ASCE/AHS/ASC Structures, Structural Dynamics and Materials Conference*, Dallas, TX, Jan. 1992.

[60] Zhao, W., Muthirevula, N., Kapania, R. K., Gupta, A., Regan, C. D., and Seiler, P. J., "Finite Element Model Updating of A Small Flexible Composite UAV," *AIAA Atmospheric Flight Mechanics Conference*, American Institute of Aeronautics and Astronautics, Jan. 2017.

[61] Holmberg, E., "FE-Model Update After GVT of a Gripen E Test Aircraft," *International Forum on Aeroelasticity and Structural Dynamics*, Savannah, GA, June 2019.

[62] Govers, Y. and Link, M., "Model Updating Using Uncertain Experimental Modal Data," *International Forum on Aeroelasticity and Structural Dynamics*, Paris, France, June 2011.

[63] Prananta, B. B., Kanakis, A., Vankan, W. J., and Houten, M. H. V., "Model Updating of Small Aircraft Dynamic Finite Element Model Using Standard Finite Element Software," Tech. rep., NLR-TP-2014-511, May 2014.

[64] Prananta, B., Kanakis, T., Vankan, J., and Van Houten, R., "Model Updating of Finite Element Model Using Optimisation Routine," *Aircraft Engineering and Aerospace Technology*, Vol. 88, No. 5, 2016, pp. 665–675.

[65] Cesnik, C. E. S., Palacios, R., and Reichenbach, E. Y., "Reexamined Structural Design Procedures for Very Flexible Aircraft," *Journal of Aircraft*, Vol. 51, No. 5, Sept. 2014, pp. 1580–1591.

[66] van de Werken, N., Hurley, J., Khanbolouki, P., Sarvestani, A. N., Tamijani, A. Y., and Tehrani, M., "Design Considerations and Modeling of Fiber Reinforced 3D Printed Parts," *Composites Part B: Engineering*, Vol. 160, 2019, pp. 684–692.

[67] Ning, F., Cong, W., Qiu, J., Wei, J., and Wang, S., "Additive Manufacturing of Carbon Fiber Reinforced Thermoplastic Composites using Fused Deposition Modeling," *Composites Part B: Engineering*, Vol. 80, 2015, pp. 369–378.

[68] Tahmasebinia, F., Jabbari, A. A., and Skrzypkowski, K., "The Application of Finite Element Simulation and 3D Printing in Structural Design within Construction Industry 4.0," *Applied Sciences*, Vol. 13, No. 6, 2023.

[69] Shu, J., Luo, H., Zhang, Y., and Liu, Z., "3D Printing Experimental Validation of the Finite Element Analysis of the Maxillofacial Model," *Frontiers in Bioengineering and Biotechnology*, Vol. 9, July 2021, pp. 1–7.

[70] Aimar, A., Palermo, A., and Innocenti, B., "The Role of 3D Printing in Medical Applications: A State of the Art," *Journal of Healthcare Engineering*, Vol. 2019, 2019, pp. 1–10.

[71] Abbot, D., Kallon, D., Anghel, C., and Dube, P., "Finite Element Analysis of 3D Printed Model via Compression Tests," *Procedia Manufacturing*, Vol. 35, 2019, pp. 164–173.

[72] Ferreira, R. T. L., Amatte, I. C., Dutra, T. A., and Bürger, D., "Experimental Characterization and Micrography of 3D Printed PLA and PLA Reinforced with Short Carbon Fibers," *Composites Part B: Engineering*, Vol. 124, 2017, pp. 88–100.

[73] Molitch-Hou, M., "FEA Analysis and Predicting the Performance of 3D Printing," Nov. 2016.

[74] Zarbakhsh, J., Iravani, A., and Amin-Akhlaghi, Z., "Sub-Modeling Finite Element Analysis of 3D printed structures," *16th International Conference on Thermal, Mechanical and Multi-Physics Simulation and Experiments in Microelectronics and Microsystems, EuroSimE*, 2015, pp. 3–6.

[75] Kashama Guzunza, M., Ozcelik, O., Yucel, U., and Girgin, O., "Application of Optimization Based Finite Element Model Updating Method On 3D Printed Model Structures," 2^{nd} *International Conference on Research in Science, Engineering and Technology*, Paris, France, Nov. 2019.

[76] Wynne, Z., Buchanan, C., Kyvelou, P., Gardner, L., Kromanis, R., Stratford, T., and Reynolds, T. P., "Dynamic Testing and Analysis of the World's First Metal 3D Printed Bridge," *Case Studies in Construction Materials*, Vol. 17, Oct. 2022, pp. e01541.

[77] Gupta, A., J. Seiler, P., and Danowsky, B., "Ground Vibration Tests on a Flexible Flying Wing Aircraft," *AIAA Atmospheric Flight Mechanics Conference*, San Diego, CA, Jan. 2016, AIAA 2016-1753.

[78] Peeters, B., Guillaume, P., Van der Auweraer, H., Cauberghe, B., Verboven, P., and Leuridan, J., "Automotive and Aerospace Applications of the PolyMAX Modal Parameter Estimation Method," *Proceedings of IMAC XXII*, Dearborn, MI, Jan. 2004.

[79] Peeters, B., Lowet, G., Van der Auweraer, H., and Leuridan, J., "A New Procedure for Modal Parameter Estimation," *Sound and Vibration*, Vol. 38, No. 1, Jan. 2004, pp. 24–29.

[80] Zhao, W., Gupta, A., Miglani, J., Regan, C. D., Kapania, R. K., and Seiler, P. J., "Finite Element Model Updating of Composite Flying-wing Aircraft using Global/Local Optimization," *AIAA Scitech Forum*, San Diego, CA, Jan. 2019.

[81] Pastor, M., Binda, M., and Harčarik, T., "Modal Assurance Criterion," *Procedia Engineering*, Vol. 48, 2012, pp. 543–548.

[82] Anon, "Test Requirements for Launch, Upper-Stage, and Space Vehicles," Tech. rep., MIL-STD-1540C, Sec. 6.2.10, Sept. 1994.

[83] Anon, "Load Analysis of Spacecraft and Payloads," Tech. rep., NASA STD-5002, Sec. 4.2.6.d, June 1996.

[84] Wan, Z. and Cesnik, C. E. S., "Geometrically Nonlinear Aeroelastic Scaling for Very Flexible Aircraft," *AIAA Journal*, Vol. 52, No. 10, 2014, pp. 2251–2260.

[85] Medeiros, R., Cesnik, C. E. S., Stodieck, O., Calderon, D., Cooper, J. E., and Coetzee, E. B., "Comparison of Structural Model Reduction Methods Applied to a Large-Deformation Wing Box," *The Aeronautical Journal*, Vol. 125, No. 1292, 2021, pp. 1687–1709.

[86] Lupp, C. A. and Cesnik, C. E. S., "An Efficient Algorithm for Determining Flutter of Geometrically Nonlinearly Deformed Aircraft," *6th Aircraft Structural Design Conference*, Bristol, England, Oct. 2018.

[87] Lupp, C. A., "MTK: The Modal Toolkit library," https://github.com/chrislupp/MTK, 2017–2019.

[88] Doyle, S., "PyNastran," https://github.com/SteveDoyle2/pyNastran, 2021.

[89] Ambur, D., Kegelman, J., and Kilgore, W., "Langley Ground Facilities and Testing in the 21st Century," *48th AIAA Aerospace Sciences Meeting Including the New Horizons Forum and Aerospace Exposition*, Orlando, FL, Jan. 2010.

[90] Greenwell, D., "Transonic Industrial Wind Tunnel Testing in the 2020s," *The Aeronautical Journal*, 2021, pp. 1–27.

[91] Weber, S., Kissinger, T., Chehura, E., Staines, S., Barrington, J., Mullaney, K., Fragonara, L. Z., Petrunin, I., James, S., Lone, M., and Tatam, R., "Application of Fibre Optic Sensing Systems to Measure Rotor Blade Structural Dynamics," *Mechanical Systems and Signal Processing*, Vol. 158, 2021, pp. 107758.

[92] Joels, T., Mayer, A., Edery-Azulay, L., and Raveh, D. E., "Design, Analysis, and Testing of the Active Aeroelastic Aircraft Testbed (A3TB) Platform," *AIAA Scitech 2021 Forum*, 2021.

[93] Sharqi, B., Cesnik, C. E. S., Yechieli, N., Mallik, W., Raveh, D. E., and Karpel, M., "Aeroelastic Analyses of the Free Flight of the Active Aeroelastic Aircraft Testbed (A3TB) Platform," *AIAA Scitech 2021 Forum*, 2021.

[94] Burnett, E. L., Beranek, J. A., Holm-Hansen, B. T., Atkinson, C. J., and Flick, P. M., "Design and Flight Test of Active Flutter Suppression on the X-56A Multi-Utility Technology Test-Bed Aircraft," *Aeronautical Journal*, Vol. 120, No. 1228, May 2016, pp. 893–909.

[95] Karpel, M., Mccrink, M., Heidersbach, R., and Seth, D., "Safe Wind Tunnel Flutter Test Using a Shaker and Mass Margins," *International Forum on Aeroelasticity and Structural Dynamics*, Madrid, Spain, June 2022.

[96] Sharqi, B., Cesnik, C. E. S., Joels, T., and Raveh, D. E., "3D-Printed Swept-Wing Wind Tunnel Model Characterization for Aeroelastic Studies," *International Forum on Aeroelasticity and Structural Dynamics*, Madrid, Spain, June 2022.

[97] Roizner, F., Raveh, D. E., and Karpel, M., "Safe Flutter Tests Using Parametric Flutter Margins," *Journal of Aircraft*, Vol. 56, No. 1, 2019, pp. 228–238.

[98] de Boer, S., Karpel, M., and Sodja, J., "Safe Flutter Determination for Wings Undergoing Large Deflections," *AIAA SciTech Forum*, Reno, MD, Jan. 2023.

[99] Iannelli, A., Marcos, A., and Lowenberg, M., "Study of Flexible Aircraft Body Freedom Flutter with Robustness Tools," *Journal of Guidance, Control, and Dynamics*, Vol. 41, No. 5, 2018, pp. 1083–1094.

[100] Schäfer, D., Vidy, C., Mack, C., and Arnold, J., "Assessment of Body-Freedom Flutter for an Unmanned Aerial Vehicle," *CEAS Aeronautical Journal*, Vol. 10, No. 3, 2019, pp. 845–857.

[101] Yechieli, N., "Modeling and aeroelastic investigation of the A3TB," Tech. rep., Technion Israel institute of technology, Dec. 2019.